Characterization of laser-driven neutron emissions

Ronan Lelievre

To cite this version:

Ronan Lelievre. Characterization of laser-driven neutron emissions. Nuclear Experiment [nucl-ex]. Institut Polytechnique de Paris, 2024. English. NNT : 2024IPPAX104 . tel-04957025

HAL Id: tel-04957025
https://theses.hal.science/tel-04957025v1

Submitted on 19 Feb 2025

NNT : 2024IPPAX104

Thèse de doctorat

Characterization of laser-driven neutron emissions

Thèse de doctorat de l'Institut Polytechnique de Paris
préparée à l'École Polytechnique

École doctorale n°626 - Ecole Doctoral de l'Institut Polytechnique de Paris (ED IP Paris)
Spécialité de doctorat : Physique

Thèse présentée et soutenue à Palaiseau, le 26/11/2024, par

Ronan Lelièvre

Composition du Jury :

Ishay Pomerantz Professeur, Tel Aviv University	Président
Vincent Gressier Directeur du Département des Rayonnements Ionisants, BIPM *Absent lors de la soutenance*	Rapporteur
Jörg Schreiber Professeur, Ludwig-Maximilians Universität München	Rapporteur
Laurent Gremillet Ingénieur-chercheur, CEA	Examinateur
Satyabrata Kar Professeur, Queen's University Belfast	Examinateur
Ishay Pomerantz Professeur, Tel Aviv University	Examinateur
Julien Fuchs Directeur de recherche, École Polytechnique	Directeur de thèse
Quentin Ducasse Ingénieur-chercheur, IRSN	Co-Encadrant de thèse
Amokrane Allaoua Chercheur/Responsable de laboratoire, IRSN	Invité

“… The Earth is a very small stage in a vast cosmic arena. Think of the rivers of blood spilled by all those generals and emperors so that, in glory and triumph, they could become the momentary masters of a fraction of a dot. Think of the endless cruelties visited by the inhabitants of one corner of this pixel on the scarcely distinguishable inhabitants of some other corner, how frequent their misunderstandings, how eager they are to kill one another, how fervent their hatreds.

Our posturings, our imagined self-importance, the delusion that we have some privileged position in the Universe, are challenged by this point of pale light. Our planet is a lonely speck in the great enveloping cosmic dark. In our obscurity, in all this vastness, there is no hint that help will come from elsewhere to save us from ourselves…”

Carl Sagan

Acknowledgements

With these few words, I would like to express my gratitude to those who contributed directly or indirectly to this thesis. First, I would like to thank Julien Fuchs for trusting me and offering me the extraordinary opportunity to work on this thesis subject. This not only allowed me to explore an exciting field of research, but also helped me considerably develop my skills, both professionally and personally. Of course, I would like to express my thanks to Quentin Ducasse, Amokrane Allaoua, François Trompier and Thibaut Vinchon, with whom it was always a pleasure to exchange ideas, their supervision and advices were also invaluable.

I acknowledge the LULI research lab (CNRS) where part of this thesis was carried out, and especially the SPRINT team (Weipeng Yao, Tessa Waltenspiel, and Konstantin Burdonov) for their help. I also extend my gratitude to the LMDN research lab (IRSN), which welcomed me several times over the past three years. In particular, I thank François Vianna-Legros, Richard Babut, Fabrice Ayad, Mikael Cardot-Martin and Michael Petit, without whom the experiments performed at the AMANDE facility would not have been possible. I would also like to acknowledge the LDRI research lab (IRSN), especially François Trompier and Yoann Ristic, for providing equipment and sharing their valuable knowledge.

I am very grateful to everyone who assisted me in preparing and conducting the experiments at different laser facilities, thus contributing to their success. I am particularly thinking of Edouard Veuillot, Jean-Philippe Delaneau, Christophe Evrard, Franck Goupille and all the staff of the Apollon facility. Additionally, I would like to thank Elias Catrix, Simon Vallières, Sylvain Fourmaux and Patrizio Antici for their assistance at the ALLS facility, as well as Guillaume Boutoux, Lucas Ribotte, Xavier Davoine, Emmanuel d'Humières and Christophe Rousseaux at the LMJ-PETAL facility.

I would also like to thank Ferid Haddad, Laurent Perrigaud and all the SPR team of ARRONAX who were the first to give me the opportunity to work in a scientific research environment and have always encouraged me to continue along this path.

Finally, I warmly thank my friends and family for their support.

Résumé

Les lasers ultra-intenses représentent un nouveau moyen de produire des champs neutroniques, plus compacte que les réacteurs nucléaires ou les accélérateurs, et avec des contraintes radiologiques moindres. Le champ électrique créé par une impulsion laser ultra-intense au sein d'une cible de taille micrométrique peut atteindre plusieurs TV/m, permettant l’accélération de protons de plusieurs dizaines de MeV. Ces protons, en interagissant avec une seconde cible appelée convertisseur, induisent des réactions nucléaires émettant des neutrons. Cette technique, dite du « pitcher-catcher », est ainsi capable de générer des flux de neutrons rapides très intenses ($> 10^{17}$ n/cm²/s) à des énergies allant jusqu’à plusieurs dizaines de MeV. Cela ouvre la voie à diverses applications, telles que l’imagerie neutronique ou la reproduction en laboratoire du processus rapide de nucléosynthèse, responsable de la création des éléments les plus lourds dans l’Univers.

Pour démontrer la faisabilité de ces applications et garantir la radioprotection de ces installations laser, il est nécessaire de bien caractériser ces champs neutroniques. Les détecteurs passifs, ou munis d’une électronique ultra-rapide, semblent être des candidats de choix pour s’adapter aux caractéristiques des sources de neutrons produites par laser (émissions très brèves et intenses, environnement bruité, …). Ce travail de thèse s'articule donc autour de la poursuite du développement d’un spectromètre neutron par activation (SPAC), particulièrement adapté pour mesurer des champs neutroniques intenses avec une forte composante gamma. En complément d’un travail de simulation des termes sources attendues et de la réponse des détecteurs via l’utilisation des codes Monte-Carlo Geant4 et MCNP, des dosimètres à bulles, un dispositif de Temps de Vol ainsi que des échantillons d’activation ont été utilisés sur diverses installations laser telles que ALLS (Canada) et Apollon (France), afin d’optimiser et de caractériser les émissions neutroniques générées.

Dans la première partie cette thèse, les propriétés des neutrons et leurs différents mécanismes d’interaction avec la matière sont présentés. Cette section aborde également les principales applications des neutrons ainsi que les caractéristiques des sources conventionnelles comme les réacteurs nucléaires, les accélérateurs ou les sources isotopiques. Une attention particulière est portée sur les sources de neutrons générées par laser, en détaillant les principes sous-jacents de la technologie laser, des mécanismes d’accélération des ions et de production de champs neutroniques. Un état de l’art de ces nouvelles sources de neutrons est proposé, avec des informations quantitatives sur leurs capacités, dont la comparaison avec les sources conventionnelles permet de mettre en lumière les avantages et inconvénients de ces sources de neutrons générées par laser.

La seconde partie se concentre sur les techniques de détection des neutrons adaptées aux caractéristiques des émissions de neutrons produites par laser. Le fonctionnement des détecteurs de traces, des détecteurs à bulles, des scintillateurs et des échantillons d’activation y est détaillé. Un accent particulier est mis sur le développement d’un spectromètre neutron par activation (SPAC), permettant de déterminer la distribution en énergie des neutrons dans un environnement bruité (rayons X/gamma, ondes électromagnétiques, …). Les matériaux les plus adaptés pour constituer le SPAC ont été sélectionnés grâce à l’étude de leurs propriétés physico-chimiques, tandis que des simulations Monte-Carlo ont été réalisées pour définir la géométrie optimale de ce nouvel outil diagnostic et calculer sa matrice de réponse.

Enfin, la dernière partie présente les résultats expérimentaux de la caractérisation des émissions de neutrons générées sur différentes installations laser. Un rendement neutronique de 5×10^{5} neutrons/tir et une fluence de 1.4×10^{5} neutrons/sr/tir ont été obtenus sur l’installation ALLS, délivrant une énergie laser de seulement 3,2 J sur cible. En comparaison, les expériences menées sur l’installation Apollon ont révélé un rendement neutronique de 4×10^{7} neutrons/tir et une fluence de 5×10^{6} neutrons/sr/tir avec le faisceau secondaire F2, délivrant une énergie laser de 10,9 J. Des valeurs presque dix fois supérieures ont ensuite été mesurées lorsque le faisceau principal F1 a été utilisé, bien que celui-ci ne délivre que quatre fois plus d’énergie laser. En outre, grâce à l’utilisation d’un

double miroir plasma, ces travaux montrent également l'importance du contraste temporel du laser pour réduire l'épaisseur des cibles pouvant être utilisées, réduisant ainsi les émissions de rayons X générées par rayonnement de freinage et ce, sans en affecter la production de neutrons. Ce dispositif a donc démontré sa capacité à ajuster le ratio rayons X/neutrons, ce qui pourrait être intéressant pour effectuer de la radiographie combinée.

En conclusion, cette thèse met en évidence la forte dépendance de la production de neutrons à l'énergie laser et la non-linéarité de leur relation, la production de neutrons évoluant à la puissance 2,5 de l'énergie laser. Le potentiel de ces sources de neutrons générées par laser est alors mis en perspective avec des applications d'ores et déjà envisageables ou futures, en considérant également quelques développements technologiques possibles pour optimiser ces sources et les rendre compétitives avec les sources conventionnelles, notamment via l'utilisation de convertisseurs multicouches ou en augmentant la fréquence des tirs.

Contents

Introduction

Neutrons, unlike charged particles or electromagnetic radiation, interact primarily with atomic nuclei rather than electron clouds. This unique property allows neutrons to penetrate deeply into materials without being significantly absorbed or deflected by electrons, making their interaction with matter fundamentally different from that of X-rays. While X-rays are particularly sensitive to high-Z elements due to their interactions with electron clouds, they often struggle to resolve light elements or penetrate thick, dense materials. Conversely, neutrons interact more effectively with lighter elements, such as hydrogen, and can penetrate materials opaque to X-rays. Additionally, neutrons can provide valuable insights into material properties, through elemental and temperature analysis, making them highly complementary to X-rays. Thus, neutrons play a crucial role in various scientific and industrial fields, ranging from biology [1, 2] to archaeology [3, 4] and homeland security [5, 6], offering unique material analysis capabilities through different techniques such as neutron imaging, neutron scattering and activation analysis.

Conventionally, neutrons are produced using a variety of sources, each with its own set of advantages and drawbacks. Isotopic neutron sources, such as ^{252}Cf or AmBe, provide a steady neutron flux but suffer from limited neutron yield ($< 10^6$ n/cm²/s) and radiological constraints for safe handling. Sealed tube neutron generators, which rely on D-D or D-T fusion reactions, offer compact and portable neutron production, but they produce only monoenergetic neutrons and, due to structural constraints, generally have lower yields compared to more sophisticated systems ($\sim 10^6$ n/cm²/s). Larger facilities, such as fission reactors or spallation sources, produce much higher neutron fluxes ($> 10^{15}$ n/cm²/s), which are suitable for demanding applications like neutron scattering and neutron radiography. However, these facilities are extremely expensive to build and maintain, require stringent safety protocols and often have limited accessibility due to the radiological hazards associated with fission and spallation processes, inducing significant material activation and radioactive waste. These sources are also bulky, inflexible and often require large-scale infrastructure, limiting their use in mobile or on-demand applications. Additionally, while isotopic neutron sources and fission reactors emit neutrons continuously, sealed tube neutron generators and accelerator-based sources can produce pulsed neutron beams with typical duration down to 1 µs, which is not appropriate for applications like Neutron Resonance Spectroscopy (NRS).

In addition to these drawbacks, conventional sources are struggling to meet the growing demand for neutrons in various applications, compounded by the planned shutdown of many research reactors. Hence, over the past 25 years, the development of Laser-Driven Neutron Sources (LDNS) [7] has emerged as a suitable alternative, addressing many of the limitations of conventional neutron sources. Among the various techniques for generating neutrons using lasers, the pitcher-catcher method [8] stands out as the most promising, offering a good balance between achievable neutron flux and the size/cost of the facilities required. This technique involves a double-target system: a first target (the pitcher) is irradiated by an ultra-intense laser pulse ($> 10^{18}$ W/cm²) to accelerate ions (usually protons or deuterons) via different mechanisms [9] and these ions are then intercepted by a second target (called catcher or converter), inducing nuclear reactions that produce neutrons.

The first demonstration of neutron production using high-intensity lasers was performed by Disdier *et al.* [10] in 1999. A table-top laser delivered 300 fs pulses with an energy of up to 7 J which were focused on deuterated polyethylene targets, inducing D-D fusion reactions inside them and yielding up to 10^7 neutrons/shot. One of the first neutron production experiments using the pitcher-catcher technique was carried out in 2004 by Lancaster *et al.* [11] at the VULCAN laser facility in the UK. Laser pulses with a duration of 1 ps and an energy of 69 J were focused on Mylar targets, producing proton beams that were captured by a 3.4 mm thick LiF converter, resulting in a neutron fluence of 3×10^8 neutrons/sr/shot. Since then, many experiments using the pitcher-catcher technique were conducted, with a record fluence of 2.4×10^{10} neutrons/sr/shot reached in 2023 by Yogo *et al.* [12] at the LFEX laser facility in Japan, using 1.5 ps laser pulses of 900 J.

These experiments demonstrated that laser facilities can produce shorter neutron bunches (< ns) [13] and higher peak fluxes (> 10^{17} neutrons/cm²/s) [12, 14] than conventional neutron sources, making them particularly suitable for applications such as NRS or to reproduce astrophysical processes in laboratory. Furthermore, since neutron production with lasers involves only light transport before interacting with the target and particle acceleration happens over very short distances, laser facilities induce far less material activation compared to large conventional sources like fission reactors or spallation sources. This reduces radioactive waste production and simplifies future decommissioning. Additionally, the unique features of LDNS, especially in terms of neutron flux and bunch duration, combined with significant X-ray emissions generated during laser/target interactions, make lasers an attractive option for combined neutron/X-ray radiography. But, this also creates a noisy environment, making neutron detection challenging. While neutron fluences are generally well-characterized, measurements of the energy distribution of these neutrons are still scarce. To demonstrate the feasibility of applications and ensure the radiological safety of laser facilities, it is however essential to fully characterize these neutron fields.

Therefore, the main objective of this thesis work was to predict neutron emissions produced from various lasers using Monte Carlo simulations and to characterize these emissions, both in terms of fluence and energy distribution, through inter-comparisons of results obtained with different diagnostics (activation samples, bubble detectors and nToF detectors). Furthermore, activation diagnostics have been relatively unexplored and have not yet been used for neutron spectrometry at laser facilities, despite their ability to detect neutrons of several tens of MeV while being insensitive to X-rays, making neutron activation spectrometry particularly well-suited for characterizing LDNS. Thus, this thesis work also focused on the development of a neutron activation spectrometer, called SPAC, specifically designed to be used at laser facilities.

The first chapter presents the context and theoretical concepts underlying neutron physics, including the history of neutron discovery, the fundamental characteristics of neutrons and their interaction properties with matter. It also explores the wide range of possible applications using neutrons and discusses conventional neutron sources and their features. This is followed by an introduction to the LDNS, detailing the principles of laser technology, ion acceleration mechanisms and various techniques used to produce neutrons with lasers.

The second chapter describes the neutron detection techniques appropriate to characterize neutron emissions produced by lasers, such as track-etch detectors, bubble detectors, scintillators and activation diagnostics, and explains their operating principles. The chapter also delves into the development of a neutron activation spectrometer (SPAC), describing the selection of materials, geometry definition and response matrix calculations necessary for accurate neutron detection and spectrometry, particularly in the context of LDNS.

The third chapter presents the experimental work conducted to characterize neutron emissions at different laser facilities. It details the setups used at the Advanced Laser Light Source (ALLS) and the Apollon laser facility, where both secondary beam (F2) and main beam (F1) were employed to produce neutrons. Monte Carlo simulations were used to predict neutron emissions and the results were compared with experimental data. The analysis covers neutron fluence and energy distribution, providing a comprehensive characterization of neutron production at these laser facilities.

Finally, the fourth chapter summarizes the main implications of this thesis work and discusses the results of neutron characterization presented in the previous chapter, exploring how the neutron emissions depend on laser parameters, particularly laser energy. This chapter also outlines potential applications of current-day LDNS and offers perspectives on enhancing their capabilities, laying the groundwork for future developments to improve this promising technology.

1. Context and theoretical concepts

This chapter introduces some basic notions about neutrons, their characteristics, and how they are used through various techniques for many applications across numerous domains. A brief overview of the conventional neutron sources used today to perform such applications will also be provided before addressing the concept of Laser-Driven Neutron Sources (LDNS), detailing their functioning and presenting a state of the art of these new neutron sources.

1.1 General information on neutrons

1.1.1 History of neutron discovery

The discovery of the neutron follows the experiments carried out by Ernest Rutherford and his collaborators Hans Geiger and Ernest Marsden, leading to the discovery of the atomic nucleus in 1909. Rutherford's research consisted in studying the scattering of alpha particles, produced by the radioactive decay of radium, on thin gold foils. It was observed that most alpha particles passed through the foils with minimal deflection, some were scattered at large angles, and a few even bounced directly backward [15, 16], which suggested that the positive charge of the atom was concentrated in a small and dense nucleus, surrounded by a compensating negatively charged distribution of electrons [17, 18]. This is the so-called Rutherford model that replaced the "plum pudding model", proposed by Joseph John Thomson in 1904 [19], in which charges were considered as being uniformly distributed in the atom.

Additional experiments were performed by Rutherford, showing that the collision of alpha particles with light atoms, like nitrogen, produces recoil particles appearing to be hydrogen nuclei [20]. As the hydrogen was known to be the lightest element and given the Prout's hypothesis, which assumed that the atomic weights are multiples of the atomic weight of hydrogen, the hydrogen nuclei were considered by Rutherford as fundamental building blocks of all nuclei, calling them "protons" from 1920. But the stability of the atomic nucleus supposed the existence of an attractive nuclear force to compensate the repulsion of positively charged protons. Proton-electron doublets were first imagined to fulfil this role, but the presence of "nuclear electrons" was inconsistent with several principles of the emerging quantum mechanics. Thus, another new particle was theorized: the neutron.

Its discovery stems from three main experiments of nuclear transmutation. In 1930, Walther Bothe and Herbert Becker used a polonium source producing alpha particles of 5.3 MeV directed onto targets composed of light elements (Li, Be, Al…). A Geiger counter was placed behind the target and a sufficiently thick shielding to absorb alpha particles and protons, allowing to detect penetrating radiations produced by the interaction of the alpha particles with the target. The signal obtained was particularly high when beryllium targets were used and the produced radiations could not be deflected by an electric field, so they deduced that they were gamma-rays coming from the de-excitation of ^{13}C nuclei induced by the ^{7}Be(α,γ)^{13}C reaction [21].

In 1931, Irène and Frédéric Joliot-Curie reproduced the same experiment by placing various screens behind the experimental setup to study the interaction of these neutral penetrating radiations with different materials. They observed that the radiations can ejected high-energy protons from the screen, especially when hydrogen-containing compound (like paraffin) was used [22]. Considering the energy and momentum conservation, if these radiations were gamma-rays, their energy should have been around 50 MeV which was considered incredibly high at that time.

James Chadwick repeated this experiment by replacing the screens with cloud chambers containing different elements (He, N, Ar, …), as shown in Figure 1.1. He observed that these nuclei, heavier than hydrogen nuclei, can also be projected by the radiations coming from the interaction of alpha particles with beryllium targets. In an article published in 1932, he demonstrated that this phenomenon can be more reasonably explained if the radiations were assumed to be neutral particles whose mass is close to that of protons and produced by the $^{7}Be(\alpha,n)^{12}C$ reaction [23]. This marks the discovery of the neutron for which Chadwick won the Nobel Prize in Physics in 1935.

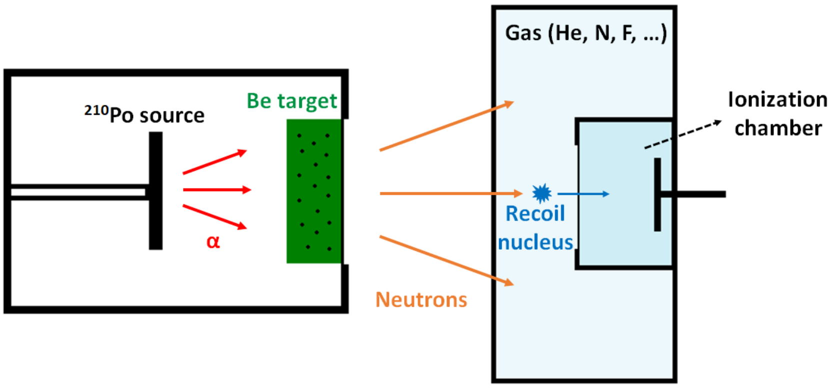

Figure 1.1 – Setup of the Chadwick experiment, leading to the discovery of the neutron.

1.1.2 Main characteristics of neutrons

Many experiments were then performed during the 20th century to characterize the nature of the neutron and its properties. It has been shown that neutrons are present in all atomic nuclei (except ^{1}H) and play an important role in the cohesion of nuclei thanks to the residual strong force that counteracts the electrostatic repulsion of protons. Long regarded as fundamental particles, neutrons are actually made of two up quarks and one down quark, and therefore have no net electric charge. Its mass is 939.565 MeV/c^2 (1.675×10^{-27} kg), slightly higher than that of the proton and around 1840 times the mass of an electron.

Neutrons can also exist as free neutrons, outside of nuclei. In this case, they are unstable and disintegrate via beta decay according to the reaction:

$$n \rightarrow p + e + \bar{\nu}_e \tag{1.1}$$

The mean lifetime of free neutrons in vacuum was measured at 886.8 ± 4.4 s [24], corresponding to a half-life of about 614.7 s. Free neutrons are mainly characterized by their kinetic energy, which determines the manner and probability of their interactions with matter. At room temperature (~290 K), they are called thermal neutrons and have an energy of around 0.025 eV, corresponding to the most probable speed considering a Maxwell-Boltzmann distribution (E = k×T). But, depending on their origin, free neutrons can have different kinetic energies, spanning several orders of magnitude, which are usually classed in five categories:

Category	Energy range
Cold neutrons	< 0.025 eV
Thermal neutrons	~ 0.025 eV
Epithermal neutrons	0.025 eV to ~ 100 keV
Fast neutrons	~ 100 keV to 20 MeV
High-energy neutrons	> 20 MeV

Table 1.1 – Classification and nomenclature of free neutrons depending on their kinetic energy.

1.1.3 Interaction of neutrons with matter

Neutrons are electrically neutral, their interaction with the electrons through the electromagnetic force is therefore negligible, making them indirectly ionizing particles. Thus, they only interact with atomic nuclei via physical collisions and the interaction of neutrons with a target nucleus, noted ${}^{A}_{Z}X$, is governed by several possible reactions (summarized in Figure 1.2) which can be categorized in two mechanisms: scattering and absorption. First, neutrons can be scattered by nuclei following two processes:

(1) Elastic scattering (n,n) described by the reaction:

$$ {}^{A}_{Z}X + {}^{1}_{0}n \rightarrow {}^{A}_{Z}X + {}^{1}_{0}n \tag{1.2} $$

The scattered neutron transfers a part of its kinetic energy to the nucleus. The total neutron energy loss is acquired by the nucleus as recoil energy, inducing a speed and direction change and ensuring the conservation of the energy and momentum of the neutron-nucleus system. The elastic scattering is the main way by which neutrons lose their energy in matter, this process can occur without threshold energy with a near-constant cross section in the epithermal region and cross sections depending of the inverse of the kinetic energy for cold and fast neutrons. The average neutron energy loss for each collision with a nucleus can be expressed as:

$$ \bar{E}_l = E_n \frac{2 \times A}{(A+1)^2} \tag{1.3} $$

Where E_n is the initial kinetic energy of the neutron and A, the atomic number of the nuclei. Given this equation, it can be deduced that the lighter the target nucleus, the higher the average neutron energy loss is, making these particles more sensitive to light elements. By multiplying the number of collisions, neutrons can lose a large part of their kinetic energy until they reach thermal equilibrium with the surrounding matter, corresponding to a kinetic energy of about 0.025 eV at room temperature. This process is called “neutron thermalization”.

(2) Inelastic scattering (n,n’) described by the reaction:

$$ {}_{Z}^{A}X + {}_{0}^{1}n \rightarrow {}_{Z}^{A}X^{*} + {}_{0}^{1}n \rightarrow {}_{Z}^{A}X + {}_{0}^{1}n + \gamma \tag{1.4}$$

During this reaction, the energy and momentum of the neutron-nucleus system are not conserved because only a part of the neutron energy loss is transferred to the nucleus as recoil energy, the rest is absorbed by the nucleus making it passing into an excited state. Thus, this reaction can only happen if the kinetic energy of the neutron exceeds the energy of an excited state (usually, several hundreds of keV). The excited nucleus can then de-excite by emitting a gamma-ray to return to its ground level. Neutrons can also be emitted if the incident neutron has a sufficiently high kinetic energy to induce a neutron multiplicity reaction, noted (n,xn), where x is the number of ejected neutrons. This requiring a threshold energy depending on the number of neutrons ejected and the binding energy of the nucleons inside the nucleus. In all cases, these inelastic reactions are threshold reactions that can only be triggered by fast neutrons.

Neutrons may also be absorbed by the nuclei, inducing the creation of compound nuclei, noted ${}^{A+1}_{Z}X^{*}$, which de-excite in less than 10^{-14} s by rearranging their internal structure and emitting one or more particles. These nuclear reactions are classified according to the particles emitted during the de-excitation and can be presented in the following categories:

(3) Neutron capture (n,γ) described by the reaction:

$$ {}_{Z}^{A}X + {}_{0}^{1}n \rightarrow {}^{A+1}_{Z}X^{*} \rightarrow {}^{A+1}_{Z}X + \gamma \tag{1.5}$$

The neutron capture results in the absorption of a neutron, forming a compound nucleus, which is de-excited by emitting a gamma-ray. This compound nucleus ${}^{A+1}_{Z}X$ is of the same nature that the initial nucleus, but it is a different isotope because having one more neutron. The neutron capture is a no-threshold reaction with cross sections depending of the inverse of neutron velocity. But, when the kinetic energy of the neutron and the binding energy it provides correspond to excited states of the compound nucleus, this facilitate the reaction and much higher cross sections are observed. These are called “resonances” and are usually present in the epithermal region (see Figure 1.7).

(4) Transmutation (n,p) described by the reaction:

$$ {}_{Z}^{A}X + {}_{0}^{1}n \rightarrow {}^{A+1}_{Z}X^{*} \rightarrow {}_{Z-1}^{A}Y + {}_{1}^{1}p \tag{1.6}$$

Neutrons can induce the emission of light charged particles like protons (but also α, d, t, …) by direct interaction with the target nucleus or by de-excitation of the compound nucleus. This leads to a change of the nature of nucleus which can become an unstable radionuclide. To be ejected from the compound nuclei, the charged particles must fight against the binding energy and overcome the Coulomb barrier, thus only neutrons with kinetic energy of several MeV can cause this type of reactions. Neutrons can also be emitted, via the neutron multiplicity reaction (n,xn) described earlier, during the direct interaction of an incident neutron with a nucleus. Finally, another process called “spallation reaction” can be initiated when the neutron interacting with the nucleus has a kinetic energy of a few hundred MeV or more, this can cause an avalanche of binary collisions with the nucleons, thus ejecting many charged particles and neutrons outside the nucleus.

(5) Fission (n,f) described by the reaction:

$$ {}^{A}_{Z}X + {}^{1}_{0}n \rightarrow {}^{A+1}_{Z}X^{*} \rightarrow {}^{A_1}_{Z_1}Y_1 + {}^{A_2}_{Z_2}Y_2 + x\,{}^{1}_{0}n \quad (1.7)$$

A neutron can be captured by a heavy nucleus ($Z \geq 90$) which is de-excited by fragmenting into 2 smaller daughter nuclei and emitting several fast neutrons. This reaction can occur with thermal or fast neutrons, depending on the target nucleus, and produce a significant amount of energy (~ 200 MeV per fission of ^{235}U nucleus), mainly in the form of kinetic energy of daughter nuclei. The neutrons emitted during the fission can in turn cause fission reactions and thus generate a chain reaction, which is the principle of fission reactors producing energy.

Despite all these different possible reactions, neutrons only interact with nuclei, which have a relatively small size, thus they interact weakly with matter and are highly penetrating particles. The transmission of neutrons through a material can therefore be described by the Beer-Lambert law defined by the following equation:

$$I = I_0 e^{-\Sigma x} \quad (1.8)$$

Where I is the emerging flux, I_0 the incident flux, Σ the macroscopic cross section, also called attenuation coefficient (in cm^{-1}) and x the thickness of the material crossed by the neutron flux (in cm). The macroscopic cross section for a material composed of i elements is calculated by:

$$\Sigma = \sum_i \frac{\rho N_A}{M}\, n_i \sigma_{tot_i} \quad (1.9)$$

With ρ the density of the material (in g.cm^{-3}), N_A the Avogadro number ($\approx 6.022\times10^{23}$ mol^{-1}), M the molecular weight (g.mol^{-1}), n_i the number of atoms of element i in a molecule of the material considered and σ_{tot_i} the total cross section (in cm^2, but often expressed in barn, with 1 barn = 10^{-24} cm^2), which corresponds to the sum of all cross sections associated to the different possible reactions previously detailed.

The mean-free-path length λ of neutrons, corresponding to the distance after which the intensity of a neutron beam decreased to 1/e of its initial intensity, can then be simply expressed (in cm) as the inverse of this macroscopic cross section:

$$\lambda = \frac{1}{\Sigma} \quad (1.10)$$

As mentioned before, the elastic scattering is the most probable interaction of neutrons with matter and the energy transferred to the recoil nuclei is maximum when the target is composed of light nuclei like hydrogen. In the human body, mainly composed of water, neutrons can induce significant doses by interacting for example with the hydrogen nuclei and generating recoil protons which deposit their energy by ionization, causing damages to cells and DNA.

The absorption of neutrons produces daughter nuclei whose internal structure changes, i.e. the number of protons and/or neutrons is different that of the initial nuclei with which the neutrons interact. This may induce the creation of unstable nuclei, called radionuclides, with their own half-life and decay process (beta decay, electron capture, …). This is responsible of material activation, producing a lot of radioactive waste in many facilities like nuclear reactors or accelerators.

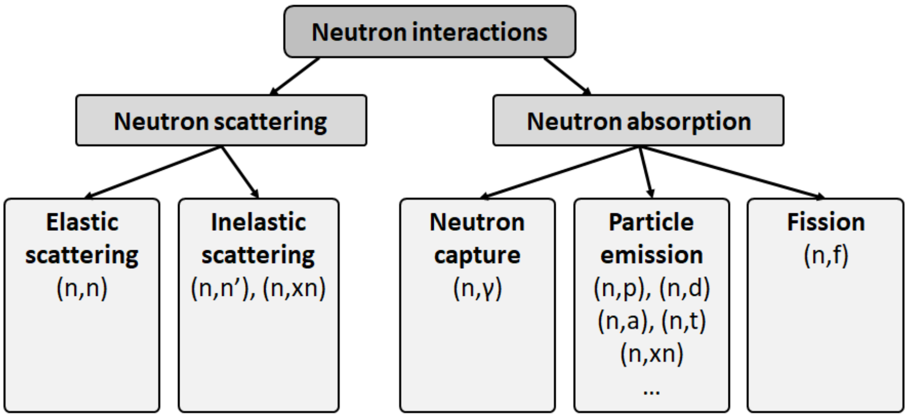

Figure 1.2 – Classification of nuclear reactions with neutrons.

1.2 Main applications using neutrons

Neutrons are widely used in several applications due to their unique properties. As described in Section 1.1.3, neutrons are neutral particles that only interact with atomic nuclei and preferably with light elements, particularly through elastic scatterings, which is the main way of interaction of neutrons with matter. Neutrons are thus interesting particles for imaging or probing light materials, which is complementary to X-rays that interact with electrons and whose probability of interaction increases with the atomic number. Figure 1.3 presents the attenuation coefficients of thermal neutrons and X-rays interacting with all elements of the periodic table, showing the difference and the complementarity of these particles regarding their interaction with matter [25].

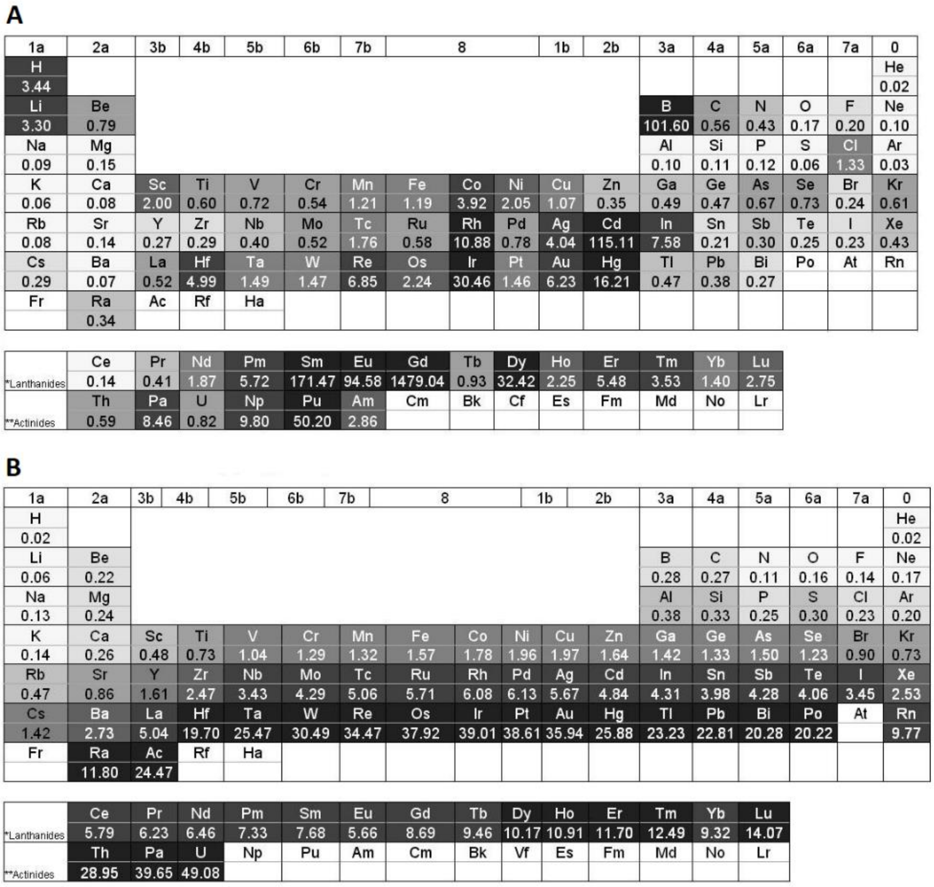

A

1a	2a	3b	4b	5b	6b	7b	8			1b	2b	3a	4a	5a	6a	7a	0
H																	He
3.44																	0.02
Li	Be											B	C	N	O	F	Ne
3.30	0.79											101.60	0.56	0.43	0.17	0.20	0.10
Na	Mg											Al	Si	P	S	Cl	Ar
0.09	0.15											0.10	0.11	0.12	0.06	1.33	0.03
K	Ca	Sc	Ti	V	Cr	Mn	Fe	Co	Ni	Cu	Zn	Ga	Ge	As	Se	Br	Kr
0.06	0.08	2.00	0.60	0.72	0.54	1.21	1.19	3.92	2.05	1.07	0.35	0.49	0.47	0.67	0.73	0.24	0.61
Rb	Sr	Y	Zr	Nb	Mo	Tc	Ru	Rh	Pd	Ag	Cd	In	Sn	Sb	Te	I	Xe
0.08	0.14	0.27	0.29	0.40	0.52	1.76	0.58	10.88	0.78	4.04	115.11	7.58	0.21	0.30	0.25	0.23	0.43
Cs	Ba	La	Hf	Ta	W	Re	Os	Ir	Pt	Au	Hg	Tl	Pb	Bi	Po	At	Rn
0.29	0.07	0.52	4.99	1.49	1.47	6.85	2.24	30.46	1.46	6.23	16.21	0.47	0.38	0.27			
Fr	Ra	Ac	Rf	Ha													
	0.34																

	Ce	Pr	Nd	Pm	Sm	Eu	Gd	Tb	Dy	Ho	Er	Tm	Yb	Lu
*Lanthanides	0.14	0.41	1.87	5.72	171.47	94.58	1479.04	0.93	32.42	2.25	5.48	3.53	1.40	2.75
	Th	Pa	U	Np	Pu	Am	Cm	Bk	Cf	Es	Fm	Md	No	Lr
**Actinides	0.59	8.46	0.82	9.80	50.20	2.86								

B

1a	2a	3b	4b	5b	6b	7b	8			1b	2b	3a	4a	5a	6a	7a	0
H																	He
0.02																	0.02
Li	Be											B	C	N	O	F	Ne
0.06	0.22											0.28	0.27	0.11	0.16	0.14	0.17
Na	Mg											Al	Si	P	S	Cl	Ar
0.13	0.24											0.38	0.33	0.25	0.30	0.23	0.20
K	Ca	Sc	Ti	V	Cr	Mn	Fe	Co	Ni	Cu	Zn	Ga	Ge	As	Se	Br	Kr
0.14	0.26	0.48	0.73	1.04	1.29	1.32	1.57	1.78	1.96	1.97	1.64	1.42	1.33	1.50	1.23	0.90	0.73
Rb	Sr	Y	Zr	Nb	Mo	Tc	Ru	Rh	Pd	Ag	Cd	In	Sn	Sb	Te	I	Xe
0.47	0.86	1.61	2.47	3.43	4.29	5.06	5.71	6.08	6.13	5.67	4.84	4.31	3.98	4.28	4.06	3.45	2.53
Cs	Ba	La	Hf	Ta	W	Re	Os	Ir	Pt	Au	Hg	Tl	Pb	Bi	Po	At	Rn
1.42	2.73	5.04	19.70	25.47	30.49	34.47	37.92	39.01	38.61	35.94	25.88	23.23	22.81	20.28	20.22		9.77
Fr	Ra	Ac	Rf	Ha													
	11.80	24.47															

	Ce	Pr	Nd	Pm	Sm	Eu	Gd	Tb	Dy	Ho	Er	Tm	Yb	Lu
*Lanthanides	5.79	6.23	6.46	7.33	7.68	5.66	8.69	9.46	10.17	10.91	11.70	12.49	9.32	14.07
	Th	Pa	U	Np	Pu	Am	Cm	Bk	Vf	Es	Fm	Md	No	Lr
**Actinides	28.95	39.65	49.08											

Figure 1.3 – Attenuation coefficients (cm^{-1}) of thermal neutrons (A) and 125 kV X-rays (B) with all elements of the periodic table [25].

Moreover, through the absorption mechanism, neutrons also have the ability to modify the nature of the nuclei by changing their internal structure, inducing the production of radionuclides and the activation of materials. This allows to use these particles to perform interrogation techniques and non-destructive material analysis. Thus, depending on the interaction mechanism (scattering or absorption), neutrons can be used in a wide range of applications, such as radiography, neutron diffraction or activation analysis, which will now be discussed in detail.

1.2.1 Neutron imaging

Neutron imaging is a non-destructive technique based on the transmission of a neutron beam through a sample, described by the Beer-Lambert law (see Section 1.1.3), producing 2D (radiography) or 3D (tomography) images of its internal structure whose contrast depends on the elemental composition and the associated attenuation of neutrons. Considering the unique characteristics of the interaction of neutrons with matter, especially their penetrating power and sensitivity to light elements, neutron imaging allows to obtain radiographs of materials with low X-ray transparency and more contrasted images of materials composed of low-Z elements. Minimal neutron fluxes of around $10^{5\text{-}6}$ n/cm²/s and acquisitions of a few seconds to a few minutes, depending on the sample and detector efficiency, are typically required for conventional neutron radiography [26, 27]. Many domains, such as heritage science or biology, employ the neutron imaging technique to perform non-destructive analysis to study ancient objects [28, 29, 30] or plant physiology [1, 2, 31]. Neutron imaging is also used in industry to examine the heterogeneity of metal components [32, 33], nuclear fuel [34] or lithium-ion batteries [35, 36, 37].

However, such radiographs only provide information about the difference of neutron absorption and the distribution of different materials inside the studied sample, but the exact nature of these materials is difficult to obtain with neutron imaging only, especially when the sample is composed of materials of the same nature (e.g. organic materials). As neutrons provide complementary information to X-rays, their combined use allows to obtain a unique signature for each material by convolving their response to these two particles [38]. Combined neutron/X-ray imaging is therefore particularly interesting for applications in contraband detection and homeland security to detect explosives or narcotics mainly composed of organic materials [5, 6, 39], difficult to distinguish from each other by simple neutron or X-ray imaging, as shown in Figure 1.4.

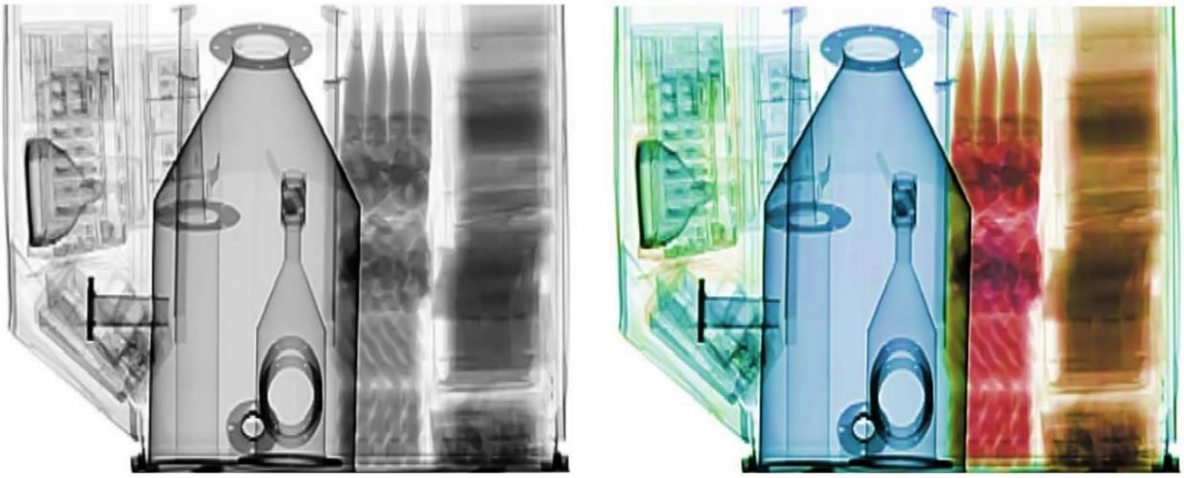

Figure 1.4 – Radiography of an air cargo, extracted from [39], with X-ray only (left) and neutron/X-ray (right). The colors indicate the R-values, which are the ratios of the neutron and X-ray attenuation coefficients. Blue corresponds to metals, green are glass, ceramics and inorganic chemicals and yellow, orange, red and pink are different organic materials.

Another technique, called neutron activation autoradiography, can be used to perform neutron imaging. This technique involves irradiating a sample with neutrons to induce nuclear reactions, leading to the creation of radionuclides which de-excite by emitting gamma-rays. By detecting these gamma-rays, characteristic of the radionuclides produced and therefore of the initial nuclei, one can map the spatial distribution of specific elements within the sample [40, 41]. Finally, neutron imaging can be used in addition to other techniques of neutron scattering to improve the contrast of the images obtained.

1.2.2 Neutron scattering

Neutron scattering techniques exploit the neutrality of neutrons to penetrate deeply in matter, without being significantly deflected by the electrons and without destroying chemical bonds, leading to the possibility of probing the structure and dynamics of materials at the atomic and molecular levels by studying the scattering of a neutron beam passing through a sample. These techniques encompass a range of experimental methods tailored to investigate different aspects of materials, at different scales.

Among these techniques, neutron diffraction uses the wave-like nature of neutrons and their elastic scatterings within a crystalline sample to produce interference figures, which patterns depend on the crystal structure, following Bragg’s law:

$$n\lambda = 2d \sin\frac{\theta}{2} \tag{1.11}$$

Where n is an integer called harmonic number, d is the distance between the lattice planes, θ is the angle between the incident beam and the scattered beam, and λ is the *de Broglie* wavelength of incident neutrons defined as:

$$\lambda = \frac{h}{m_n v} \tag{1.12}$$

With h the Planck constant, m_n the mass of the neutron and v its velocity.

Thus, by analyzing these scattering patterns, information about the position and arrangement of atoms within crystal lattices can be obtained. This technique is therefore very similar to X-ray crystallography but provides complementary information because, unlike X-rays, neutrons interact only with atomic nuclei and these interactions are isotope-dependent and more important with light elements. Hence, neutron diffraction is particularly interesting to study materials composed of oxides [42]. Thermal or cold neutrons are generally used to perform this technique as their energy corresponds to wavelengths comparable to atomic spacings, which allows to have sufficiently large scattering angles to form easily detectable interferences. Neutron diffraction can therefore find applications in various scientific disciplines such as biology to determine the atomic structure of proteins [43] and enzymatic mechanisms [44], or in materials science to characterize nuclear materials [45] or crystal structures by providing insights into defects or lattice distortions [42, 46, 47].

Another technique, called Small-Angle Neutron Scattering (SANS), can be employed to characterize bigger structures. This technique is also based on the neutron scattering, but the scattered neutrons of interest are those with small scattering angles (< a few degrees), which are characteristic of structures in the mesoscopic scale (from 1 to > 100 nm), such as nanostructured materials or polymers. The scattering patterns observed for small scattering angles can provide valuable information about the shape and arrangement of nanostructures within a sample. Thus, materials science commonly uses this technique to study the structure and dynamics of polymers [48, 49, 50] and alloys [51, 52, 53].

Finally, neutron reflectometry is another method using the refractive properties of thermal or cold neutrons to study the surface and structure of materials with a sub-nanometer resolution. Due to their wave-like behavior, these low-energy neutrons can be reflected at the boundary between two media, as light would be via optical phenomena. Thus, neutron reflectometry provides information about the depth profile, roughness and interfacial properties of materials, making it a powerful tool for studying the structure of thin films (e.g. polymer films) [54, 55, 56] or biological interfaces (e.g. lipid membranes) [57, 58, 59].

1.2.3 Neutron activation analysis

Neutron activation analysis includes several analytical and non-destructive techniques aiming to determine the elemental composition of materials. These techniques are based on the neutron activation process in which, as mentioned in Section 1.1.3, the interaction of neutrons with target nuclei induces the creation of compound nuclei which then lead to a change of the nature of initial nuclei and thus to the production of radionuclides. These compound nuclei and radionuclides, also called activation products, are unstable and can be de-excited by emitting gamma-rays.

The energies of these gamma-rays are characteristic of the activation products created by the neutron-induced reactions and the nature of these activation products depends on the target nuclei in which the reactions occur. Thus, the composition of a sample and the mass fraction of each element can be obtained considering the cross sections of the neutron-induced reactions producing the activation products and by determining the nature and quantity of these activation products, measured by gamma spectrometry.

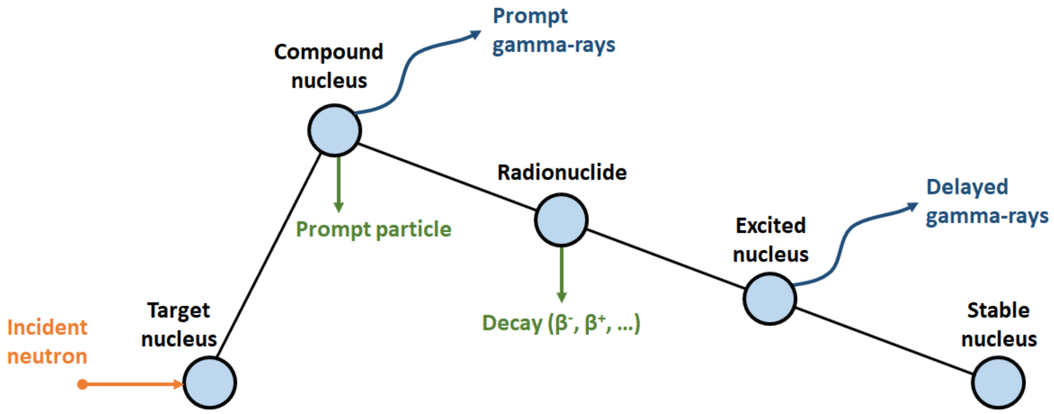

Figure 1.5 – Neutron activation process of a target nucleus and standard decay scheme.

Two distinct types of gamma-ray emissions therefore occur after the interaction of neutrons with target nuclei: the prompt gamma-rays coming from the de-excitation of the compound nuclei and the delayed gamma-rays coming from the de-excitation of the radionuclides. These two processes of gamma-ray emissions lead to two methods allowing to characterize the neutron-induced reactions and thus the nature of the target nuclei. The Prompt Gamma-ray Activation Analysis (PGAA) uses the prompt gamma-rays emitted by the compound nuclei while the Instrumental Neutron Activation Analysis (INAA) uses the delayed gamma-rays following the de-excitation of the radionuclides.

These two methods consist in irradiating a sample with a neutron beam to generate activation products inside. Neutrons of all energy can be used to perform this kind of analysis, depending on the expected elements and the desired reactions (neutron capture (n,γ), transmutation (n,p), (n,α), …). The activation products created then are de-excited by emitting gamma-rays, which can be measured by different types of gamma spectrometer. In the PGAA method, gamma-rays from the de-excitation of compound nuclei have high energies (up to ~ 12 MeV) that require the use of large HPGe spectrometers or BGO scintillators, sometimes with Compton suppression techniques, to perform the gamma spectrometry measurements of the irradiated samples. While in the INAA method, the gamma-rays of interest are those coming from the de-excitation of radionuclides, with lower energies (up to ~ 3 MeV), which can be easily measured by cheaper spectrometers like NaI(Tl) scintillators [60].

Among the main advantages of the PGAA and INAA methods, one can cite the possibility of neutrons to penetrate and create activation products deeply in matter, allowing to perform non-destructive elemental analysis of thick samples, which is limited for other similar techniques using charged particles (e.g. PIXE/PIGE techniques). Another major characteristic is the extreme sensitivity of these methods, capable of detecting trace levels of elements down to parts per billion or lower [61] (see Figure 1.6).

The PGAA method stands out in the detection of elements whose interaction with neutrons produces radionuclides with very short half-life or radionuclides that do not emit gamma-rays, making them impossible to be detected by the INAA method. Low-Z elements, such as hydrogen, carbon or nitrogen are particularly concerned by this, thus the PGAA method is very suitable to analyze organic materials, which is very interesting for applications in homeland security to detect explosives or narcotics [60, 62, 63]. Conversely, the INAA method is rather employed to detect heavier elements in archaeological objects to perform provenance studies [3, 4, 64] or in geological samples [65, 66], especially to detect rare-earth elements [67, 68, 69].

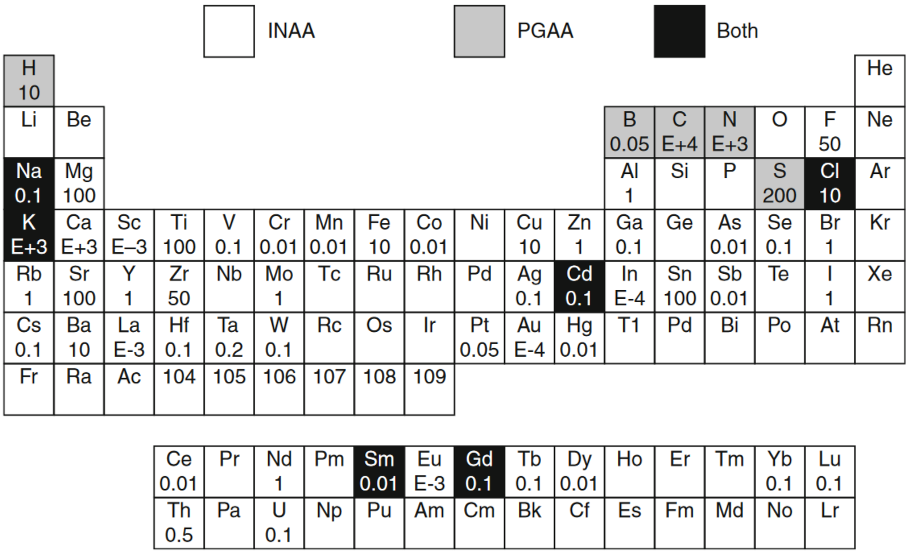

☐ INAA ▨ PGAA ■ Both

▨ H 10																	He
Li	Be											▨ B 0.05	▨ C E+4	▨ N E+3	O	F 50	Ne
■ Na 0.1	Mg 100											Al 1	Si	P	▨ S 200	■ Cl 10	Ar
■ K E+3	Ca E+3	Sc E–3	Ti 100	V 0.1	Cr 0.01	Mn 0.01	Fe 10	Co 0.01	Ni	Cu 10	Zn 1	Ga 0.1	Ge	As 0.01	Se 0.1	Br 1	Kr
Rb 1	Sr 100	Y 1	Zr 50	Nb	Mo 1	Tc	Ru	Rh	Pd	Ag 0.1	■ Cd 0.1	In E-4	Sn 100	Sb 0.01	Te	I 1	Xe
Cs 0.1	Ba 10	La E-3	Hf 0.1	Ta 0.2	W 0.1	Rc	Os	Ir	Pt 0.05	Au E-4	Hg 0.01	T1	Pd	Bi	Po	At	Rn
Fr	Ra	Ac	104	105	106	107	108	109									

Ce 0.01	Pr	Nd 1	Pm	■ Sm 0.01	Eu E-3	■ Gd 0.1	Tb 0.1	Dy 0.01	Ho	Er	Tm	Yb 0.1	Lu 0.1
Th 0.5	Pa	U 0.1	Np	Pu	Am	Cm	Bk	Cf	Es	Fm	Md	No	Lr

Figure 1.6 – Sensitivities in part per million for neutron activation analysis, using thermal neutrons, of elements composing biological and environmental samples [61].

1.2.4 Neutron Resonance Spectroscopy

Neutron Resonance Spectroscopy (NRS) is another non-destructive elemental analysis technique complementary to activation analysis. It relies on the presence of resonances which drastically increase the cross section of neutron reactions, especially in the epithermal region. As mentioned in Section 1.1.3, these resonances appear for energies depending on the excited states of nuclei, they are therefore specific to each element and isotope [70] (see Figure 1.7).

These properties are exploited in two techniques for analyzing the composition of a sample. If the resonances are related to neutron capture reactions, a neutron beam with a broad energy spectrum passing through a sample will have some of its neutrons, whose energy corresponds to these resonances, preferentially captured by the nuclei composing the sample to analyze. This induces the production of compound nuclei that emit prompt gamma-rays to de-excite. These are then measured by a detector as function of time. As the duration associated to the formation and de-excitation of compound nuclei is negligible ($< 10^{-14}$ s) and knowing the distances between the neutron source, sample and detector, the detection of each gamma-ray can be assigned to the capture of a neutron whose energy is determined by its Time-of-Flight (ToF). This technique, called Neutron Resonance Capture Analysis (NRCA), is similar to PGAA but differs in how gamma-rays are detected. In NRCA, gamma-rays are measured as function of time to retrieve the neutron Time-of-Flights (nToF) and therefore, the energy of neutrons having induced these gamma-rays. Conversely, in PGAA, the quantity of interest is the gamma-ray energy, which is specific to each element and isotope.

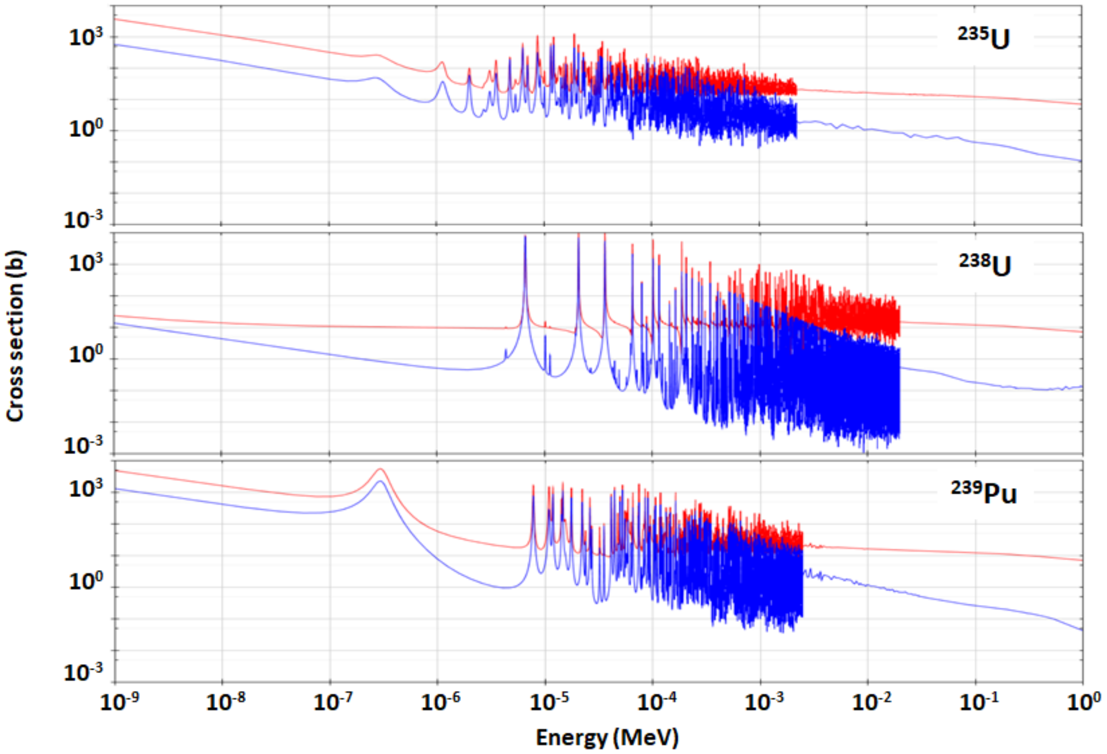

Figure 1.7 – Total (red) and capture (blue) cross sections for neutron reactions on ^{235}*U,* ^{238}*U and* ^{239}*Pu, according to the ENDF/B-VIII.0 library [70].*

The NRCA technique is generally used when the transmitted neutron spectrum cannot be measured (e.g. due to a low signal induced by a thick sample), otherwise the Neutron Resonance Transmission Analysis (NRTA) is preferred. The NRTA technique is based on the measurement of a transmitted neutron spectrum passing through a sample. Due to the presence of the resonances, inducing a preferential interaction of neutrons, some absorption lines specific of each element and isotope can be observed. These absorption lines are usually revealed by measuring the transmitted neutron spectrum using the ToF technique, which allows to have a good energy resolution for neutron energies in the epithermal region. This therefore requires to have pulsed neutron beam of duration as short as possible to reduce the uncertainty associated to the measurement of the neutron ToF (nToF) and, consequently, to the neutron energy.

These techniques are particularly used in the nuclear industry for the characterization of nuclear fuel and in archaeology to study ancient objects of cultural heritage interest [71, 72]. Some experiments have also demonstrated the possibility of using NRS to perform thermometry measurements thanks to the Doppler effect, affecting the width of resonances. Indeed, the thermal motion of the nuclei increases with the temperature of the sample, this inducing a broadening of the resonances. The temperature of the sample can therefore be determined by measuring the broadening of the absorption lines [73, 74, 75].

1.2.5 Astrophysical interest

Neutrons can also be used to reproduce and study astrophysical events which play an important role in the nucleosynthesis of elements. Nucleosynthesis involves different processes by which new atomic nuclei are created from nucleons (protons and neutrons) or pre-existing nuclei. Initially, hydrogen and helium isotopes (^{2}H, ^{3}He and ^{4}He) as well as a small fraction of lithium isotopes (especially, ^{7}Li) were created thanks to the cooling of the universe, a few seconds after the Big Bang. This cooling allowed the formation of deuterium nuclei from the association of a proton and a neutron, which was impossible in the very first moment of the universe because the temperature was too high and the photons were too energetic, causing the dissociation of deuterium nuclei. The other light elements were then created by a cascade of fusion reactions involving these deuterium nuclei with protons, neutrons or other deuterium nuclei. This process, known as primordial nucleosynthesis or Big Bang nucleosynthesis, occurred in the first 20 minutes after the Big Bang, when the universe was still hot and dense enough to allow these nuclear reactions to occur. After that, the temperature and density became too low to form other nuclei, which interrupted the nucleosynthesis [76].

Later on, most of elements heavier than lithium were produced in stars. These astrophysical objects, formed by the gravitational collapse of interstellar clouds of gas, primarily consist of hydrogen and helium in their early stages. Some stars also contain a small amount of heavier elements, such as carbon, oxygen or iron, produced by fusion in previous generations of stars. Due to the gravitational force, stars contract and their temperature rises, allowing protons to overcome the Coulomb barrier and initiate fusion reactions, called pp chains, which produce ^{4}He nuclei. In stars containing carbon, nitrogen and oxygen nuclei, ^{4}He can also be produced through fusion reactions involving these elements with protons, in processes called CNO cycles. These reactions transform hydrogen into helium nuclei, releasing energy that contributes to the radiation pressure, which balances the gravitational force and puts the star in a state of equilibrium. This process is known as hydrostatic hydrogen burning. When stars have exhausted their hydrogen, the gravitational collapse resumes and the temperature increases until ^{4}He nuclei fuse, mainly through the $3\,{}^{4}He \rightarrow {}^{12}C$ reaction. This new phase is called hydrostatic helium burning, which transform the helium core of the stars into carbon cores [77].

For low-mass stars (< 9 solar masses), electron degeneracy pressure is high enough to counter the gravitational force, so the carbon core cannot collapse and sufficient temperatures cannot be reached to initiate the next burning stages. But, helium burning continues in the layer around the carbon core, until most of the helium is consumed. At this point, only hydrogen burning still occurs, producing helium which accumulates until it can reignite. This initiates a new phase of helium burning, raising the star's overall temperature and enhancing hydrogen burning, until the helium is once again exhausted, and the cycle repeats. This cyclic behavior inducing thermal changes causes different layers to mix through convection. Thus, protons can interact with the carbon core, producing ^{13}C and ^{14}N nuclei with which helium nuclei interact and induce the production of neutrons (e.g., via the ^{13}C(α,n) ^{16}O reaction). These neutrons are then responsible of another nucleosynthesis process, called s(low)-process, in which heavy nuclei (^{56}Fe, usually) formed by older stars, capture a neutron and become new neutron-enriched stable nuclei or unstable nuclei disintegrating via β^{-} decay. In this latter case, the unstable nuclei are converted into new nuclei with an atomic number increased by one. These new nuclei, in turn, capture neutrons, creating heavier and heavier nuclei. Thus, the s-process is responsible for the creation of many of the isotopes from ^{56}Fe to ^{209}Bi. Beyond ^{209}Bi, nuclei are unstable and disintegrate via alpha decay or fission reactions, reducing the atomic number of the daughter nuclei and halting the nucleosynthesis of heavier nuclei induced by the s-process [78].

The ^{56}Fe nuclei used as seeds in the s-process are produced in massive stars (> 9 solar masses). In such stars, pressure and temperature conditions can be met to initiate fusion reactions inside the carbon core, producing heavier nuclei (^{20}Ne, ^{23}Na, ^{24}Mg, …) which will then fuse during the next burning stages until nuclei with mass number of 56 (mainly composed of ^{56}Fe nuclei) are reached. For heavier nuclei, the Coulomb barrier is so high that cross sections of reactions with charged-particles are very small and fusion reactions become largely endothermic, which stops the stellar nucleosynthesis. At this point, massive stars are composed of several layers of different elements surrounding an iron core. If the iron core reaches 1.4 solar masses (Chandrasekhar limit), it can collapse to such an extent that it reaches extremely high nuclear densities, causing other layers to rebound off the core, which induces a supernova explosion and the expulsion of many nuclei resulting from nucleosynthesis into the different layers of the star. The iron core then becomes a neutron star producing significant neutrino radiation. Neutrons and protons accelerated by the neutrino-driven winds travel through the different ejected layers and are captured by nuclei, transforming them into heavier nuclei. This nucleosynthesis process, called νp-process, is responsible for a significant portion of the synthesis of nuclei between iron and the region around A=100 [79].

Although the nucleosynthesis of most of the nuclei between iron and bismuth are described by the s-process and νp-process, they are insufficient to explain the existence of actinides (thorium and uranium) and the observed abundances of nuclei, especially above A≈100. Another process therefore needs to be introduced and must be driven by neutron captures, since the capture of a charged-particle by a high mass number nucleus is highly unlikely due to the increasing Coulomb barrier. This process, called r(apid)-process, is similar to the s-process but involving higher neutron fluxes ($> 10^{20}$ n/cm²/s) [80]. It involves successive neutron captures to happen in time scales shorter than that of the β^- decay of the newly created nuclei. This leads to the capture of several neutrons by the seed nucleus, which rapidly increases its mass number before β^- decays transform it into a much heavier nucleus. Thus, this mechanism allows to overcome the alpha decay or fission reactions of heavy nuclei and to explain the existence of thorium or uranium in the universe [81, 82]. Neutron star mergers or neutron star/black hole mergers are suspected to be the most likely sites where neutron fluxes are sufficient to trigger the r-process [83, 84].

We have seen, through various nucleosynthesis processes, that neutrons play an important role in the creation of certain elements, particularly the heaviest nuclei. To explain the observed abundance of elements, models attempt to reproduce these different nucleosynthesis processes by varying different parameters (neutron density, temperature, ...). However, the nuclear data of many neutron-rich nuclei, which play a predominant role in the r-process, are not known experimentally, thus this is a significant source of uncertainty in the results obtained by these models. Therefore, many experiments are planned to produce neutron-rich nuclei and study their characteristics in order to faithfully reproduce the nucleosynthesis processes and understand how the elements around us were created either with conventional neutrons sources [81], or laser-driven neutron sources [85].

1.3 Conventional neutron sources

As mentioned in the previous section, neutrons are used through several techniques for many applications spanning a wide range of domains. Since neutrons are electrically neutral, they cannot be directly accelerated by conventional particle accelerators and require different nuclear reactions to be produced. Various approaches exist to induce such nuclear reactions in order to create different neutrons sources that meet specific needs. We will now describe the most common neutron sources and discuss their features, advantages and disadvantages.

1.3.1 Isotopic neutron sources

Neutron sources based on the radioactive decay of different isotopes are probably the most widespread sources. These isotopic neutron sources can be divided in three categories: heavy radioisotopes disintegrating by spontaneous fissions and emitting neutrons, alpha-emitters that generate neutrons via (α,n) reactions, gamma-emitters that produce neutrons through (γ,n) reactions.

Many transuranic radioisotopes have a significant probability of undergoing spontaneous fission. During each fission event, several neutrons are emitted, making a sample of such a radioisotope a straightforward neutron source. However, only ^{252}Cf radioisotopes are produced in sufficient quantity (in nuclear reactors) and have a suitable half-life to be considered in a neutron source. The ^{252}Cf sources, composed of californium oxide or californium-palladium alloy encapsulated in stainless steel [86], have a neutron yield of 0.12 n/s/Bq, equivalent to 2.3×10^{12} n/s/g, allowing to make sources of small sizes (containing tens of micrograms, usually). These ^{252}Cf sources emit neutron spectra similar to that of a fission reactor, with an average energy of 2 MeV and a maximum energy of about 12 MeV (see Figure 1.8). But their short half-life (2.65 y) necessitates frequent replacement of the sources to maintain a sufficient neutron flux [87].

Alpha neutron sources are also used to produce neutrons. These sources combine alpha-emitting radioisotopes and light elements with which alpha particles interact via (α,n) reactions, thereby inducing neutron production. Elements like Li, B, C or F can serve as target material, but neutrons are typically generated from Be nuclei through the ^{9}Be(α,n)^{12}C reaction, which produces the highest neutron yield [88]. Currently, the most common alpha-emitters used are ^{241}Am and $^{238/239}$Pu, found in sources called AmBe and PuBe, respectively. In the past, ^{226}Ra, ^{210}Po and ^{242}Cm were also used, but are no longer employed due to the high level of gamma radiation for the ^{226}Ra and the short half-lives of ^{210}Po and ^{242}Cm nuclei [89]. Due to the short range of alpha particles, alpha-emitters and target nuclei must be in immediate vicinity. Alpha neutron sources are therefore composed of a mixture of beryllium metal with an oxide of the alpha-emitter, encapsulated in stainless steel cylinders of a few centimeters long and diameter [86]. The AmBe sources have a yield of 8.2×10^{-5} n/s/Bq and between 6.5×10^{-5} n/s/Bq and 7.9×10^{-5} n/s/Bq for the PuBe sources, depending on the proportion of ^{238}Pu and ^{239}Pu nuclei [88]. Both sources emit neutrons with an average energy of around 4.2 MeV and a maximum energy of 11 MeV [86, 90]. They can achieve neutron yields similar to ^{252}Cf sources, ranging from 10^{6} to 10^{9} n/s, but require much more radioactive material due to the indirect way by which neutrons are produced.

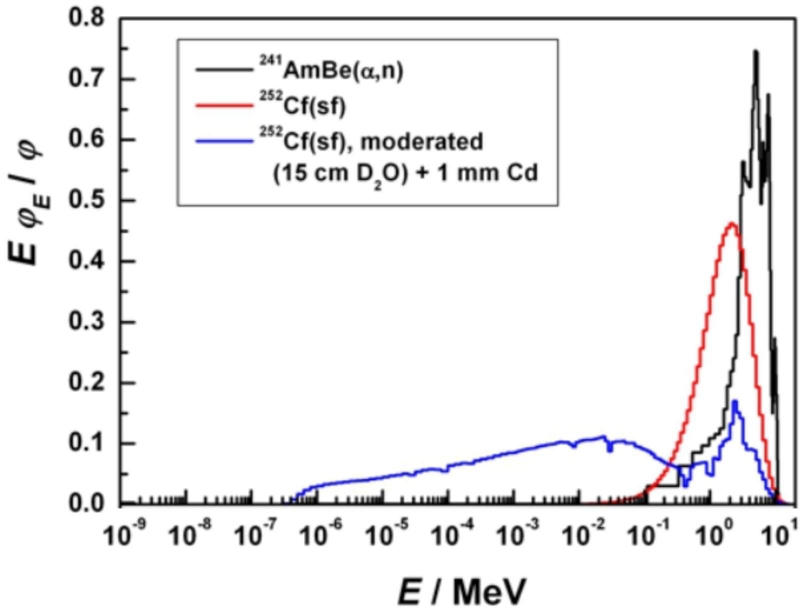

Figure 1.8 – Neutron spectra of isotopic sources: AmBe (black), ^{252}Cf (red) and ^{252}Cf with a D_2O moderator [90].

Gamma neutron sources, also called photoneutron sources, operate on the same principle as the alpha neutron sources, but they use (γ,n) reactions instead of (α,n) reactions to produce neutrons. To occur, the gamma-ray must have an energy higher than the neutron binding energy, which is above 6 MeV for all nuclei except for ^{9}Be and ^{2}H, which require only 1.67 and 2.23 MeV, respectively. Gamma neutron sources are therefore composed of a radioisotope that emits sufficiently energetic gamma-rays (such as ^{24}Na, ^{88}Y or ^{124}Sb), surrounded by a beryllium or D_2O layer [87]. Unlike alpha particles in alpha neutron sources, gamma-rays are not slowed down in the target material, resulting in gamma neutron sources emitting nearly monoenergetic neutrons. For example, the most common gamma neutron source, named SbBe and composed of ^{124}Sb as gamma-ray emitter and ^{9}Be as target material, produce neutrons of 23 keV. However, the neutron yield of such sources is very low, about 2.1×10^{-5} n/s/Bq, requiring high-activity gamma-ray sources. This induces neutron emissions in a very noisy environment and radiological constraints during handling due to the high dose rate [88]. These disadvantages, combined with their short lifespan, mean that these sources are no longer widely used.

Neutron sources based on radioisotopes can deliver isotropic neutron emissions up to around 10^{9} n/s [91], with energies spanning several orders of magnitude (for ^{252}Cf and alpha neutron sources). They can be contained in small volumes of a few cubic centimeter and do not require any power supply. However, their fluxes are relatively low, and they continually emit neutrons which is not suitable for applications requiring pulsed emissions (like NRS).

1.3.2 Sealed tube neutron generators

Sealed tube neutron generators are compact devices that rely on ^{2}H(d,n)^{3}He or ^{3}H(d,n)^{3}He reactions, producing neutrons of 2.45 or 14.1 MeV, respectively. These D-D and D-T fusion reactions are particularly suitable for small generators to produce neutrons since their cross sections and the small Coulomb barrier induced by these light elements do not require them to be accelerated to very high energies. Indeed, the deuterium nuclei, produced from ionized deuterium gas in the ion source, only need to be accelerated to a few hundred keV, which can be easily achieved in small devices by applying a potential difference of typically between 50 and 300 kV [92]. The deuterium nuclei then interact with a target, which generally consists of a titanium deposition on a metal substrate in which high concentration of deuterium or tritium are stored. Such neutron generators, contained in a portable vacuum-tight sealed tube of a few kilograms, can reach neutron yields up to 10^{7} n/s with D-D reactions and 5×10^{8} n/s with D-T reactions [93, 94]. Neutron yields of 10^{10} n/s can be reached but requiring much larger generators [95]. The maximal neutron flux is limited by the ion source output and the target's ability to withstand the beam power, which induces high temperatures. However, these neutron generators are switch-on/off devices which can emit pulsed neutron beams, features that isotopic neutron sources do not have. But only fast monoenergetic neutrons are produced with minimal pulse durations of about 1 µs, which is suitable for performing fast neutron radiography but not appropriate for NRS experiments [92].

1.3.3 Accelerator-based neutrons sources

Conventional particle accelerators are also used to produce neutrons from light charged particles (protons or deuterons) accelerated and directed onto different light element targets (^{2}H, ^{3}H, Li, Be, Sc, V, …), which induces nuclear reactions, typically (p,n) or (d,n) reactions, which cross sections are particularly interesting. Electrostatic accelerators such as Van de Graaff or Cockcroft-Walton accelerators are the simplest and the more accessible machines to produce neutrons from accelerators since they use very proven technologies based on static electric fields to accelerate ions. These ions, which have energies from a few tens keV to several MeV, are characterized by tight energy distributions, representing a major advantage in producing monoenergetic neutrons. Thus, they are widely employed in several facilities (like AMANDE [96], NPL [97] or PTB [98]) to produce reference monoenergetic neutron fields. In such facilities, monoenergetic neutrons from a few keV to around 20 MeV can be emitted with fluxes of about 10^{6} n/cm²/s (at 10 cm from the target), depending on the reaction considered [96].

To obtain higher neutron energies and fluxes, cyclotrons are preferred because they use radiofrequency-modulated electric fields to accelerate more energetic ions (up to a few hundred MeV) with higher beam currents (up to around 1 mA) [92]. Thus, neutron fluxes of 2×10^{12} n/cm²/s [99] and energies up to 200 MeV [100] has been achieved using (p,n) reactions on light element targets made of Be or Li. However, this induces important radiological constraints, such as significant material activation and high dose rates during irradiations, which may require thick concrete shielding to ensure radiation protection for the staff and users. Cyclotrons are therefore heavier and more complex machines, occupying larger facilities than other neutron sources previously discussed. This has a strong impact on the total cost of such facilities, which can easily reach several million US dollars. Nevertheless, quasi-monoenergetic neutron emissions in both continuous and pulsed modes (in the nanosecond scale range) are possible with cyclotrons, making these accelerators very versatile neutron sources [92].

Another method to produce neutrons involves using spallation reactions, which require accelerating protons to GeV energy levels and targeting them onto high-Z materials, such as tungsten, mercury or lead. At these energies, the *de Broglie* wavelength of protons is smaller than the diameter of heavy nuclei, so the protons interact directly with the nucleons instead of the whole nucleus. Thus, protons transfer their kinetic energy through nucleon-nucleon collisions and eject neutrons and protons from the target nuclei, this is referred to as intra-nuclear cascades. The ejected nucleons can have sufficient energies to induce nuclear reactions in adjacent nuclei and produce other neutrons, these are the inter-nuclear cascades [101]. The spallation regime is therefore a combination of these two processes which can generate between 20 and 50 neutrons per incoming proton, depending on the proton incident energy and the target material [102]. The obtained neutron spectrum follows a nearly Maxwell-Boltzmann distribution (see Figure 1.9), but neutrons are usually slowed down by elastic collisions in low-Z moderators (H_2, H_2O, D_2O, …) to obtain more thermal or cold neutrons, which are used for neutron scattering applications (see Section 1.2.2).

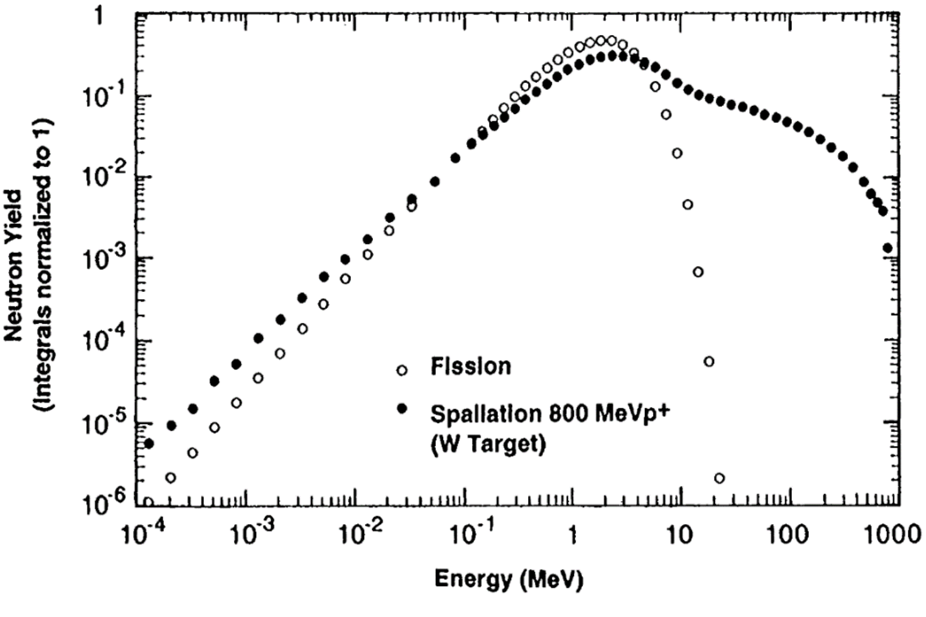

Figure 1.9 – Neutron spectra obtained by fission reactions of ^{235}U *(empty circles) and spallation reactions in a tungsten target (black circles) [101].*

Spallation neutron sources generally use linear accelerators and/or synchrotrons to accelerate protons with sufficient energy to trigger spallation reactions. They operate in pulsed mode (from µs to several ms pulse duration) and generate the most intense neutron bursts with peak thermal fluxes up to around 10^{17} n/cm²/s and average fluxes of about 10^{14} n/cm²/s (at the moderator surface) [101, 103]. However, the high particle energies and fluxes involved require large accelerators, many secondary systems (vacuum pumping systems, cooling systems, …) and thick radiation shielding, making these neutron sources huge facilities whose costs can reach several hundred million or several billion US dollars [104, 105].

Finally, (γ,n) reactions are also used to generate neutrons from electrons accelerated to a few tens MeV using a linear accelerator and directed onto a high-Z target (Ta, W, Pb, …) to produce Bremsstrahlung emissions. The produced gamma-rays, having a maximum energy equals to the electron kinetic energy, then interact with a secondary target to induce neutron emissions via photonuclear reactions. As with the gamma neutron sources discussed earlier (see Section 1.3.1), the most suitable secondary targets are those with the lowest neutron binding energies, i.e. ^{9}Be and ^{2}H [92]. To improve the neutron production, uranium can be used as a high-Z target to take advantage of photofission reactions which increases the number of neutrons emitted. By using this technique, the Geel Electron Linear Accelerator Facility (GELINA) is one of the brightest neutron sources generated by an electron linear accelerator, with a peak flux of 4.3×10^{10} neutrons produced in a 1 ns pulse, while the average flux is typically around 2.5×10^{13} n/s with neutron energies spanning several orders of magnitude, from subthermal to around 20 MeV, with a peak at a few MeV [106]. However, such facilities have a low electrical efficiency with significant heat to be dissipated and emit neutrons in a very noisy environment due to the correlated high gamma-ray emissions [92].

1.3.4 Fission reactors

Nuclear reactors based on fission reactions represent another way to produce neutrons. The fission reactions consist in the capture of a neutron by a heavy nucleus, called fissile nucleus, which formed compound nucleus is unstable and disintegrates by splitting into two lighter nuclei, known as fission fragments (see Figure 1.10). Neutrons are released during this process and also by the disintegration of the fission fragments, which are neutron-rich too.

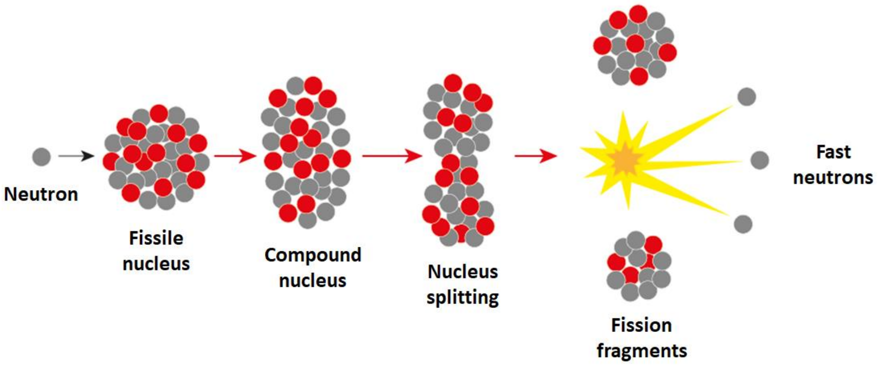

Figure 1.10 – Schematic illustration of a fission reaction

Fission reactors typically use ^{235}U-enriched uranium as fuel. These fissile nuclei emit an average of 2.5 fast neutrons per fission reaction and some of them can in turn induce fission reactions that trigger and sustain a chain reaction. The other neutrons are absorbed by control rods to control the chain reaction or they exit the reactor core to be used in various applications [31]. At this stage, the neutron spectrum is described by a Maxwell-Boltzmann distribution (see Figure 1.9), via the following equation [101]:

$$\frac{dN}{dE}(E) = \frac{2E^{1/2}}{\pi^{1/2}E_T^{3/2}} \exp\left(-\frac{E}{E_T}\right) \tag{1.13}$$

With E_T the mean temperature of the nucleons in the nucleus, which is equal to 1.29 MeV for ^{235}U fission.

However, most of the applications (see Section 1.2) as well as chain reactions of fission with ^{235}U nuclei require thermal neutrons. Thus, neutrons are slowed down using low-Z moderators, usually consisting in water or heavy water, which also serve as coolants for the reactor core. Fission reactors are currently the neutron sources producing the highest average fluxes. The ILL reactor (Grenoble, France) and the HFIR (ORNL, USA) can, indeed, reach neutron fluxes up to 1.5×10^{15} n/cm²/s. As shown in Figure 1.11, it is one order of magnitude greater than the average fluxes obtained by accelerator-based spallation neutron sources [31, 101]. Nevertheless, these research reactors suffer from several disadvantages, such as safety constraints related to all nuclear reactors and important nuclear waste production due to material activation and the spent fuel generating long-lived transuranic radioisotopes. Although they still play an important role in scientific research involving neutrons, most of these reactors were commissioned in the 1960s or 1970s, making them aging facilities that will soon be dismantled. Due to the aforementioned constraints and the large size of these facilities, the decommissioning operations could be very costly, estimated to several hundred million US dollars per facility [107].

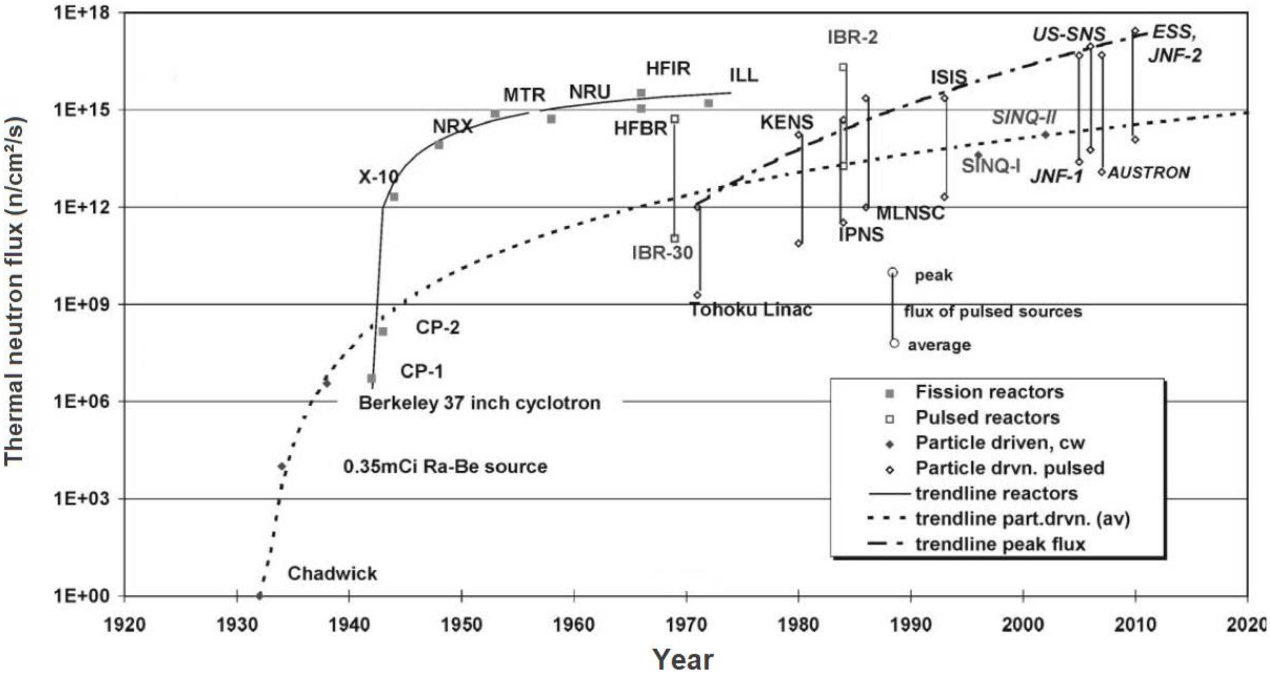

Figure 1.11 – Evolution of thermal neutron fluxes available with different neutron sources [101].

1.4 Laser-driven neutron sources

The previous section detailed the main characteristics of conventional neutron sources but also their limitations. We saw that isotopic neutron sources, sealed tube neutron generators and small accelerators-based neutron sources produce relatively low fluxes due to structural constraints, with neutron emissions that are not appropriate for applications such as NRS. Spallation neutron sources or fission reactors produce higher fluxes, suitable for most applications using neutrons, but they require larger and much more expensive facilities. Their number is limited and tends to decrease, making them difficult to access. These facilities also suffer from serious radiological constraints, such as significant material activation, which produces large quantities of radioactive waste during their lifespan and decommissioning. Thus, new neutron sources need to be developed to overcome these limitations. In this section, the interaction of laser with matter will be described as well as how the induced processes can be used to produce neutron emissions. We will see that laser-driven neutron sources could therefore represent an interesting alternative to common neutron sources.

1.4.1 Laser technology

Lasers, which stand for Light Amplification by Stimulated Emission of Radiation, are devices that emit light through optical amplification based on the stimulated emission principle described in 1917 by Albert Einstein [108]. These light sources typically consist of three main components: a gain medium, an energy source (or pump source) and an optical cavity. The energy source, which can be electrical currents, chemical reactions or another light source like a flashlamp or another laser, provides energy to the gain medium. This excites its atoms or molecules, making the electrons passing from the ground level to excited states. These excited electrons eventually return to lower energy levels, emitting photons randomly in all directions in a process called spontaneous emission. But, when a photon of a specific wavelength passes through the excited gain medium, it can stimulate the emission of another photon with the same phase, direction, wavelength, and polarization, this is known as stimulated emission. The optical cavity, made of two mirrors facing each other and on either side of the gain medium, amplifies the light by reflecting these photons back and forth between the mirrors, passing through the gain medium multiple times. Many passes through the gain medium stimulate the emission of more and more photons, which build up within the optical cavity. One of the mirrors of the optical cavity is partially reflective, letting photons escape when the light intensity reaches a certain threshold. This produces a coherent and highly collimated beam of laser light.

The first functioning laser, built in 1960 by Theodore H. Maiman, was based on a ruby crystal pumped by a flashlamp, emitting photons of 694 nm wavelength with a maximum power of 1 kW in continuous mode [109]. Between the 1960s and the 1980s, major improvements have been made to the laser technology to reach higher powers. The invention of Q-switching [110] and mode-locking [111] techniques allowed to develop pulsed lasers, with rapid progress in decreasing the pulse duration and increasing the peak power up to the gigawatt range. However, the amplification was limited by the energy density causing damages in the gain medium. This issue was resolved in 1985 by Donna Strickland and Gérard Mourou, who developed a technique called Chirped Pulse Amplification (CPA) [112]. As shown in Figure 1.12.A, the CPA involves dispersing the different wavelength components of the initial pulse using a grating, which induces different path lengths for each wavelength and temporally stretches the pulse. This longer, temporally stretched pulse is then amplified without reaching the energy density in the gain medium that would have caused damage if the initial shorter pulse was directly amplified. Finally, the amplified, temporally stretched pulse is recompressed, by a symmetric grating system called compressor, to regain the initial pulse duration and obtain higher peak powers up to the terawatt range.

Another technique, called Optical Parametric Amplification (OPA) [113], is also used to amplify laser pulses. In the OPA, a laser pulse and a pump pulse, characterized by their respective frequency ν_L and ν_P, are sent into a nonlinear crystal. In such crystals, photons from the pump pulse can be converted into photons whose frequency corresponds to that of the laser pulse and photons, called idler photons, with a frequency $\nu_I = \nu_P - \nu_L$ (see Figure 1.12.B). Since both laser photons and idler photons exit the nonlinear crystal, the energy deposition is minimal, leading to a laser pulse amplification with reduced thermal effects. However, the OPA requires that the laser pulse and the pump pulse must be synchronized for this non-linear effect to appear. This synchronization can be facilitated by using pulses having a large bandwidth, which induces significant temporal stretching. Since the temporal stretching of pulses is also an important requirement for performing CPA, these two amplification techniques can be combined and used together, this is the so-called OPCPA technique [114]. Thus, in the high intensity facilities, large bandwidth amplification crystals, such as Ti:Sapphire crystals or Nd:YAG crystals, are often used in configurations involving multiple amplification stages, whose OPCPA is used for the first stages while CPA is used for the last stages, usually. Such facilities can therefore produce laser pulses with duration down to few tens of femtoseconds, reaching peak power of several petawatts. These PW-class, short duration lasers are now present all around the world [115] with, for example, the Apollon laser (LULI, France) [116, 117], CoReLS laser (CoReLS, South Korea) [118] or BELLA (LBNL, USA) [119].

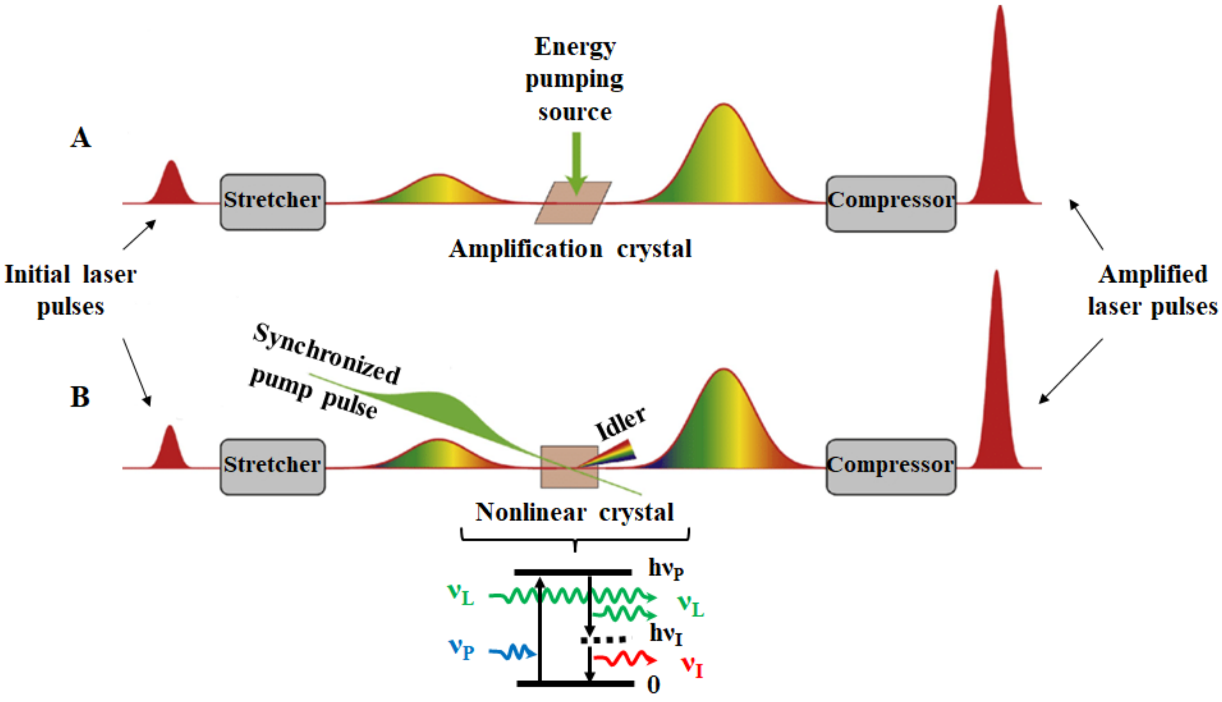

Figure 1.12 – Schematic view of the CPA (A) and OPA (B) techniques.

1.4.2 Laser/matter interaction

Target ionization

A high power, short duration laser pulse can be focused using an off-axis parabolic mirror and directed onto a target. A focal spot of a few square micrometers can be obtained, leading to a peak intensity of up to 10^{23} W/cm² [118]. This focused laser pulse then transfers its energy to the target causing ionization and producing a plasma. The ionization can be explained by three mechanisms: multiphoton ionization [120, 121], tunneling ionization [122, 123] and barrier-suppression ionization [123, 124].

The multiphoton ionization is characterized by the absorption of two or more photons by an atom until the sum of the energy of each photon reaches the ionization energy, which is the minimum energy required for an electron to be ejected from an atom. This effect is predominant for intensities ranging from 10^{10} W/cm² to 10^{12} W/cm². Unfortunately, such intensities can be easily reached by Amplified Spontaneous Emissions (ASE), causing a pedestal on the picosecond or nanosecond scale before the main pulse, or by pre-pulses induced by amplified reflections in the laser system. These unwanted emissions can therefore ionize the target and create a plasma, called pre-plasma, before the arrival of the main pulse, which alters the laser/target coupling.

When the intensity reaches 10^{13} W/cm², the superposition of the electric potential of the atom and that created by the laser combine, causing a potential suppression. This reduces the potential barrier for electrons within the nucleus's field, allowing the electrons to escape the atom either through the tunnel effect or by direct ionization, if the barrier drops below the ground state. These are known as tunneling ionization and barrier-suppression ionization, respectively.

Plasma production

These ionization mechanisms induce the production of a plasma, characterized by partly or fully ionized matter, leading to a sufficient proportion of free electrons and ions for collective behaviors to occur due to electromagnetic interactions, which have an influence over large distances. The plasma produced can then be described by several quantities that play an important role in laser/matter interaction [125].

When a perturbation is applied to a plasma, the electrons move and the electron distribution changes. The ions, having barely moved since they are much heavier, exert an attractive force via Coulomb interactions, which forces the electrons to return to their initial position. This creates a harmonic oscillator whose oscillations of electrons are characterized by the plasma frequency (which is actually a pulsation). Thus, this pulsation describes the movement of the electrons inside a plasma, following the equation:

$$\omega_P = \sqrt{\frac{n_e e^2}{\varepsilon_0 m_e}} \tag{1.14}$$

With n_e the electron density, e the elementary electric charge, ε_0 the vacuum permittivity and m_e the electron mass.

A laser can only propagate inside a plasma if its pulsation ω_L is greater than the plasma frequency ω_P. Since this plasma frequency only varies as a function of the electron density n_e, we can define an upper limit density for which the laser pulse can still propagate in the plasma. This is the so-called critical density, defined by:

$$n_c = \frac{\varepsilon_0 m_e \omega_L^2}{e^2} \approx \frac{1.1 \times 10^{21}}{\lambda_L^2[\mu m]} cm^{-3} \tag{1.15}$$

With λ_L the laser wavelength (in µm).

If the electron density is lower than the critical density ($n_e < n_c$), the plasma is underdense and allows the laser to propagate inside. Conversely, if the electron density is greater than the critical density ($n_e > n_c$), the plasma is overdense and opaque to the laser. In this case, the transmitted pulse is described by an evanescent wave whose skin depth – the distance over which the amplitude of the laser wave is reduced by a factor $\frac{1}{e}$ – is expressed by the following equation:

$$\delta = \frac{c}{\sqrt{\omega_P^2 - \omega_L^2}} \tag{1.16}$$

For a Ti:Sapphire laser emitting photons of about 820 nm wavelength and interacting with a solid target, the skin depth is typically of a few tens of nanometers.

Heating processes

After having transformed the target into a plasma, a laser pulse transfers its energy to the electrons through several mechanisms, called heating processes. These processes are based on the setting in motion of electrons by the electromagnetic wave of the laser pulse via the Lorentz force defined as:

$$F_L = -e(\vec{E} + \overrightarrow{v_e} \times \vec{B}) \tag{1.17}$$

With e the elementary electric charge, $\vec{E}$ the electric field, $\overrightarrow{v_e}$ the electron velocity and $\vec{B}$ the magnetic field.

The electromagnetic wave therefore induces an oscillation of the electrons with velocities characterized by a dimensionless electric field amplitude, noted a_0 [126]:

$$a_0 = \frac{eE_0}{m_e \omega_L} = \sqrt{\frac{I_0 \times \lambda_L^2}{1.37 \times 10^{18}}} \tag{1.18}$$

With E_0 the electric field amplitude, I_0 the laser intensity (in W/cm²) and λ_L the laser wavelength (in µm).

This value also makes it possible to classify the laser/target interaction regimes. Typically, relativistic velocities are reached when a_0 is greater than 1, which corresponds to laser intensities above 2×10^{18} W/cm² for a Ti:Sapphire laser. In such cases, several heating processes can occur, such as inverse Bremsstrahlung or resonance absorption [127], allowing the energy transfer from the laser to the electrons, thereby increasing their temperature.

Another process of electron heating, called ponderomotive force, plays an important role in the energy transfer. In a homogeneous oscillating electric field, an electron can oscillate at the electric wave frequency but stays on average in the same position. However, in experimental conditions, a laser is focused on a target and the resulting focal spot has a Gaussian shape with the highest intensity at the center. This induces a strong gradient of intensity and an inhomogeneous electric field in the target. Thus, electrons, which were first pushed away from the center by the laser electric field, will not return at their initial position when they will be pushed back in the center during the phase inversion of this electric field, since the laser electric field weakens as we move away from the center. Therefore, this asymmetric oscillation tends to move electrons from the high laser intensity region towards the low intensity regions, this is the so-called ponderomotive force.

For relativistic electron velocities, the magnetic field becomes significant and adds an additional component to the ponderomotive force, resulting in electron acceleration in the forward direction, in addition to the previously mentioned radial expansion. A representation of the electron trajectory inside the target is depicted in Figure 1.13. All these processes lead to energy transfer from the laser pulse to the electrons by increasing their kinetic energy through different processes. The kinetic energies of these hot electrons follow a Maxwell-Boltzmann distribution, characterized by a mean temperature following this equation [128]:

$$k_B T_{hot} = m_e c^2 \left(\sqrt{1 + \frac{I_0 \times \lambda_L^2}{1.37 \times 10^{18}}} - 1 \right) \tag{1.19}$$

With I_0 the laser intensity (in W/cm²) and λ_L the laser wavelength (in µm). An electron temperature of around 3 MeV can thus be obtained from a Ti:Sapphire laser with an intensity of 10^{20} W/cm².

1.4.3 Ion acceleration

The phenomena of target ionization, plasma production and electron heating previously discussed are the bases for understanding ion acceleration using lasers, as they are involved in the different acceleration mechanisms. Ion acceleration with lasers is a relatively recent research field, compared to conventional acceleration mechanisms used in particle accelerators. The first experimental demonstrations of this concept were carried out almost simultaneously in 1999 by two research teams who used PW-class lasers. These lasers delivered pulses of around 50 J focused on solid targets, with peak intensities of 5×10^{19} W/cm² at the VULCAN facility [129] and 3×10^{20} W/cm² at the Lawrence Livermore National Laboratory, where protons up to 58 MeV were measured [130]. Since then, significant progress was made over the last 25 years to understand the different processes that occur during the laser/target interaction and to improve the ion acceleration.

Nowadays, it is well-established that there are four main mechanisms of ion acceleration involving lasers [131]:

- Target Normal Sheath Acceleration (TNSA)
- Radiation Pressure Acceleration (RPA)
- Break-out Afterburner (BOA)
- Collisionless Shock Acceleration (CSA).

Target Normal Sheath Acceleration

Target Normal Sheath Acceleration (TNSA), described for the first time in 2001 [132], is the most widely used ion acceleration mechanism using lasers. It relies on the interaction of an ultra-intense linearly polarized laser pulse (> 10^{18} W/cm²) with a solid target that is a few hundred nanometers to a few hundred micrometers thick. In Section 1.4.2, we saw that such intense laser pulses are preceded by ASE or pre-pulses with intensities high enough to ionize the target, which forms a pre-plasma on its front face before the arrival of the main pulse (see Figure 1.13). When the main pulse arrives, it propagates inside this underdense pre-plasma and transfers its energy to the electrons, accelerating them to the MeV regime via the heating processes discussed earlier. Bunches of hot electrons then radially expand, travel through the target bulk and reach the rear face thanks to the oscillating ponderomotive force. At this stage, some of the electrons escape into the vacuum, forming a dense electron cloud (or sheath) in the vicinity of the rear face [133]. Other electrons move back to the front face via return currents and interact once again with the laser electric field, which increases their temperature and pushes them back to the rear face, this is known as electron recirculation process. A few recirculation cycles can occur, ultimately leading to an accumulation of electrons near the target's rear face, inducing significant charge separation and creating an electric field that can reach several TV/m [128].

This very high electric field can therefore ionize the atoms present on the rear face. The induced free electrons are pushed back to the front face due to the negative potential created by the electron sheath at the rear face, while ions are accelerated in the forward direction (see Figure 1.13). Note that most of these ions come from a contamination layer present on the rear face, composed of water and hydrocarbons [134]. Consequently, various ion species can be accelerated, but protons are predominant since the contaminants are hydrogen-rich and protons have the highest charge-to-mass ratio. The proton beam produced by TNSA usually exhibits an exponentially decaying spectrum with a sharp energy cut-off and a broad divergence angle (up to around 50°), which decreases with the energy [128]. Some examples of TNSA proton spectra are shown in Section 3. Ions can also be accelerated in the backward direction due to the electric field induced by the electrons present in the front face, but the beam is affected by the pre-plasma and the acceleration is less efficient than in the forward direction.

Several factors, such as laser parameters, affect the TNSA mechanism. Higher laser intensities and energies generally produce hotter electrons, leading to stronger acceleration fields and a higher number of ions with higher energies [135, 136]. Bunches of 10^{11} to 10^{13} protons per laser shot are generally produced [137, 138, 131], with a maximum energy of up to 150 MeV [139]. The laser-to-proton conversion efficiency can also be enhanced by improving the temporal contrast of the laser, defined as the ratio of the peak intensity to the ASE intensity, by reducing the ASE and pre-pulses [117]. The target material also plays an important role, as different materials have different ionization potentials and thermal properties. To reduce the energy losses of electrons via Bremsstrahlung emissions, low-Z targets are preferred. Moreover, the target thickness influences the transport of hot electrons, with thin targets allowing more efficient electron transport and ion acceleration. But, the target thickness is limited by the laser contrast because high-level ASE or pre-pulses can destroy a too-thin target before the arrival of the main pulse [128]. Finally, optimizing laser and target parameters can enhance ion acceleration via TNSA, but in such cases, other acceleration regimes may be reached.

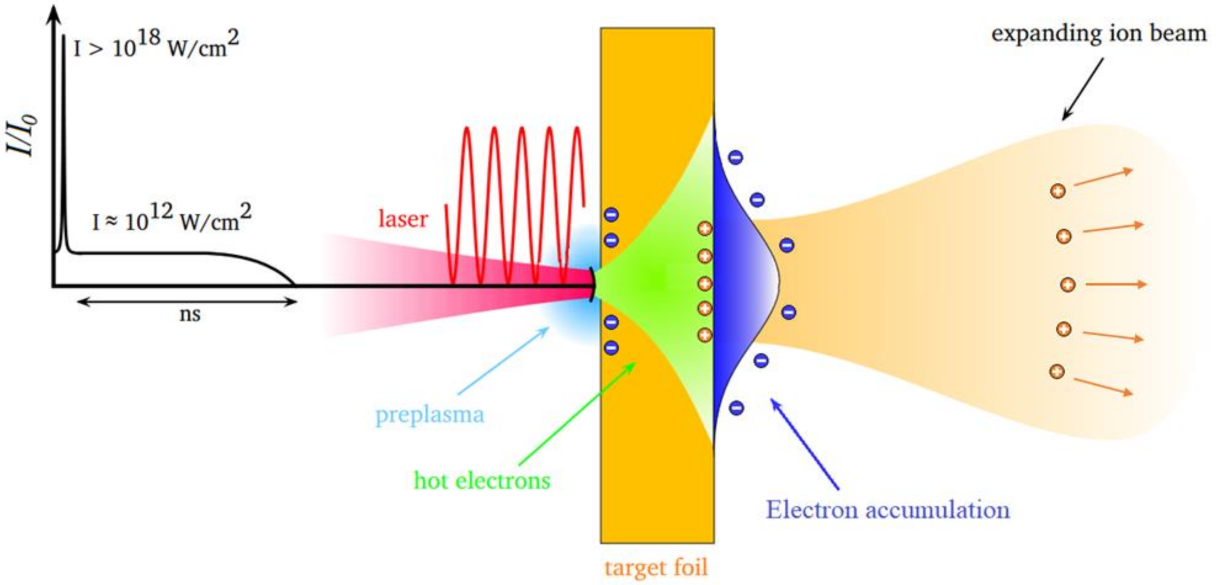

Figure 1.13 – Drawing, inspired by [128], detailing the Target Normal Sheath Acceleration (TNSA) mechanism, with a graph showing a typical temporal profile of the laser intensity.

Transparency Regime: Break-Out Afterburner

The Break-Out Afterburner (BOA) mechanism, which is an extension of the TNSA in a relativistic transparency regime, involves an ultra-intense laser pulse interacting with the front face of a very thin target (tens of nano…meters thick). This interaction generates a hot electron population that penetrates the target and sets up a sheath field at the rear face, similar to classical TNSA. As the laser pulse continues to deposit energy, the target undergoes relativistic transparency (also known as break-out), where the plasma density becomes comparable to the relativistic critical density. Thus, the plasma becomes transparent, allowing the laser pulse to propagate through the entire target, effectively accelerating electrons throughout the plasma volume.

The afterburner phase begins as the laser pulse exits the rear face of the target. The hot electrons, now moving at relativistic velocities, create a strong electrostatic field, in addition to the sheath field, which significantly enhances ion acceleration and dramatically increases the ion energy. The BOA mechanism thus involves a synergistic combination of direct laser acceleration, sheath acceleration and collective plasma effects [140].

Thanks to this transparency regime, the energy transfer from the laser pulse to the electrons is therefore enhanced compared to the TNSA mechanism, where only electrons present near the target's front face are accelerated. Ions with much higher energies, reaching 1 GeV for fully ionized carbon ions and a few tens MeV for protons, were thus experimentally obtained [141, 142, 143]. However, this requires laser pulses with ultra-high contrast to prevent preheating and early destruction of the thin targets by ASE or pre-pulses.

Radiation Pressure Acceleration

Radiation Pressure Acceleration (RPA) is another ion acceleration mechanism using a laser pulse with a circular polarization focused on a solid target. Unlike the linear polarization used in the TNSA mechanism, which induces an oscillating ponderomotive force and accelerates electron bunches from the front face to the rear face, circular polarization creates a steady ponderomotive force that applies a constant radiation pressure on the electrons. RPA can therefore operate through two regimes: the hole-boring regime and the light-sail regime.

In the hole-boring regime, a laser pulse with a sharp front edge impacts a thick target (a few micrometers thick). The laser's radiation pressure pushes the electrons into the target, creating a dense electron plasma near the front face. This pressure effectively bores a hole into the target, with ions being accelerated forward behind the electron front. On the other hand, the light-sail regime involves using a thin target (a few tens of nanometers thick). In this case, the entire target is accelerated as a single entity, much like a sail being pushed by the wind. The intense radiation pressure of the laser acts on the electrons at the target surface, creating an electric field that accelerates ions in the same direction as the laser pulse [131].

RPA offers several advantages, including the potential to produce ion beams in the MeV to GeV range with narrow-band energy distributions [9, 144, 145]. However, achieving efficient acceleration using this mechanism requires very high laser intensities ($> 10^{20}$ W/cm²), thin targets and therefore a very good contrast to avoid damage induced by pre-pulses. As a result, ions with only a few tens of MeV were experimentally obtained by RPA so far [146, 147, 148].

Collisionless Shock Acceleration

Collisionless Shock Acceleration (CSA) relies on the interaction of a high-intensity laser pulse with a plasma. This generates a strong electromagnetic shock wave, formed by collisionless shocks between particles, i.e. by collective electromagnetic interactions rather than binary collisions. This shock wave propagates through the plasma, and its front acts as a moving electric field, accelerating ions and electrons to high velocities [131].

CSA can be performed using lasers with intensities in the same order of magnitude as those used for TNSA ($10^{18\text{-}21}$ W/cm²), and ions with energies from tens to several hundreds of MeV can be obtained. However, it generally requires large laser systems with low repetition-rates, producing pulse trains or at least two synchronized laser pulses: one to ionize the target and form a plasma, and another to interact with the plasma to induce the shock wave [149, 150, 151, 152].

***

Although there are several laser ion acceleration mechanisms, TNSA remains the most commonly used to routinely generate ion beams, as it is the simplest to implement with current laser technologies. This new type of particle accelerator is particularly interesting since it can generate electric fields of several TV/m, compared to a few tens of MV/m for conventional accelerators. Hence, it is possible to accelerate protons to more than 100 MeV with laser systems that are more compact than conventional accelerators capable of reaching similar energies. Bunches of up to 10^{13} protons per laser pulse can be emitted over short durations (usually in the picosecond scale), thus generating very high currents of up to several megaamperes. However, laser-driven ions suffer from several drawbacks compared to conventional ion beams, including large beam divergences and broadband energy spectra, which are not suitable for certain applications, such as radiation therapy, but can be adapted to produce secondary reactions that generate neutron emissions.

1.4.4 Neutron production

The interaction of intense laser pulses with targets induces several physical processes, producing ion beams, hot electrons and gamma-rays via Bremsstrahlung emissions generated in a secondary target. These particles can then be used to induce secondary reactions that generate neutron emissions, making lasers a new source of neutrons. Laser-driven neutron sources generally rely on four main techniques to generate such particles: photoneutron reactions, ion beam-fusion reactions, laser implosion and pitcher-catcher technique.

Photoneutron reactions

Nuclear reactions based on the interaction of gamma-rays with target nuclei can produce neutrons, these reactions are called (γ,n) reactions. Ultra-intense lasers can indirectly induce such reactions using the hot electrons accelerated during the interaction of a laser pulse with a target. These relativistic electrons, with energies of several MeV, then generate Bremsstrahlung radiation in the form of gamma-rays. This process can occur inside the target or using a secondary converter target, also known as a converter, placed behind the first target. When gamma-rays reach sufficient energies (several MeV), they can excite the surrounding nuclei to excited states such that neutrons can be emitted during the de-excitation of these excited nuclei.

This mechanism of neutron production was demonstrated in 2000 by Ledingham *et al.* [153], who conducted an experiment at the VULCAN laser facility [154] in the UK. Laser pulses with durations of 1 ps, delivering up to 50 J, were focused on 1.75 mm thick tantalum targets. Bremsstrahlung emissions produced by the hot electrons inside the targets induced (γ,n) reactions within secondary targets. Radionuclides of ^{62}Cu were measured inside secondary copper targets, highlighting that the $^{63}\mathrm{Cu}(\gamma,n)^{62}\mathrm{Cu}$ reaction occurred and demonstrating the possibility of producing photoneutrons using lasers.

In 2014, Pomerantz *et al.* [13] performed an experiment at the Texas Petawatt laser facility [155]. In this experiment, a laser delivering 150 fs pulses with an energy of 90 J was focused on solid plastic targets of a few micrometers thick, producing bunches of relativistic electrons. An 18 mm thick converter made of natural copper was placed behind the primary target to intercept these relativistic electrons, which produce Bremsstrahlung emissions. The resulting gamma-rays were sufficiently energetic to induce (γ,n) reactions from Cu nuclei contained in the converter. Isotropic neutron emissions of up to 2×10^9 neutrons/shot were measured, with a neutron bunch duration shorter than 50 ps [13]. This resulted in peak fluxes of up to 3×10^{18} neutrons/sr/s, corresponding to 3×10^{16} neutrons/cm²/s at 10 cm from the converter, and mean fluxes of less than 5×10^2 neutrons/cm²/s (considering the laser repetition rate of 1 shot/hour).

In 2022, Günther *et al.* [156] performed a similar experiment, enhancing the maximum neutron yield obtained with this technique by almost a factor of ten. 20 J laser pulses of 100 fs duration, produced at the PHELIX laser facility [157], were focused on polymer aerogel foams. The accelerated relativistic electrons were directed into a gold converter to generate Bremsstrahlung emissions and induce (γ,n) reactions in the Au nuclei. A neutron yield of 1.4×10^{10} neutrons/shot was measured [156], corresponding to a mean flux of 3.1×10^3 neutrons/cm²/s at 10 cm from the converter.

Since the durations of nuclear reactions are negligible (< fs) [158], the neutron bunch durations correspond only to the transit time of electrons from the primary target to the converter. Given that the electron mass is much lower than that of ions, the transit time for electrons with similar kinetic energy is much shorter. Therefore, this neutron production mechanism using electrons instead of ions should result in shorter neutron bunch durations and higher peak fluxes. However, the quantity of emitted neutrons is limited by the low laser-to-photon energy conversion efficiency (< 1%) and the cross sections of (γ,n) reactions, which are lower than those of reactions producing neutrons with ions [8].

A recent paper [159] proposes a scaling law of neutron emissions produced by photoneutron reactions depending on the laser strength parameter a_0, and suggests that the neutron emissions produced from this technique follow an asymptotic behavior as laser intensity increases and a maximum neutron yield close to that already achieved by Günther *et al.* [159]. Thus, the neutron peak flux could be rapidly limited and the mean flux may only be improved by increasing the laser repetition rate. For the most powerful current-day laser systems with the highest repetition rates (e.g. ELI-NP at 10 PW and 1 shot/min [160]), up to 10^{13} neutrons/hour could be reached in a 4π solid angle [159]. This corresponds to a mean flux of around 2×10^6 neutrons/cm²/s at 10 cm from the source, which is on the same order of magnitude as isotopic neutron sources or sealed tube neutron generators (see Table 1.2) but requires much larger facilities, with however the advantage of providing ultra-short bunched sources.

Ion beam-fusion reactions

Neutrons can also be produced using ion beam-fusion reactions. For example, an ultra-intense laser pulse interacts with a solid target made of a deuterated material. This accelerates deuterons via different mechanisms (TNSA, hole-boring, …), which then travel through the target and interact with other deuterium nuclei, inducing D-D fusion reactions that produce 2.45 MeV neutrons. Gaseous or cluster targets containing deuterium nuclei can also be used [161, 162]. In these configurations, the ultra-intense laser pulse strips away the electrons from the nuclei, causing a Coulomb explosion that accelerates the deuterons with sufficient energies to induce D-D fusion reactions with neighboring deuterium nuclei.

In 1999, Disdier *et al.* [10] demonstrated the feasibility of this technique using a table-top laser delivering 300 fs pulses with an energy of up to 7 J, focused on deuterated polyethylene targets. A neutron yield of up to 10^7 neutrons/shot was obtained. A similar neutron yield of 5.5×10^6 neutrons/shot was measured by Lu *et al.* [162] by using 50 fs laser pulses of 5 J and deuterated methane clusters. Finally, Curtis *et al.* [163] achieved 1.2×10^7 neutrons/shot with 45 fs laser pulses of 8 J, but this required complex solid targets composed of a CD_2 substrate with CD_2 nanowires on its front face.

Several experiments were performed to propose scaling laws for neutron emissions produced via this technique as a function of the laser energy. It appears that the neutron yield varies linearly with the laser energy when deuterated methane clusters are used [162], and with the square of the laser energy when deuterium clusters are used [164]. In all cases, the neutron yields achievable with this technique are significantly lower compared to other methods, such as photoneutron reactions (see before) or pitcher-catcher technique [165, 166]. As a result, beam-fusion reactions in bulk materials are no longer widely used as laser-driven neutron sources.

Laser implosion

Neutron emissions induced by laser implosion are based on Inertial Confinement Fusion (ICF). ICF involves compressing a micro capsule containing deuterium and/or tritium to reach extremely high densities and temperatures, creating the conditions necessary for nuclear fusion to occur [167]. There are two main methods used to achieve this compression: direct drive implosion and indirect drive implosion [168].

In the direct drive approach, a spherical fuel pellet is directly illuminated by several laser pulses (see Figure 1.14). These laser pulses are synchronized and precisely arranged around the pellet to ensure uniform energy delivery. When the laser intensity reaches at least 10^{14} W/cm², the outer layers of the pellet are rapidly heated and ionized, turning into high-temperature plasma. This heated material is ablated, or blown off, from the surface, creating a reaction force that drives the rest of the pellet inward. This inward force causes the pellet to implode, compressing the fuel in the core to extremely high pressures and temperatures. The aim is to achieve a central "hot spot" where the fusion reactions can begin. If the implosion is symmetric and the energy is applied uniformly, the fuel can reach conditions where nuclear fusion occurs, releasing a significant amount of neutrons and energy [168].

Indirect drive implosion, on the other hand, uses a different approach to deliver energy to the fuel pellet. In this method, the pellet is placed inside a hollow cylindrical structure called a hohlraum, typically made of a high-Z material like gold. Instead of directly illuminating the pellet, the lasers are aimed at the inner walls of the hohlraum. When the laser energy strikes these walls, it generates intense X-rays. These X-rays then uniformly irradiate the fuel pellet, causing it to implode in a similar manner to the direct drive approach (See Figure 1.14). The X-rays heat the surface of the pellet, leading to the ablation of the outer layers and driving the implosion of the inner fuel. The use of X-rays can help achieve more uniform compression because the X-rays naturally smooth out any irregularities in the laser beams, leading to a more symmetric implosion [168].

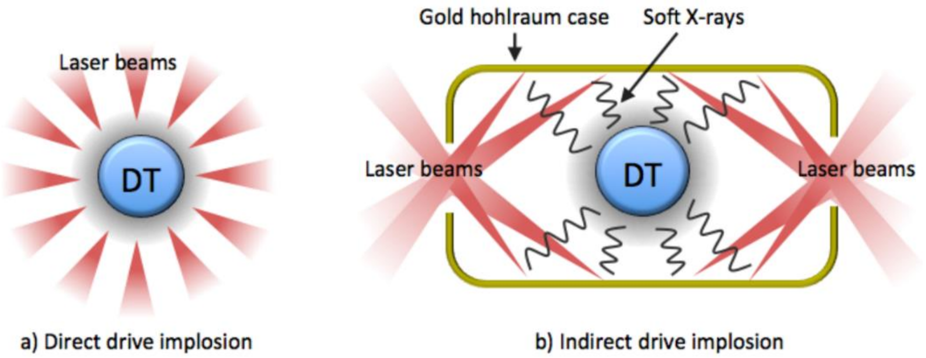

Figure 1.14 – Representation of direct (a) and indirect (b) drive implosion.

Direct drive implosions were performed at the OMEGA facility [169] in the USA, where 60 laser beams delivering a total laser energy of 37 kJ were focused on plastic capsules containing deuterium and tritium as fuel. D-T fusion reactions were ignited, producing 14.1 MeV neutrons with a maximum yield of 2×10^{14} neutrons/shot and a peak flux of 1.6×10^{22} neutrons/sr/s [170, 171]. Considering a maximum repetition rate of one shot per hour [172], a mean flux of 4.4×10^{7} neutrons/cm²/s at 10 cm from the source can be reached in this facility.

However, the indirect drive method is currently the more commonly used method in ICF experiments because it helps to mitigate the challenges of achieving a symmetric implosion. Indirect drive implosions were performed at the Laser Mega Joule (LMJ) Facility [173] in France using 48 laser beams with a total laser energy of up to 150 kJ. They interacted with rugby-shaped gold hohlraums, inducing the implosion of capsules filled with deuterium, which produced D-D fusion reactions and the emission of 2.45 MeV neutrons with a neutron yield up to 3×10^{11} neutrons/shot [174]. Considering a neutron bunch duration on the nanosecond scale and isotropic emissions [175], peak fluxes of up to 2.4×10^{19} neutrons/sr/s were achieved. However, a maximum of one shot per day are performed in this facility, resulting in relatively low mean fluxes of up to 2.8×10^{3} neutrons/cm²/s at 10 cm from the source.

The current record for neutron yield obtained with lasers is held by the National Ignition Facility (NIF) [176] in the USA. It was achieved with 192 laser beams delivering a total energy of 2.05 MJ. This record was set during the first successful “ignition” in history, where more energy was produced by the fusion reactions (3.1 MJ) than the total laser energy delivered (2.05 MJ), demonstrating the potential of using lasers to produce energy. A deuterium-tritium fuel capsule was used, producing a neutron yield of 1.1×10^{18} neutrons/shot [177], with a peak flux of around 9×10^{27} neutrons/sr/s. However, the low repetition rate of one shot per day results in a reduced mean flux of 1×10^{10} neutrons/cm²/s at 10 cm from the source.

Thus, neutron sources based on ICF produce the highest neutron flux among laser-driven neutron sources. The mean fluxes obtained are comparable to those produced by small light ion accelerators. However, ICF requires a complex illumination configuration involving tens or hundreds of laser beams, which consume a substantial amount of energy with significant losses (e.g. ~300 MJ to deliver 2.05 MJ of on-target energy at NIF). This requires very large facilities of several thousands of square meters which can cost billions of dollars.

Pitcher-catcher technique

The pitcher-catcher technique uses a double-target system to produce neutrons (see Figure 1.15). A first target (the pitcher) is irradiated by an ultra-intense laser pulse to accelerate ions (usually protons or deuterons) via the different possible mechanisms described in Section 1.4.3. These ions are then intercepted by a second target (called catcher or converter), inducing nuclear reactions that produce neutrons. As mentioned in Section 1.4.3, ion beams are generally produced using the TNSA mechanism, which generates exponentially decaying energy spectra. Although energies of several tens of MeV can be easily reached, most of the ions have relatively low energy (a few MeV). To maximize neutron production, converters are therefore composed of low-Z materials to exploit the favorable cross sections of (ion,n) reactions in these materials. Beryllium or lithium, in form of lithium fluoride (LiF) which is more chemically stable, are commonly used as converter material.

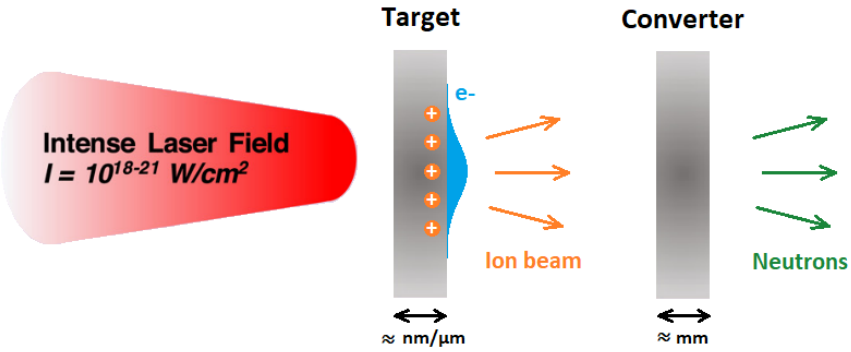

Figure 1.15 – Schematic view of the pitcher-catcher configuration.

One of the first neutron production experiments using the pitcher-catcher technique was performed in 2004 by Lancaster *et al.* [11] at the VULCAN laser facility in the UK. Laser pulses with a duration of 1 ps and an energy of 69 J were focused on Mylar targets, producing proton beams that were captured by a 3.4 mm thick LiF converter, leading to a neutron fluence of 3×10^8 neutrons/sr. In 2013, several experiments were carried out at the Trident laser facility [178] in the USA to produce higher neutron fluxes using 600 fs laser pulses of 80 J. Deuterated plastic targets (CD_2) were used to generate deuteron beams, which interacted with a beryllium converter, inducing (d,n) reactions and neutron fluences of 4.4×10^9 neutrons/sr for Jung *et al.* [179] and 5×10^9 neutrons/sr for Roth *et al.* [180]. Guler *et al.* [181] used these neutron emissions to perform neutron radiography, marking the first attempt to use laser-driven neutrons for practical application. In 2018, Kleinschmidt *et al.* [14] replicated the experiment at the PHELIX laser facility [157] in Germany, using the same configuration – deuterated plastic targets as the pitcher and a beryllium converter. The PHELIX laser delivers pulses of 600 fs duration but with higher energy, around 175 J. This increased the maximum neutron fluence produced by the pitcher-catcher technique, reaching 1.42×10^{10} neutrons/sr.

Other types of converters were also tested. For example, Alejo *et al.* [166] conducted an experiment at the VULCAN laser facility using deuterated plastic as converter. This setup induced D-D fusion reactions and neutron production with deuterons accelerated from deuterated copper targets. Despite a laser energy of 200 J, the measured neutron fluence was only of 2×10^9 neutrons/sr, nearly ten times lower than the record established by Kleinschmidt *et al*. Günther *et al.* [156] also tested a high-Z converter at the PHELIX laser facility to take advantage of good cross sections of (p,xn) reactions in such materials for protons of several tens of MeV. Protons were accelerated from aerogel-foam targets using laser pulses of only 20 J, producing proton energies higher than 40 MeV. The interaction of these protons with a gold converter, where up to (p,3n) reactions occurred, generated a neutron fluence of 4.9×10^9 neutrons/sr. This was only three times lower than the previous record, despite using ten times less laser energy. Additionally, Zimmer *et al.* [182] tested a hybrid converter composed of a layer of LiF and a layer of beryllium. LiF has advantageous neutron production cross sections at lower energies compared to beryllium, so the combination of both allows to benefit from all deuteron energies and maximize the neutron production. A neutron fluence of 1.43×10^9 neutrons/sr was measured with this hybrid converter, which is three times higher than that obtained with a simple beryllium converter, thus demonstrating the benefits of such hybrid converters. This experiment also showcased the potential of using this laser-driven neutron source to carry out NRS on a tungsten sample [182].

Currently, the maximum neutron fluence obtained using the pitcher-catcher technique is 2.4×10^{10} neutrons/sr. This record was set in 2023 by Yogo *et al.* [12] at the LFEX laser facility [183] in Japan, using 1.5 ps laser pulses of 900 J. Deuterated polystyrene targets were used as the pitcher, accelerating deuterons that interacted with a beryllium converter. Considering the transit time of deuterons between the pitcher and the catcher on the nanosecond scale, a peak flux of 2.4×10^{19} neutrons/sr/s was reached, corresponding to approximately, 2.4×10^{17} neutrons/cm²/s at 10 cm from the catcher, and a mean flux of 6.4×10^4 neutrons/cm²/s, since the LFEX laser can operate at a repetition rate of one shot per hour.

Hence, the pitcher-catcher technique can generate higher peak and mean neutron fluxes compared to photoneutron and beam-fusion reactions, while requiring much more compact and less complex facilities than those used for ICF experiments. The pitcher-catcher technique thus offers a favorable compromise between reachable neutron flux and the size/cost of facilities. Furthermore, this method holds promising potential for further development, as scaling laws suggest that the neutron yield could increase by a power from 2.5 to 3.5 with laser energy or intensity. [12, 184]. Finally, several improvements could enhance neutron flux, such as using optimized hybrid and/or high-Z converters and accelerating ions with RPA or BOA mechanisms. These advancements may enable reaching the spallation regime in the converter, significantly increasing the neutron yield [185, 186].

***

In summary, laser-driven neutron sources produce shorter neutron bunches (< ns) and higher peak fluxes compared to conventional neutron sources (see Table 1.2), making them particularly suitable for applications such as NRS [182, 12] or to reproduce astrophysical processes in laboratory [80]. Furthermore, the interaction of laser pulses with targets generates significant amounts of X-rays, suggesting that combined neutron/X-ray radiography could be a promising future application for these new neutron sources [187].

Beyond generating very short neutron bunches, laser-driven neutron sources offer several advantages. Neutron production with lasers involves only light transportation before the interaction with the target. Furthermore, the particle acceleration that induces neutrons occurs over very small distances. Consequently, much less material activation is induced in such laser facilities compared to accelerator-based neutron sources or fission reactors. This results in reduced radiation shielding, less radioactive waste production and easier decommissioning. Moreover, unlike particle accelerators, laser facilities do not require energy-intensive electromagnetic elements (such as dipoles or quadrupoles) to control ion beams. These factors make lasers more compact and less expensive neutron sources.

However, the laser-driven neutron sources still have lower mean fluxes compared to those of conventional neutron sources (see Table 1.2). But, ongoing research aims to improve laser technology by enhancing laser amplification and repetition rates to overcome the current limitations. Such advancements could make laser-driven neutron sources a viable alternative to conventional sources, especially as their number tends to decrease due to the planned shutdown of many research reactors [188, 189].

Neutron source	**Peak neutron flux [n/cm²/s]**	**Mean neutron flux [n/cm²/s]**	**Neutron bunch duration**	**Repetition rate**
Isotopic neutron sources	$< 10^{6\,*}$	$< 10^{6\,*}$	Continuous	-
Portable sealed tube neutron generators *(P385, Thermofisher)*	$10^{9\,*}$	$10^{6\,*}$	> 1 µs	~ kHz
Small accelerator-based neutron sources *(AMANDE, France)*	$10^{6\,*}$	$10^{6\,*}$	Continuous	-
Cyclotron-based neutron sources *(SINQ, Switzerland)*	10^{14}	10^{14}	Continuous	-
Spallation neutron sources *(SNS, USA)*	10^{17}	10^{14}	~ 1 µs	60 Hz
Fission reactors *(ILL, France)*	1.5×10^{15}	1.5×10^{15}	Continuous	-
LDNS – Photoneutrons *(Texas Petawatt, USA)*	$3\times10^{16\,*}$	$5\times10^{2\,*}$	50 ps	1 shot/hour
LDNS – Beam-fusion reactions *(ALEPH, USA)*	$\sim 10^{15\,*}$	$\sim 3\times10^{4\,*}$	~ 10 ps	3.3 Hz
LDNS – Laser implosion *(NIF, USA)*	$\sim 10^{26\,*}$	$\sim 10^{10\,*}$	~ 10 ps	1 shot/day
LDNS – Pitcher-catcher technique *(LFEX, Japan)*	$2.4\times10^{17\,*}$	$6.4\times10^{4\,*}$	~ 1 ns	1 shot/hour

** Flux at 10 cm from the source*

Table 1.2 – Comparison of characteristics of conventional and present-day laser-driven neutron sources.

2. Neutron detection

As mentioned in Section 1.1, neutrons are indirectly ionizing particles that can subsequently cause material activation and severe damage to cells and DNA. The doses induced by neutrons in the human body depend on their energy [190], it is therefore necessary to characterize the flux and energy distribution of neutron sources to ensure the radiation protection for both goods and people. Neutrons are neutral particles and their interactions with matter are relatively weak since they only interact with atomic nuclei. Consequently, neutrons are indirectly detected through secondary reactions such as scattering or absorption (detailed in Section 1.1.3).

Elastic scattering of neutrons produces recoil nuclei within the detector material, leaving a trace of the neutrons' passage via excitation mechanisms. As explained in Section 1.1.3, the energy transfer during such reactions is most efficient when the neutron interacts with particles of similar mass (e.g. protons). Therefore, hydrogen-rich materials or light elements are typically used for neutron detection when elastic scattering reactions are implied.

Absorption reactions are also used for neutron detection because they induce nuclear reactions that produce charged particles, which are easier to detect, or radionuclides via activation processes. By measuring the induced radionuclides and knowing the cross sections of the reactions that produced them, information about the flux and energy of the interacting neutrons can be deduced. Hence, this chapter presents the main techniques used to detect neutrons produced by lasers with a focus on the optimization, for laser-driven neutron sources, of a neutron activation spectrometer: the SPAC (Spectromètre par Activation).

2.1 Neutron detectors

The most commonly used neutron detectors are gas proportional detectors. These are tubes filled with ^{3}He or BF$_3$ gas, where neutrons interact and are captured through the following reactions:

$$\begin{gathered} n + {}^{3}_{2}He \rightarrow p + {}^{3}_{1}H \\ n + {}^{10}_{5}B \rightarrow \alpha + {}^{7}_{3}Li \end{gathered} \tag{2.1}$$

Charged particles are released, which ionize the neighboring atoms. A high voltage is applied inside the tube to collect the charges, allowing to detect when a neutron interacts with the detector. This type of detector is well-known and highly efficient, especially for low-energy neutrons, which have favorable cross sections to induce such reactions [88].

However, their electronics, like those of most other types of neutron detectors (such as proton recoil telescopes, fission chambers, etc), are too slow to be used in laser facilities. Indeed, laser-driven neutron sources are mainly characterized by very short (< ns) and intense neutron bunches emitted in a noisy environment (with electromagnetic and X-ray emissions). Therefore, only passive detectors or detectors with ultra-fast electronics are suitable for characterizing neutron emissions produced by lasers. The most commonly used detectors are track-etch detectors, bubble detectors, scintillators used as nToF detectors and activation detectors, which will now be described.

2.1.1 Track-etch detectors

Track-etch detectors, such as CR-39, are solid-state plastic detector that can be used for neutron detection. They work by observing tracks made by charged particles in the detector. As explained earlier, the charged particles can be induced by neutrons via elastic scattering or absorption processes. The passage of the charged particles through the detector material ionizes the atoms, resulting in energy transfer to the electrons. Theses electrons break the chemical bonds of the polymer molecular chains and produce free radicals, creating tracks in the detector. A certain threshold of energy loss is required to induce such damages, making these detectors insensitive to electromagnetic, X-ray and gamma-ray emissions [88].

A neutron fluence can thus be measured by counting the tracks and applying an appropriate efficiency calibration factor. The tracks are revealed after etching the detector material in an acid or base solution, typically composed of sodium hydroxide [191]. The hydroxide ions attack the entire material surface and break the polymer structure. Since the tracks are already made of broken molecular chains, they are etched much faster than the intact parts. After the etching process, the tracks become pits on the surface which can be observed by a microscope [88].

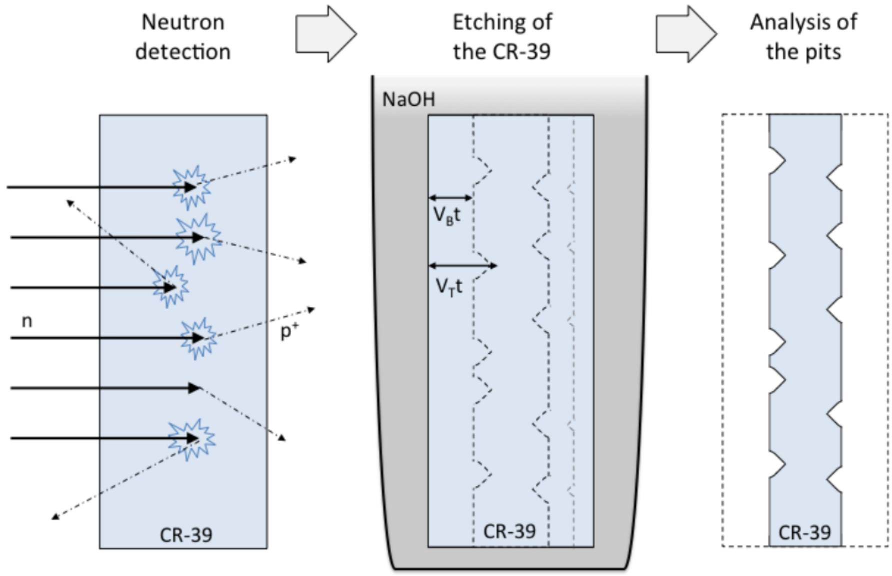

Figure 2.1 – Schematic drawing of the interaction of neutrons with a CR-39 detector, and etching and analysis processes [248].

Neutrons with energies of several tens of MeV can be measured by inducing recoil protons or other recoil ions (carbon or oxygen) in the detector [88, 192]. Thus, track-etch detectors are passive detectors particularly suitable for detecting fast neutrons and are compatible with a use at laser facilities because they are insensitive to the background radiation. However, they require a complex etching process and difficult analysis, as a microscope is needed to count the pits, which is time consuming. Furthermore, track-etch detectors have low efficiencies, typically lower than 10^{-4} etched tracks per incident neutrons. But, particular attention needs to be paid to avoid having a too high-density of neutrons on the detector, otherwise overlap of the tracks can take place, which leads to artifacts in the resulting patterns [193]. Finally, the efficiency calibration strongly depends on the etch time, the molarity of the acid or base and the side of the detector being observed, as neutron-scattered ions are generally forward-directed, which decreases the number of pits on the front side (facing the neutron source) [191].

2.1.2 Bubble detectors

Bubble detectors consist of transparent polycarbonate sealed tubes, a few cubic centimeters in volume, filled with an elastic polymer matrix containing 10^4 to 10^5 small droplets (< 100 µm) of a superheated halogen liquid (see Figure 2.2). In this state, the droplets remain in a liquid phase even though they are above their normal boiling point. This is achieved by the polymer matrix, which maintains the droplets under pressure and prevents boiling [88, 194].

When a neutron passes through the detector, it can interact with matter, typically through elastic scattering, which induces a recoil ion. This ion ionizes the molecules, which produces electrons that deposit their energy inside the droplets, inducing a sufficiently high energy density to overcome the pressure and cause boiling. This forms a visible bubble with a diameter of up to a millimeter. Each neutron interaction leads to the formation of a bubble and the total number of bubbles, which remain visible in the detector, is directly proportional to the neutron dose [88, 194]. The bubbles can be counted by eye or using a specially designed readout system with a camera and software that automatically count the bubbles.

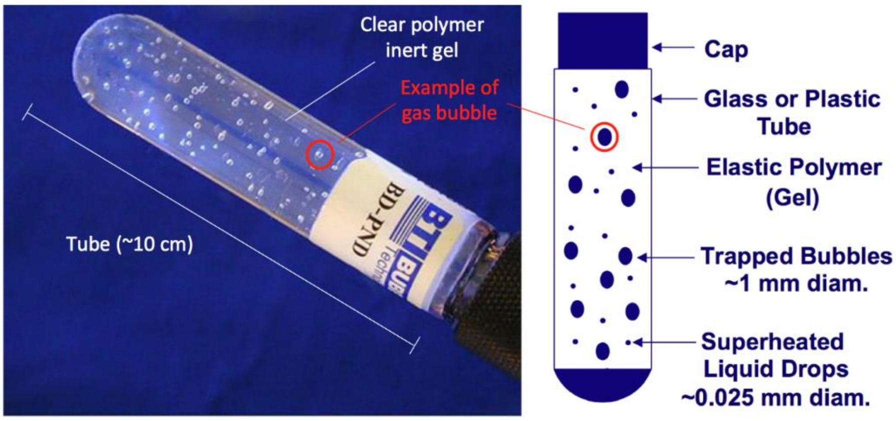

Figure 2.2 – A bubble detector (left) with a schematic view of its composition (right) [195].

Only heavy charged particles induce sufficient energy loss to produce the energy density needed to trigger the vaporization of the superheated liquid droplets. Bubble detectors are therefore insensitive to electrons, electromagnetic, X-ray and gamma-ray emissions, making them particularly suitable for use in noisy environments, such as those of laser-driven neutron sources. However, due to the minimum energy deposition required to turn droplets into visible bubbles, bubble detectors are initially not sensitive to thermal or epithermal neutrons, which induce recoil ions with too low energy. For example, the BD-PND model supplied by *Bubble Technology Industries* is sensitive to neutrons from 200 keV to around 15 MeV [194, 195]. But, chlorine-containing fluid can be incorporated in the superheated liquid to allow low energy neutron absorption through the ^{35}Cl(n,p)^{35}S reaction, producing recoil sulfur ions that induce sufficient energy deposition to form bubbles [88]. As a result, a bubble detector called BDT was designed by *Bubble Technology Industries* to be specifically sensitive to thermal neutrons [195].

Due to their relatively low energy-dependent response (shown in Figure 2.3), BD-PND detectors can be used to deduce neutron fluences, within the energy sensitivity range, from the measured doses. This requires an efficiency calibration using a reference neutron source, typically isotopic neutron sources such as AmBe or ^{252}Cf. Hence, the neutron fluence, expressed in n/cm², can be calculated from the following equation:

$$\Phi = \frac{N_B}{S \times h^*(10)} \tag{2.2}$$

Where N_B is the number of bubbles formed, S is the sensitivity factor of the bubble detector (typically a few bubbles/µSv) and $h^*(10)$ is the fluence-to-dose conversion factor associated to the calibration neutron source (3.91×10^{-4} µSv/n.cm^{-2} for an AmBe source and 3.85×10^{-4} µSv/n.cm^{-2} for a ^{252}Cf source) [196].

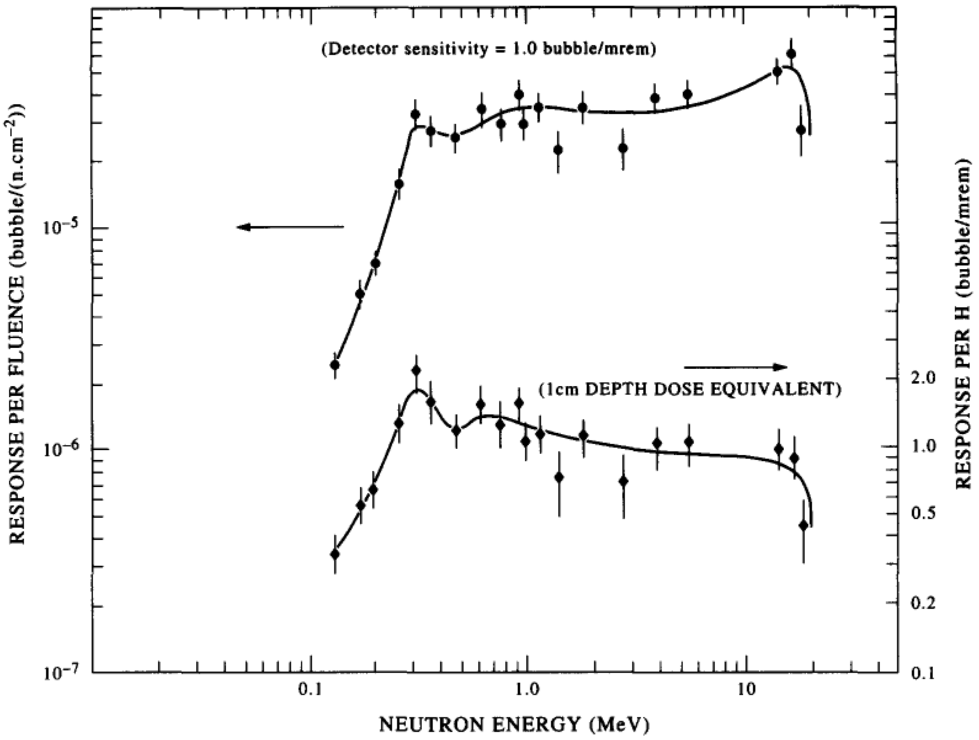

Figure 2.3 – BD-PND normalized response per unit fluence (circles) and per unit dose equivalent (diamonds). Extracted from [194].

As mentioned before, by varying the composition of the detector material, the energy required to form bubbles can be adjusted, thereby changing the neutron energy thresholds of the detectors [197]. This enables the simultaneous use of bubble detectors with different thresholds and response functions to perform neutron spectrometry. For this purpose, *Bubble Technology Industries* designed a bubble spectrometer called BDS, which consists of six types of bubble detectors with thresholds of 10, 100, 600, 1000, 2500 and 10000 MeV (see Figure 2.4). This setup allows for the reconstruction of neutron spectra with six energy bins via an unfolding technique [194].

The unfolding process involves first calculating, using the appropriate calibration factor, the neutron fluence in the 10 to 20 MeV range as measured by the detector with the highest threshold, i.e. BDS-10000 detector with a threshold at 10000 keV. Since the detector with the second highest threshold, i.e. BDS-2500 detector with a threshold at 2500 keV, is sensitive to neutrons from 2.5 to 20 MeV, the neutron fluence in the 2.5 to 10 MeV range can be calculated by subtracting the contribution of neutrons in the 10 to 20 MeV range, previously determined from the BDS-10000 detector. Then, the neutron fluence in the 1 to 2.5 MeV range can be calculated from the value measured by the BDS-1000, after subtracting the contributions from the 2.5 to 10 and 10 to 20 MeV ranges. Thus, by subtracting the contribution of the previous detectors, the neutron fluences in each energy bin can be determined.

An error estimate for the unfolded neutron fluence values can be calculated using the uncertainties in the counts from each type of detector. The uncertainties in each bin of the spectrum arise due to the statistical uncertainties in the measured counts from the detectors. The counts in the detectors are expected to follow a Poisson distribution, with an uncertainty equal to the square root of the number of counts observed in the detector. Each bin in the unfolded spectrum may have contributions to its uncertainty that originate from the uncertainties in all of the individual bubble counts. So, after the neutron spectrum was unfolded, the counts for a single detector are artificially incremented by one standard deviation and the unfolding is repeated to generate an artificial spectrum. Thus, the neutron fluence values in each bin of the artificial spectrum will differ from those of to the initial spectrum, so the difference in each bin can be calculated, leading to the uncertainty in the spectrum due to the count from one bubble detector. This process is then repeated independently for all detector types, allowing for the determination of each detector's contribution to the uncertainty of each bin. Since the counts are statistically independent, the uncertainty of each bin is therefore a sum-in-quadrature of the contributions of each detector.

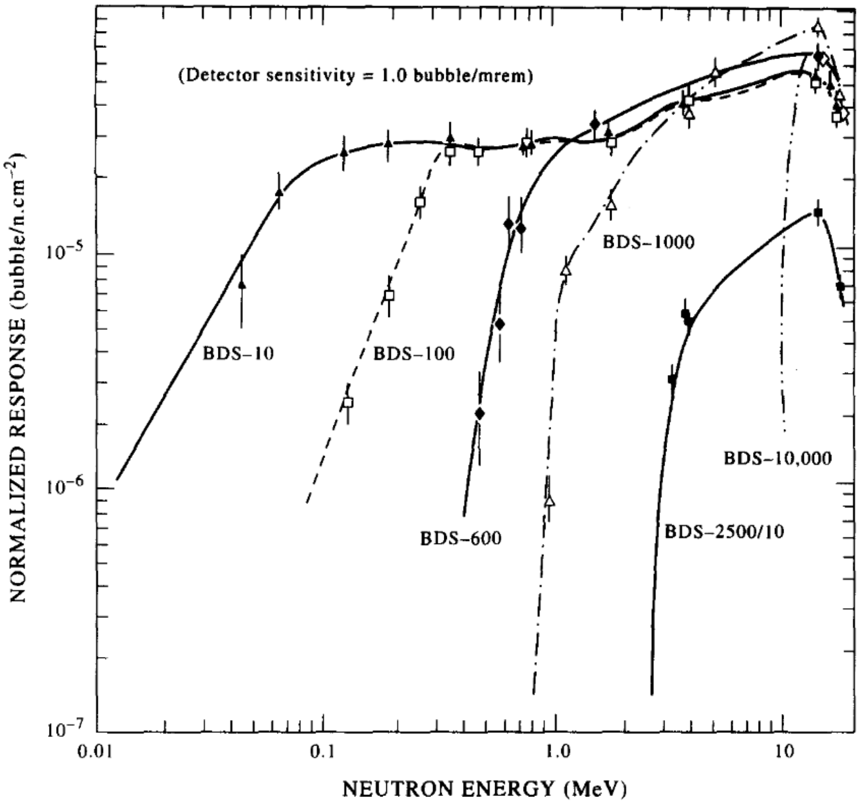

Figure 2.4 – Normalized response per unit fluence of the Bubble Detector Spectrometer (BDS), extracted from [194]. BDS-10 has the threshold at 10 keV, BDS-100 at 100 keV and so on.

Unlike track-etch detectors, neutron fluences can be easily determined by bubble detectors without the need for complex and time-consuming analysis processes. They can also be reused after being recompressed using the piston provided with the BDT and BD-PND detectors or with an appropriate recompression chamber for the BDS detectors. Repressurizing the detectors causes the bubbles to disappear by returning the droplets to a superheated liquid state, this makes the detectors ready for a new measurement.

However, when the number of bubbles exceeds 100, they become difficult to distinguish. Since the uncertainty associated with the measured neutron fluences is defined by the square root of the count, it is challenging to achieve an uncertainty lower than 10%. Nevertheless, it is important to have as many bubbles as possible to improve statistical accuracy. Therefore, due to their low dynamic range, bubble detectors must be placed at a specific distance from the source to maximize the number of bubbles while avoiding saturation. Finally, bubble detectors enable the possibility of performing neutron spectrometry using detectors with different thresholds. But, the neutron spectra obtained are generally not very precise, as they only contain six energy bins.

2.1.3 Scintillators

Scintillators are another type of detectors in which neutrons interact and transfer their energy to recoil ions, generally via elastic scattering. These ions interact with the electrons of surrounding molecules, bringing them to excited states. When the electrons return to their ground state, they emit photons, which are then converted in an amplified electrical signal using a photomultiplier tube (PMT) or microchannel plates (MCP) (see Figure 2.5). There are two types of scintillators: inorganic and organic. Inorganic scintillators are usually dense crystals composed of high-Z elements, such as sodium iodide (NaI) or bismuth germanate (BGO), making them more adapted for gamma detection. Organic scintillators, on the other hand, are liquid or solid materials made of aromatic compounds (carbon rings with hydrogen), such as xylene or polyvinyl toluene (PVT), which are particularly suitable for neutron detection due their high proportion of hydrogen atoms [88].

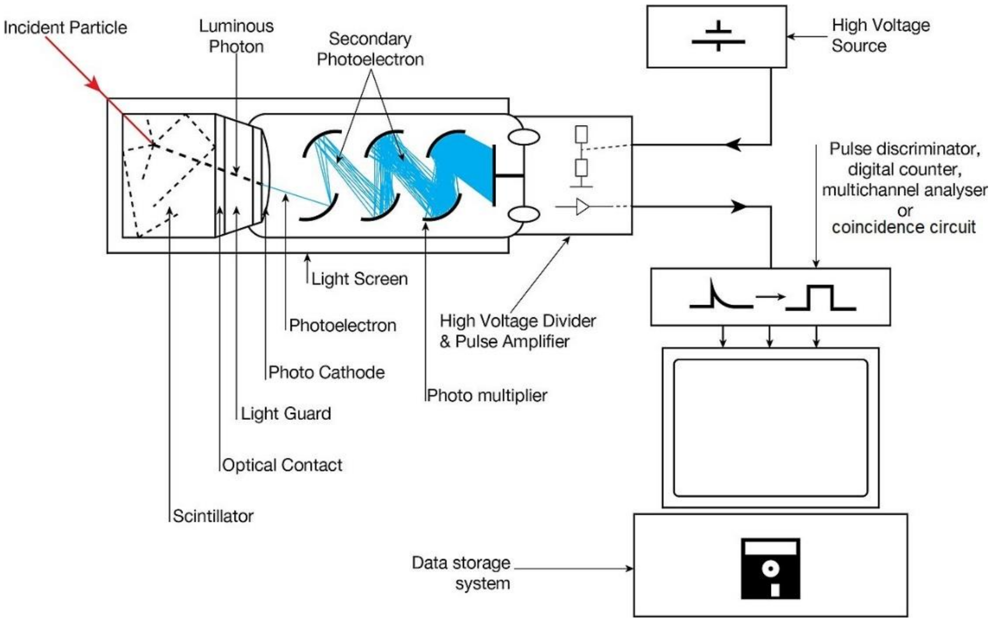

Figure 2.5 – Scheme of a typical detection system using a scintillator.

In organic scintillators, neutrons induce recoil ions that excite the electrons of the molecules in the scintillating medium. These molecules, in an excited electronic state, can reach discrete energy levels that differ depending on the spin of the excited electrons. These energy levels are referred to as singlet states (S_0, S_1, S_2, etc.) and triplet states (T_1, T_2, etc.). Subsequently, these molecules de-excite by emitting optical photons according to three de-excitation modes (see Figure 2.6) [88, 198]:

- De-excitation from a singlet state: prompt fluorescence.
- De-excitation from a triplet state: phosphorescence.
- Transformation of a triplet into a singlet state and de-excitation: delayed fluorescence.

Prompt fluorescence from the first singlet state is the principal scintillation process in organic scintillators, providing them with a very fast response time (usually on the nanosecond scale). Since the stopping power of protons is greater than that of electrons, the same amount of energy is deposited in a smaller volume by the protons. The probability of exciting molecules into either a singlet or triplet state is the same for both protons and electrons. However, the high concentration of triplet states resulting from ionization by protons increases the likelihood of the triplet-triplet annihilation phenomenon. This annihilation produces a ground energy state (S_0) as well as an excited singlet state (S_1) as follows: $T_1 + T_1 \rightarrow S_0 + S_1$. The de-excitation of this excited singlet state then leads to the emission of delayed fluorescence [88, 199].

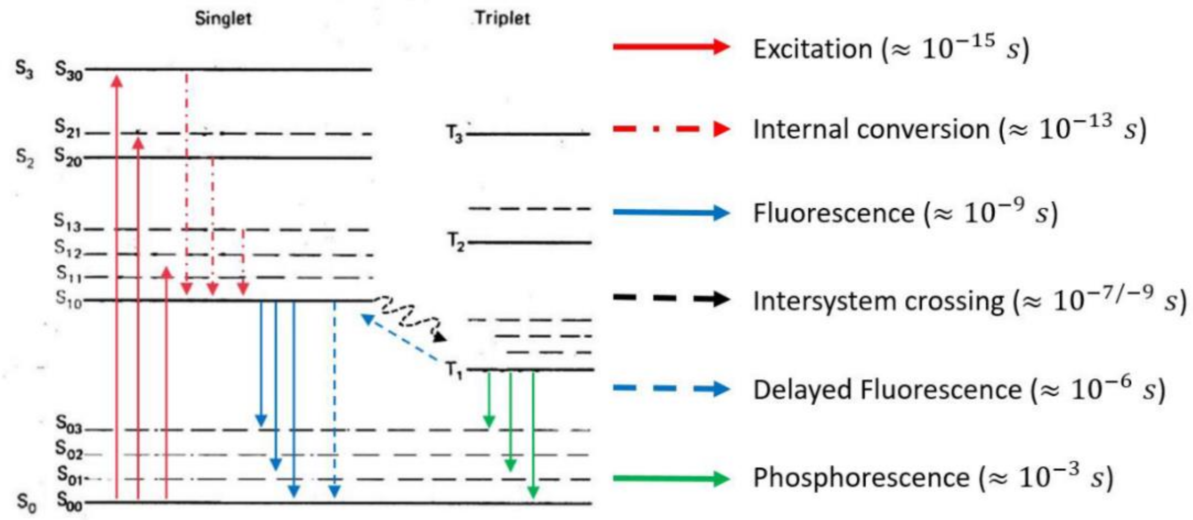

Figure 2.6 – Jablonski diagram with the different mechanisms involved in the scintillation processes [198].

The total de-excitation (decay) time results from the three de-excitation modes described earlier. However, the decay time for recoil protons is slightly longer than that for electrons due to the triplet-triplet annihilation phenomenon and the resulting delayed fluorescence. This difference forms the basis of a neutron/gamma-ray discrimination technique called Pulse Shape Discrimination (PSD), which is achieved by comparing the different decay times of the detected pulses [199]. This technique is effective when the device detects individual events, but it is not applicable to laser-driven neutron sources, where multiple neutrons can be detected simultaneously due to the very short bunch durations and the intense fluxes.

To describe the light produced, several formulas have been defined based on different observations. First, since organic scintillators have a linear response to electrons, the light produced per path length unit, denoted as $\frac{dL}{dx}$, from the excitation induced by electrons can be described as being proportional to the energy loss $\frac{dE}{dx}$ [88]:

$$\frac{dL}{dx} = S\frac{dE}{dx} \tag{2.3}$$

Where S is the scintillation efficiency (usually expressed in photons/MeV).

Birks [200] demonstrated that the high ionization density induced by heavy charged particles, such as protons, results in quenching effects due to damaged molecules, which lower the scintillation efficiency. Initially, the density of damaged molecules was considered proportional to the energy loss, leading to the Birks' formula:

$$\frac{dL}{dx} = \frac{S\frac{dE}{dx}}{1 + kB\frac{dE}{dx}} \tag{2.4}$$

Where kB represents a proportionality constant which describes the fraction of damaged molecules leading to quenching effects.

Finally, semi-empirical formulas, such as Chou's formula [201], were defined to better match experimental data:

$$\frac{dL}{dx} = \frac{S\frac{dE}{dx}}{1 + kB\frac{dE}{dx} + C\left(\frac{dE}{dx}\right)^2} \tag{2.5}$$

Where C is a correction factor adjusted to fit more closely with the experiment data.

The light indirectly produced by the interaction of neutrons with the scintillating medium must then be converted into a measurable electric signal. To achieve this, PMTs optically coupled to the scintillator are used. A PMT consists of a photocathode, a light-sensitive surface that emits electrons via the photoelectric effect when struck by photons. The emitted electrons from the photocathode are directed towards a series of electrodes called dynodes, which are secondary electron emitters (see Figure 2.5). An electrical potential is applied between each dynode, causing the incoming electrons to accelerate towards them. When an electron strikes a dynode, typically made of BeO, MgO or SbCs, it releases multiple secondary electrons. This process is repeated across a chain of dynodes, leading to an exponential multiplication of the initial number of electrons by up to a factor of 10^7 [88]. Finally, an anode collects the electrons and converts them into an electrical signal, which can then be measured.

MCPs can also be used instead of PMTs. These devices consist of a thin plate, typically made of glass, with a large number of tiny, closely packed channels, usually of a few tens of micrometers in diameter. The inside of these channels is coated with a material that exhibits secondary electron emission properties. When a photon strikes the input side of the MCP, it enters one of the microchannels. The impact causes the emission of secondary electrons from the channel wall. These secondary electrons are then accelerated down the length of the channel by a strong electric field applied across the plate. As they move, they strike the walls of the channel, causing further emission of secondary electrons. This cascade effect results in the amplification of the original signal by a factor between 10^3 and 10^4. Although the amplification is lower than that of PMTs, MCPs are often used in a system of two or three MCPs to compensate for their reduced efficiency. Hence, they are generally more expensive than PMTs but offer very advantageous timing properties, such as a much lower electron transit time compared to PMTs and the ability to be switched on and off on the nanosecond scale. This allows MCPs to avoid saturation of the detection system when the scintillator receives a too high particle flux [88].

As mentioned earlier, when scintillators are used to characterize neutron emissions from laser-driven neutron sources, the electrical signals obtained are not individual, discrete events. Due to the intense neutron bunches with very short durations, multiple neutrons can be detected simultaneously, leading to pile-up signals. Thus, the nToF technique is employed to characterize the neutron emissions. A typical nToF signal from a laser-driven neutron source is composed of two parts (see Figure 2.7):

- A gamma-ray flash produced by the hot electrons accelerated during the laser-target interaction, which generate Bremsstrahlung emissions within the target. Since the gamma-rays travel at the speed of light, they are detected first.
- A broader neutron signal that reflects the energy distribution of the neutrons. The higher a neutron's energy, the greater its speed and the shorter its time of flight towards the detector.

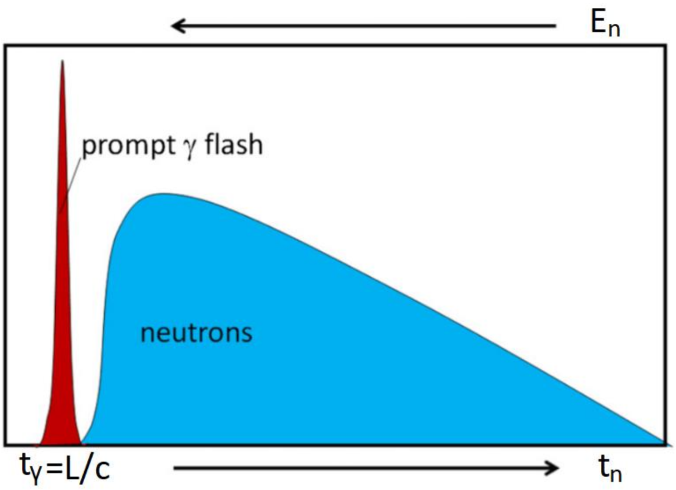

Figure 2.7 – Typical neutron signal obtained with laser-driven neutron sources [248].

The nToF technique relies on the different velocities of the neutrons, depending on their energy, which produces a signal spread over time where a ToF corresponds to a specific kinetic energy E_n following this equation:

$$E_n = (\gamma - 1)m_n c^2 = \left(\frac{1}{\sqrt{1 - \left(\frac{L}{c \times t_n}\right)^2}} - 1 \right) m_n c^2 \tag{2.6}$$

Where L is the source-detector distance, c the speed of light, m_n the mass of the neutron and t_n its Time-of-Flight.

Since gamma-rays propagate at the speed of light and knowing the distance from the source to the detector, the gamma-ray flash serves as time reference to define the instant at which the neutrons are emitted. Information such that the minimum or maximum neutron energy can therefore be calculated using equation (2.6).

To perform quantitative analysis and reconstruct a neutron spectrum, the gamma-ray flash must be removed by subtracting exponential fit functions that accurately describe the shape of the gamma-ray flashes. This isolates the neutron signal, where the integral of each bin must then be converted into a corresponding number of neutrons. Since the signal induced by a neutron depends on the energy deposition, which in turn depends on its kinetic energy, an efficiency calibration is required to establish the relationship between the integral value and the number of neutrons for each neutron energy. Given that these efficiency calibrations depend on the entire detection configuration (source-detector distance, shielding, surrounding materials, etc.), they are typically carried out using Monte Carlo simulations that account for the scintillation processes. Thus, the number of neutrons, N, detected for each ToF, t_n, can be calculated using the following equation:

$$N(t_n) = \frac{I(t_n)}{C(t_n)} \tag{2.7}$$

Where $I(t_n)$ is the integral of the bin at time t_n, usually expressed in pC, and $C(t_n)$ is the corresponding efficiency calibration factor computed through simulations and expressed in pC/neutron.

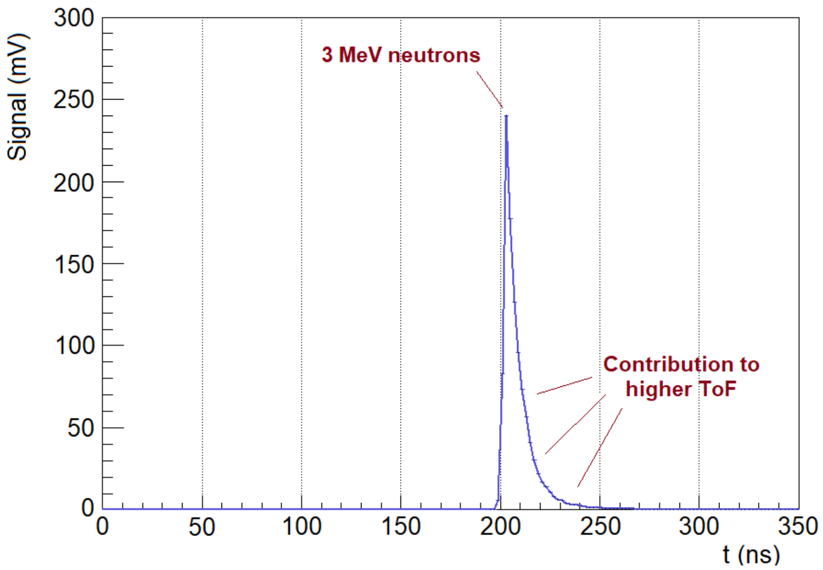

Figure 2.8 – Simulated nToF signal induced by 3 MeV monoenergetic neutrons in a scintillator placed at 5 m from the source.

However, as shown in Figure 2.8, neutrons of a given energy also contribute to the signal at higher ToF (i.e. at lower energies) due to the temporal characteristics of the detector system. Therefore, the number of neutrons $N(t_n)$ previously obtained must be adjusted by subtracting the contribution of higher energy neutrons (with lower ToF) to the signal. These contributions can be approximated as decreasing exponential functions, with the slope depending on the neutron energy and, consequently, on the ToF. The final number of neutrons at a given ToF t_n can therefore be defined as:

$$N(t_n) = N(t_n) - \left(\sum_{i}^{n} N(t_n - i) \times e^{-A(t_n - i) \times i} \right) \tag{2.8}$$

Where $A(t_n - i)$ is the slope of the exponential function describing the contribution to the signal of neutrons that interacted at $(t_n - i)$, and i the bin width.

Finally, after replacing the ToF of each bin by the corresponding neutron energy using equation (2.6), a neutron spectrum can be obtained using equation (2.8). The energy resolution depends on the distance between the source and the detector, as well as the bin width, which can be tuned by the sampling frequency of the electrical signal digitizer. Modern digitizers typically operate in the GHz range, resulting in a bin width of one nanosecond. With such digitizers and a detector placed at 5 m from the source, energy resolutions of about 5 keV can be achieved for neutron energy of 1 MeV and around 200 keV at 10 MeV. These energy resolution performances are much better than for bubble detectors.

However, because these detectors are sensitive to gamma rays, which are emitted intensively at laser facilities, appropriate lead shielding must be installed around the scintillators to prevent saturation of the photomultiplier tubes. Limiting the gamma-ray-induced signal is also crucial for improving the detection of high-energy neutrons. Without this shielding, the nToF signal from high-energy neutrons could overlap with the gamma-ray flash, resulting in a low signal-to-noise ratio for the shortest ToF (i.e., the highest energy neutrons). Typically, the front face of the scintillators is shielded with lead bricks several tens of centimeters thick, while a few centimeters of lead bricks are used on the top, bottom, and rear faces to shield scattered neutrons. Despite this shielding, achieving a good signal-to-noise ratio beyond about 20 MeV remains challenging (see Section 3).

2.1.4 Activation

The characterization of neutron emissions can also be achieved by measuring the radioactivity generated through the interaction of neutrons with specific samples. In these samples, neutrons may induce nuclear reactions, such as (n,n'), (n,p) or (n,2n) reactions, depending on their energy. These reactions produce radionuclides that emit characteristic radiation, typically gamma-rays, which are then measured using gamma spectrometry. By knowing the quantity of radionuclides produced and the cross sections of the involved nuclear reactions, neutron fluxes can be determined using equation 2.10.

The activity A_0, in Bq, of a radionuclide produced in a sample irradiated by neutrons for an irradiation time t_{irr} can be expressed by the following equation:

$$A_0(t_{irr}) = N_i \sigma \varphi \left(1 - e^{-\lambda t_{irr}}\right) = A_\infty \left(1 - e^{-\lambda t_{irr}}\right) \tag{2.9}$$

Thus, a neutron flux φ, in n/cm²/s, can be deduced:

$$\varphi = \frac{A_0}{N_i \sigma (1 - e^{-\lambda t_{irr}})} \tag{2.10}$$

Where N_i is the number of irradiated nuclei, σ is the cross section of the reaction (in cm²) and λ the decay constant of the radionuclide (in s^{-1}). The decay constant is defined as $\lambda = \frac{\ln(2)}{T_{1/2}}$, where $T_{1/2}$ is the half-life of the radionuclide, which is the time after which its activity is reduced by a factor 2.

Once irradiation ceases, the decay process of the radionuclides begins, causing a reduction in activity (see Figure 2.9). To determine the activity A_0 and calculate the associated neutron flux, the measured activity A_{meas} must be corrected, accounting for the decay time t_d between the end of irradiation and the start of measurement, as well as the decay time t_{meas} during the measurement. The activity A_0 is therefore defined as:

$$A_0 = A_{meas} \times e^{\lambda t_d} \times \frac{\lambda t_{meas}}{(1 - e^{-\lambda t_{meas}})} \tag{2.11}$$

With the measured activity A_{meas} following this equation:

$$A_{meas} = \frac{S_{net}}{I_\gamma \times \varepsilon_{abs} \times t_{meas}} \tag{2.12}$$

And the associated statistical uncertainty σ_{meas} is defined as:

$$\sigma_{meas} = \frac{2 \times \sqrt{S_{gross} + (S_{gross} - S_{net})}}{S_{net}} + \sigma_{cal} \tag{2.13}$$

Where S_{gross} and S_{net} are, respectively, the total integral and the net integral (subtracted from the background noise) of the gamma-ray peak of interest, I_γ is the probability of gamma-ray emission per disintegration (also known as branching ratio or intensity), ε_{abs} is the absolute efficiency of the spectrometer, t_{meas} the measurement time and σ_{cal} is the uncertainty associated to the activity of the calibration source.

Since the produced radionuclides decay according to their own half-life, the activity generated during neutron irradiation competes with the decay of the radionuclides. For a given neutron flux, there is a maximum achievable activity, called saturated activity and noted A_∞. As a result, the activity produced follows an asymptotic trend as the irradiation time increases (see Figure 2.9). To maximize the activity, it is therefore preferable to optimize sample dimensions or select reactions with the largest possible cross sections.

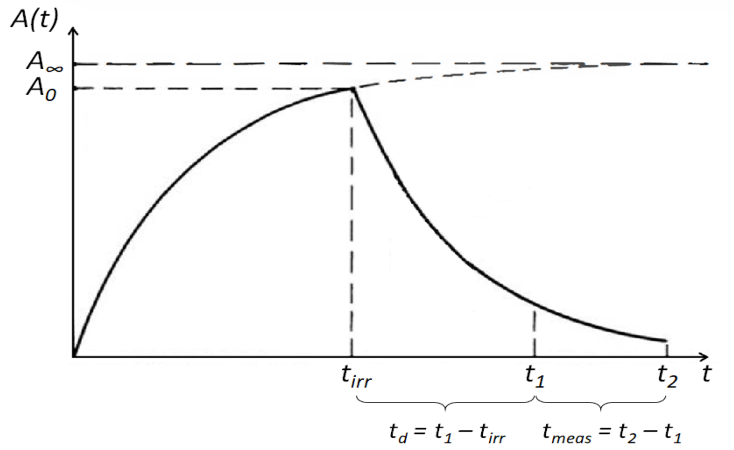

Figure 2.9 – Evolution of the activity produced and decay curve after the end of irradiation at t_{irr}.

For example, the ^{115}In(n,n’)^{115m}In reaction is widely used at laser facilities to characterize neutron emissions [156, 174, 202, 203], as it has an almost flat cross section profile between 2 and 10 MeV (see Figure 2.11) with an average cross section of 314 mb, which induces significant activation and allows for easy calculation of neutron fluences within this energy range using the following equation:

$$\Phi = \frac{A_0}{\lambda} \times \frac{M}{\bar{\sigma} \times t \times \rho \times \chi \times N_A} \times \frac{1}{\Omega} \tag{2.14}$$

With:

Φ, the neutron fluence (n/sr)
A_0, the activity (Bq) at the end of the irradiation
λ, the decay constant (s^{-1})
$\bar{\sigma}$, the average cross section (cm^2)
M, the molar mass (g/mol)
t, the sample thickness (cm)
ρ, the density (g/cm^3)
χ, the isotope abundance
N_A, the Avogadro constant (mol^{-1})
Ω, the solid angle covered by the sample (sr)

Activation samples are a valuable diagnostic tool for characterizing laser-driven neutron sources because, depending on the nuclear reactions of interest, they are insensitive to the background radiations. However, they must be measured using gamma spectrometry to determine the induced activity, which can be time-consuming depending on the activation level. Despite this drawback, activation samples can be reused indefinitely and the measurable neutron fluence is not limited, as very high fluence will simply induce significant activation without the risk of detector saturation. A decay time will be just necessary before measurement to prevent excessive radiation exposure to personnel while handling the irradiated sample, and to avoid saturation of the gamma spectrometer. Finally, several activation samples, sensitive to different neutron energies, can be used simultaneously to perform neutron activation spectrometry, which is the focus of the next section.

2.2 Development of a neutron activation spectrometer

Neutron activation spectrometry involves using several activation samples in which neutrons induce radionuclide production through various nuclear reactions with specific threshold energies and cross section profiles. By combining different samples with known activation cross sections across various energy ranges, information about neutron energy distribution can be derived. Since neutron activation spectrometers are passive detectors, insensitive to gamma-rays, requiring no power supply or specific maintenance, they were initially designed to measure neutron energy distributions for dosimetry analysis after criticality accidents in nuclear reactors [204]. These characteristics, along with the ability to detect neutrons with energies up to several tens of MeV – depending on the materials and nuclear reactions chosen – make neutron activation spectrometers particularly suitable for characterizing laser-driven neutron sources, in addition to other diagnostics described in Section 2.1. A neutron activation spectrometer, called SNAC2 [205], was already designed by the Institute for Radiological protection and Nuclear Safety (IRSN) for dosimetry purposes in nuclear reactors. It consists of a set of metal foils of different thicknesses, including bare and cadmium shielded copper, gold, indium, nickel, magnesium and ebonite. These materials cover a typical reactor energy range from 10^{-10} MeV to 20 MeV. Since laser-driven neutron sources can emit more energetic neutrons, a neutron activation spectrometer with an extended energy range must be specifically designed. The development process of this activation spectrometer, called SPAC (SPectrometer of ACtivation), will now be described.

2.2.1 Selection of materials and geometry definition

In order to perform spectrometry, the SPAC must be composed of materials that allow neutrons across different energy ranges to induce nuclear reactions and radionuclide production. To complement bubble spectrometers, nToF detectors and the neutron activation spectrometer SNAC2, it must be sensitive to neutrons in the high-energy range, i.e. to neutron energies exceeding 20 MeV. Several other criteria must be considered to select the more suitable materials:

- The materials must be chemically stable, have low toxicity, and pose no risk of explosion; therefore, pure alkali metals are excluded. Solid materials are preferred over gases and liquids, as they do not require specific encapsulation.

- Pure materials are preferred over alloys and the isotope of interest should have the highest possible relative abundance to avoid confusion between neutron-induced reactions on different isotopes of the same element. Thus, monoisotopic elements with high purity are preferred.

- Fissile and other radioactive elements are excluded due to the many challenges in handling them. Furthermore, the requirement for special authorization to handle fissile materials makes them unsuitable for use in many facilities.

- The neutron-induced reactions must have significant cross sections in their energy range of interest, typically above 100 mb, to maximize the produced activities, which reduces the counting time during the gamma spectrometry measurements.

- The radionuclides produced must be gamma-ray emitters with favorable branching ratios, typically greater than 10%, to ensure efficient detection with gamma spectrometers. Additionally, radionuclides emitting gamma-rays in the range of a few hundred keV are preferred over those emitting gamma-rays beyond 1 MeV, facilitating their detection by conventional gamma spectrometers.

- These radionuclides should also have suitable half-lives, typically ranging from several hours to days. This ensures that they do not decay completely before measurement, while also minimizing the measurement time during gamma spectrometry. Furthermore, it allows the possibility of reusing the samples without requiring excessively long decay periods.

An examination of sensitivity of each material meeting these criteria was conducted to select the most appropriate materials. The cross sections were compared using the JANIS 4 database [206], which compiles data from evaluated libraries and experimental cross sections from the EXFOR database [207]. The half-lives and gamma emission lines of radionuclides were examined using the NuDat 3.0 database [208]. After a thorough analysis of the materials' characteristics, neutron-induced reactions and the produced radionuclides, five elements were selected: manganese, indium, iron, zirconium and bismuth. We will now describe their advantages and associated constraints.

Manganese:

Manganese is a monoisotopic element that exists as a silvery-gray hard metal. Although it is relatively chemically stable, it can slowly oxidize in air at room temperature, forming a layer of manganese oxide on its surface. It is therefore necessary to store it away from air between uses, such as in plastic bags, to prevent significant oxidation. While excessive exposure to manganese can lead to health issues, its toxicity remains low and wearing gloves is sufficient for safe handling. The ^{55}Mn(n,γ)^{56}Mn reaction can be induced in this sample, which is particularly useful for characterizing thermal neutrons, as this radiative capture has no threshold energy (see Figure 2.10). The resulting radionuclide, ^{56}Mn, has a half-life of 2.58 hours and emits a gamma-ray of 847 keV with an intensity of 98.9%, making it easy to detect using gamma spectrometry.

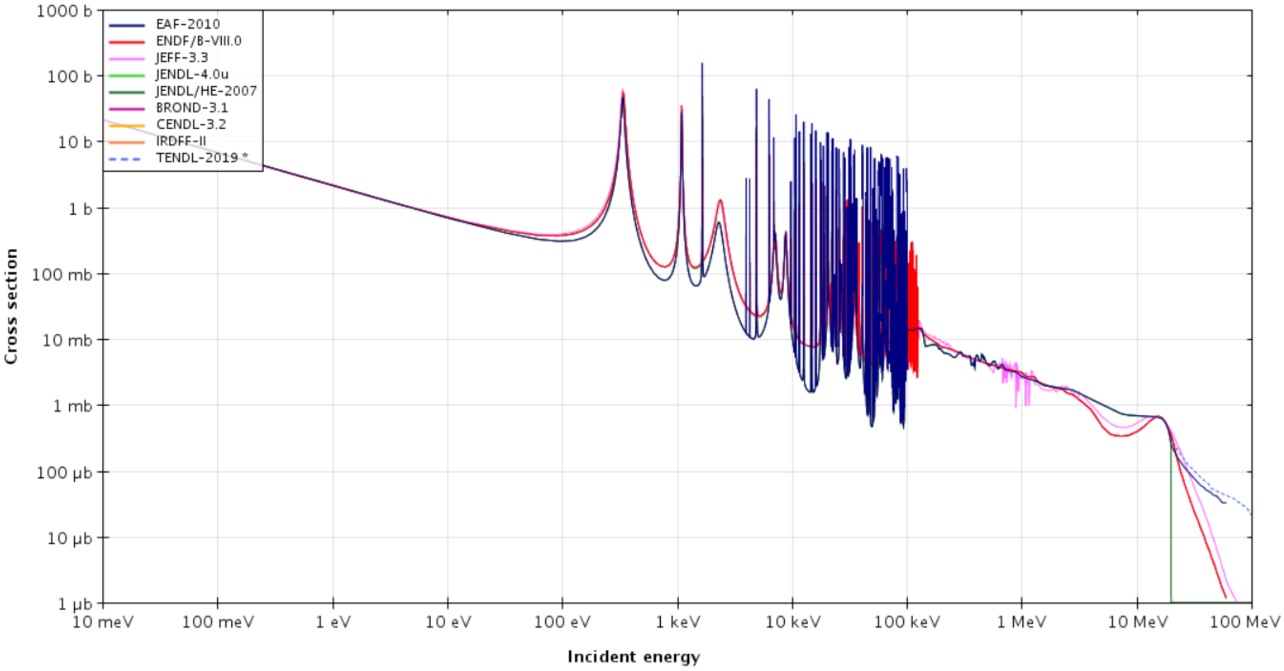

Figure 2.10 – Cross sections of the ^{55}Mn(n,γ)^{56}Mn reaction according to different libraries.

Gold is often chosen for characterizing thermal neutrons through radiative capture. Although the cross sections of the ^{197}Au(n,γ)^{198}Au reaction is about 10 times higher than those of the ^{55}Mn(n,γ)^{56}Mn reaction, the radionuclide produced, ^{198}Au, has a half-life 25 times longer (2.70 d), resulting in much lower counting rates in gamma spectrometry. Additionally, the neutron fluences available at laser facilities would require samples with volumes of several cubic centimeters, making gold samples prohibitively expensive.

Other elements, such as copper, were excluded due to the presence of multiple isotopes, which could lead to confusion between reactions. Copper was initially considered for characterizing thermal neutrons, as the ^{63}Cu(n,γ)^{64}Cu reaction offers good cross sections, similar to those of manganese. However, the ^{65}Cu(n,2n)^{64}Cu reaction can also produce the same radionuclide with neutrons above 10 MeV. Since neutrons exceeding 10 MeV were measured at laser facilities (see Section 3.2.3), copper was ultimately not selected.

Indium:

Indium is a soft, malleable and ductile metal that is unaffected by air or water and poses no particular toxicity. The reaction of interest is the inelastic scattering, ^{115}In(n,n')^{115m}In, occurring in one of these two stable isotopes, ^{115}In, which has a relative abundance of 95.7%. This reaction has a threshold energy of around 340 keV and produces an isomeric state of the initial nuclei with a half-life of 4.49 hours. Its cross-section profile makes it particularly suitable for detecting neutrons with energies of a few MeV (see Figure 2.11). The ^{115m}In radionuclides can be easily detected, as they emit gamma-rays of 336 keV with an intensity of 45.9%.

The other stable isotope composing indium, ^{113}In, has a low relative abundance (4.3%) and a lower atomic mass, thus eliminating the risk of confusion between reactions. However, another reaction of interest can occur with ^{115m}In nuclei. The radiative capture ^{115}In(n,γ)^{116m}In produces an isomeric state of ^{116}In nuclei with a half-life of 54 minutes. It emits several gamma-rays, such as one at 417 keV with an intensity of 27.2%. The results obtained with this reaction can be compared to those obtained with the reaction in the manganese sample, since they are both sensitive to thermal neutrons.

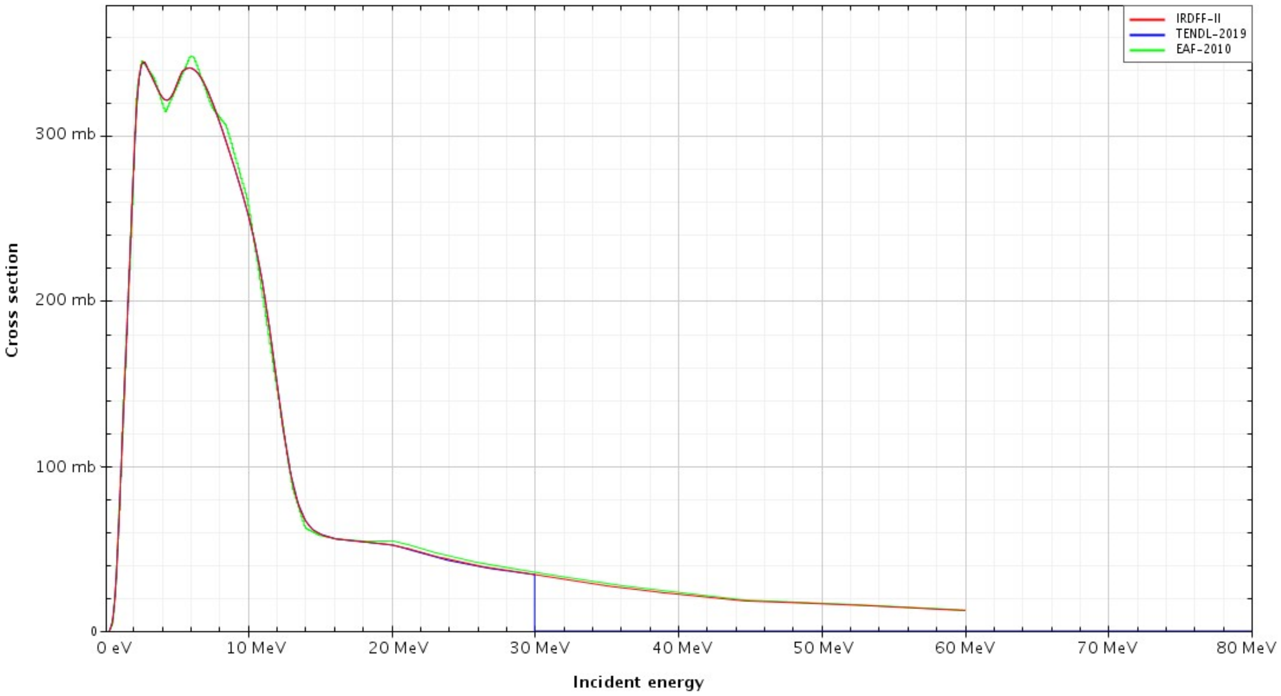

Figure 2.11 – Cross sections of the ^{115}In(n,n')^{115m}In reaction according to different libraries.

Reactions involving other elements with similar cross-section profiles were excluded. For example, the ^{32}S(n,p)^{32}P reaction was not considered because it produces a radionuclide that does not emit gamma-rays. Besides, although the ^{103}Rh(n,n')^{103m}Rh reaction has a maximum cross section around 4 times higher than that of the ^{115}In(n,n')^{115m}In reaction, the ^{103m}Rh radionuclide only emits X-rays of a few tens of keV with low intensities, making it difficult to detect.

Iron:

Iron is one the most abundant elements on Earth, making it very inexpensive. It reacts slowly with oxygen, forming iron oxide (rust), so it is recommended to store it away from air. Like indium, iron has no particular toxicity and can be handled easily. As shown in Figure 2.12, the ^{56}Fe(n,p)^{56}Mn reaction is sensitive to neutrons from 3 MeV, with a maximum cross section around 13 MeV. Thus, the iron sample allows for the characterization of neutrons with higher energy compared to the indium sample. This reaction produces the same radionuclide as in the manganese sample, ^{56}Mn, but there is no possibility of confusion regarding its origin since the samples are measured separately.

However, iron has four different isotopes, two of which could cause confusion between reactions producing the ^{56}Mn radionuclide, specifically the ^{57}Fe(n,d)^{56}Mn and ^{58}Fe(n,t)^{56}Mn reactions. Nevertheless, these reactions have much higher threshold energies and lower cross sections. Additionally, the relative abundances of the ^{57}Fe and ^{58}Fe isotopes – 2.1% and 0.3%, respectively – are much lower compared to the ^{56}Fe isotope, which accounts for 91.7% of iron nuclei.

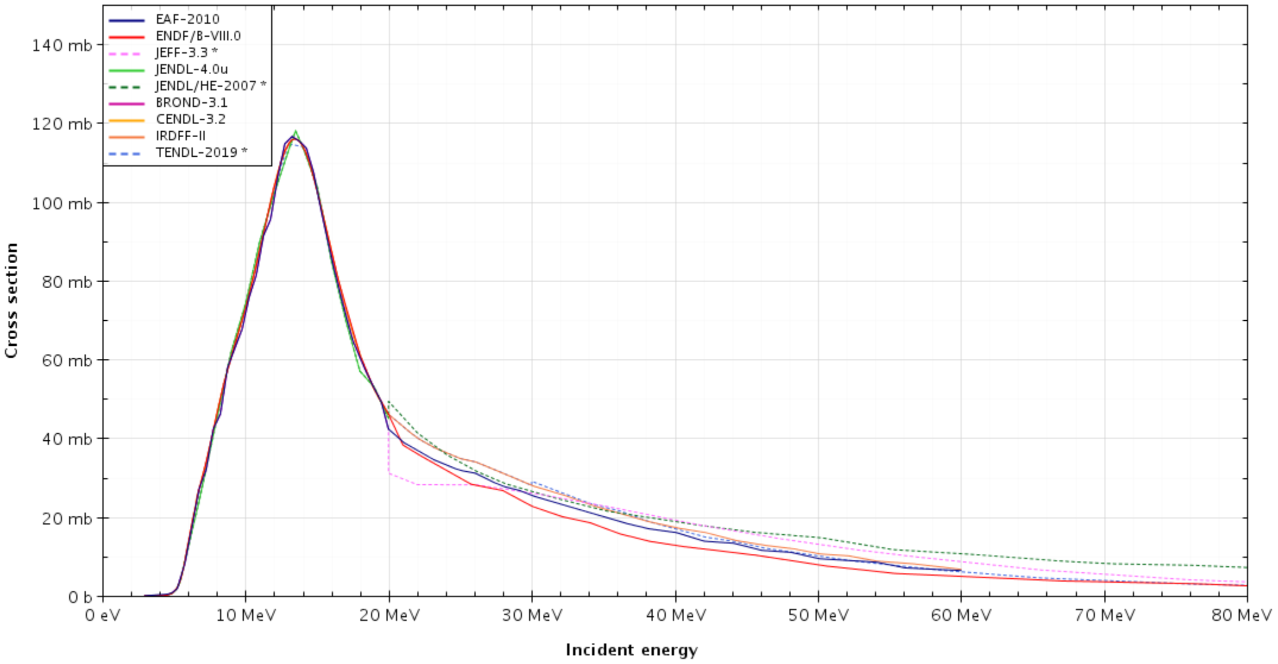

Figure 2.12 – Cross sections of the ^{56}Fe(n,p)^{56}Mn reaction according to different libraries.

The induced activity depends on the number of irradiated nuclei (see equation 2.9) and, therefore, on the target material's density. The ^{27}Al(n,α)^{24}Na reaction, which has cross sections very similar to the ^{56}Fe(n,p)^{56}Mn reaction, was excluded because aluminum has a density approximately three times lower than that of iron, leading to significantly fewer produced radionuclides. Furthermore, the ^{24}Na radionuclide has a longer half-life (14.96 h) compared to ^{56}Mn and emits more energetic gamma-rays (1369 keV), resulting in a lower counting rate during gamma spectrometry measurement.

For the same reasons, the ^{24}Mg(n,p)^{24}Na reaction, used in the SNAC2, was also excluded, although its cross sections are slightly higher, with a maximum of 220 mb at 13 MeV. Furthermore, magnesium contains two other isotopes, ^{25}Mg and ^{26}Mg, each with a relative abundance of around 10%. This increases the likelihood of confusion between reactions producing ^{24}Na radionuclides, especially for the ^{25}Mg(n,d)^{24}Na reaction, which has non-negligible cross sections in the same energy range as the ^{24}Mg(n,p)^{24}Na reaction.

Zirconium:

The fourth layer of the SPAC will be composed of zirconium, a silvery-gray metal. It poses no specific toxic risk and is relatively unreactive in many environments due to its ability to form a thin stable oxide layer that prevents further corrosion. The reaction of interest, ^{90}Zr(n,2n)^{89}Zr, occurs with neutrons ranging from 12 MeV to more than 30 MeV, with significant cross sections particularly around 20 MeV (see Figure 2.13). The produced radionuclide, ^{89}Zr, has a half-life of 78.4 hours and emits gamma-rays of 909 keV with an intensity of 99%.

Other reactions that produce the ^{89}Zr radionuclide can occur with different zirconium isotopes, particularly through (n,3n) and (n,4n) reactions with ^{91}Zr and ^{92}Zr, respectively. However, their lower relative abundances compared to ^{90}Zr, along with the cross sections and neutron energy required to trigger such reactions limit their contribution to the production of ^{89}Zr. Additionally, the neutron energy spectra from laser-driven neutron sources typically exhibit an exponentially decaying shape (see Section 3.2.3), further reducing the impact of these parasitic reactions.

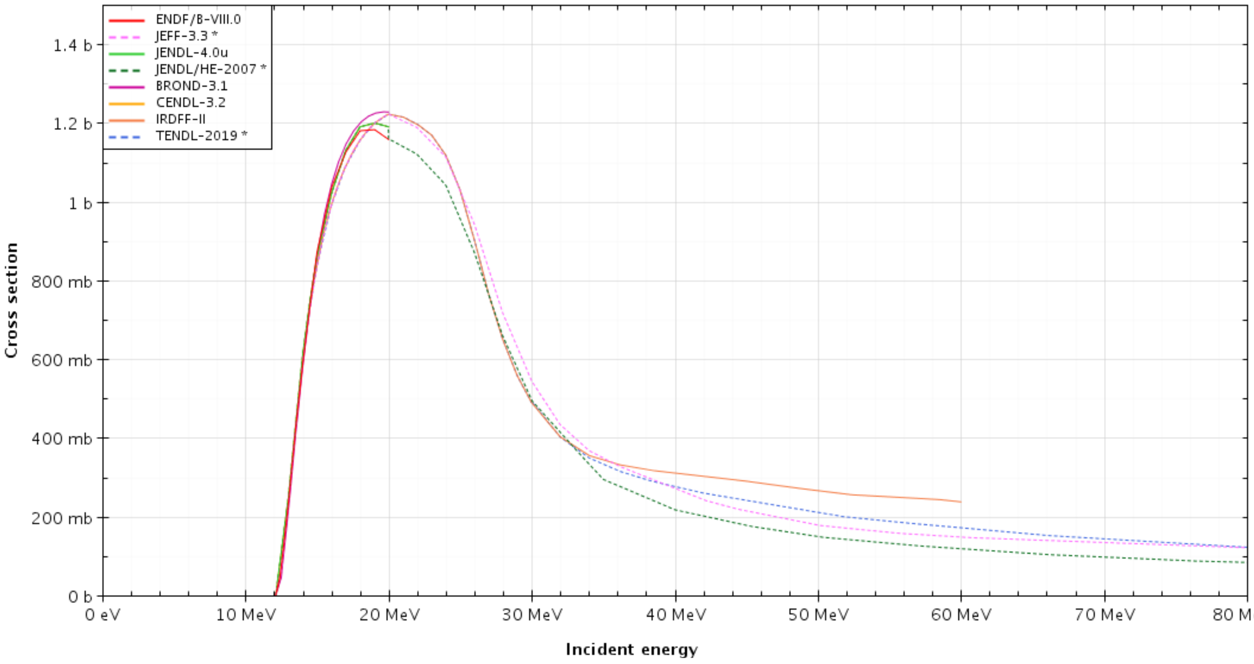

Figure 2.13 – Cross sections of the ^{90}Zr(n,2n) ^{89}Zr reaction according to different libraries.

Other (n,2n) reactions with similar cross-section profiles, such as ^{197}Au(n,2n)^{196}Au, ^{59}Co(n,2n)^{58}Co or ^{89}Y(n,2n)^{88}Y, were initially considered during the materials selection process. However, the resulting radionuclides have longer half-lives (6.2 d, 70.9 d and 106.7 d, respectively), which would result in lower counting rates during gamma spectrometry measurements. Conversely, the ^{63}Cu(n,2n)^{62}Cu reaction was excluded due to the short half-life (9.7 min) of ^{62}Cu nuclei, leading to significant decay of activity between the end of a laser shot and the start of the gamma spectrometry measurement.

The (n,2n) reaction with scandium was also excluded, despite scandium being a monoisotopic element. This is because it produces a radionuclide in two isomeric states, ^{44}Sc and ^{44m}Sc, with ^{44m}Sc decaying into ^{44}Sc, which complicates the analysis. Furthermore, scandium has a density that is twice as low as that of zirconium and the reactions have relatively low cross sections, with a maximum of around 300 mb for the ^{45}Sc(n,2n) ^{44}Sc and 180 mb for the ^{45}Sc(n,2n) ^{44m}Sc, thus resulting in much lower activation.

Bismuth:

Bismuth is a monoisotopic heavy metal that remains stable in air at room temperature. It has low toxicity, especially compared to other heavy metals like lead or mercury. This element is particularly interesting for the SPAC because neutrons with energies of several tens of MeV can induce several (n,xn) reactions, all of which producing gamma-ray-emitting radionuclides. Bismuth is therefore well-suited for neutron activation spectrometry and for characterizing high-energy neutrons, beyond the capacity of bubble spectrometers and nToF detectors. In the context of the SPAC, only the ^{209}Bi(n,4n)^{206}Bi, ^{209}Bi(n,5n)^{205}Bi and ^{209}Bi(n,6n)^{204}Bi reactions are exploited, as other reactions either produce radionuclides with excessively long half-lives (several years) or have cross sections not described by evaluated libraries, making response function calculations impossible.

The half-lives of the ^{204}Bi, ^{205}Bi and ^{206}Bi radionuclides are 11.3 hours, 14.9 days and 6.2 days, respectively. Although these half-lives are relatively long – particularly for ^{205}Bi and ^{206}Bi – which could result in low counting rates during gamma spectrometry measurements, this is compensated by the high cross sections of the reactions producing these radionuclides (see Figure 2.14) and the high density of bismuth (9.79 g/cm^3), thus increasing the probability of such reactions to occur and inducing high activation.

Since different radionuclides are produced in the same sample, they are measured simultaneously. It is therefore crucial to select the appropriate gamma-ray lines for quantifying these radionuclides to avoid considering overlapped gamma-ray peaks, especially when using gamma spectrometers with relatively low energy resolution, such as NaI spectrometers. Thus, the ^{206}Bi nuclei, which have a half-life 6.2 days, can be measured using the 803 keV gamma-ray line emitted with an intensity of 99%. The activity of the ^{205}Bi nuclei, with a half-life of 14.9 days, can be determined using the 703 keV gamma-ray line with an intensity of 31.1%. Finally, the ^{204}Bi nuclei, with a half-life of 11.3 hours, can be measured using the 375 keV gamma-ray line with an intensity of 82%.

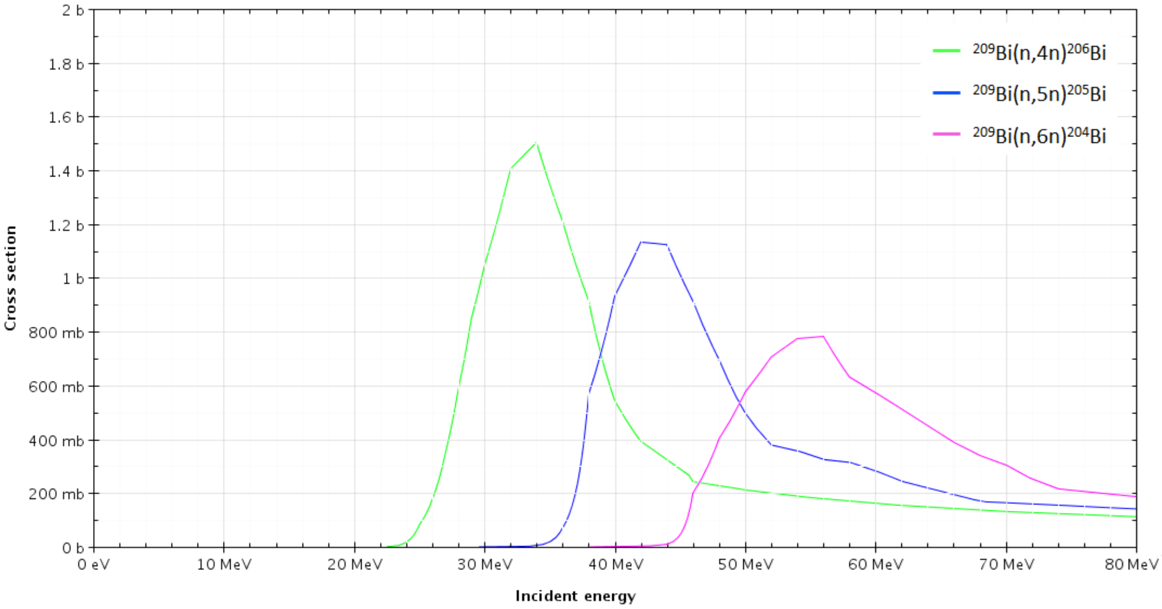

Figure 2.14 – Cross sections of ^{209}Bi(n,4n) ^{206}Bi, ^{209}Bi(n,5n) ^{205}Bi and ^{209}Bi(n,6n) ^{204}Bi reactions according to the IRDFF-II library [218].

Table 2.1 summarizes the chosen materials, the neutron-induced reactions, and their threshold energies. The half-lives of the produced radionuclides are also included, along with the energy and intensity of the emitted gamma-rays.

Element	Reaction of interest	Threshold energy [MeV]	Half-life	Gamma-ray energy [keV]	Gamma-ray intensity
Manganese	^{55}Mn(n,γ)^{56}Mn	0	2.58 h	846.8	98.9%
Indium	^{115}In(n,γ)^{116m}In	0	54 min	416.9	27.2%
	^{115}In(n,n’)^{115m}In	0.34	4.49 h	336.2	45.9%
Iron	^{56}Fe(n,p)^{56}Mn	3	2.58 h	846.8	98.9%
Zirconium	^{90}Zr(n,2n)^{89}Zr	12.1	78.4 h	909.2	99.0%
Bismuth	^{209}Bi(n,4n)^{206}Bi	22.5	6.2 d	803.1	99.0%
	^{209}Bi(n,5n)^{205}Bi	29.6	14.9 d	703.5	31.1%
	^{209}Bi(n,6n)^{204}Bi	38.1	11.3 h	374.8	82.0%

Table 2.1 - Summary of all the reactions exploited in the SPAC and information about the radionuclides produced.

Now that we have chosen the most suitable materials for the SPAC, the next step is to define the detector geometry, considering several key factors. First, to effectively characterize neutron emissions produced by lasers, all samples must be irradiated simultaneously. They will be arranged in a stack, rather than on a single circular plane, to minimize the effects of neutron emission anisotropy on the measurements and to measure neutron emissions over the smallest possible solid angle. To achieve this, the samples need to be compact but not too small to ensure sufficient activation. Circular samples with a standardized diameter of 1 inch provide a good balance, as they can be easily measured using conventional gamma spectrometers with typical diameters of 2 or 3 inches.

Since low-energy neutrons interact more with matter (see Section 1.1.3), the samples are arranged in the stack in order of increasing reaction threshold energies. This arrangement prevents the scattering or the complete absorption of low-energy neutrons before they reach the sample with which they are intended to interact. Hence, the samples are arranged as follows: manganese, indium, iron, zirconium and bismuth. Additionally, a second manganese sample is placed after the bismuth to assess the contribution of low-energy scattered neutrons from the surrounding structure.

Then, the thickness of each sample needs to be optimized, because a thick sample absorbs more neutrons and produces more activation but acts also as a shield for the following samples and increases the self-attenuation of gamma-rays, thereby reducing the counting rate during gamma spectrometry measurements. Simulations using the Monte Carlo transport code Geant4 [209] were performed, considering a typical neutron spectrum produced by a laser and sample thicknesses ranging from 1 to 30 mm, to assess activation levels in such samples. Additionally, a modeling of a NaI spectrometer was made to simulate gamma spectrometry measurements and reproduce the self-attenuation effects, in order to determine the optimal sample thicknesses. Furthermore, some samples were tested under experimental conditions at the Apollon facility (see Section 3.2.1), which established an upper limit for the thickness of certain samples, such as indium, for which the activation is sufficient to be easily measured. Figure 2.15 presents the optimal thicknesses of each sample.

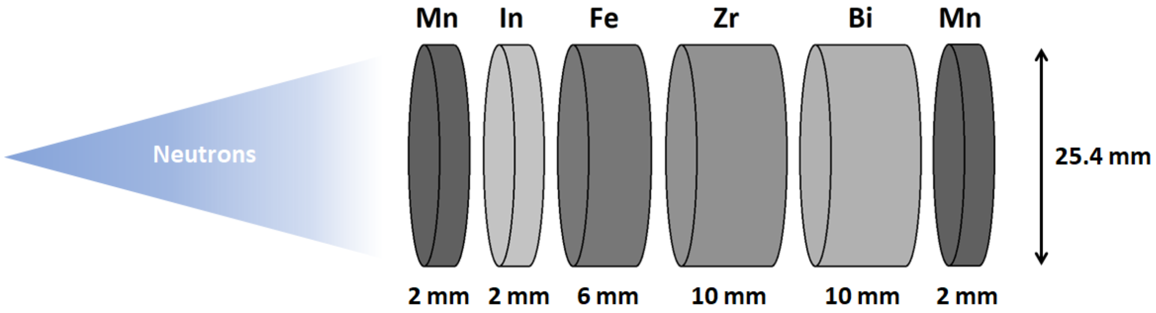

Figure 2.15 – Schematic view of the SPAC. For clarity, the samples are represented with space between them, which is not the case in reality.

2.2.2 Response matrix calculation

The response matrix is required to calculate neutron spectra using unfolding algorithms. It consists of a response function for each sample, which can be expressed as the activity induced per incident neutron as a function of neutron energy. Thus, these response functions link the energy distribution of neutron fluences to the measured activities through the following equation:

$$A_{0_i} \propto \int R_i(E).\Phi(E).dE \tag{2.15}$$

Where A_{0_i} and $R_i(E)$ are, respectively, the measured activity of the sample i and its response function. $\Phi(E)$ is the neutron spectrum.

The response matrix is calculated using Monte Carlo simulations, which rely on an evaluated cross-section library. Therefore, nuclear data are a key parameter in determining the response matrix as accurately as possible, but some samples may present significant differences in cross sections data depending on the library considered. To identify the most suitable cross-section library, we irradiated the sample composing the SPAC with monoenergetic neutrons produced at the AMANDE facility [96] at IRSN (Cadarache, France). We then compared the induced activities with the results of Monte Carlo simulations performed with Geant4 [209] and MCNP6 [210], using different libraries. The use of both Monte Carlo Code enabled to compare and validate the results through extensive simulations.

The AMANDE facility produces reference monoenergetic neutron fields, ranging from a few keV to around 20 MeV, which are used for metrology experiments to calibrate neutron dosimeters or spectrometers. It is equipped with a 2 MV Tandetron accelerator, capable of accelerating pulsed or continuous beams of charged particles, such as protons or deuterons, to energies between 0.1 and 4 MeV (up to 6 MeV for alpha particles). The charged particles are directed through beam lines to an experimental hall (see Figure 2.16), where the beam strikes a specific target to produce monoenergetic neutrons. The experimental hall measures 20 meters in length and width and 16 meters in height, and the target is positioned approximately 7 meters above the ground, thereby limiting the contribution of scattered neutrons to the measurements.

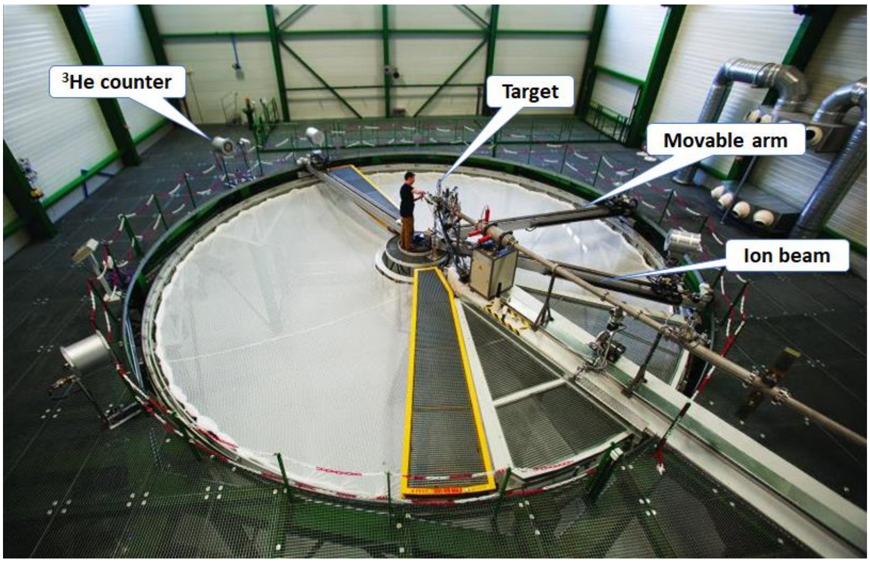

Figure 2.16 – Experimental hall of the AMANDE facility.

Neutrons are produced uisng scandium, lithium fluoride (LiF) and deuterated or tritiated titanium targets (TiD or TiT) through five different reactions (see Table 2.2). The neutron energy depends on both the energy of the incident charged particles and the angle relative to the beam axis. Thus, instruments or samples to be irradiated can be placed at angles ranging from -150° to +150°, using movable arms, to expose them to different neutron energies without changing the ion energy. It is also possible to increase the neutron flux by using thicker targets, although this results in a broader neutron energy spectrum due to multiple scattering and greater energy loss of the incident ion beam inside the target. Finally, to ensure nominal irradiation, neutron fluxes are continuously monitored, before and during irradiation, by calibrated and moderated ^{3}He proportional counters [211].

Incident ion	**Target**	**Reaction**	**Ion energy**	**Neutron energy (in the beam axis)**
Proton	Scandium	^{45}Sc(p,n)^{45}Ti	2.91 – 2.95 MeV	8 – 52 keV
Proton	Lithium (LiF)	^{7}Li(p,n)^{7}Be	1.9 – 2.5 MeV	120 – 650 keV
Proton	Tritium (TiT)	^{3}H(p,n)^{3}He	1.15 – 4 MeV	0.29 – 3.2 MeV
Deuteron	Deuterium (TiD)	^{2}H(d,n)^{3}He	0.2 – 4 MeV	2.45 – 7.3 MeV
Deuteron	Tritium (TiT)	^{3}H(d,n)^{4}He	0.1 – 4 MeV	14.7 – 20.8 MeV

Table 2.2 – Nuclear reactions producing monoenergetic neutrons at the AMANDE facility. The energy values correspond to the available minimum and maximum neutron energies (fifth column) produced for each reaction by the corresponding ion energies (fourth column). D-D and D-T fusion reactions produce neutrons with higher energies than the incident deuterons due to their exothermic nature.

During our experiment, we irradiated the SPAC samples, both individually and in the stacked configuration, with neutrons of various energies: 0.565 MeV, 1.2 MeV, 1.9 MeV, 2.5 MeV, 4 MeV, 5 MeV, 7.2 MeV, 15.1 MeV and 20.7 MeV. The bismuth sample was not irradiated because the minimum threshold energy for the reactions of interest is 22.5 MeV, which exceeds the capabilities of the AMANDE facility. Furthermore, irradiation with neutron energies below 565 keV was not considered due to the low neutron fluxes at such energies, which would have required irradiation times of several days. The samples were placed at 10 cm from the neutron source (see Figure 2.17) to ensure sufficient neutron fluences and limit irradiation times to several hours.

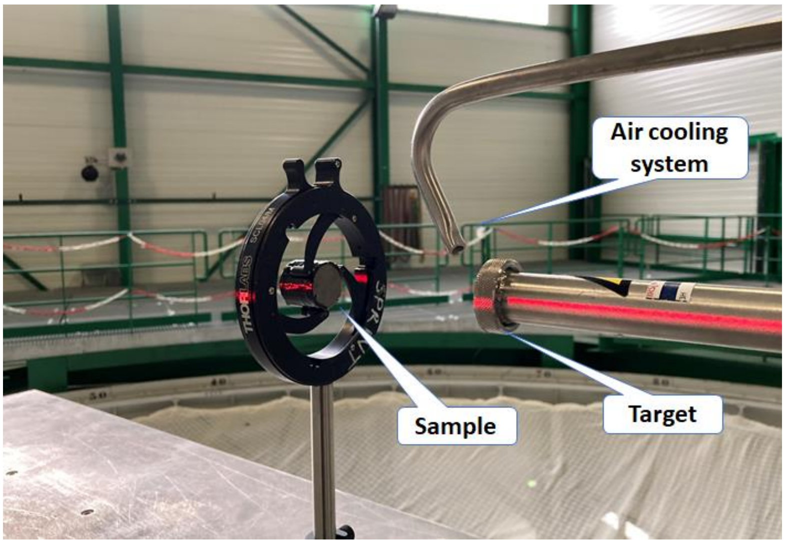

Figure 2.17 – Irradiation setup with the air cooling system allowing the dissipation of heat induced by the interaction of ions with the target.

After irradiation, the activation of the samples was measured using gamma spectrometry performed with a detector system consisting of two 2×2" NaI spectrometers placed face-to-face and shielded by 10 cm thick lead bricks. The samples were positioned between the two spectrometers, with a near 4π solid angle coverage around the samples that allowed to maximize the detection efficiency. The efficiency calibration of these spectrometers was performed with a ^{152}Eu calibration point source and extrapolated to the geometries of samples using Geant4 simulations and the efficiency transfer method [212, 213] based on the Moens concept [214], which states that, for a given gamma-ray energy, the ratio between the number of counts in the photopeak and the total number of counts in the gamma spectrum does not vary according to the geometry of the measured samples, but depends only on the detector. This can be expressed by the following equation, accounting for the absolute efficiency ε_{abs}, which is the probability that the emitted gamma-rays interact with the detector via the photoelectric effect, and the total efficiency η, which is the probability that the emitted gamma-rays interact via any interaction process:

$$\frac{\varepsilon_{abs}^{sample}}{\eta^{sample}} = \frac{\varepsilon_{abs}^{^{152}Eu}}{\eta^{^{152}Eu}} \tag{2.16}$$

Therefore, the absolute efficiency, $\varepsilon_{abs}^{sample}$, associated to the geometry of a specific sample can be calculated from the absolute efficiency, $\varepsilon_{abs}^{^{152}Eu}$, measured with the calibration source and the total efficiencies, η^{sample} and $\eta^{^{152}Eu}$, obtained via Geant4 simulations. Thus, this approach allows to consider the sample geometry and the self-attenuation effects of gamma-rays on the measurements. Consequently, the activity of the samples at the end of irradiation was determined using equation (2.11).

The measured activities were then compared with the results obtained from Geant4 and MNCP6 simulations. These simulations reproduced the experimental setup by using a conical neutron source placed at 10 cm from the sample and scaled according to the neutron fluences encountered during the experiment. Initially, the JEFF-3.3 [215] cross-section library was used for both Monte Carlo transport codes because it was also employed for the response matrix calculation of the SNAC2 and the cross sections of reactions of interest are very close to those provided by other major libraries, such as ENDF/B-VIII.0 [216] or TENDL-2019 [217] (see Figure 2.10, Figure 2.12 or Figure 2.13), thus minimizing the need for additional time-consuming simulations. However, another library, called IRDFF-II [218], was also considered in the simulations. It provides cross sections similar to the EAF-2010 library (see Figure 2.11) and includes the ^{115}In(n,n')^{115m}In reaction, which is not covered by the JEFF-3.3 library. Thus, the measured activities were compared to simulated activities obtained using Geant4 with JEFF-3.3, MCNP6 with JEFF-3.3 and MCNP6 with IRDFF-II (IRDFF-II not being implementable in Geant4). The results are presented in Appendix A.

Several observations can be made regarding the results of these measurement/simulation comparisons. First, as previously mentioned, the JEFF-3.3 library does not account for reactions in indium that produce radionuclides in metastable states, ^{115m}In and ^{116m}In. As a result, Geant4 and MCNP6 simulations using this library cannot predict the activity of these radionuclides. Significant discrepancies are also observed between the measurements and Geant4 simulations for the ^{55}Mn(n,g)^{56}Mn, ^{56}Fe(n,p)^{56}Mn and ^{90}Zr(n,2n)^{89}Zr reactions. However, MCNP6 simulations using the JEFF-3.3 library yield better results for the ^{55}Mn(n,g)^{56}Mn and ^{90}Zr(n,2n)^{89}Zr reactions, with relative differences of less than 30%.

The MCNP6 simulations using the IRDFF-II library provide even better results, particularly for the ^{115}In(n,n')^{115m}In and ^{115}In(n,γ)^{116m}In reactions, which are also well reproduced because this library includes the production of radionuclides in metastable states. Hence, relative differences lower than 30% are typically observed for all the reactions of interest. However, the simulated activity of ^{115m}In is significantly overestimated for neutrons with energies of 0.565 MeV and 1.2 MeV. This can be explained by an inaccurate fitting of the evaluated cross sections by IRDFF-II compared to experimental data. As shown in Figure 2.18, the IRDFF-II library tends to overestimate the experimental cross sections, especially near the threshold energy of the reaction, which is consistent with the overestimated simulated activities observed at the lowest neutron energies.

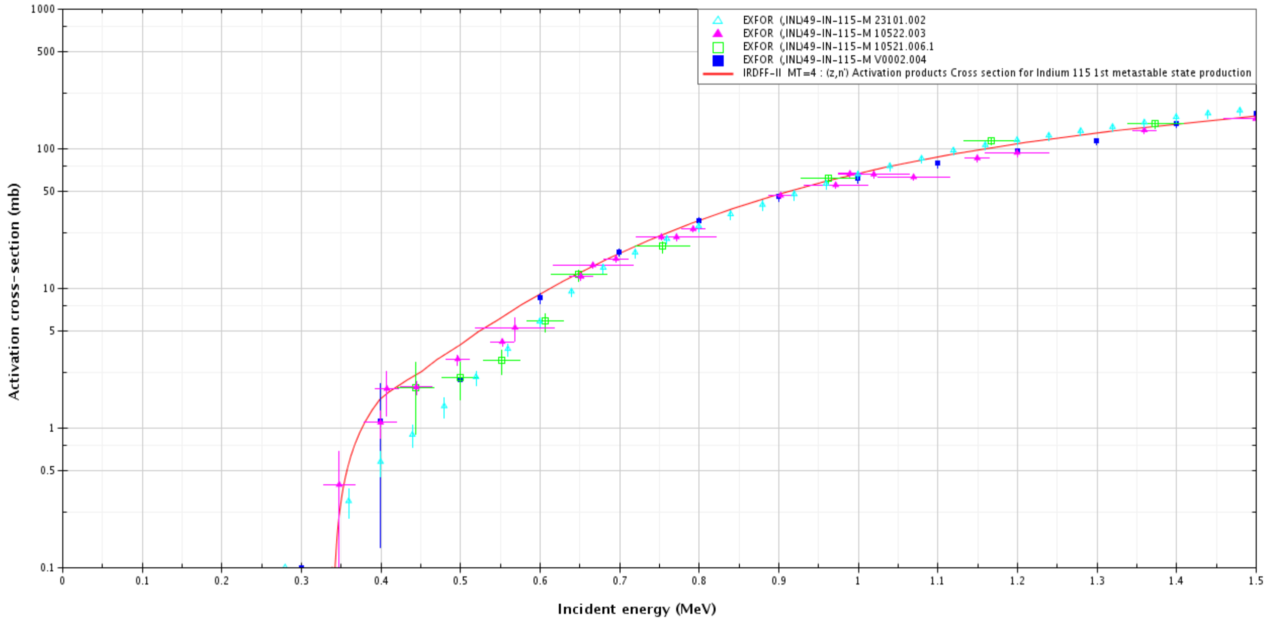

Figure 2.18 – Comparison of experimental and evaluated cross sections of the ^{115}In(n,n') ^{115m}In reaction.

Finally, even with the IRDFF-II library, significant differences between the measured and simulated activities are observed for irradiations using neutrons of 7.2 and 20.7 MeV, especially for the ^{55}Mn(n,g)^{56}Mn, ^{115}In(n,n')^{115m}In and ^{115}In(n,γ)^{116m}In reactions. These discrepancies arise from the interaction of 4 MeV deuterons with the deuterated or tritiated titanium target, which normally produce only 7.2 or 20.7 MeV neutrons, respectively. However, such deuterons have sufficient energy to induce (d,n) reactions in titanium nuclei, generating additional neutrons of several MeV [219]. As shown in Appendix A, the ^{56}Fe(n,p)^{56}Mn and ^{90}Zr(n,2n)^{89}Zr reactions are less affected by these parasitic neutrons because their threshold energy are close to or higher than the energy of these neutrons.

Geant4 simulations reproducing the interaction between 4 MeV deuterons and tritium, with and without considering the titanium substrate, confirm that parasitic neutrons originate from the interaction of deuterons with titanium (see Figure 2.19). For the target composition and thickness used during the experiment at the AMANDE facility, the simulations indicate that these parasitic neutrons can have energies exceeding 6 MeV and contribute to more than 59% of the total neutron emission along the beam axis. Thus, comparisons between the simulated and measured activities induced by neutrons of 7.2 or 20.7 MeV are inconsistent, especially for the ^{55}Mn(n,g)^{56}Mn, ^{115}In(n,n')^{115m}In and ^{115}In(n,γ)^{116m}In reactions, which are more significantly affected by these parasitic neutrons.

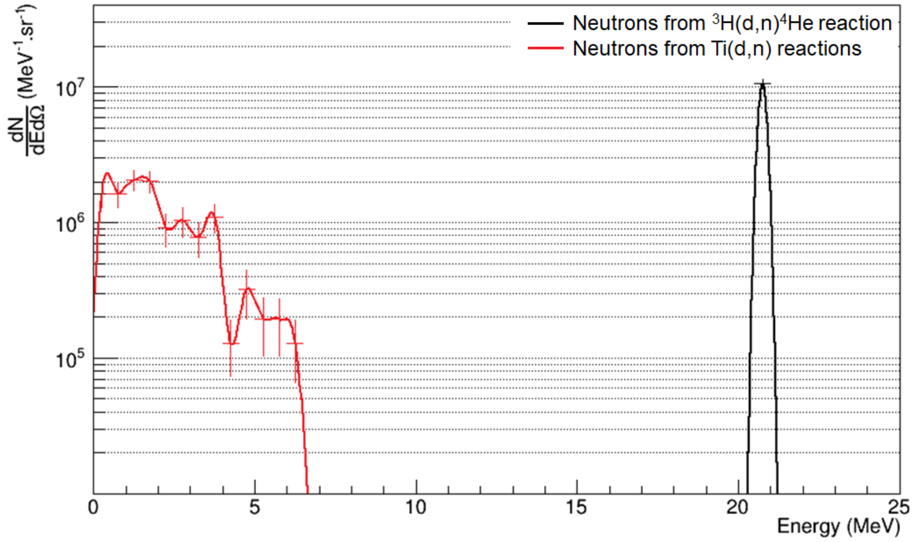

Figure 2.19 – Geant4 simulation of the differential neutron spectrum, in the beam axis, induced by the interaction of 4 MeV deuterons with a 780 µg/cm² thick tritiated titanium target.

However, based on the comparison between simulated and measured activities, it was found that MCNP6 with the IRDFF-II library most accurately reproduces the activation of SPAC samples irradiated at the AMANDE facility. This Monte Carlo transport code and this cross-section library were therefore preferred to calculate the response function of each sample, which constitutes the response matrix of the SPAC.

Hence, the response functions were calculated considering a conical neutron source positioned 10 cm from the front side of the SPAC and covering the entire detector surface, as shown in Figure 2.15. This configuration was selected to closely match the experimental conditions under which the SPAC will be used at laser facilities. The response functions were defined using 1024 bins ranging from 10^{-9} MeV to 80 MeV. This binning facilitates an easier unfolding process when using artificial intelligence with neural networks. Then, the bins are defined in two parts: 226 variable bins from 10^{-9} MeV to 0.2 MeV with a bin ratio of $\frac{E_{i+1}}{E_i} = 1.088$, and 798 constant bins with a width of 0.1 MeV between 0.2 MeV and 80 MeV. This binning allows for the calculation of response functions across several orders of magnitude, from thermal to high-energy ranges, with a specific focus on high-energy neutrons, which is the primary objective of the SPAC.

To calculate the reaction rates in each sample, the *F4* tally is used in the MCNP6 input file to obtain the volumetric flux, which represents the average neutron flux within each sample. This flux is then multiplied by the *FM4* multiplier, which accounts for the cross section of the reaction of interest, and by a normalization factor *C* which considers the number of target nuclei depending on the sample mass. Thus, the reaction rates are defined as the number of radionuclides produced per gram per incident neutron, as given by the following equation:

$$R = F4 \times FM4 \times C \tag{2.17}$$

Where *F4* is the volumetric flux given by the *F4* tally in neutrons/cm² per incident neutron, *FM4* represents the cross section in barn and *C* is the constant giving the number of target nuclei and expressed as:

$$C = \frac{\chi \times N_A}{M} \times 10^{-24} \tag{2.18}$$

With χ the isotope abundance, N_A the Avogadro constant (mol^{-1}) and *M* the molar mass (g/mol). The constant *C* is normalized by 10^{-24}, which is the conversion factor from barn to cm² to transform the cross sections given in barn by MCNP6 into cm². This normalization allows for the calculation of a reaction rate *R*, defined as the number of radionuclides produced per gram per incident neutron.

The response functions were therefore calculated with the script shown in Appendix B, where the constant *C* for each sample is listed alongside the *FM4* multiplier. The number of incident neutrons considered in these calculations was 10^8 for neutrons ranging from 10^{-9} MeV to 10^{-7} MeV, and 10^7 for neutrons ranging from 10^{-7} MeV to 80 MeV. This ensures tally statistical errors are below 1%, except for the ^{55}Mn(n,g)^{56}Mn reaction in the manganese sample located at the rear face of the SPAC where tally errors can reach up to 4% for neutrons between 10^{-9} MeV and 5×10^{-9} MeV. This increase in error is attributed to the absorption of low-energy neutrons as they pass through the SPAC, reducing the number of neutrons reaching the rear face and thus increasing the statistical error.

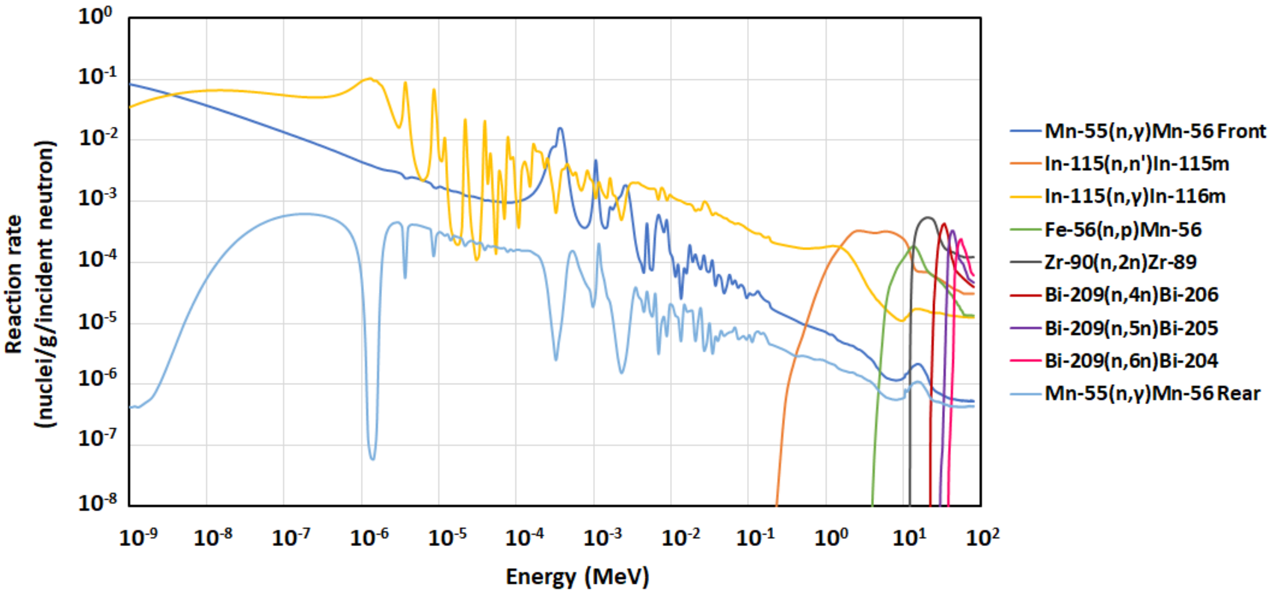

Figure 2.20 - Reaction rate of reactions of interest as function of neutron energy simulated with MCNP6 (IRDFF-II). The discrepancy of the front and rear manganese sample radiative capture reaction is due to neutron absorption in other samples.

As shown in Figure 2.20, the absorption of neutrons as they pass through the SPAC results in different response functions for the manganese sample located at the front and rear faces. This variation allows for qualitative measurements. For example, if the activation level of the rear face manganese sample is similar to or higher than that of the front face sample, it indicates a significant quantity of scattered neutrons. Furthermore, if activation simulations of the front face manganese sample, considering the neutron spectrum unfolded from the other samples, yield lower activity than measured, it suggests that the contribution of thermal and epithermal neutrons is not negligible.

Figure 2.21 highlights the response functions in the high-energy domain, which is the focus of the SPAC. Given the selected reactions and their threshold energy, these reactions can unambiguously discriminate neutron energies across the range of interest. This confirms the relevance of the chosen materials and the possibility to use unfolding algorithms to obtain neutron spectra from the measured activity of samples.

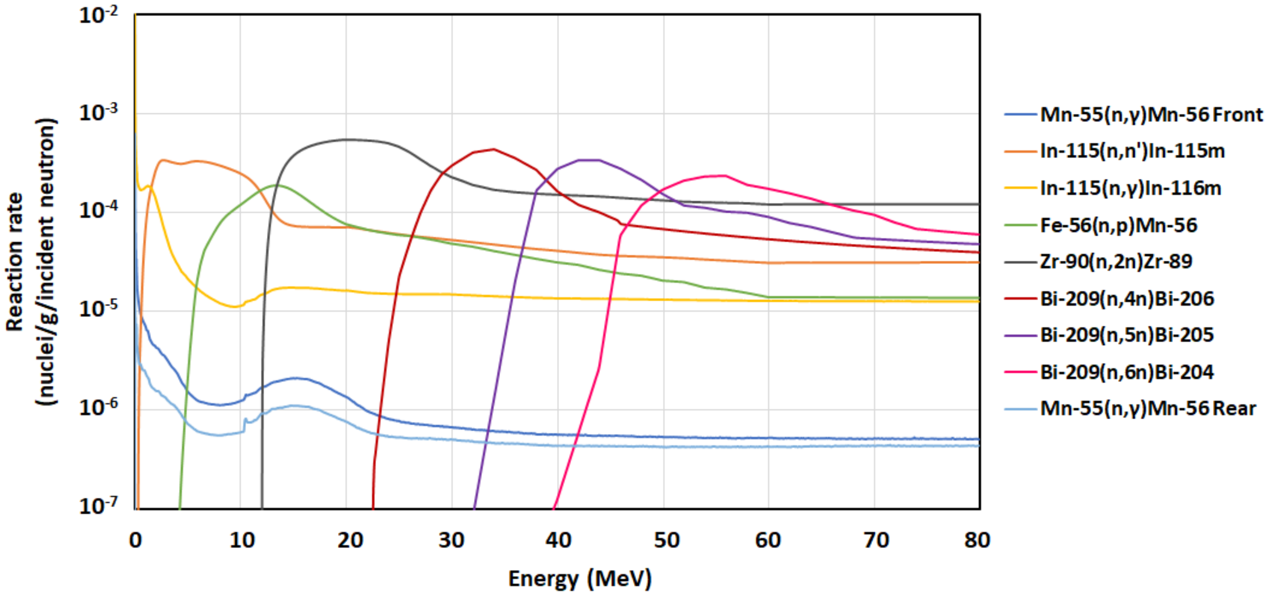

Figure 2.21 – Response functions in the energy range of interest for laser facilities, i.e. in the high-energy domain.

The unfolding process consists in inverting equation (2.15) to determine the neutron spectrum $\Phi(E)$ knowing the measured activity A_0 of samples and their response function $R(E)$. This inversion can be performed using different historical codes such as GRAVEL or MAXED. The GRAVEL algorithm [220] reconstructs neutron spectra by iteratively adjusting an initial spectrum guess until it matches with the measured activities, after convolution with the response matrix. To achieve this, GRAVEL calculates the contribution (i.e. the weight) of each response function composing the response matrix to the neutron spectrum being unfolded. A non-linear least squares method is therefore used, following this equation:

$$\Phi_j^{n+1} = \Phi_j^n exp\left(\frac{\sum_i w_{ij}^n \, ln\left(\frac{A_{0_i}}{\sum_j R_{ij}\Phi_j^n}\right)}{\sum_i w_{ij}^n}\right) \tag{2.19}$$

$$w_{ij}^n = \frac{R_{ij}\Phi_j^n}{\sum_j R_{ij}\Phi_j^n} \times \left(\frac{A_{0_i}}{\sigma_i}\right)^2 \tag{2.20}$$

Where Φ_j^n is the fluence in the energy bin j at the n$^{\text{th}}$ iteration, A_{0_i} is the measured activity of the sample i, R_{ij} is the response of the sample i at the energy bin j, w_{ij}^n is the weight factor at the n$^{\text{th}}$ iteration and σ_i is the relative standard deviation of A_{0_i}.

Thus, GRAVEL is initialized considering several inputs, including the response matrix, the energy range of the unfolded spectrum and an initial spectrum guess Φ^0. The unfolding process continues until either the maximum number of iterations is reached or a convergence criterion is met.

The MAXED algorithm [221] is based on the Bayesian theory combined with the maximum entropy principle. In this approach, the admissible unfolded neutron spectra are defined by the following two equations:

$$A_{0_i} + \varepsilon_i = \sum_i R_{ij} \Phi_j \tag{2.21}$$

$$\sum_i \frac{{\varepsilon_i}^2}{{\sigma_i}^2} = \Omega \tag{2.22}$$

Where A_{0_i} is the measured activity of the sample i, ε_i is the difference between the predicted activity and the measured activity, R_{ij} is the response of the sample i at the energy bin j, Φ_j is the fluence in the energy bin j and σ_i is the uncertainty associated to A_{0_i}. Ω is typically set equal to the number of samples.

Hence, equation (2.22) constraints the possible values of ε_i and therefore the spectra that satisfy equation (2.21). Among these admissible spectra, the most appropriate result is the one which maximizes the entropy S defined as:

$$S = -\sum_i \left(\Phi_j ln\left(\frac{\Phi_j}{\Phi_j^0}\right) + \Phi_j^0 - \Phi_j \right) \tag{2.23}$$

Where Φ_j^0 is the fluence in the energy bin j of the initial spectrum guess.

The MAXED code stops when it finds the maximum possible value of S, which typically takes less time than iterative algorithms like GRAVEL. However, both GRAVEL and MAXED require a priori information about the measured neutron spectra to produce consistent results. Recently, there has been a focus on using artificial intelligence methods for neutron spectrum unfolding, as artificial neural networks do not require a priori information about the measured neutron spectrum [222, 223, 224]. Nonetheless, a large dataset is essential to train and optimize an artificial neural network, enabling it to establish complex relationships between inputs and outputs, which is crucial for accurately retrieving neutron spectra from measured activities in neutron activation spectrometry.

***

To ensure radiation protection at laser facilities and evaluate their ability to produce useful neutron emissions for applications, laser-driven neutron sources must be characterized in terms of both neutron flux and energy distribution. However, due to the characteristics of such neutron sources, which emit very short (< ns) and intense neutron bunches along with significant background radiation (electromagnetic and X-ray emissions), the number of suitable detectors is very limited. These detectors have also constrained capabilities, especially for performing neutron spectrometry beyond 20 MeV. Therefore, a compact neutron spectrometer based on the activation principle was specifically designed for laser-driven neutron sources, allowing to complement the sensibility range of the other diagnostics to neutron energy up to 80 MeV.

3. Characterization of neutron emissions produced at different laser facilities

As mentioned in Section 1.4.4, numerous neutron production experiments using lasers were already conducted, often resulting in neutron flux measurements. However, due to the characteristics of laser-driven neutron sources, which make neutron detection challenging, the characterization of their energy distribution was more rarely carried out, despite this information being crucial for evaluating the potential of these new neutron sources to perform applications. Additionally, even a partial information about the spectrum is needed when wanting to use detectors such as neutron activation spectrometers, in combination with classical or artificial intelligence-based unfolding algorithms, in order to fully reconstruct neutron spectra. Indeed, these algorithms require either a priori information about the neutron energy distribution or a dataset from which they are trained. Thus, this chapter focuses on the characterization of laser-driven neutron sources produced at various laser facilities with different characteristics and in particular on the neutron energy distribution. These lasers used here span a wide range of laser energies from 3 to 43 J. We will notably show that we have been able to perform accurate neutron measurements over such a wide range of parameters.

3.1 Neutron production at the Advanced Laser Light Source (ALLS)

Although laser-driven neutron sources still have lower mean fluxes compared to those of conventional neutron sources (see Section 1.4.4), ongoing improvements of laser technology are made to overcome the current limitations, especially in enhancing the laser repetition rate. Currently, high repetition rate lasers are relatively small and deliver pulses in the Hz range with energies of only a few Joules, while most of the characterization of laser-driven neutron emissions was performed up to now using large-scale, low repetition rate (1 shot/hour, typically) and high-energy (tens or hundreds of Joules) lasers. However, the yield of the protons used to generate the neutrons is very non-linear with respect to the laser energy [136]. Hence, an important aspect of evaluating the usefulness of high repetition rate table-top lasers as neutron drivers is to measure how the neutron yield is affected by moving from high-energy lasers to such lasers having much more moderate energies, in the few Joules range. This is the main objective of the experiment which will now be described.

3.1.1 Experimental setup

The experiment was performed on the laser-driven ion acceleration beamline at the Institut National de la Recherche Scientifique (INRS) in Varennes, near Montréal, Canada. We used the ALLS 150 TW Ti:Sapphire laser [225] based on a double Chirped Pulse Amplification (CPA) system, delivering pulses at a repetition rate of 0.5 Hz with an on-target energy of 3.2 J. The pulses had a duration of 22 fs at Full-Width-Half-Maximum (FWHM) with a central wavelength of 800 nm. The experimental setup, shown in Figure 3.1.B, uses an f/3 off-axis parabola to focus the 95×95 mm square beam down to a spot size of 5 µm FWHM. Parabola alignment and wavefront optimization, using a feedback loop between a wavefront sensor and a deformable mirror, are both performed at full laser power, which allows to compensate aberrations arising from thermalization in the laser system. This results in a peak intensity on target around 1.3×10^{20} W/cm². Prior to entering the second CPA amplification stage, a cross-wave polarizer (XPW) and a booster stage relying on saturable absorber are employed to clean the incoming laser beam, achieving an Amplified Spontaneous Emission (ASE) pre-pulse contrast lower than 10^{-10} at -100 ps before the main pulse, along with a steep power rise with contrast lower than 10^{-6} at -3 ps.

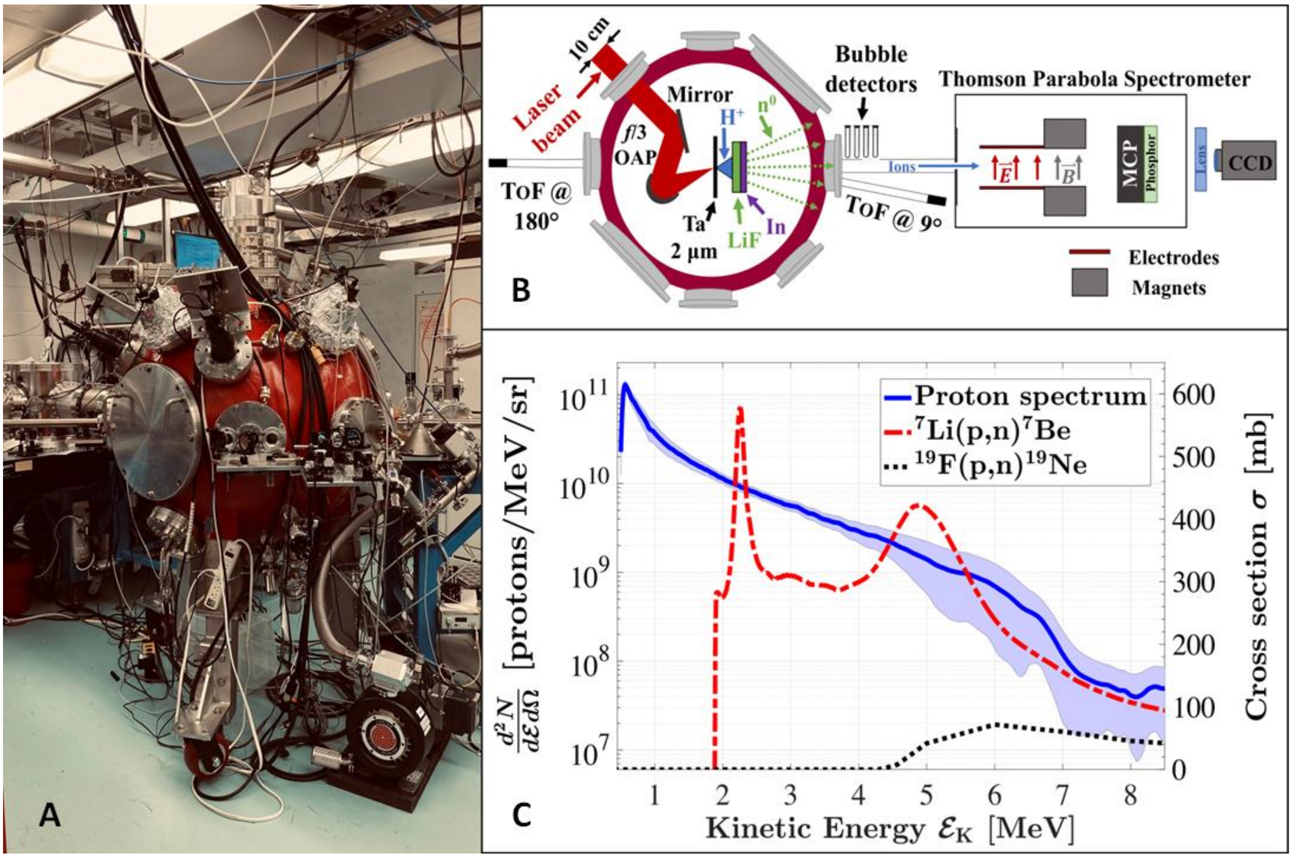

Figure 3.1 – (A) Target chamber at ALLS. (B) Top-view of the experimental setup. (C) Mean proton spectrum averaged over 38 shots using a 2 μm thick tantalum foil (full blue). The shaded area is delimited by one standard deviation. The cross sections for the nuclear reactions ^{7}Li(p,n)^{7}Be (dashed red) and ^{19}F(p,n)^{19}Ne (dotted black) are also shown, as given by the ENDF/B-VIII and TENDL-2019 libraries, respectively.

The p-polarized laser pulses were focused on 2 µm thick tantalum foils with an incident angle of 20° with respect to the target normal, allowing to produce ion beams using the TNSA regime (see Section 1.4.3). A custom-made target holder on a motorized stage was used during the experiment with a multi-shot mode. This setup allowed for pre-setting the target positions in the software controlling the motorized stage, which was synchronized with the laser trigger at 0.5 Hz, enabling up to 400 consecutive shots without opening the target chamber.

The energy distribution of the accelerated ions (mainly protons) was measured using a calibrated Thomson Parabola spectrometer with a MicroChannel Plate (MCP) detector positioned at 0° with respect to the target normal axis, which allows to acquire the images of the ion spectra for each laser shot. A mean proton spectrum (averaged over 38 shots) is shown in Figure 3.1.C, confirming the good shot-to-shot repeatability of these laser source [137]. The mean proton spectrum is characterized by around 10^{11} protons/sr/shot and an energy cutoff of 7.3 MeV. Finally, two Time-of-Flight (ToF) spectrometers are deployed, one positioned at 9° and the other at 180° from the main axis, to monitor the number of protons and their energies in correlation with the TP spectrometer. The 180° ToF spectrometer is primarily utilized when the proton-to-neutron converter is inserted into the ion beam path to verify that the TNSA acceleration occurs efficiently.

For the neutron generation, we selected lithium fluoride (LiF) as the converter material in order to maximize the neutron production. Indeed, since the maximum proton cutoff energy is limited to about 7.3 MeV and the proton spectrum has a typical decreasing exponential shape, LiF is optimum due to its high cross sections of (p,n) reactions for low-energy protons. Furthermore, it has a threshold energy of about 1.9 MeV and a specific resonance at 2.2 MeV for the ^{7}Li(p,n)^{7}Be reaction (see Figure 3.1.C). SRIM [226] calculations were performed to design the converter and ensure that all protons interact with it. Thus, a 1 mm thick, 1-inch diameter LiF converter was used and placed 20 mm behind the target holder (see Figure 3.1.B).

Several techniques were employed to characterize the neutron emissions, including bubble detectors, activation measurements and scintillators used as nToF detectors. Two types of bubble detectors, supplied by *Bubble Technology Industries*, were used: BD-PND and BDT. BD-PND detectors are sensitive to neutrons from 200 keV to around 15 MeV, while BDT detectors are sensitive to thermal neutrons. Besides, an activation diagnostic consisting of a 1-inch diameter, 6 mm thick pure indium sample was placed right behind the LiF converter. As described in Section 2.2.1, the interaction of neutrons with this sample can cause two main reactions: ^{115}In(n,n')^{115m}In and ^{115}In(n,γ)^{116m}In. As shown in Figure 3.4.B, the cross sections of the first reaction are significant between 2 and 10 MeV, allowing to detect neutrons in this energy range, while the second reaction is more sensitive to neutrons from the thermal region to few MeV, serving as a qualitative low-energy neutron diagnostic.

Two ultra-fast organic scintillators, based on a plastic matrix of polyvinyl toluene, were also used during this experiment. Each scintillator consisted of a 1-inch diameter and 40 cm long scintillator tube (EJ-254) [227] connected to one photomultiplier tube (9112B) [228] on each side (see Figure 3.2). The signal was digitized at a sampling frequency of 1.25 GHz using a PicoScope 6402C [229]. These two scintillators were placed at 5° relative to the ion beam axis and 1.8 m from the converter, and at 20° relative to the ion beam axis and 4 m from the converter, respectively. The idea was to position them as close as possible to the 0° axis, where the indium sample and the bubble detectors were also located, to enable potential inter-comparisons between the results obtained from these different diagnostics. However, because the Thomson Parabola and the associated beamline occupy much of this axis (see Figure 3.1.B), the scintillators had to be slightly displaced. They were shielded with 1 cm thick lead cylinder surrounding the scintillators, along with lead bricks up to 15 cm thick on the front face, to avoid saturation effects caused by X-ray and gamma-ray emissions.

Figure 3.2 - Design of the nToF detectors, inspired by [236].

Finally, since neutron production via the ^{19}F(p,n)^{19}Ne reaction can be neglected (see next section), neutrons are generated exclusively through the ^{7}Li(p,n)^{7}Be reaction, the total number of neutrons therefore corresponds to the number of ^{7}Be nuclei produced in the converter. This total number of neutrons is therefore determined by measuring this radionuclide, which emits a gamma-ray of 478 keV with an intensity of 10.44% and a half-life time long enough ($T_{1/2}$ = 53.22 d), making it easily to measure using gamma spectrometry.

3.1.2 Simulation of neutron emissions

To predict the characteristics of the neutron emissions, Geant4 simulations were made using the averaged proton spectrum shown in Figure 3.1.C, injected into the LiF converter within a maximum half-angle of 21°, replicating the typical beam divergence of a TNSA proton beam [230]. The same typical beam divergence described in [230] was also used to extrapolate the averaged proton spectrum, which was measured over a small solid angle corresponding to the aperture of the Thomson Parabola spectrometer, to obtain the overall proton spectrum intercepted by the LiF converter. These considerations, along with the use of the ENDF/B-VIII.0 and TENDL-2019 libraries, allow to faithfully reproduce the experimental conditions and nuclear reactions inside the converter.

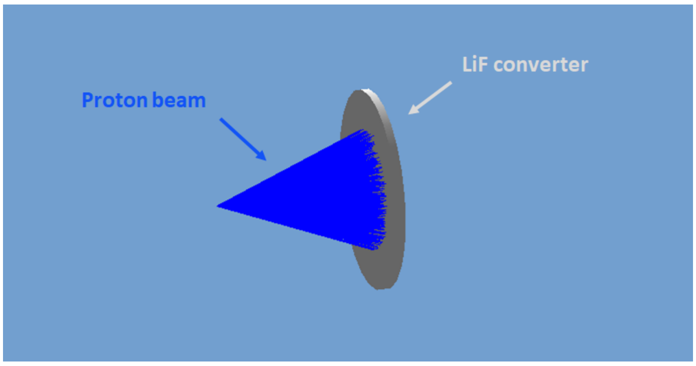

Figure 3.3 – Configuration of the Geant4 simulations: A conical proton beam is interacting with the LiF converter placed in air.

Figure 3.4 presents the simulated angular distribution of neutron emissions and the simulated neutron spectra obtained at different angles, ranging from 0° to 180°. These simulations results show that more neutrons, with higher energies, are emitted in the forward direction compared to the backward direction. This suggests that within the converter, not only compound nuclear reactions occur, but also direct nuclear reactions, contributing to the distinctive emission anisotropy. However, the broad angular distribution of protons induces a smoothed angular distribution of forward-directed neutron emissions, resulting in similar neutron spectra between 0° and 45°.

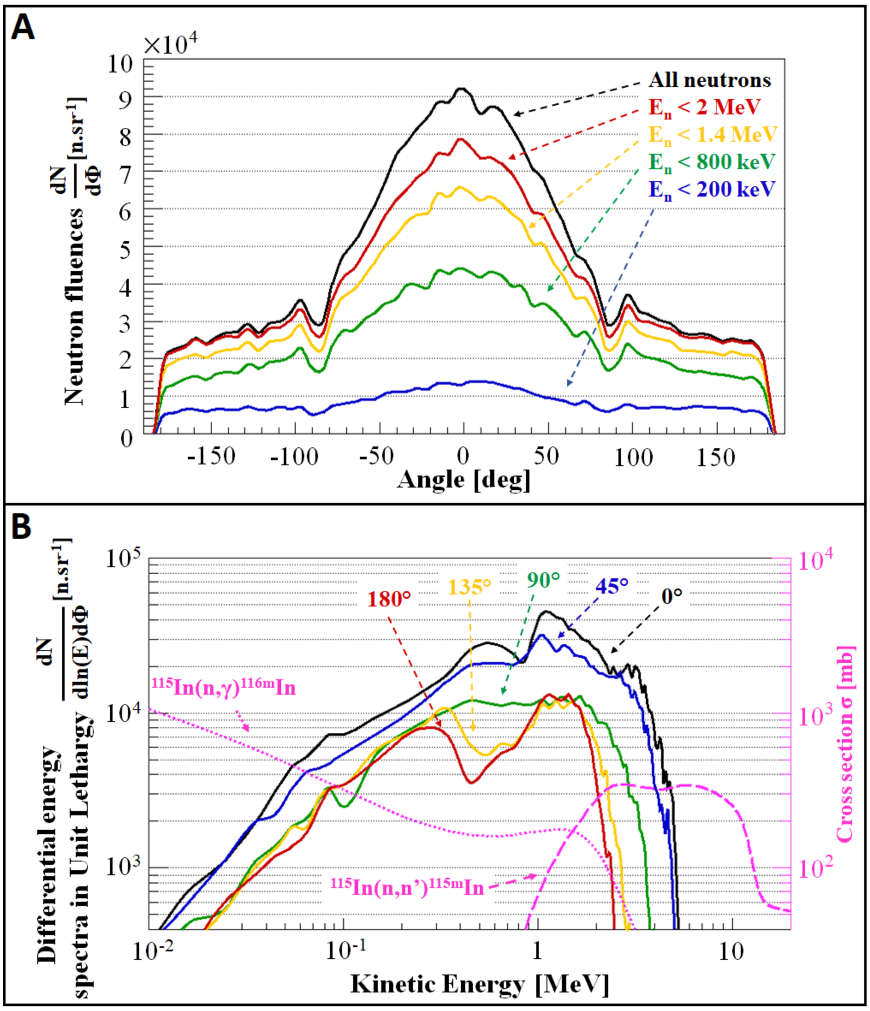

Figure 3.4 – (A) Simulated angular distribution of the neutron emissions recorded in the equatorial plane, and (B) differential energy spectra, in unit lethargy, obtained at different angles from Geant4 simulations. Overlaid are the cross sections (in pink) of the ^{115}In(n,γ)^{116m}In and ^{115}In(n,n')^{115m}In reactions, according to the IRDFF-II library. These are used for the activation simulations.

Additional simulations indicate that the ^{7}Li(p,n)^{7}Be reaction is responsible for all neutron emissions. This is due to a much lower cross section for the ^{19}F(p,n)^{19}Ne reaction, its higher threshold energy of 4 MeV, and the fact that protons above 4 MeV account for only 3% of the total number of protons emitted.

Thus, the total number of neutrons calculated by the simulations is 5.44×10^{5} neutrons/shot, corresponding to a simulated ^{7}Be activity of 0.082 Bq/shot, determined by the following equation:

$$A_{sim} = \lambda N_{Be-7} = \frac{\ln(2)}{T_{1/2}} N_{tot} \tag{2.23}$$

Where $T_{1/2}$ is the half-life of the ^{7}Be radionuclide (53.22 d) and N_{tot} is the total number of neutrons, corresponding to the number of ^{7}Be nuclei, $N_{Be\text{-}7}$, produced in the converter.

The simulations also yield a fluence of up to 9.20×10^{4} neutrons/sr/shot at 0°, with a mean value of 5.42×10^{4} neutrons/sr/shot in the specific solid angle covered by the indium sample (~ 2π sr). This value and the corresponding neutron spectrum were used to perform activation simulations of the indium sample using MCNP6 with the IRDFF-II library, which is more appropriate for such modeling than the libraries available in Geant4 (see Section 2.2.2). This led to a ^{115m}In activity of 0.025 Bq/shot and a ^{116m}In activity of 0.274 Bq/shot.

3.1.3 Analysis and results

nToF measurements:

Despite efforts to optimize the lead shielding of the scintillators, the gamma-ray flash remained too intense, and the neutron signal too weak, preventing the observation of significant pile-up signals. As shown in Figure 3.5, a few neutrons were detected sporadically, but not enough for proper spectrum reconstruction.

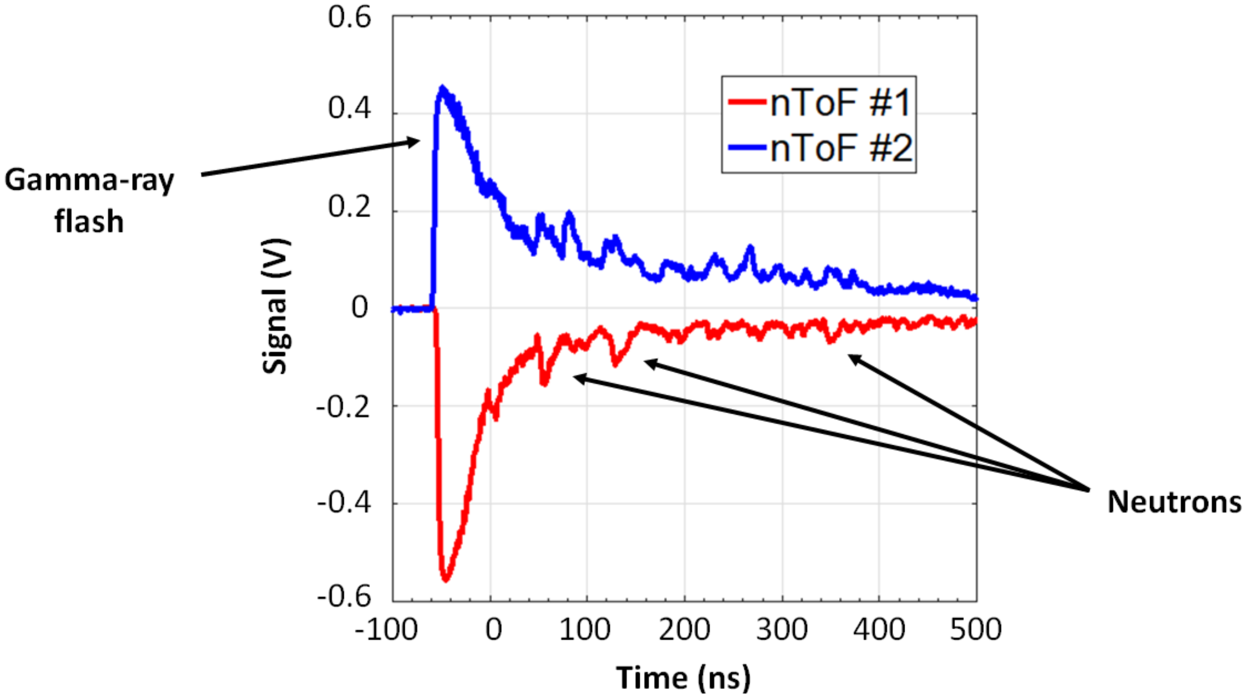

Figure 3.5 – nToF signals obtained by the scintillator placed at 4 m (red) and 1.8 m (blue) from the converter. The signals are measured in negative voltage, the blue signal was inverted for better visibility.

Activation measurements:

A 2×2" NaI gamma spectrometer, shielded by 10 cm thick lead bricks, was used to experimentally measure the activation of the converter and the indium sample. The efficiency calibration of the spectrometer was performed using the efficiency transfer method described in Section 2.2.2. This involved using a ^{152}Eu calibration point source in combination with Geant4 simulations to extrapolate the calibration to the geometries of the LiF converter and indium sample.

The LiF converter was used during a series of 292 shots to accumulate a measurable ^{7}Be activity (see Figure 3.6.A). The gamma spectrometry measurement, using equation (2.12), revealed an activity of 0.072 ± 0.009 Bq/shot. Since the number of ^{7}Be nuclei is equivalent to the number of neutrons emitted, we can infer a total neutron production of $(4.76 \pm 0.62)\times10^{5}$ neutrons/shot, which is 12.5% lower than the 5.44×10^{5} neutrons/shot obtained from the Geant4 simulations.

The indium sample was placed behind the LiF converter (see Figure 3.1.B), during the same series of 292 shots. Both ^{115m}In and ^{116m}In activities were measured by gamma spectrometry (see Figure 3.6.B), yielding activities of 7.89 ± 2.47 Bq and 39.56 ± 11.68 Bq, respectively. Given the nearly flat cross-section profile of the ^{115}In(n,n')^{115m}In reaction between 2 and 10 MeV (see Figure 3.4.B), the neutron fluence in this energy range can be evaluated using equation (2.14).

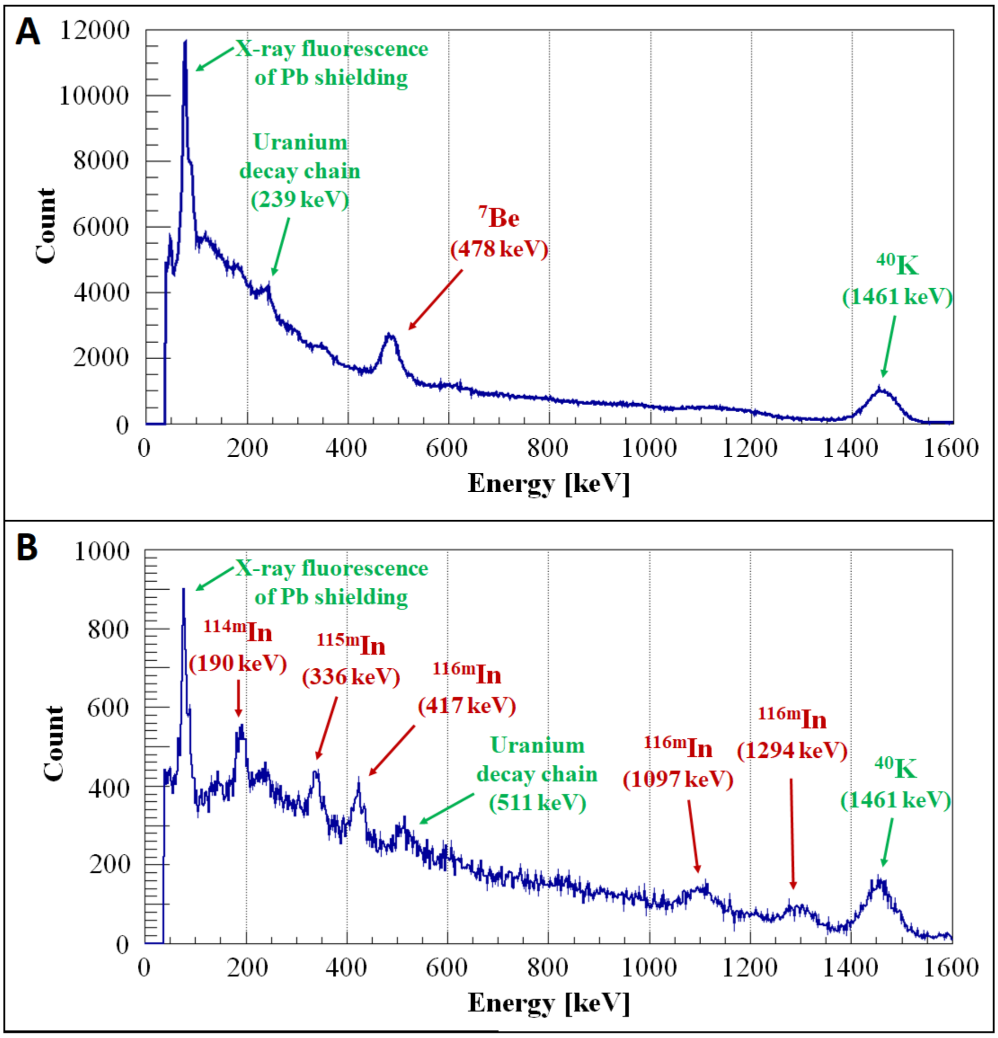

Figure 3.6 – Gamma-ray spectra emitted from the LiF converter (A) and the indium sample (B), obtained after acquisition times of 4.9 and 2.4 hours, respectively. The peaks indicated by green arrows originate from background noise, caused by the presence of uranium and potassium in the soil and concrete walls, as well as from the excitation of the lead shielding by the gamma-rays. In the following analyses, ^{114m}In nuclei were not considered, as this radioisotope can be produced by two reactions – ^{113}In(n,γ)^{114m}In and ^{115}In(n,2n)^{114m}In – making it impossible to distinguish between their respective contributions.

Thus, the ^{115m}In measured activity of 0.013 Bq/shot corresponds to a neutron fluence of (6.99 ± 2.19)×10^3 neutrons/sr/shot between 2 and 10 MeV, within the specific solid angle covered by the indium sample. This is very close to the fluence of 6.76×10^3 neutrons/sr/shot predicted by the simulations (and normalized by the ^{7}Be activity measurement) for the same energy range and solid angle. The measurement therefore confirms the proportion of around 1.45% of neutrons above 2 MeV obtained by the simulations.

However, as shown in Table 3.1, the ^{115m}In simulated activity (0.022 Bq/shot) is approximately twice as high as the measured value, which contradicts the good agreement between the evaluated and simulated fluences. This discrepancy is due to an inaccurate evaluation of the cross sections of the ^{115}In(n,n')^{115m}In reaction by the IRDFF-II library for neutrons below 2 MeV, leading to an overestimation of the simulated activity. This was confirmed by the experiment conducted at the AMANDE facility (see Section 2.2.2), where indium samples were irradiated by monoenergetic neutrons. A comparison between the measured and simulated activities revealed an overestimation of the simulated activities, particularly for neutrons between 0.565 and 1.2 MeV. Nevertheless, if only neutrons above 2 MeV are considered in the activation simulations, the resulting ^{115m}In activity si 0.011 Bq/shot, which aligns more closely with the measured activity.

The comparison between the measured and simulated ^{116m}In activities is also presented in Table 3.1. The measured activity is about four times lower than expected, indicating that, considering the cross section distribution of the ^{115}In(n,γ)^{116m}In reaction, the actual low-energy part of the neutron spectrum appears to be reduced compared to the predictions from the simulations. In summary, these activation measurements suggest that fewer neutrons are emitted in the lower energy part of the neutron spectrum, while the proportion of high-energy neutrons (> 2 MeV) is in a good agreement with the simulations.

Reaction	**A_{sim}/shot (Bq)**	**A_{meas}/shot (Bq)**	**Measurement uncertainty**
^{7}Li(p,n)^{7}Be	0.082	0.072	13.0%
^{115}In(n,γ)^{116m}In	0.240	0.065	29.5%
^{115}In(n,n')^{115m}In	0.022	0.013	31.3%

Table 3.1 – Comparison between the simulated activities, A_{sim}, and the measured activities, A_{meas}, after the last laser shot of the series. The simulated activities of the ^{115m}In and ^{116m}In were normalized by the measured ^{7}Be activity (i.e. by a factor of 0.875), to account for the actual neutron production being 12.5% lower than the simulated predictions. The measurement uncertainties are calculated from equation (2.13).

Bubble detectors:

BDT and BD-PND bubble detectors were placed outside the target chamber, along the target normal axis (0°), at 60 cm from the LiF converter (see Figure 3.1.B) and during the same series of 292 laser shots as before.

The BDT detectors revealed no bubble, indicating that thermal neutron emissions are negligible. This result is consistent with the simulated neutron spectra, which show a significant and continuous decrease in the spectrum as neutron energy decreases. In contrast, bubbles were observed in the BD-PND detectors. Considering their quasi-energy-independent response to neutrons from 200 keV to around 15 MeV, the bubble count resulted in a neutron fluence, according to equation (2.2), of (1.37 ± 0.15)×10^5 neutrons/sr/shot in this energy range. This neutron fluence is 70% higher than the expected fluence obtained with the Geant4 simulations (normalized by the ^{7}Be activity measurement). Since the total neutron production was consistent with the simulations, this could indicate that the neutron emissions were more forward-directed than predicted by the simulations.

Figure 3.7 – Bubble detectors used during the experiment. Eight BD-PND were placed simultaneously at the same position to increase the total number of bubbles produced and reduce the statistical error.

In summary, the various diagnostics used enabled the first experimental characterization of neutron emissions generated through the pitcher-catcher technique in a high repetition rate TNSA regime operating at 0.5 Hz, which produces laser-based ion acceleration through the interaction of a high-power laser and thin-foil solid targets.

The measurement of ^{7}Be activity resulting from proton interaction with the LiF converter led to an estimation of total neutron production of $(4.76 \pm 0.62)\times10^5$ neutrons/shot, which is 12.5% lower than the simulation predictions. The indium sample, measured by gamma spectrometry, indicated a neutron fluence of $(6.99 \pm 2.19)\times10^3$ neutrons/sr/shot between 2 and 10 MeV, with fewer low-energy neutrons compared to the simulations. This was corroborated by the absence of bubbles in the BDT detectors. However, the BD-PND detectors showed bubbles, leading to a neutron fluence of $(1.37 \pm 0.15)\times10^5$ neutrons/sr/shot between 200 keV to around 15 MeV, along the normal axis (0°).

Hence, these quantitative results, summarized in Table 3.2, suggest that only fast neutrons were produced by this laser-driven neutron source, with a higher-than-expected emission in the forward direction and a sharper energy distribution between a few hundred keV and 2 MeV, while neutron emissions above 2 MeV are consistent with the simulations. Insights into potential applications enabled by such neutron emissions will be discussed in detail in Section 4.

Quantity	**Energy range**	**Φ_{sim}**	**Φ_{meas}**	**Measurement uncertainty**
Total neutron yield (n/shot)	All neutrons	5.44×10^5	4.76×10^5	13.0%
Neutron fluences (n/sr/shot)	~ 0.025 eV	0	0	-
	[2-10 MeV]	6.76×10^3	6.99×10^3	31.3%
	[0.2-15 MeV]	8.05×10^4	1.37×10^5	10.9%

Table 3.2 – Summary of the neutron emission measurements, showing both the simulated Φ_{sim} and measured Φ_{meas} total neutron yields, along with neutron fluences between 2 and 10 MeV obtained from the indium sample, and between 200 keV and 15 MeV as measured by the bubble detectors.

3.2 Neutron production at the Apollon facility – Secondary beam (F2)

As mentioned earlier, most of the characterization of laser-driven neutron emissions was so far performed using large-scale, low repetition rate (typically 1 shot/hour) and high-energy (tens or hundreds of Joules) lasers. Therefore, the Apollon laser delivering intermediate energies and repetition rate was used to produce neutrons, aiming to gather more information about how neutron production evolves with varying laser energy and the energy distribution of neutrons generated by such lasers. The experiment also aimed to use thinner targets by improving laser contrast, which reduces X-ray emissions but also the laser on-target energy, and to assess how this affects the neutron/X-ray ratio.

3.2.1 Experimental setup

The experiment was conducted using the secondary laser beam (F2) in the short focal area (SFA) of the Apollon laser facility in Saclay, France [116]. This beam uses a Ti:Sapphire laser, operating at a repetition rate of up to 1 shot/min. The F2 beam delivers pulses of 24 fs duration, a mean on-target energy of 10.9 J and a central laser wavelength of 815 nm, spanning from 750 to 880 nm. The 140 mm diameter beam was focused using an f/3 off-axis parabola (OAP), inducing an elliptical focal spot with dimensions of 2.8 × 3.7 µm FWHM, which contains 42% of the total laser energy, resulting in an on-target peak intensity of approximately 2×10^{21} W/cm².

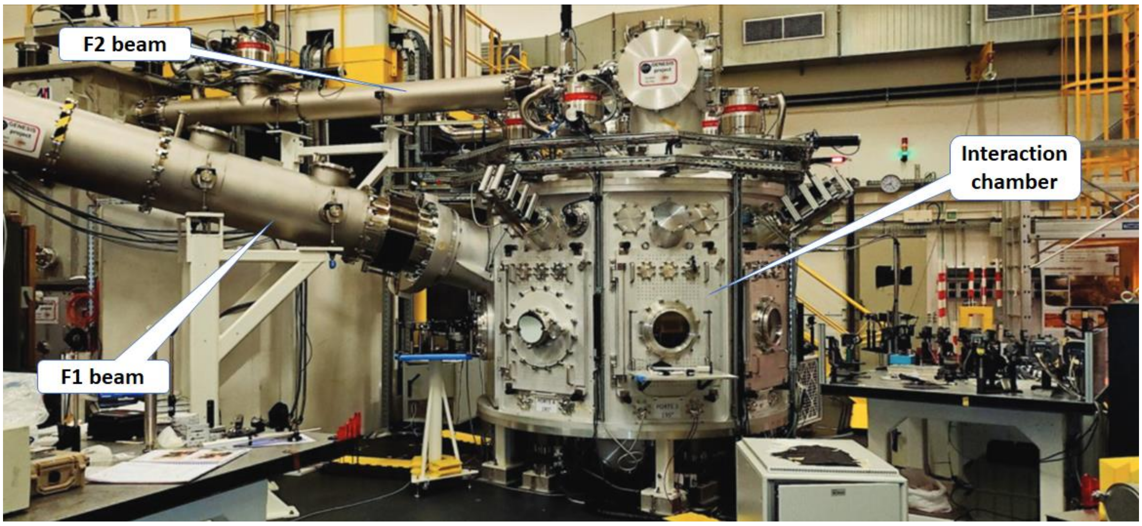

Figure 3.8 - SFA experimental room at Apollon.

The laser was used both with its inherent temporal contrast as well as with a Double Plasma Mirror (DPM) [231], which was placed inside the interaction chamber between the OAP and the target (see Figure 3.9). A plasma mirror consists of a polished glass slab through which Amplified Spontaneous Emissions (ASE) and pre-pulses are first transmitted. Then, when the main pulse arrives, the intensity increases and ionization occurs on the plasma mirror surface. As the electron density exceeds the critical density, it allows to reflect most of the main pulse, which is therefore cleared of the ASE and pre-pulses. The DPM induces a lower mean on-target energy (~ 5.7 J), due to its 52% reflectivity, but it improves the temporal contrast by reducing ASE and pre-pulses. This prevents premature heating and ionization of the target before the arrival of the main pulse, thereby allowing to shoot on thinner targets thanks to the improvement of the laser/target coupling.

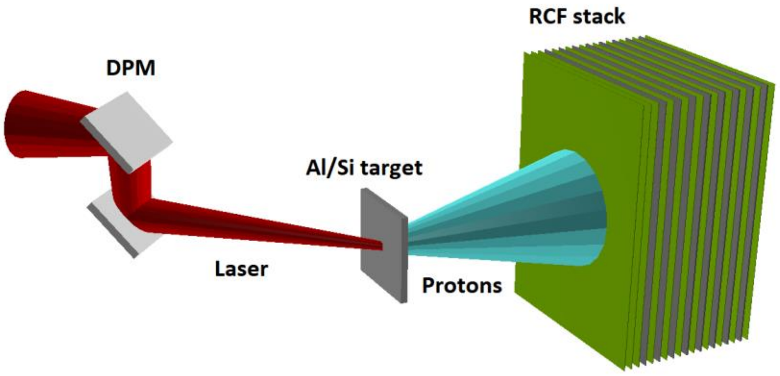

Figure 3.9 – Experimental setup of proton acceleration.

The beam was focused on targets with an 45° incidence angle. Different targets were used: 0.8 µm, 1.5 µm and 2 µm thick aluminum targets for direct shots (without the DPM), and thinner silicon targets, from 20 nm to 300 nm, for shots with the DPM. The produced protons were accelerated from the rear surface of the target using the TNSA mechanism, achieving energies up to 25.3 MeV in direct shots and 35.2 MeV during DPM shots.

As shown in Figure 3.9, proton spectra were measured using stacks of EBT3 Gafchromic RadioChromic Films (RCF) [232] and aluminum filters, placed at 25 mm from the target. A deconvolution was done from the doses obtained on each RCF films to retrieve the proton spectra. Figure 3.10 show two typical proton spectra produced during direct and DPM shots. The proton spectra are well-fitted by exponential functions considering the following equation:

$$\frac{dN}{dE}(E \leq E_{max}) = \frac{N_p}{E_0} exp\left(-\frac{E}{E_0}\right) \tag{2.24}$$

Where N_p is the total proton number, E_0 is the slope of the spectrum and E is the proton energy.

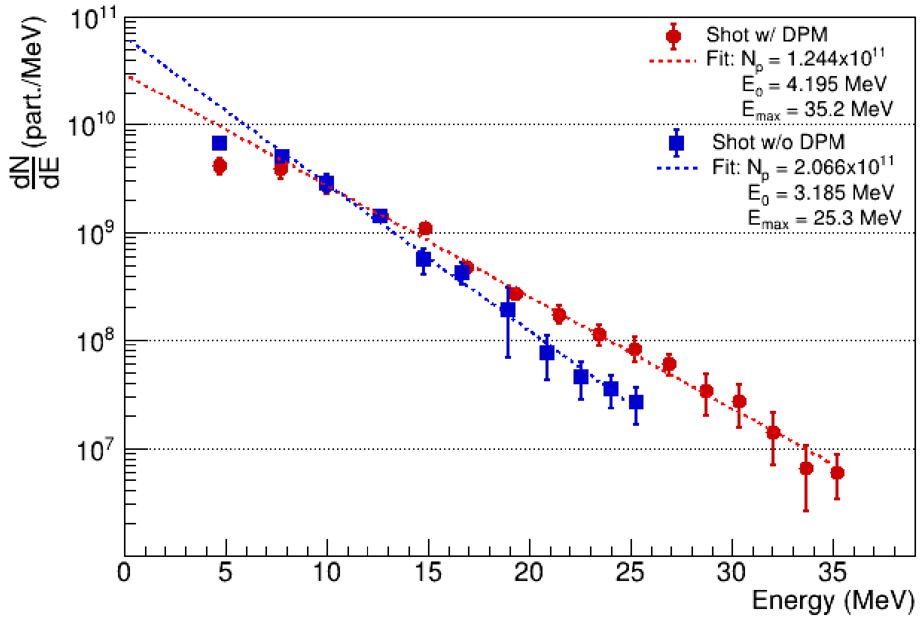

Figure 3.10 – Measured proton spectra, extracted from RCF stacks, for a shot with DPM on a 200 nm Si + 50 nm Al target (red circles), and a shot without DPM on a 1.5 µm Al target (blue squares). Respective exponential fits are represented by dashed lines. The error bars reflect the uncertainties associated with the calibration of the RCF film responses.

The first RCF films were not considered for the fit function calculation because proton divergence is higher at low energies and a significant portion of the proton beam is not recorded in the films, so the values obtained with these films are certainly underestimated. Additionally, a quenching effect can also occur for low-energy protons, causing the first RCF films to under-respond [233]. Thus, including these films in the fit function calculation would result in an underestimation of the total proton number N_p of 28% for the direct shot and 21% for the DPM shot, as well as an overestimation of the slope E_0 of approximately 5% in both cases.

Despite reducing the on-target energy by nearly a factor of 2, the measured proton spectra show that the DPM allows for higher maximum proton energies while maintaining a similar total proton number compared to shots without the DPM. This indicates that the DPM significantly enhances conversion efficiency by improving the laser/target interaction [117].

To produce neutrons, the RCF stack was replaced by a LiF converter, positioned 15 mm behind the TNSA target (see Figure 3.11). As in the neutron production experiment performed at ALLS, this low-Z converter was chosen to benefit from the favorable cross sections of (p,n) reactions, especially for low proton energies (< 10 MeV), which account for more than 90% of the protons generated in this experiment. The converter was 4 mm thick, which ensures that all protons with energies below approximately 30 MeV are absorbed. Most neutrons were produced via the ^{7}Li(p,n)^{7}Be reaction (see Section 3.2.2); the ^{19}F(p,n)^{19}Ne reaction produced much fewer neutrons due to lower cross sections and a higher threshold energy (as shown in Figure 3.1.C).

The neutron emissions were characterized using the same diagnostics as in the ALLS experiment: bubble detectors, scintillators used as nToF detectors, activation samples and direct measurement of the total neutron production by assessing the activity of the ^{7}Be residual nuclei inside the LiF converter. Two types of bubble detectors were used: BD-PND detectors, sensitive to neutrons from 200 keV to around 15 MeV, and a bubble detector spectrometer (BDS), which can reconstruct neutron spectra between 10 keV and 20 MeV (see Section 2.1.2).

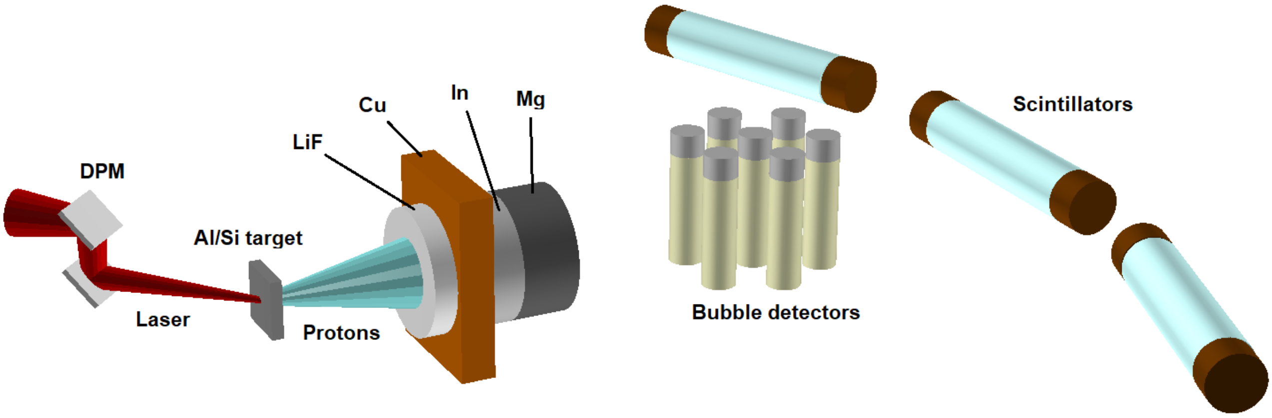

Figure 3.11 – Schematic view of the setup and diagnostics used during neutron production with the DPM.

The same PVT-based scintillators described in Section 3.1.1 were used at the Apollon facility. However, the measured signals were here digitized at a sampling frequency of 500 MHz using a CAEN VX1730B digitizer [234]. To prevent saturation effects caused by X-rays emitted during the laser/target interaction, the scintillators were shielded with 15 cm thick lead bricks on the front face and 5 cm thick lead bricks on the top, bottom and rear faces.

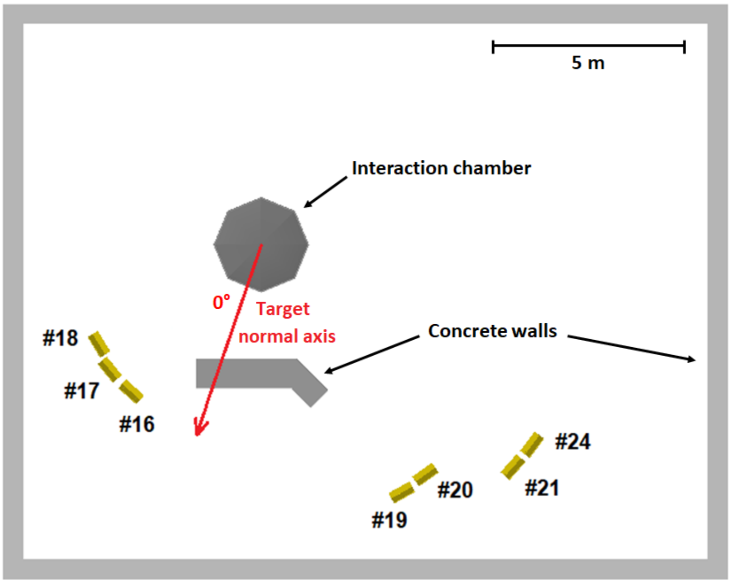

Figure 3.12 – Experimental room with the position of the nToF detectors inside lead shielding (in yellow), the interaction chamber and the concrete walls. The concrete wall near the interaction chamber is an additional radiation shield protecting the users working in the adjacent room. The target normal axis, corresponding also to the main axis of proton emission, is represented by the red arrow.

Additionally, three different activation samples were used: copper, indium and magnesium, selected according to the criteria described in Section 2.2.1. These samples were positioned directly behind the LiF converter (as shown in Figure 3.11) to capture as many neutrons as possible and maximize the activation. Note that some of these samples (copper and magnesium) were not part of the final SPAC composition. Indeed, this experiment was conducted before the final selection of the SPAC samples, allowing us to test activation samples that were potential candidates.

Copper was initially selected thanks to the ^{63}Cu(n,γ)^{64}Cu reaction, which can be induced without a threshold energy, making it useful for characterizing low-energy neutrons. The resulting radionuclide, ^{64}Cu, has a half-life of 12.7 hours and decays via positron emission producing 511 keV gamma-rays with an intensity of 35%. The ^{24}Mg(n,p)^{24}Na reaction, that can be induced in the magnesium sample, produces ^{24}Na which emits 1369 keV gamma-rays with an intensity of 99.99% and a half-life of 14.96 h. This reaction has a threshold energy of around 5 MeV and a maximum cross section at 13 MeV, allowing to detect neutrons with higher energies compared to the ^{115}In(n,n')^{115m}In reaction induced in the indium sample and described earlier.

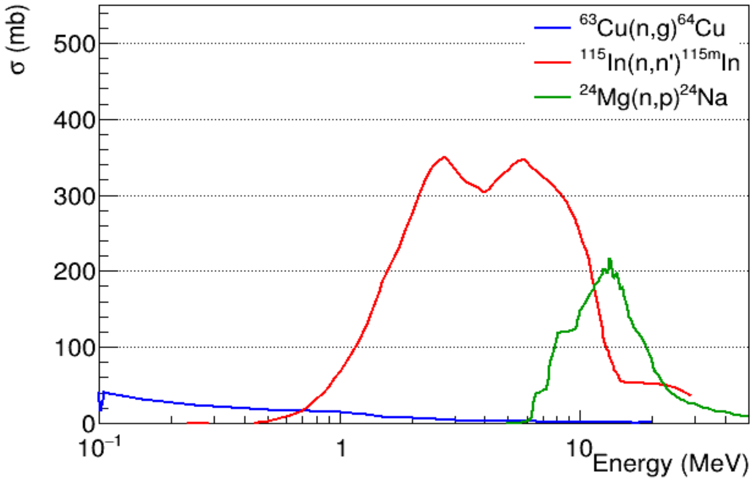

Figure 3.13 – Experimental cross sections of neutron-induced reactions in the activation samples, according to the EXFOR database.

A modeling of the NaI spectrometer used for gamma spectrometry was made using Geant4, to optimize the thickness of the samples and minimize self-attenuation effects of gamma-rays during measurements. Simulations considered various thicknesses for the three samples, ranging from 3 to 30 mm. The optimized thicknesses determined were 6 mm for the copper and indium samples and 10 mm for the magnesium sample.

Finally, X-ray emissions from the laser/target interaction were measured using a set of GD-351 radio-photo-luminescent dosimeters [235]. These dosimeters were positioned around the target in the equatorial plane at distances ranging from 87 cm to 115 cm. Encapsulated in 1.5 mm thick tin holders, the dosimeters were sensitive to X-rays in the energy range from approximately 30 keV to a few MeV, with an energy-independent response. The tin holder also protected the dosimeters from protons up to 23 MeV and electrons up to 1.5 MeV by absorbing these particles and preventing them from depositing energy into the dosimeters.

3.2.2 Monte Carlo simulations

Simulations were carried out, using the Monte Carlo transport code Geant4, to estimate the total number of neutrons and the angular distribution of these emissions resulting from the interaction of proton beams, which we experimentally characterized, with the LiF converter. Averaged proton spectra over 13 and 8 shots, obtained respectively from direct and DPM shots, were used to simulate the neutron emissions, in order to take into account the shot-to-shot variability of the laser/target interaction and the proton beam.

These protons were injected into a simulated 4 mm thick LiF converter and virtual detectors allowed to derive the neutron fluence at different angles and the total number of neutrons emitted. The aluminum chamber and the concrete walls (see Figure 3.12) were also considered in the simulations to more accurately reflect the experimental conditions.

Figure 3.14 displays the simulated neutron fluences at different angles for direct and DPM shots. The neutron emissions are very similar in both cases and nearly isotropic. A dip at 90° can be observed, this is due to the diameter of the LiF converter (22 mm) which is greater than its thickness Consequently, neutrons emitted transversally must traverse more material to exit the converter, leading to more deflection or absorption of neutrons.

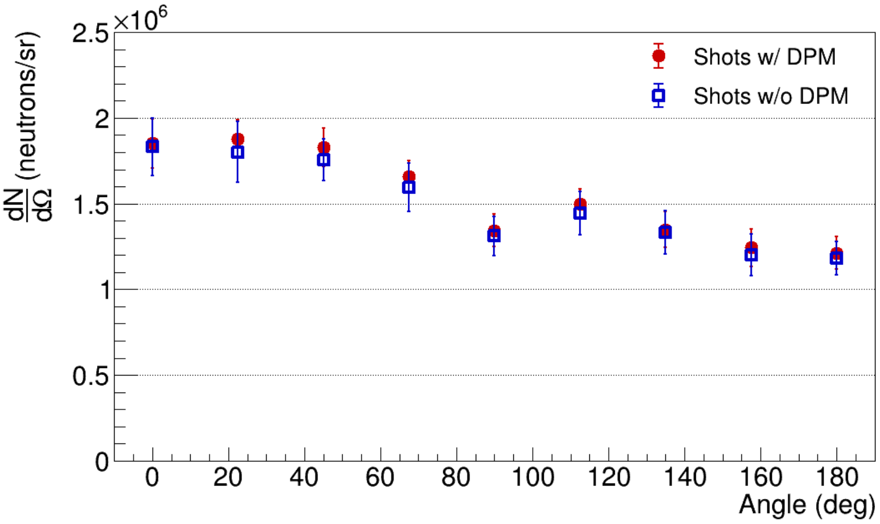

Figure 3.14 – Neutron fluences at different angles obtained from the Geant4 simulations for direct and DPM shots. The error bars correspond to the standard deviations of the values obtained considering the different proton spectra used in the simulations, i.e. considering the observed shot-to-shot variability of the proton beam.

Figure 3.15 shows the simulated neutron spectra obtained in the forward direction (rear surface of the converter) and the backward direction. We see that the most energetic neutrons are preferentially emitted forward, which agrees with the kinematics of the interactions. The total number of neutrons computed by these simulations was (2.69 ± 0.24)×10^7 neutrons/shot in the direct shot configuration and (2.78 ± 0.18)×10^7 neutrons/shot when the DPM is used. The given errors are defined as the standard deviations of the values obtained considering the different proton spectra used in the simulations, reflecting the observed shot-to-shot variability of the proton beam. As depicted in Figure 3.15, the simulated neutron spectra obtained with and without the DPM are very similar, indicating that the DPM does not significantly affect the neutron emissions.

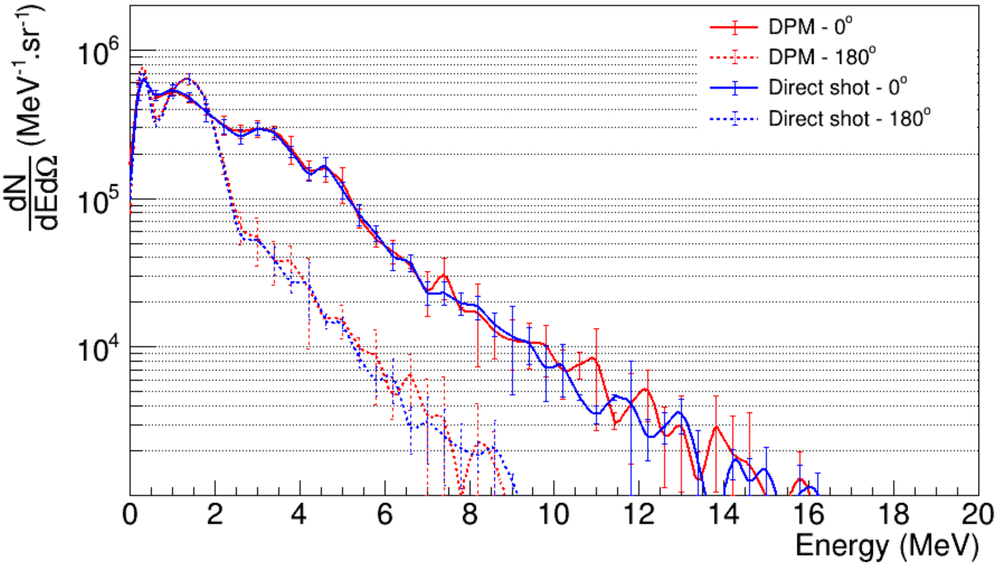

Figure 3.15 – Simulated energy differential neutron spectra in the forward (0°) and backward (180°) directions for shots with and without DPM.

Additional simulations were made to determine the number of neutrons produced exclusively from the Li nuclei. These numbers were found to be (2.52 ± 0.23)×10^7 neutrons for direct shots and (2.60 ± 0.17)×10^7 neutrons for shots with DPM, corresponding to ^{7}Be activities of 3.80 ± 0.34 Bq and 3.92 ± 0.25 Bq, respectively. Thus, the neutrons are mainly produced from the Li nuclei, which contribute to around 93.5% of the neutron emissions, the rest being generated by the ^{19}F(p,n)^{19}Ne reaction.

The simulated neutron spectra in the forward direction were used to predict the induced activities inside the activation samples via MCNP6 with the IRDFF-II library. The results are compared with the experimental measurements in Table 3.4. Geant4 was employed to simulate the nToF signals of the scintillators considering the simulated neutron spectra obtained at different angles. The concrete walls, the aluminum chamber and lead shielding were considered to take into account the influence of neutron scattering on the nToF signals. Scintillation processes were modeled according to a previous energy calibration performed using a ^{137}Cs source [236], allowing to obtain simulated nToF signals in mV, which can be directly compared to the measured nToF signals (see Section 3.2.3).

Further simulations involving monoenergetic neutrons were also carried out to determine the response function of the scintillators. Due to the temporal characteristics of the scintillators, the signal from monoenergetic neutrons extends over a time interval longer than the corresponding Time of-Flight (ToF) (see Section 2.1.3). Thus, the contribution of neutrons of specific energies to different ToF intervals and lower energies was assessed and will be factored into the unfolding procedure, as described in equation (2.8), to derive neutron spectra from the measured nToF signals.

3.2.3 Analysis and results

Activation measurements:

The LiF converter and activation samples were measured by gamma spectrometry using a 3×3” NaI scintillator shielded by 10 cm of lead and a layer of copper to absorb the fluorescence X-rays emitted by the lead shielding. The gamma-ray emission spectra were digitized with a Canberra OSPREY Multi-Channel Analyzer (MCA) and analyzed using Genie2000 software, which allows background noise subtraction and peak fitting.

Since the indium and magnesium samples were previously used in the SNAC2 activation spectrometer, the efficiency calibrations associated to the measurement of these samples were already determined. This was achieved through a dissolution procedure conducted by the Laboratoire National Henri Becquerel (LNHB, CEA). Initially, the samples were measured with our NaI gamma spectrometer before being sent to LNHB. At LNHB, the samples were dissolved in suitable acids, placing the radionuclides of interest into solution within containers with well-characterized self-absorption properties. This process allows for precise measurement of radionuclide activity. By comparing the activities induced in these samples with those measured by our gamma spectrometer, efficiency calibrations for each sample were performed.

For the copper sample and the LiF converter, the efficiency calibrations were performed using the efficiency transfer method, described in Section 2.2.2, using a ^{152}Eu calibration point source and Geant4 simulations. Thus, a LiF converter, on which we cumulated neutrons produced during 20 direct shots as well as 20 DPM shots, was measured by gamma spectrometry, resulting in an activity of ^{7}Be of 221.3 ± 12 Bq. This corresponds to the production of $(3.67 \pm 0.20)\times10^{7}$ neutrons/shot from the Li nuclei, which contribute to 93.5% of the neutron production (see Section 3.2.2). The total number of neutrons produced during these shots is therefore $(3.93 \pm 0.21)\times10^{7}$ neutrons/shot. This value is, on average, 1.46 and 1.41 times higher than the simulation predictions for a direct shot and a DPM shot, respectively (as shown in Table 3.3).

	A/shot (Bq)	**$N_{Be\text{-}7}$/shot**	**$N_{neutrons}$ (n/shot)**	**Uncertainty**
Simulation (Direct shots)	3.80	2.52×10^{7}	2.70×10^{7}	9.02%
Simulation (DPM shots)	3.92	2.60×10^{7}	2.78×10^{7}	6.47%
LiF converter measurement	5.53	3.67×10^{7}	3.93×10^{7}	5.44%

Table 3.3 – Simulated and measured activities, as well as number, $N_{Be\text{-}7}$, of ^{7}Be nuclei residuals produced during a series of direct and DPM shots. The total neutron production per shot is also shown with the associated relative uncertainty calculated from equation (2.13) for the measurement, and corresponding to the shot-to-shot variability of the proton beam for the simulation results.

Activation samples were used in two separate series, one of 20 direct shots and the other of 5 DPM shots. In both cases, we accumulated the activation to increase the probability of obtaining measurable activities. Table 3.4 presents the results of the gamma spectrometry measurements of these samples and compares them with the simulated values. Since these results are averaged over several shots, they are affected by the decay of radionuclides between shots. Therefore, a correction was applied to account for the mean decay time between shots, given the repetition rate of approximately one shot every 8 minutes.

No measurable activation was induced in the magnesium sample, either during direct or DPM shots. This indicates that neutrons with energies above 5 MeV are produced in insufficient quantities to induce measurable activities, as predicted by the simulations.

The activation of the copper sample, measured via the annihilation peak (producing gamma-rays of 511 keV), is significantly higher than the simulated value. This discrepancy could partly be due to a greater number of low-energy neutrons emitted compared to the simulation predictions. Additionally, as shown in Figure 3.11, the copper sample was not fully covered by the LiF converter and, due to the divergence of the protons, some of them were able to directly interact with the copper sample.

Geant4 simulations were therefore made considering the direct interaction of protons with the copper sample. These simulations revealed the possibility of producing ^{64}Cu nuclei via the ^{65}Cu(p,d)^{64}Cu reaction, as well as ^{63}Zn nuclei via the ^{63}Cu(p,n)^{63}Zn reaction. Since both ^{64}Cu and ^{63}Zn nuclei emit gamma-rays of 511 keV, this could potentially lead to a misinterpretation of the signal measured by gamma spectrometry. Furthermore, the simulations indicated that the number of ^{63}Zn nuclei was approximately 31 times higher than the number of ^{64}Cu nuclei produced. Given the shorter half-life (38.47 min) of ^{63}Zn nuclei, they would be responsible for almost all of the 511 keV peak. Finally, the simulations showed that the direct interaction of just 0.3% of protons with the copper sample would be sufficient to induce the measured peak. This finding aligns with expectations regarding the interaction of a small portion of the proton beam with the copper sample.

	Reaction	A_{sim}/shot (Bq)	A_{meas}/shot (Bq)	Uncertainty
Direct shots	^{63}Cu(n,γ)^{64}Cu	0.22	18.98	6.84%
	^{115}In(n,n')^{115m}In	1.58	1.15	13.66%
	^{24}Mg(n,p)^{24}Na	0.02	< DL*	-
DPM shots	^{63}Cu(n,γ)^{64}Cu	0.21	< DL*	-
	^{115}In(n,n')^{115m}In	1.56	0.77	36.75%
	^{24}Mg(n,p)^{24}Na	0.02	< DL*	-

Table 3.4 – Measured activities, A_{meas}, in direct and DPM mode, and the corresponding uncertainties calculated from equation (2.13). A_{sim} are the simulated activities calculated in Section 3.2.2 from the spectra presented in Figure 3.15. These simulated activities were normalized by the number of ^{7}Be nuclei observed (i.e. 1.46 and 1.41 times, for direct and DPM shots, respectively), to consider the actual neutron production.

**DL: Detection Limit*

The discrepancies between the simulated and measured activities of ^{115m}In can be explained by inaccuracies in the evaluation of the cross sections of the ^{115}In(n,n')^{115m}In reaction in the IRDFF-II library, which tends to overestimate the expected activities. On the other hand, the activities obtained from direct and DPM shots are comparable, with overlapping uncertainties suggesting similar neutron emissions during these two shot configurations.

The activity of ^{116m}In nuclei, produced through the ^{115}In(n,γ)^{116m}In reaction, was not measured because the time between the last laser shot and the measurements was too long (several hours), leading to significant decay due to the short half-life (54 min) of this radionuclide. Finally, neutron fluences between 2 and 10 MeV can be inferred from the ^{115m}In activities using equation (2.14). Thus, $(1.69 \pm 0.37)\times10^6$ neutrons/sr/shot were obtained for direct shots and $(1.14 \pm 0.51)\times10^6$ neutrons/sr/shot for DPM shots.

<u>Bubble detectors:</u>

The BDS bubble spectrometer and BD-PND bubble dosimeters were placed inside the interaction chamber, along the target normal axis (0°), at 20 and 60 cm from the converter, respectively. The calibration of bubble detectors composing the bubble spectrometer was verified at the CEZANE facility (IRSN, Cadarache) using a ^{252}Cf neutron source. Significant discrepancies were found compared to the calibrations provided by the supplier, *Bubble Technology Industries*, with some detectors showing an overestimation of response by a factor of more than 10. The results are presented in Appendix C. Thus, the new calibration values will be used in the following analyses.

The BD-PND were employed during the same series of direct and DPM shots as those where the activation samples were used. The results obtained with these BD-PND indicate neutron fluences of $(4.38 \pm 0.76)\times10^6$ neutrons/sr/shot for the direct shots and $(4.72 \pm 1.93)\times10^6$ neutrons/sr/shot for the DPM shots. Thus, the neutron fluences obtained during the direct and DPM shots are very close, which supports the hypothesis of similar neutron production during these two shot configurations.

However, these neutron fluences are much higher than those obtained with the indium samples (i.e. $(1.69 \pm 0.37)\times10^6$ and $(1.14 \pm 0.51)\times10^6$ neutrons/sr/shot for the direct shots and the DPM shots, respectively). This may be mainly due to the larger sensitivity range of the bubble dosimeters, from 200 keV to around 15 MeV, compared to the 2 to 10 MeV range for the indium samples. Additionally, the positions and solid angles covered by these two diagnostics can also explain this difference because the bubble dosimeters were placed at 60 cm from the converter and detected neutrons emitted at 0°, whereas the indium samples were much closer to the converter and covered a solid angle of approximately 2.3 sr. This placement reduced the average neutron fluence intercepted, considering the angular distribution of neutrons, which are preferentially emitted at 0° (see Figure 3.14), although this anisotropy in neutron emission was shown to be relatively moderate.

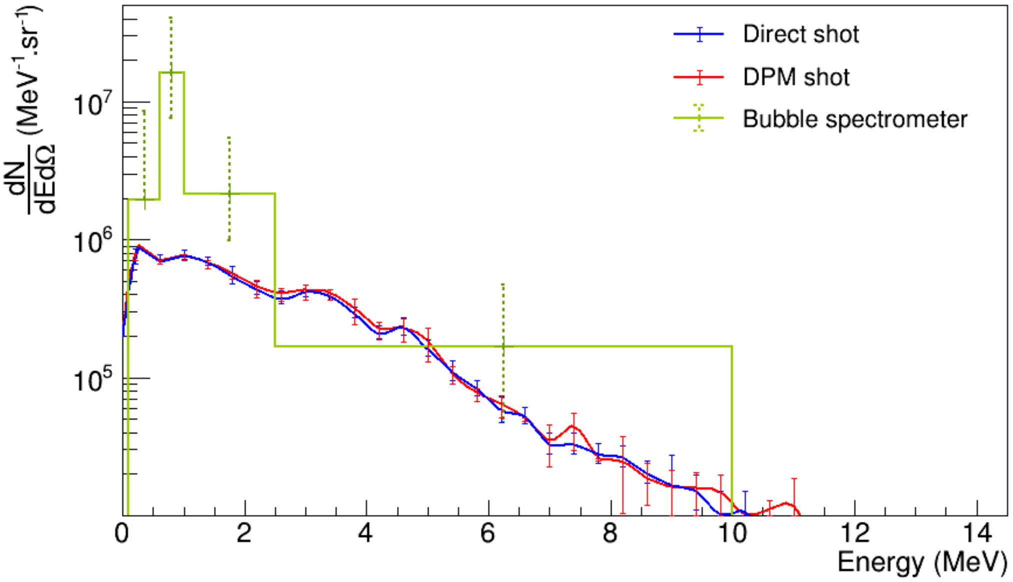

Figure 3.16 – Neutron energy spectrum measured with the bubble spectrometer (green line) during the series of direct shots, overlaid with the simulated neutron spectra for a direct shot (blue line) and a DPM shot (red line).

The integral of the expected neutron spectra (shown in Figure 3.15) for these two energy ranges and solid angles covered was calculated and suggests that there should be more than twice as many neutrons in the sensitivity range of the bubble dosimeters compared to that of the indium samples, which aligns with this explanation.

Figure 3.16 shows a comparison between the neutron energy spectrum at 0° measured with the bubble spectrometer and the simulated neutron spectra for a direct and a DPM shot, which have been multiplied, respectively, by a factor of 1.46 and 1.41 to normalize them considering the total number of neutrons observed from the ^{7}Be measurement.

The Geant4 simulations seem to underestimate the low-energy part of the neutron spectrum, especially below 2 MeV, where a difference of an order of magnitude is observed. However, due to the uncertainties associated with this measurement, the significance of this difference is limited. This discrepancy could also be partly attributed to the detection of neutrons scattered within the interaction chamber.

nToF measurements and X-ray emissions:

As shown in Figure 3.17, clear neutron signals were observed with the scintillator #16, placed at 4.95 m from the LiF converter and 19° from the normal axis (0°). Furthermore, Figure 3.17.A shows similar amplitude for the neutron signals but significant discrepancies in X-ray emissions for shots with and without DPM.

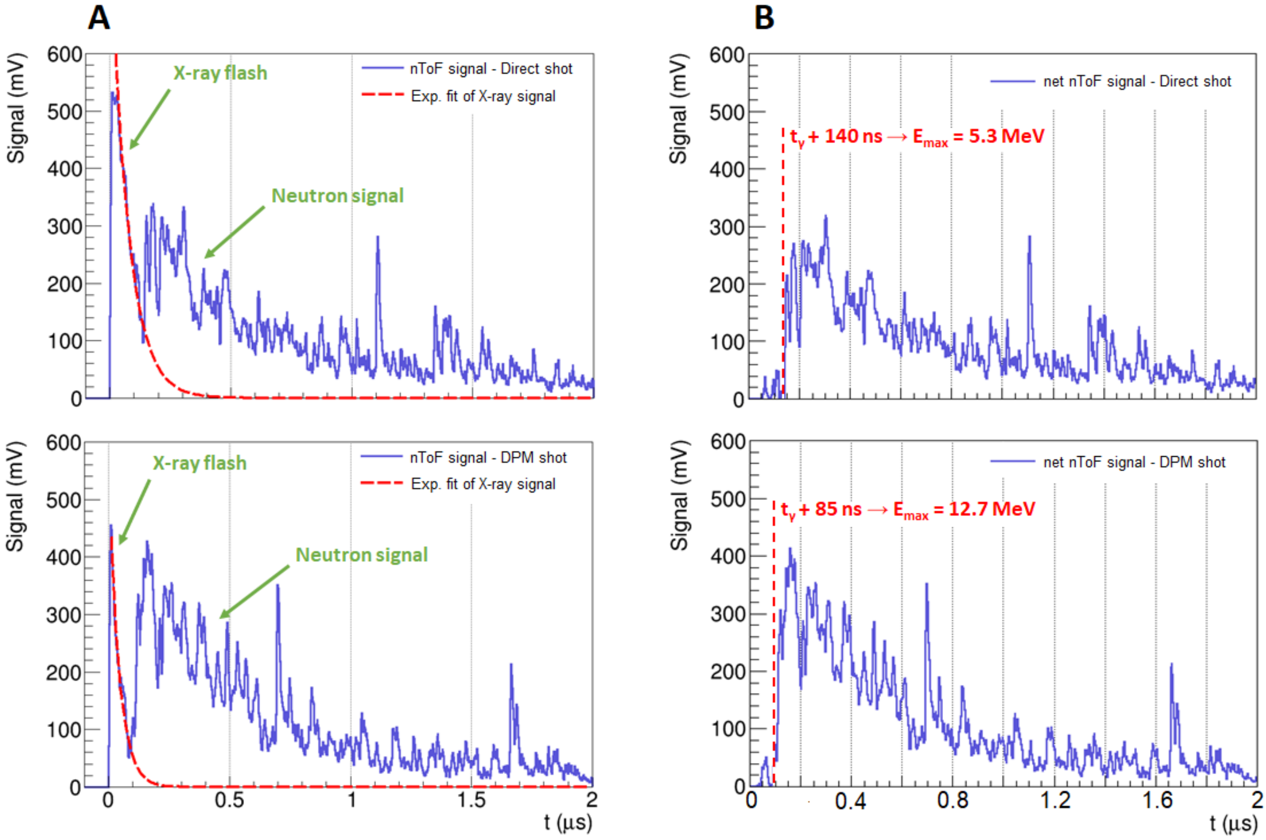

Figure 3.17 – (A) nToF signals obtained with scintillator #16. These signals were acquired during a direct shot with a 1.5 µm Al target (top) and a DPM shot with a 200 nm Si + 50 nm Al target (bottom). The exponential fits of the X-ray signals used for the background noise subtraction are shown in red dashed lines. (B) Net neutron signals obtained after removal of the signal induced by the X-rays. The red dashed lines correspond to the ToF of the most energetic neutrons detected.

The integral of the X-ray flashes was calculated to quantify the charge induced by the X-rays (considering the measured voltage over time on a 50 Ω load). This leads to a factor of around 2.5 between the direct shot and the DPM shot, with 924.6 pC and 378.9 pC, respectively. RPL dosimeters, placed at 1.15 m from the target and on the same axis as the scintillator #16, confirm this factor by measuring, respectively, doses of 16.1 μGy/shot and 5.8 μGy/shot during the series of direct and DPM shots.

In Figure 3.18, the spatial dose distributions obtained from the RPL dosimeters, during direct and DPM shots, also revealed significant differences in X-ray emissions between the two shot configurations. For direct shots, the doses are preferentially distributed in a broad lobe extending from the target normal to the laser specular reflection axis. In contrast, DPM shots produce a much narrower emission cone centered along the laser specular direction. A factor of up to 130 was measured between the doses emitted in the backward direction for direct and DPM shots, with approximately 1670 μGy and 12.8 μGy per shot, respectively.

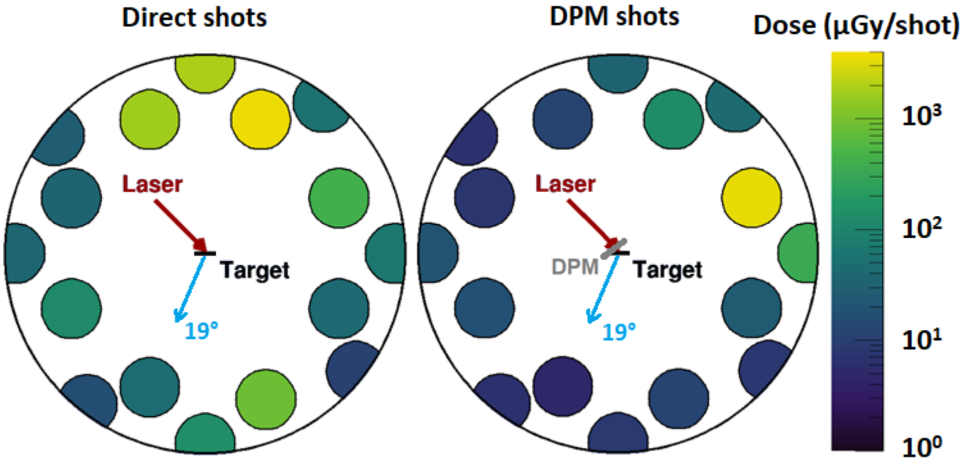

Figure 3.18 – Spatial dose distributions recorded inside the interaction chamber by the RPL dosimeters during direct shots on Al target of 0.8 μm, 1.5 μm and 2 μm thicknesses (left) and DPM shots on Si/Al targets of 150 nm, 200 nm and 250 nm thicknesses (right). Each circle represents a dosimeter, and its color corresponds to the measured dose. The outer circle in both graphs represents the actual diameter of the target chamber. The gray bar representing the DPM in the right panel is to scale.

The broad angular distribution and high doses observed in the direct shots are consistent with dominant Bremsstrahlung emission. This is likely due to the presence of a significant pre-plasma at the target front, where laser-driven electrons can recirculate and radiate [237, 238]. In contrast, the substantial reduction in dose and the directional nature of the X-ray emission in the DPM case suggest a different radiation generation mechanism. The thinner targets used with the DPM reduce the hot-electron path length in matter, thereby decreasing the probability of Bremsstrahlung. Furthermore, in high-contrast, oblique laser-solid interactions such as those with the DPM, electrons can be accelerated along the target surface to high energies, radiating predominantly in the near-surface direction [239, 240]. In addition, the laser beam reflected off the solid surface can directly accelerate some electrons [241], possibly leading to X-ray emission through betatron oscillations. Both mechanisms align well with the observed narrow cone of emission in the DPM case.

Hence, the DPM clearly influences the X-ray production, due to the possibility to shoot on thinner target inducing less X-rays. This allows to obtain a better signal-to-noise ratio for the short ToF and to measure more energetic neutrons, as shown in Figure 3.17.B, where neutrons up to 12.7 MeV were detected.

To isolate the neutron signal, the X-ray-induced signals can be removed by subtracting exponential fit functions that accurately describe the shape of the X-ray flashes (see Figure 3.17.A). The results of this background noise removal are presented in Figure 3.17.B. The neutron signal obtained during the DPM shot shows higher amplitude compared to that measured during the direct shot, particularly for ToF values from 85 to 500 ns, which corresponds to greater emissions of fast neutrons, from 500 keV to 12.7 MeV. As shown in Figure 3.10, the proton spectra generated during the DPM shots contain a higher proportion of high-energy protons, which could explain the more important emission of fast neutrons.

Therefore, this diagnostic confirms the possibility to produce similar neutron emissions using the DPM, which is consistent with the results obtained via the bubble detectors and activation samples, while emitting less X-rays.

Geant4 simulations of the nToF signals were made using the simulated neutron spectra along the axis of the scintillator #16, for direct and DPM shots. A comparison between the measured and simulated results, normalized considering to the total number of neutrons observed from the ^{7}Be measurement, are shown in Figure 3.19 for both direct and DPM shots.

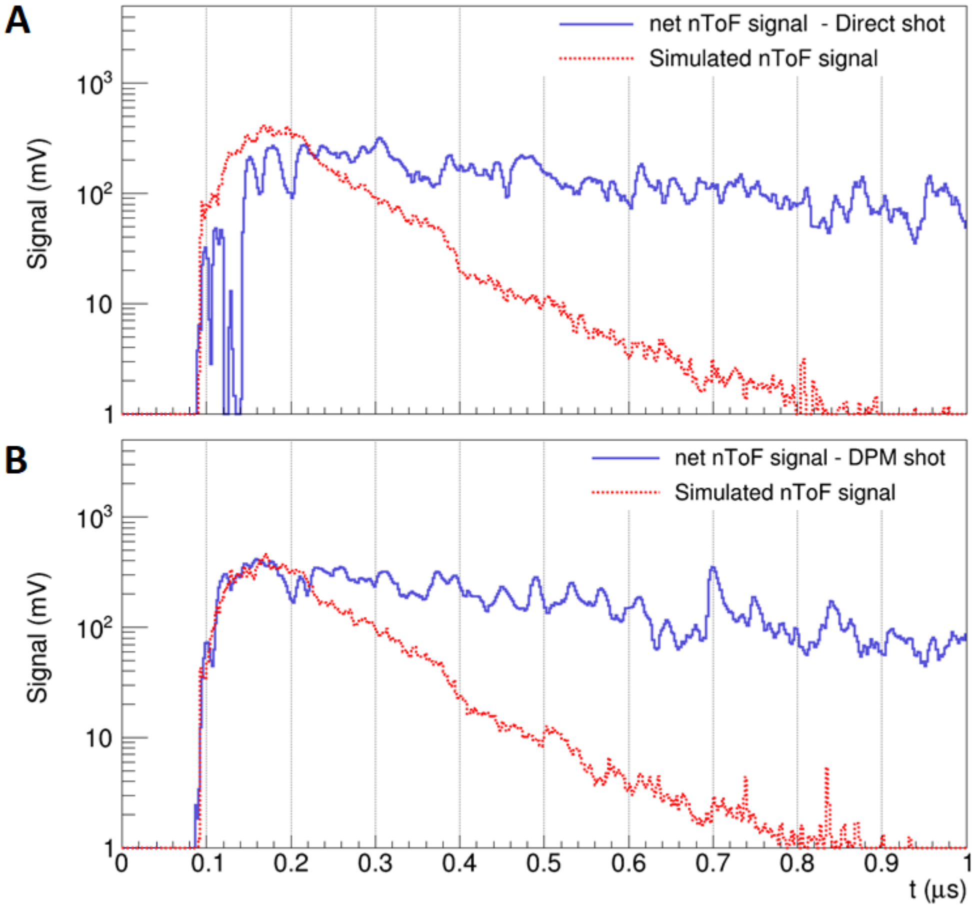

Figure 3.19 – Comparison between simulated (red) and experimental nToF signals (blue) for the direct (A) and DPM shot (B).

The experimental signal during the direct shot is much lower than expected at low ToF, possibly due to the detection limit imposed by significant X-ray emissions, which hampers the detection of high-energy neutrons. Another possible explanation is a lower number of high-energy protons generated during this shot compared to the spectrum used in the simulations, resulting in fewer high-energy neutrons. Significant discrepancies also emerge at higher ToF values, which may indicate an underestimation of low-energy neutron emissions and/or insufficient consideration of scattered neutrons in the simulations. This observation is also seen in the comparison between the experimental and simulated signals for the DPM shot. However, this comparison shows a very good agreement at low ToF, from 85 to 225 ns, corresponding to neutrons between 2.2 and 12.7 MeV. This highlights the effectiveness of the DPM in reducing X-rays to improve our ability to detect high-energy neutrons.

Finally, an iterative algorithm specifically developed during this thesis and based on equation (2.7) and (2.8), was applied to obtain neutron spectra from the net nToF signals presented in Figure 3.17.B, considering the simulated response of the scintillator obtained from Geant4 simulations (see Section 3.2.2). Figure 3.20 shows a comparison between the simulated spectra, normalized by the number of ^{7}Be nuclei measured, and the experimental nToF spectra obtained for the direct and the DPM shot. For the direct shot, the nToF spectrum is lower than the simulated one for energies above 2.5 MeV and higher below this threshold, which is consistent with the discrepancies observed in Figure 3.19.A.

However, a good agreement is observed between the simulated and nToF spectra for the DPM shot, especially between 2.2 and 8 MeV. This consistency is also reflected in the similar nToF signals obtained experimentally and from simulations in this energy range (Figure 3.19.B). Discrepancies arise for energies above 8 MeV, which could be due to a lower number of high-energy protons generated, resulting in fewer high-energy neutrons.

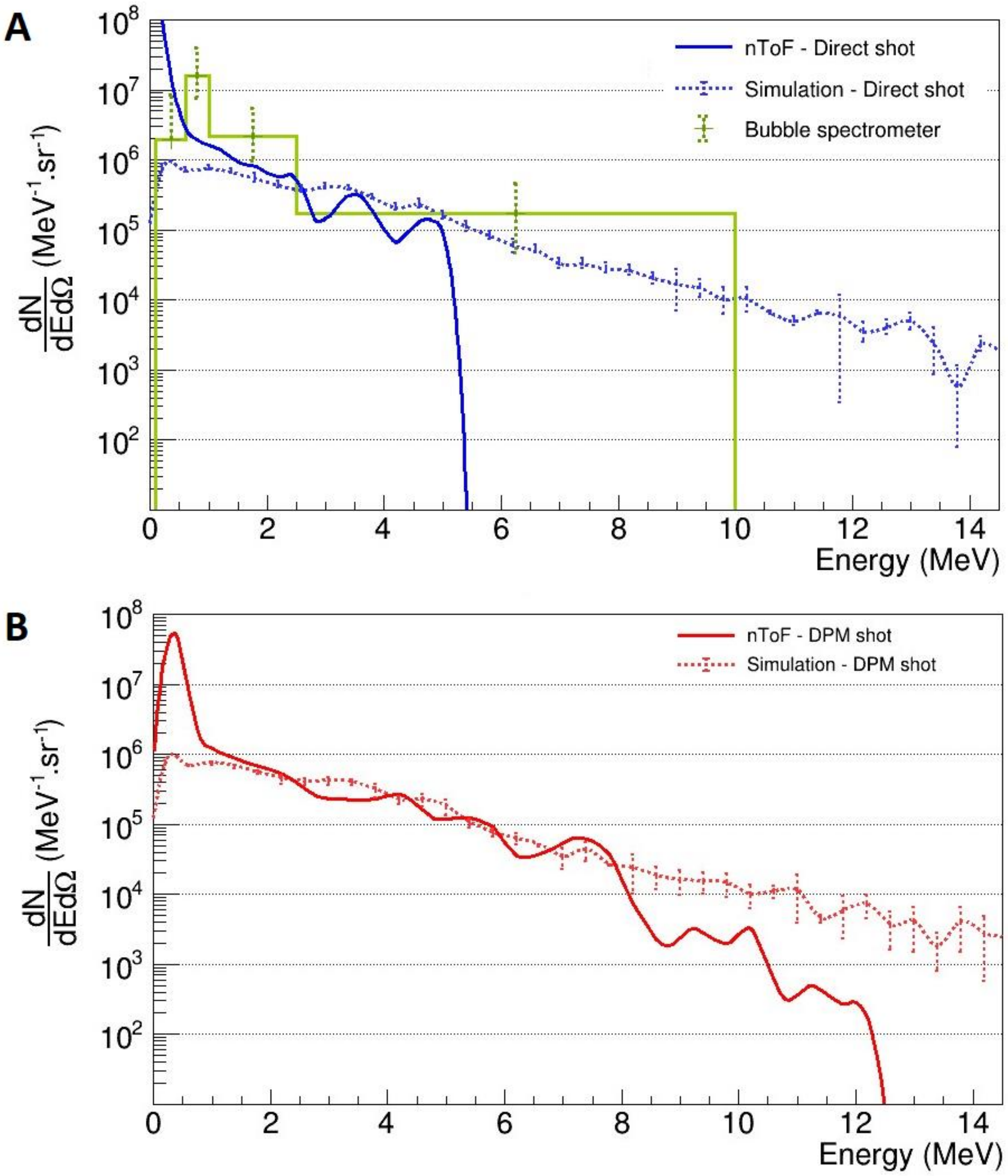

Figure 3.20 – Comparison between simulated and experimental neutron spectra measured using the nToF diagnostic during direct (A) and DPM (B) shots. The neutron spectrum obtained with the bubble spectrometer during the series of direct shots is shown in panel (A).

Both nToF spectra show significantly higher emissions of low-energy neutrons compared to the simulations. The integral of the nToF spectra, considering the large amount of low-energy neutrons obtained, yields values of one order of magnitude higher than the neutron fluences measured with the bubble dosimeters in the same energy range. This suggests that the low-energy part is likely overestimated by the nToF diagnostic, possibly due to the contribution of scattered neutrons within the experimental room, whose probability of interaction with the detector can be significant, considering the dimensions of the scintillators.

The normalization of the simulated spectra, by the number of ^{7}Be nuclei measured, leads to overall good agreement between these simulated spectra and the nToF spectra. This supports the previous estimation of 3.93×10^7 neutrons emitted per shot, which was derived from the measurement of the LiF converter by gamma spectrometry.

In summary, we have performed a detailed characterization of the neutron fields produced using the secondary F2 beam at the Apollon facility, both with its inherent temporal contrast and with a contrast enhancement achieved using a DPM. Simulations were carried out using Geant4 and MCNP6 to predict the characteristics of the neutron emissions, design and calculate the expected activation of samples, and evaluate the response of the scintillators.

An estimation of the total number of neutrons emitted was obtained through direct measurement of the LiF converter using gamma spectrometry, resulting in an average of (3.93 ± 0.21)×10^7 neutrons per shot. This is approximately 1.4 times greater than the predictions from the simulations. In addition to the total number of emitted neutrons, we can also report the number of neutrons recorded in various energy bins due to the different spectral sensitivities of our diagnostics. Between 2 and 10 MeV, as measured by the indium samples, we recorded neutron fluences of (1.69 ± 0.37)×10^6 neutrons/sr/shot for direct shots and (1.14 ± 0.51)×10^6 neutrons/sr/shot for DPM shots. The extended sensitivity range of the bubble dosimeters, from 200 keV to 15 MeV, resulted in recorded neutron fluences of (4.38 ± 0.76)×10^6 neutrons/sr/shot for direct shots and (4.72 ± 1.93)×10^6 neutrons/sr/shot for DPM shots.

Finally, a bubble spectrometer was used to determine the neutron energy distribution. Its results were consistent with the simulations, particularly for high-energy neutrons. However, significant differences were observed for neutrons with lower energies (< 2 MeV), where the simulations seem to underestimate the emissions. This discrepancy was also noted with the results from the nToF diagnostic. An iterative deconvolution algorithm was applied to the nToF signals, leading to the determination of neutron energy spectra and showing good agreement with the simulations for energies above 2 MeV.

	Quantity	**Energy range**	**Φ_{sim}**	**Φ_{meas}**	**Measurement uncertainty**
Direct shots	**Total neutron yield (n/shot)**	All neutrons	2.70×10^7	3.93×10^7	5.44%
	Neutron fluences (n/sr/shot)	[2-10 MeV]	8.45×10^5	1.69×10^6	13.66%
		[0.2-15 MeV]	1.71×10^6	4.38×10^6	17.41%
DPM shots	**Total neutron yield (n/shot)**	All neutrons	2.70×10^7	3.93×10^7	5.44%
	Neutron fluences (n/sr/shot)	[2-10 MeV]	8.70×10^5	1.14×10^6	36.75%
		[0.2-15 MeV]	1.73×10^6	4.72×10^6	40.81%

Table 3.5 – Summary of the measurement of neutron emissions, showing the simulated Φ_{sim} and measured Φ_{meas} total neutron yields, along with neutron fluences between 2 and 10 MeV obtained from the indium sample, and between 200 keV and 15 MeV as measured by the bubble detectors.

3.3 Neutron production at the Apollon facility – Main beam (F1)

To acquire more data on laser-driven neutron sources under varying conditions, the previous neutron production experiment was replicated, using the same diagnostics, with higher laser energy during the commissioning experiment of the main beam (F1) of the Apollon facility.

3.3.1 Experimental setup

The F1 beam utilizes a Ti:Sapphire laser operating at a repetition rate of up to 1 shot/min and delivering pulses with a duration of 22 fs, similar to the F2 beam. The F1 beam is designed to be able to develop a final on-target energy of 220 J. However, during this initial commissioning phase, the F1 beam was limited to an effective peak power of approximately 2 PW, resulting from a mean energy on target of 42.8 J, which is four times higher than that of the F2 beam. The 400 mm diameter beam was focused on targets at a 45° incidence angle using an f/2.5 off-axis parabola (OAP), inducing a nearly circular focal spot with FWHM dimensions of 2.3 × 2.5 µm (see Figure 3.21.A). This focal spot contained 44% of the total laser energy, leading to an on-target peak intensity of approximately 1.7×10^{22} W/cm².

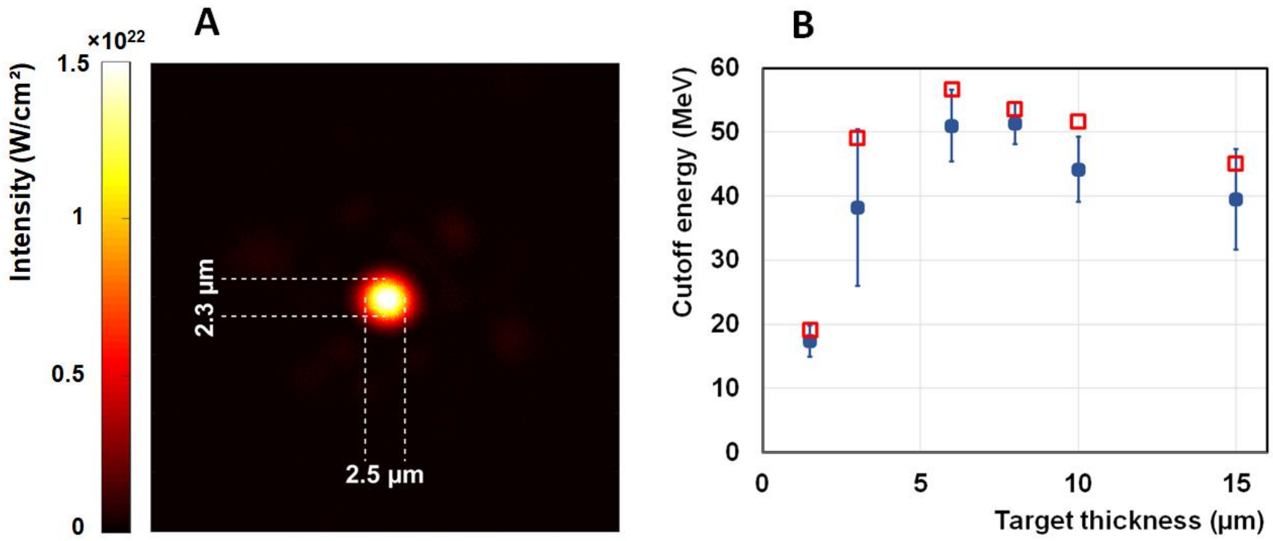

Figure 3.21 - (A) Laser focal spot measurement. (B) Target thickness dependence of the proton cutoff energy. Empty red squares correspond to the maximum energy measured for each target thickness, while filled blue squares indicate the mean energies, with error bars corresponding to the standard deviations.

Various target thicknesses, ranging from 1.5 to 10 µm, were tested to identify the best ones for proton acceleration and, consequently, neutron production. The best results were obtained with 6 µm and 8 µm thick aluminum targets, which typically accelerated protons up to 56.6 MeV (see Figure 3.21.B). An average proton spectrum, determined from three typical shots measured using RCF films, is shown in Figure 3.22. Despite the fact that the laser energy and intensity were, respectively, four and ten times higher than those achieved with the F2 beam, we can observe that the total number of protons was not drastically increased. Nevertheless, the maximum and mean proton energy was doubled, leading to a greater proportion of high-energy protons, which can significantly enhance the neutron production.

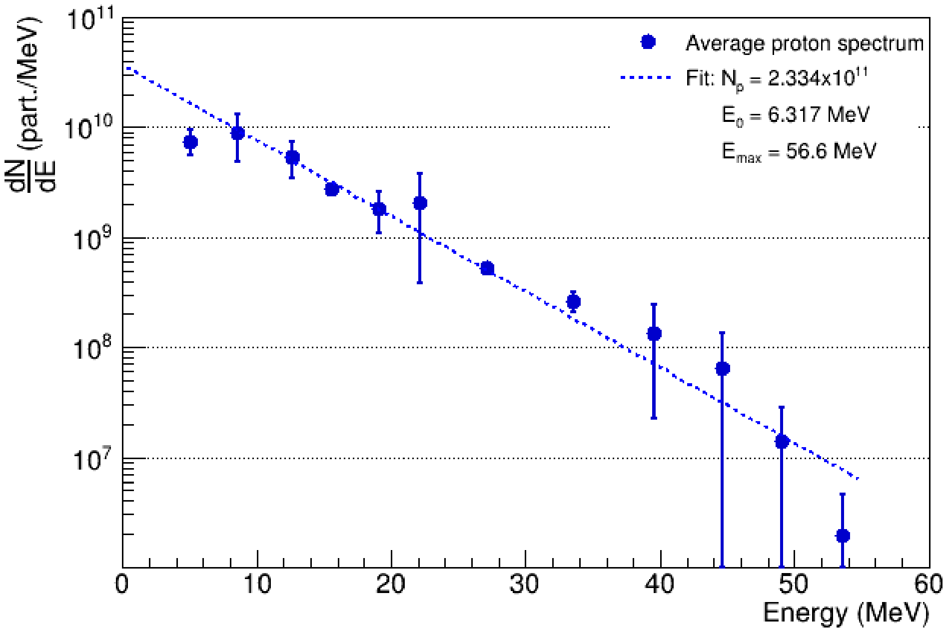

Figure 3.22 - Proton spectrum averaged over 3 shots on 6 µm and 8 µm Al targets. The error bars correspond to the standard deviation of values obtained from the different proton spectra considered. An exponential fit, calculated from equation (2.24), is represented by the dashed line, and the associated total number of protons (N_p), mean (E_0) and maximum proton energy (E_{max}) are given.

As in previous experiments, a LiF converter was used to produce neutrons from the proton beams. However, its thickness was increased to 8 mm and a 2 mm thick lead slab was added behind the converter to prevent the direct interaction of protons with energies below 56 MeV with the activation samples. This measure was taken to avoid the artificial increase in the activity of the copper sample observed during the experiment with the F2 beam.

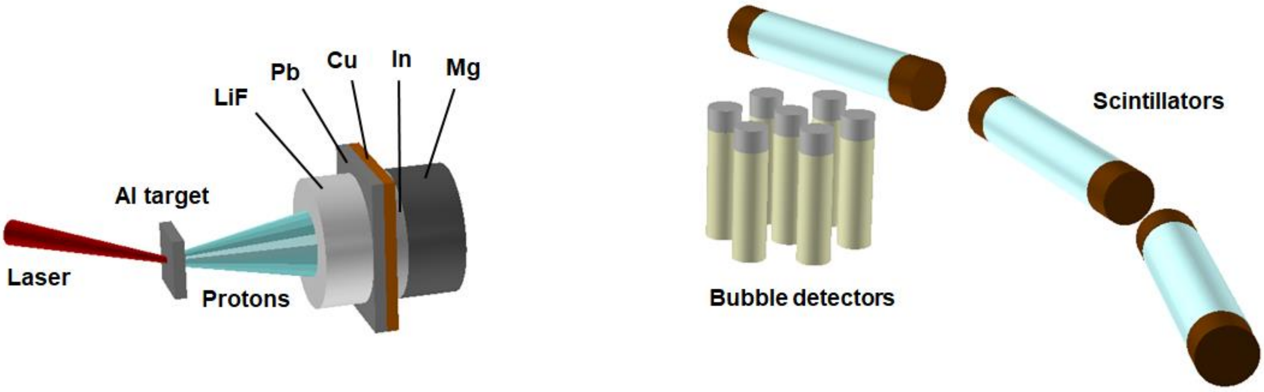

Figure 3.23 – Representation of the experimental setup.

The thickness of the copper and indium samples was reduced to 2 mm, as more neutrons and activation levels were expected during this experiment. This also reduced neutron absorption and maximized the probability of achieving measurable activation in the magnesium sample, which was not activated during the F2 experiment (see Section 3.2.3).

BD-PND bubble detectors were positioned outside the interaction chamber, along the target normal axis (0°), at a distance of 130 cm from the converter. A bubble detector spectrometer (BDS) was also used and placed in the same axis, at 60 cm from the converter. Their positions are shown in Figure 3.25.

Scintillators, described in Section 3.1.1, were placed from 5° to 90° relative to the target normal axis and at distances from 5 m to 8 m (see Figure 3.24). These positions covered a wide range of angles and distances to maximize the chances of detecting neutron signals with minimal interference induced by X-rays. Indeed, given the higher laser energy and thicker target thicknesses, higher X-ray emissions were expected. Consequently, lead shielding was enhanced, with up to 20 cm thick lead bricks on the front face and still 5 cm thick lead bricks on the top, bottom and rear faces.

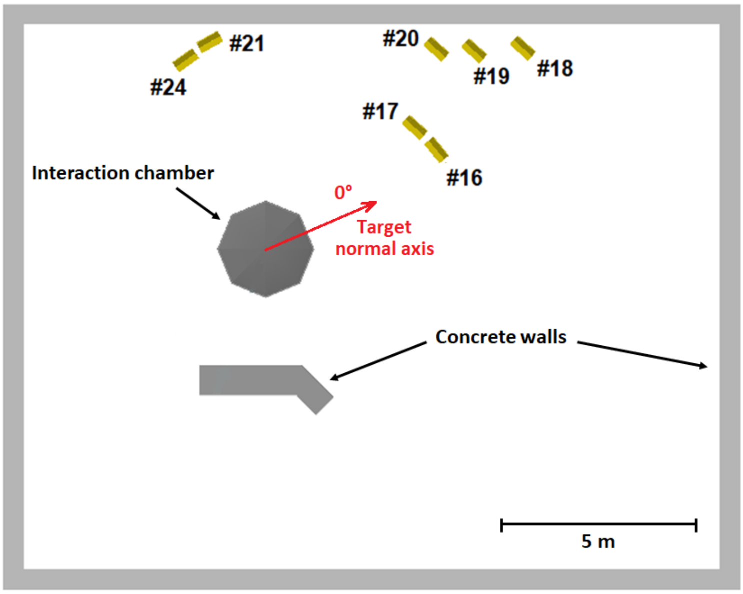

Figure 3.24 – Experimental room with the position of the nToF detectors inside their lead shielding (in yellow).

Finally, GD-351 radio-photo-luminescent (RPL) dosimeters were also used to measure the X-ray emissions. They were placed at the same positions as in the F2 experiment, i.e. all around the target in the equatorial plane at distances ranging from 87 cm to 115 cm (see Figure 3.25). This setup enables a quantitative comparison of the X-ray emissions generated by the interaction of F1 and F2 beams with targets.

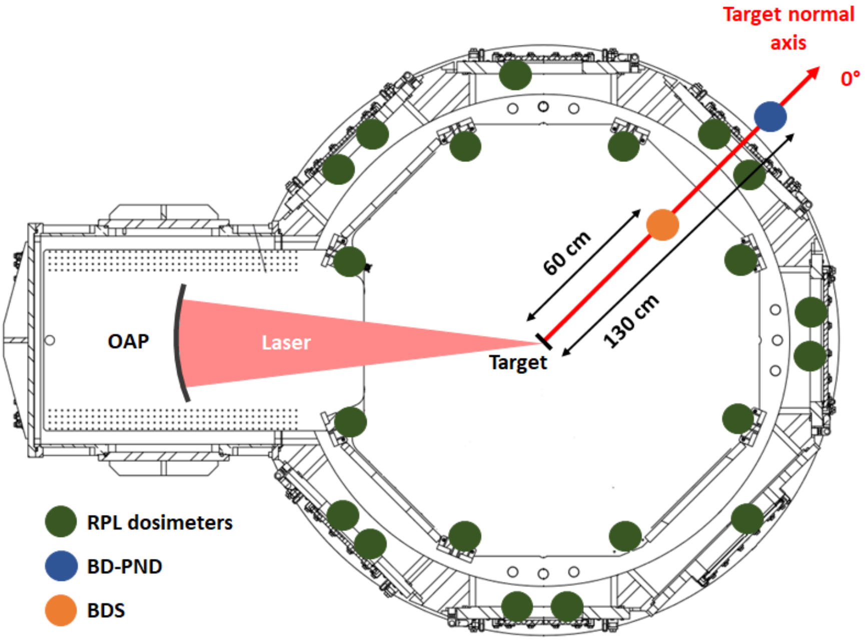

Figure 3.25 – Schematic view of the interaction chamber and positions of the RPL and BD-PND dosimeters, as well as the bubble detector spectrometer (BDS).

3.3.2 Monte Carlo simulations

The average proton spectrum shown in Figure 3.22 was used in Geant4 simulations, considering the previously described experimental setup, to estimate the total number of neutrons produced, as well as the expected neutron energy spectra and angular distributions.

A total neutron yield of $(2.38 \pm 0.37)\times10^{8}$ neutrons/shot was computed. The associated error corresponds to the shot-to-shot variability described by the standard deviation considered in the average proton spectrum calculation.

Additional simulations focused solely on the Li nuclei in the converter were conducted to determine their contribution to neutron production and the expected ^{7}Be activity, which will be measured by gamma spectrometry. It was found that the Li nuclei contribute to around 90.5% to neutron production, which is lower than the 93.5% obtained in the F2 experiment. This is due to the higher proportion of high-energy protons from, which favor (p,n) reactions in the F nuclei due to more favorable cross sections. Thus, the simulations indicate that $(2.15 \pm 0.34)\times10^{8}$ neutrons/shot are produced exclusively from the Li nuclei, which corresponds to a ^{7}Be activity of 29.33 ± 4.64 Bq/shot.

Figure 3.26 presents the simulated angular distributions of neutron emissions across different energy ranges, illustrating a clear anisotropy of emissions, particularly for neutron above 200 keV. A maximum neutron fluence of 3.19×10^{7} neutrons/sr/shot was obtained, with a fluence of 2.91×10^{7} neutrons/sr/shot in the sensitivity range of BD-PND dosimeters, represented by the red curve. This confirms that their sensitivity range encompasses nearly all the neutron emissions, providing reliable estimations of the emitted neutron fluences. Finally, a mean neutron fluence of 1.57×10^{7} neutrons/sr/shot was expected in the solid angle covered by the indium sample and in its sensitivity range, i.e. between 2 MeV and 10 MeV. These values will be used for comparison with the measurements in the following Section.

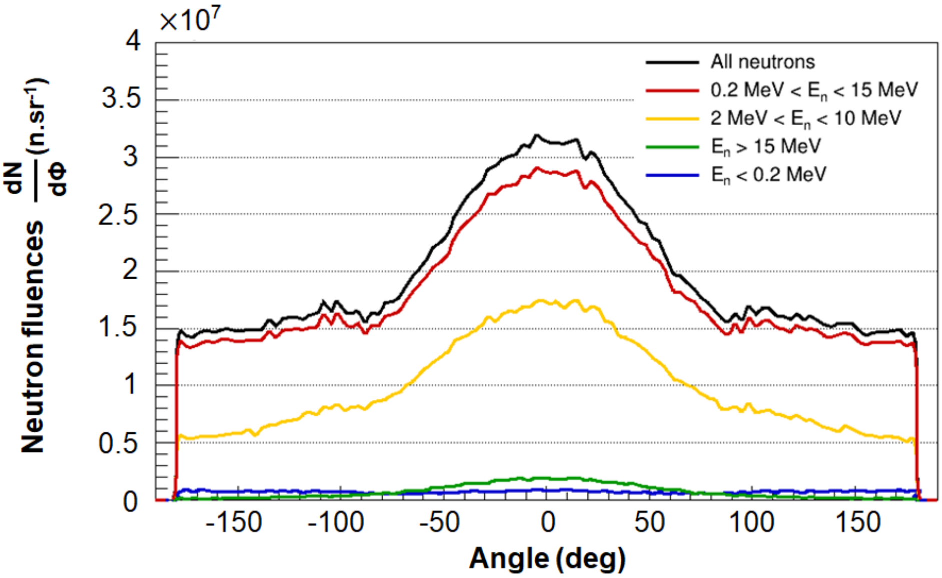

Figure 3.26 - Simulated angular distribution of neutron emissions in the equatorial plane. The different curves represent the angular distribution in different energy ranges. The red and yellow curves correspond specifically to the angular distribution in the sensitivity range of the BD-PND dosimeters and the indium sample, respectively.

Simulated neutron spectra in the forward and backward directions are presented in Figure 3.27, confirming that the most energetic neutrons, particularly those above 2 MeV, are preferentially emitted forward. The simulated neutron spectrum in the forward direction was then used to perform activation simulations of the copper, indium and magnesium samples using MCNP6 with the IRDFF-II library. The simulation results are shown inTable 3.7, compared with the measurements.

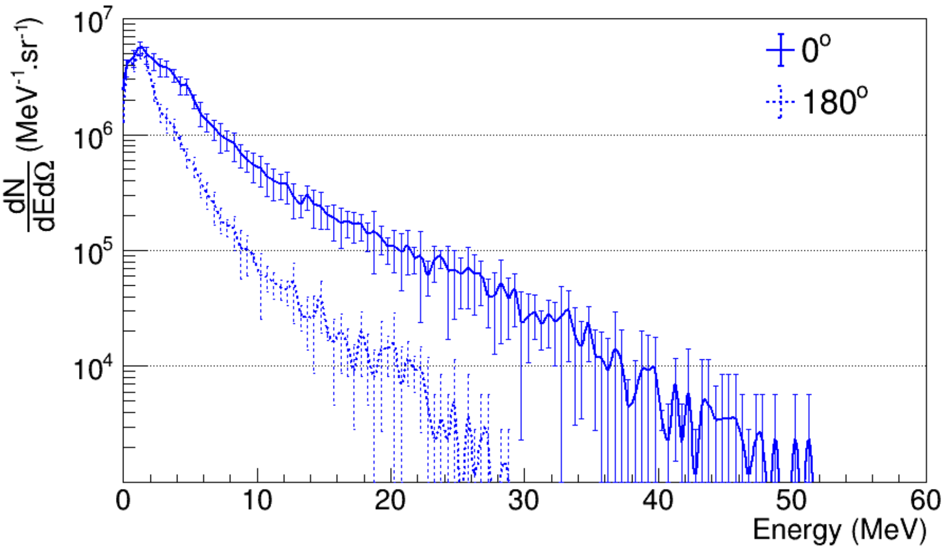

Figure 3.27 - Simulated energy differential neutron spectra in the forward (0°) and backward (180°) directions. The error bars are derived from the shot-to-shot variability of proton spectra shown in Figure 3.22.

3.3.3 Analysis and results

Activation measurements:

The same 3×3" NaI spectrometer used during the F2 experiment, along with the Canberra OSPREY Multi-Channel Analyzer (MCA) and Genie2000 software, was employed to perform gamma spectrometry measurements of the LiF converter and activation samples. Since the thickness of the LiF converter and some of activation samples has changed compared to the previous experiment, their associated efficiency calibration was recalculated using the efficiency transfer method described in Section 2.2.2.

The LiF converter, used during a series of 19 shots, revealed an activity of ^{7}Be of 900.04 ± 50.80 Bq, corresponding to 47.37 ± 2.99 Bq/shot and a neutron production of $(3.14 \pm 0.20)\times10^{8}$ neutrons/shot from the Li nuclei. Considering their contribution of 90.5% to the total neutron production, it can be deduced that approximately $(3.47 \pm 0.22)\times10^{8}$ neutrons/shot were emitted during this series of shots, which is 1.46 times higher than the simulation predictions.

	A/shot (Bq)	**$N_{Be\text{-}7}$/shot**	**$N_{neutrons}$ (n/shot)**	**Uncertainty**
Simulation	29.33	2.15×10^{8}	2.38×10^{8}	15.55%
LiF converter measurement	47.37	3.14×10^{8}	3.47×10^{8}	6.31%

Table 3.6 - Simulated and measured activities and the corresponding number, $N_{Be\text{-}7}$, of ^{7}Be nuclei residuals produced in the LiF converter. The total neutron production was calculated considering the contribution of 90.5% of the Li nuclei to the neutron production. The measurement uncertainties are calculated from equation (2.13) and the uncertainty associated to the simulation result considers the shot-to-shot variability defined by the standard deviations of the values composing the proton spectrum shown in Figure 3.22.

The activities of samples, used during the same series of 19 shots, are presented inTable 3.7, compared with the simulation results. These activities were measured at the end of the series of shots, they are therefore affected by the decay of radionuclides between shots. Thus, the measured activities were corrected by the mean decay time of 5.3 minutes between shots to obtain the average activities induced per shot.

Although the measured activity of ^{116m}In, produced via the ^{115}In(n,γ)^{116m}In reaction in the indium sample, suggests that fewer low-energy neutrons were emitted compared to the simulations, the activity of ^{64}Cu in the copper sample is still significantly higher than expected. This indicates that protons above 56 MeV were accelerated during this series of shots, allowing them to pass through the LiF converter and the lead slab and inducing parasitic reactions similar as those observed during the F2 experiment (see Section 3.2.3).

Furthermore, considering the non-negligible neutron emissions above 10 MeV, two other parasitic reactions involving neutrons can occur: ^{65}Cu(n,2n)^{64}Cu and ^{63}Cu(n,2n)^{62}Cu. Additional simulations revealed that the first reaction produced indeed the majority of the ^{64}Cu nuclei, with an activity of 3.58 Bq/shot, which is more than 3 times higher than the contribution from the reaction of interest. Moreover, the simulations also predict a significant activity of ^{62}Cu (394 Bq/shot), which also emits 511 keV gamma-rays with an intensity of 196%. Given this high intensity and its much shorter half-life (9.7 min), the counting rate in the 511 keV peak can be significantly affected by this radionuclide if the gamma spectrometry measurement is performed before its complete decay.

Considering all these parasitic reactions, it was decided to exclude the copper sample from the final SPAC design and replace it with a manganese sample, which is a monoisotopic element that does not present possible confusions between reactions and has similar radiative capture cross sections.

Reaction	**A_{sim}/shot (Bq)**	**A_{meas}/shot (Bq)**	**Measurement uncertainty**
^{63}Cu(n,γ)^{64}Cu	1.00	37.38	6.00%
^{115}In(n,γ)^{116m}In	22.36	9.92	13.40%
^{115}In(n,n')^{115m}In	11.57	7.17	7.10%
^{24}Mg(n,p)^{24}Na	1.66	1.02	9.16%

Table 3.7 - Measured activities, A_{meas}, and corresponding uncertainties calculated from equation (2.13). The simulated activities, A_{sim}, are calculated from the average proton spectrum shown in Figure 3.22, and were normalized by the number of ^{7}Be nuclei measured (i.e. by a factor of 1.46), to consider the actual neutron production.

A neutron fluence of (1.97 ± 0.14)×10^7 neutrons/sr/shot between 2 and 10 MeV was obtained from the activity of ^{115m}In nuclei using equation (2.14). This measured fluence is 1.26 times higher than the simulated value in the same energy range, which is consistent with the higher number of neutrons emitted, as observed from the measurement of ^{7}Be nuclei in the LiF converter.

Finally, the activation of the magnesium sample is lower than expected, suggesting that less high-energy neutrons were produced. Although activation was induced in the magnesium sample, the activity remained low and, since neutrons with energies beyond the threshold energies of parasitic reactions, such as the ^{25}Mg(n,d)^{24}Na reaction, were expected, we chose to replace magnesium with iron in the SPAC. This change will yield higher activation due to the significantly greater density of iron, while also reducing the potential for confusion between reactions.

Bubble detectors:

The BD-PND dosimeters were positioned along the target normal axis at a distance of 130 cm from the converter (see Figure 3.25). The calibration conducted at the CEZANE facility (IRSN, Cadarache), as mentioned in Section 3.2.3, allowed us to determine a neutron fluence of $(4.66 \pm 0.43)\times10^7$ neutrons/sr/shot from the measured dose. This result is very close to the simulated value of 4.37×10^7 neutrons/sr/shot, normalized by the number of residual ^{7}Be nuclei in the LiF (i.e. by a factor of 1.46).

A comparison between the simulated neutron spectrum in the forward direction, normalized by the measured number of ^{7}Be nuclei, and the spectrum measured by the bubble detector spectrometer (BDS) is shown in Figure 3.28. The fluence obtained between 2 and 10 MeV closely matches the simulations, corroborating the good agreement between the measured fluence obtained from the ^{115m}In activity and the simulated value in this energy range. Furthermore, the fluence above 10 MeV is lower than expected, which is consistent with the lower activation measured in the magnesium sample compared to the simulation predictions (see Table 3.7).

However, although the uncertainties of the experimental and simulated fluences below 2 MeV overlap, the measured value is much higher, which contradicts the measurement of ^{116m}In nuclei that suggested fewer low-energy neutrons were emitted than expected. This discrepancy may be attributed to scattered neutrons, as the probability of interaction with the BDS can be significant, considering it comprises several detectors occupying a substantial volume (> 500 cm^3).

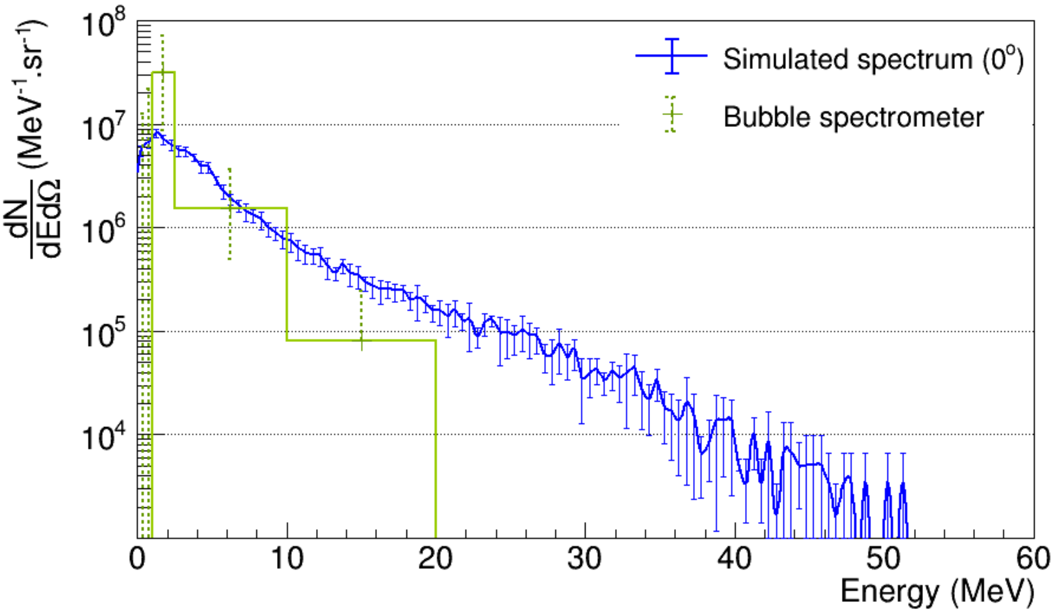

Figure 3.28 - Comparison between the measured neutron spectrum obtained with the BDS and the simulated spectrum, normalized by the number of ^{7}Be nuclei measured in the LiF converter.

nToF measurements and X-ray emissions:

Due to the higher laser energy and thicker target thicknesses compared to the F2 experiment, hot electrons accelerated from the laser/target interaction produced more Bremsstrahlung emissions, resulting in significantly higher X-ray doses. A dose map obtained from measurements performed using RPL dosimeters during a series of 31 shots is shown in Figure 3.29. These measurements revealed an average maximum dose of 15450 µGy/shot, in the transmitted direction of the laser, which is approximately 10 times higher than the maximum dose measured during the F2 experiment.

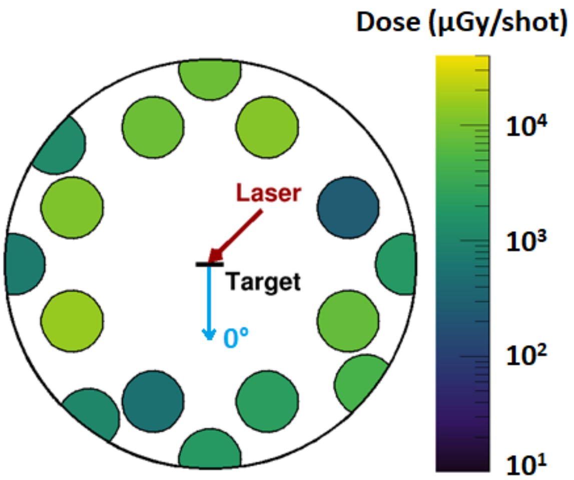

Figure 3.29 – Spatial dose distribution measured inside the interaction chamber using RPL dosimeters during shots on 6 µm and 8 µm thick Al targets. Each circle represents the position of a dosimeter, and its color corresponds to the measured dose.

X-ray emissions appeared relatively homogeneous, though slightly lower doses were observed in the forward direction (0°), which is beneficial for neutron detection with the nToF detectors as it reduces the X-ray flash and potentially improves the signal-to-noise ratio. However, doses of up to 2305 µGy/shot were measured along this axis, causing saturation effects in the photomultiplier tubes (PMT). Different gains and lead shielding thicknesses were therefore tested to mitigate the influence of X-ray emissions and prevent these saturation effects, while minimizing the impact on the neutron signal. Despite these optimizations, as shown in Figure 3.30, most of the nToF signals still revealed significant X-ray flashes without distinct neutron signals, making analysis impossible and preventing any information from being obtained about the neutron emissions.

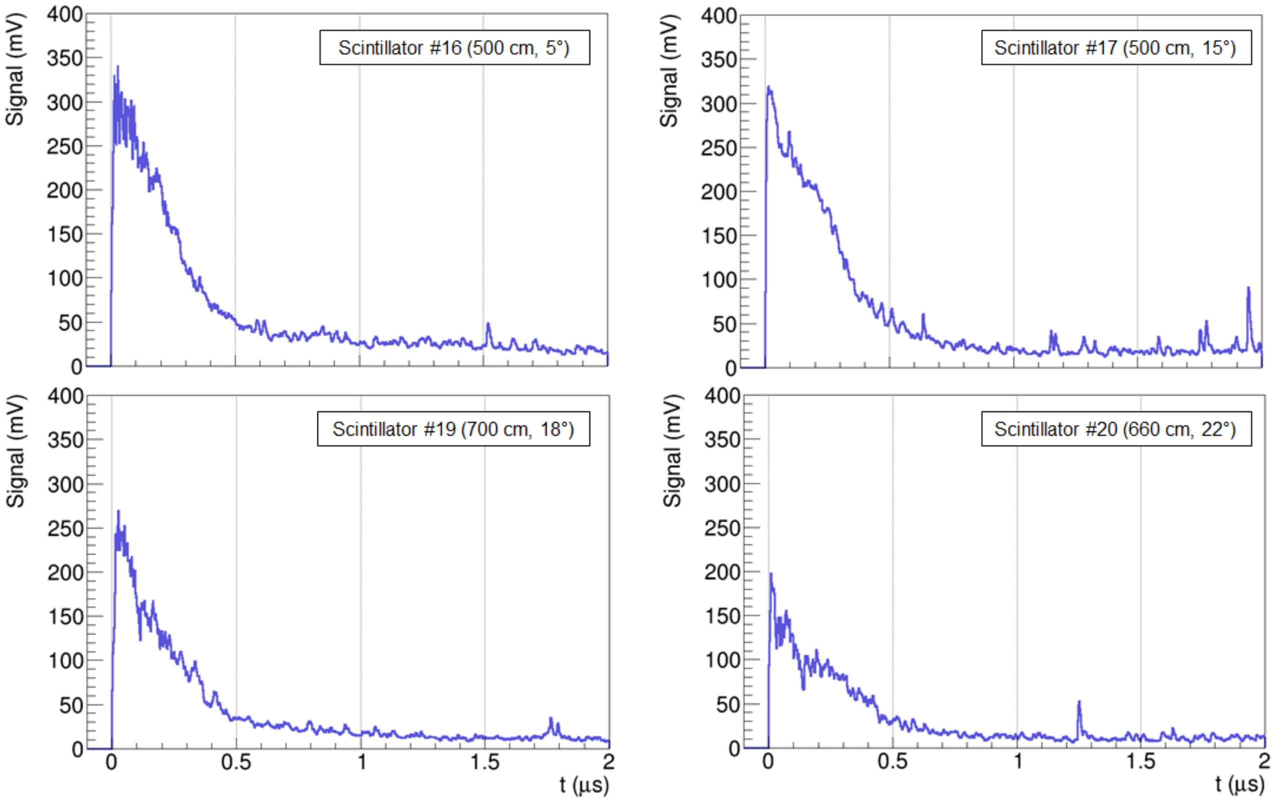

Figure 3.30 – nToF signals obtained with different scintillators, placed at different angles and positions, during shots on 6 µm and 8 µm thick Al targets with a LiF converter for neutron production.

However, clear neutron signals could be observed with scintillator #18 (see Figure 3.31), which is the detector furthest from the converter, positioned at 8 m and 13° from the normal axis (0°). This distance allowed sufficient separation between the X-ray and neutron signals. A gain reduced by a factor of 4 compared to the nominal value used during the F2 experiment and a lead shielding consisting of 15 cm thick lead bricks on the front face and 5 cm thick lead bricks on the top, bottom and rear faces, were also necessary to obtain distinct neutron signals.

The X-ray-induced signals were removed by subtracting their corresponding exponential fit functions, revealing the net neutron signals shown in Figure 3.31.B. A maximum neutron energy of approximately 26.1 MeV was measured, which is twice as high as the maximum neutron energy measured during the F2 experiment. This result is consistent with the simulation predictions and the data obtained from the bubble detector spectrometer and activation samples, indicating that more high-energy neutrons were generated compared to the F2 experiment.

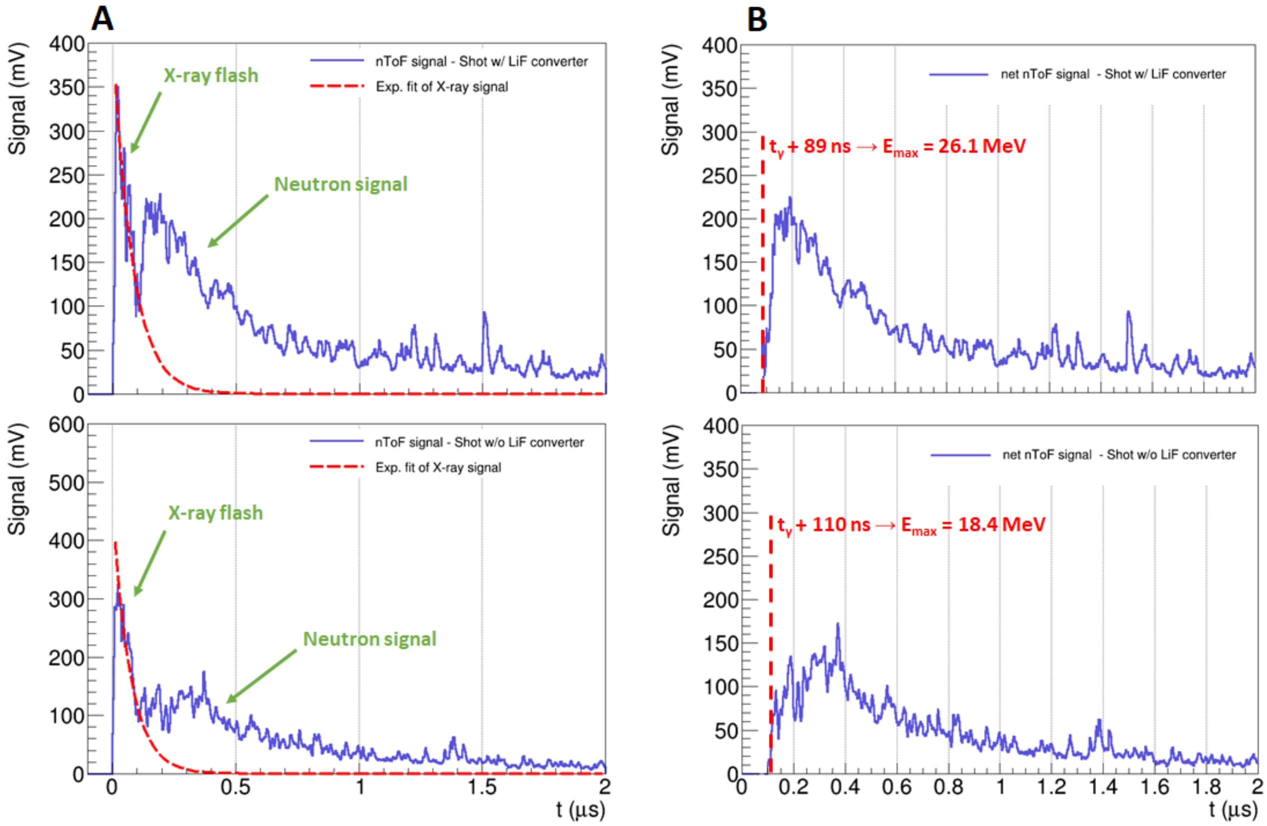

Figure 3.31 – (A) nToF signals measured with scintillator #18 during shots on 6 µm Al targets with (top) and without (bottom) a LiF converter. The exponential fits of the X-ray signals used for the background noise subtraction are shown in red dashed lines. (B) Net neutron signals obtained after removal of the signal induced by the X-rays. The red dashed lines correspond to the Time-of-Flight (ToF) of the most energetic neutrons detected.

Neutron signals were also observed during shots without converter (see Figure 3.31), suggesting that neutron production occurred through (γ,n) or (p,n) reactions in the walls of the interaction chamber or adjacent elements, such as diagnostics placed inside the chamber. No neutron signals were measured during shots without converter in the F2 experiment, even though the number of protons was similar to that in this experiment. This suggests that neutron production via (γ,n) reactions is more likely responsible for the neutron generation without converter, as doses induced by Bremsstrahlung emissions were measured to be around 10 times higher in this experiment.

A gamma-ray, travelling at the speed of light toward the scintillator, can generate a photoneutron at any distance from the target chamber center (TCC). The Time-of-Flight (ToF) of the detected neutron will be artificially shortened, given the gamma ray's much faster velocity, leading to a misinterpretation of the neutron ToF, with the corresponding neutron energy potentially being significantly overestimated.

Thus, the maximum neutron energy of 18.4 MeV determined for the shot without converter (see Figure 3.31.B) represents an upper limit, as the exact location of the neutron emission is unknown, making it impossible to accurately define the path length and ToF of these photoneutrons. For instance, a neutron generated via a (γ,n) reaction inside the chamber wall with the minimum observed ToF (i.e. 110 ns) would have an energy of 13.2 MeV. However, if a neutron with the same ToF were produced through a (γ,n) reaction inside the lead shielding of the scintillator, its energy would only be 6.3 keV.

Hence, Figure 3.32 presents a comparison of neutron signals obtained with and without converter, as a function of neutron energy determined from the ToF using equation (2.6). For the shot without converter, the different curves represent the relationship between the neutron signal and neutron energy, taking into account various distances from the TCC where (γ,n) reactions were considered to occur. It can be seen that the location where these photoneutrons are produced plays an important role in determining their energy through the Time-of-Flight technique.

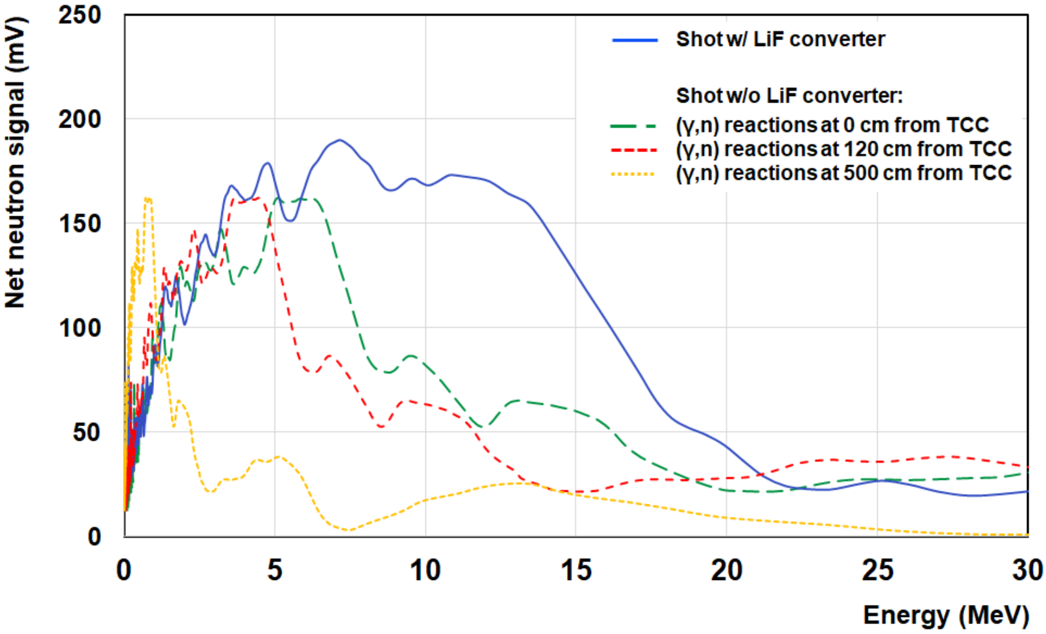

Figure 3.32 – Neutron signal as a function of the neutron energy for shots with (solid line) and without (dashed lines) LiF converter. For the shot without converter, different positions where (γ,n) reactions occurred were considered. The distance of 120 cm from TCC corresponds to the chamber walls, while 500 cm is the distance from the TCC to scintillator #17, placed in front of scintillator #18 (see Figure 3.24) from which these signals were obtained.

Since the neutron fluences measured via the indium sample and bubble detectors are close the simulation results, which do not account for (γ,n) reactions, it appears that these reactions have a low contribution to the overall neutron production. Thus, based on the data presented in Figure 3.32, photoneutrons seem to be produced several meters away from the TCC, near the scintillator. These (γ,n) reactions could therefore occur in the lead shielding, where the maximum cross section is 40 times higher than that of the aluminum composing the interaction chamber.

Finally, the unfolding procedure described in Section 2.1.3 was applied to the net nToF signal shown in Figure 3.31.B, which was obtained during the shot with converter. Figure 3.33 presents a comparison between the simulated spectrum, normalized by the number of ^{7}Be nuclei measured, and the experimental nToF spectra obtained from both the nToF diagnostic and the bubble spectrometer.

The neutron spectrum measured by the nToF diagnostic is in good agreement with that measured by the bubble spectrometer. This confirms the steeper slope of the experimental spectrum compared to the simulated spectrum, as well as the lower emission of high-energy neutrons than expected, which also corroborates the lower activation of the magnesium sample compared to simulation predictions.

However, as with the spectrum measured by the bubble spectrometer, the nToF spectrum presents significantly higher emissions of low-energy neutrons compared to the simulation. The integral of the nToF spectrum yields a neutron fluence of 2.81×10^8 neutrons/sr/shot in the sensitivity range of the bubble dosimeters, which is 6 times higher than the value obtained from these detectors. This suggests that the low-energy part of the nToF spectrum is likely overestimated, possibly due to the contribution of scattered neutrons within the experimental room. Indeed, their probability of interaction with the detector may be significant, considering the dimensions of the scintillators and their proximity to the concrete walls (see Figure 3.24).

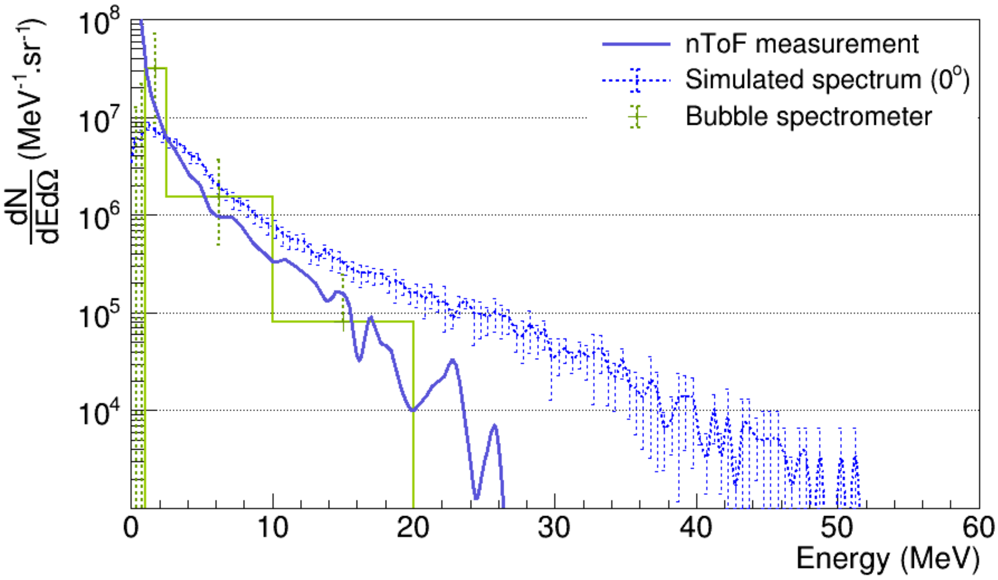

Figure 3.33 – Comparison between the simulated and measured neutron spectra obtained with the nToF diagnostic and the bubble spectrometer.

In summary, the pitcher-catcher technique using a LiF converter was employed to produce neutrons during the commissioning experiment of the main beam (F1) of the Apollon facility. The higher laser on-target energy (~ 43 J) induced significantly more neutron emissions compared to those obtained during the experiments at the ALLS facility or at the Apollon facility with the secondary beam (F2). A total neutron yield of (3.47 ± 0.22)×10^8 neutrons/shot obtained from the gamma spectrometry measurement of the LiF converter, which is 1.46 times greater than the simulation predictions.

Neutron fluences in different energy ranges were also determined using the indium sample and bubble detectors. Between 2 and 10 MeV, a neutron fluence of (1.97 ± 0.14)×10^7 neutrons/sr/shot was obtained from the gamma spectrometry measurement of the indium sample, while a neutron fluence of (4.66 ± 0.43)×10^7 neutrons/sr/shot was measured, between 200 keV and 15 MeV, by the bubble dosimeters. These two values are, respectively, 1.26 and 1.60 times higher than the simulation predictions, which is consistent with the higher-than-expected total neutron production observed with the direct measurement of the LiF converter.

The nToF and bubble spectrometer diagnostics were also used to characterize the energy distribution of neutrons. The results are consistent with those from activation samples, revealing that fewer high-energy neutrons were emitted than expected. However, significantly more low-energy neutrons (< 2 MeV) were measured by these diagnostics. Similar to the F2 experiment, this result is inconsistent with the measurements performed with the bubble dosimeters and activation samples, possibly due to the presence of scattered neutrons.

Finally, the nToF detectors revealed neutron emissions above 20 MeV with, however, some difficulties to limit the influence of X-rays on the measured signals. Thus, this supports the interest of the SPAC, with its extended sensitivity range and gamma insensitivity, to characterize laser-driven neutron emissions. Additionally, this experiment allowed us to test various activation samples, confirming that copper and magnesium are not the most suitable elements for the SPAC due to parasitic reactions that complicate analysis and insufficient activation, respectively.

Quantity	**Energy range**	Φ_{sim}	Φ_{meas}	**Measurement uncertainty**
Total neutron yield (n/shot)	All neutrons	2.8×10^{8}	3.47×10^{8}	6.31%
Neutron fluences (n/sr/shot)	[2-10 MeV]	1.57×10^{7}	1.97×10^{7}	7.10%
	[0.2-15 MeV]	2.91×10^{7}	4.66×10^{7}	9.23%

Table 3.8 – Summary of the neutron emission measurements, showing both the simulated Φ_{sim} *and measured* Φ_{meas} *total neutron yields, along with neutron fluences between 2 and 10 MeV obtained from the indium sample, and between 200 keV and 15 MeV as measured by the bubble detectors.*

4. Discussion & perspectives

The enhancement of laser technology and our understanding of ion acceleration mechanisms using lasers have enabled the development of laser-driven neutron sources over the past 25 years. As mentioned in the first section, these new neutron sources offer several advantages over conventional ones, such as their relative compactness and the ability to generate very short and intense neutron bursts, with lower radioactive waste production and fewer safety constraints. Despite current limitations, particularly in terms of mean flux, laser-driven neutron sources could become a viable alternative to conventional sources, which are becoming less accessible due to the planned shutdown of many research reactors.

The main objective of this thesis work was to predict neutron emissions produced by different lasers using Monte Carlo simulations and to characterize these emissions, both in terms of fluence and energy distribution, to assess how neutron emission properties evolve as a function of laser parameters, particularly laser energy. This was achieved through inter-comparisons of results obtained using various diagnostics (activation samples, bubble detectors and nToF detectors).

A first experiment of neutron production using the pitcher-catcher technique was conducted at the ALLS facility (Varennes, Canada) with a 150 TW laser, delivering a relatively low on-target energy of 3.2 J at a high repetition rate of 0.5 Hz. A total neutron yield of approximately 5×10^5 neutrons/shot was measured, with a fluence of up to 1.4×10^5 neutrons/sr/shot, mainly in the energy range of a few hundred keV to 2 MeV. The neutron yield per shot is about 10^5 lower than what could be obtained using much higher-energy lasers delivering on-target energies of several hundreds of Joules, but which have a very poor repetition rate (with typically one shot per several hours) (see Section 1.4.4). This means that using laser-based neutrons for applications demonstrated with such high-energy lasers (i.e., thermal neutron radiography or neutron resonance spectroscopy (NRS)) [12, 182, 187] is not feasible in the conditions demonstrated here, as this would require accumulating neutron signals over tens of hours.

Nonetheless, other applications requiring lower neutron fluxes can be considered using the presently demonstrated high-repetition-rate, low-yield source. The significant activation of the indium sample, measured by gamma spectrometry, reveals indeed the possibility of carrying out Instrumental Neutron Activation Analysis (INAA) for the elemental analysis of objects composed of elements with neutron interaction cross sections that are similar or higher to those of indium. This highlights a significant advantage of using a laser-based neutron source, as a range of nondestructive elemental analysis techniques, such as INAA, X-ray fluorescence (XRF), and particle-induced X-ray emission (PIXE), can be simultaneously deployed at the same facility [242]. This contrasts with conventional accelerator-based sources, where X-ray and neutron sources are produced by different machines.

Fast neutron radiography could also be feasible with the neutron flux demonstrated here because, unlike thermal neutron radiography, it does not require to use a moderator to thermalize the neutrons, which usually reduces the neutron flux. Such an application was already performed [243, 244, 245] using conventional neutron sources with neutron fluences of about $10^{7\text{-}8}$ neutrons/cm². Considering the neutron fluences measured here, around 6×10^4 neutrons/cm²/shot can be inferred in the fast neutron range. Therefore, we estimate that fast neutron radiography could be performed using the ALLS laser by accumulating several hundred shots, which represent only a few minutes of irradiation.

We have also performed a detailed characterization of neutron emissions produced using the secondary beam (F2) of the Apollon facility (Saclay, France), both with its inherent temporal contrast and with contrast enhancement achieved using a Double Plasma Mirror (DPM). This 500 TW laser beam has a lower repetition rate of up to 1 shot/min but delivers higher on-target energies: 10.9 J in direct shot configuration and 5.7 J when a DPM is used. The total neutron yield was around

4×10^7 neutrons/shot, with a fluence of up to 5×10^6 neutrons/sr/shot. Therefore, the neutron emissions were almost two orders of magnitude higher than those produced at the ALLS facility, though the repetition rate was two orders of magnitude lower, resulting in similar mean neutron fluxes and potential applications.

The neutron energy distribution was also characterized by a bubble spectrometer and nToF diagnostics, revealing an exponentially decreasing shape of the neutron spectra, consistent with the simulation predictions. However, these experimental spectra showed significant emissions of low-energy neutrons (< 2 MeV) that were not predicted by the simulations. This discrepancy could be due to challenges in taking accurately in consideration the noise removal in the nToF signals or insufficient consideration of scattered neutrons in the simulations. An in-depth investigation of the origin of these significant emissions of low-energy neutrons should be carried out through additional simulations or experimental studies using the shadow cone technique [246, 247].

Additionally, fewer X-ray emissions were recorded during the shots with the DPM, according to the results obtained from the radio-photo-luminescent (RPL) X-ray dosimeters and nToF detectors, which improved our ability to detect high-energy neutrons with this diagnostic. Indeed, the improvement of the laser/target interaction, by reducing the pre-pulses, allowed to shoot on thinner targets which produce less X-rays. At the same time, the results obtained by all diagnostics demonstrated that the production of neutrons was similar to that in direct shots, although the DPM reduces the on-target energy by 48%. Thus, the DPM appears to be a valuable tool to adjust the neutron/X-ray ratio using different target thicknesses, which is a feature that could be beneficial for applications such as combined neutron/X-ray radiography, which allows probing both light and heavy materials.

The pitcher-catcher technique was also employed during the commissioning experiment of the main beam (F1) at the Apollon facility. During this first commissioning phase, the F1 laser beam had a peak power limited to 2 PW and delivered pulses at the same repetition rate as the F2 beam, but with nearly 4 times on-target energy (42.8 J). A total neutron yield of approximately 3×10^8 neutrons/shot, with a fluence of up to 5×10^7 neutrons/sr/shot, was measured. As in the previous experiment with the F2 beam, these neutron emissions were about 1.4 times higher than the simulation predictions. This systematic discrepancy could be due to inaccuracies in the evaluation of the cross sections for (p,n) reactions in the LiF converter, as provided by the cross-section libraries used in the Geant4 simulations. A thorough study of the cross sections considered in these simulations should therefore be conducted to improve the accuracy of future neutron emission predictions.

The neutron spectra obtained with the nToF diagnostics showed that neutrons with energies above 20 MeV were detected, although the signal-to-noise ratio at these energies was low due to significant X-ray emissions, which hindered the detection of high-energy neutrons. This highlights the importance of developing a neutron activation spectrometer, such as the SPAC, with an extended sensitivity range and gamma-ray insensitivity.

As part of this thesis work, efforts were focused on optimizing such a neutron activation spectrometer to characterize neutron emissions produced by lasers. The materials composing the SPAC were selected based on several physical and chemical criteria, and some were tested at the Apollon facility to assess their suitability. This led in a final design, whose response was verified by irradiating it with monoenergetic neutrons at the AMANDE facility (Cadarache, France). The results were compared to Monte Carlo simulations to select the most appropriate cross-section library for the response matrix calculation. The SPAC can now be used under experimental conditions at laser facilities or other facilities producing high-energy neutrons to test the associated unfolding procedure and validate its ability to reconstruct neutron spectra.

Besides, although the previously mentioned high-energy lasers, which demonstrated the capability of lasers to perform thermal neutron radiography or NRS, produce neutron emissions two orders of magnitude higher than when using the F1 beam, the higher repetition rate of the F1 beam enables the possibility of performing similar applications. Thus, we have shown that a wide range of neutron-based applications can already be performed at the Apollon facility.

Furthermore, the neutron emissions measured during this experiment were approximately 10 times higher than those detected in the F2 experiment and around 1000 times higher compared to the experiment performed at the ALLS facility, while the laser energy was only 4 and 13 times higher, respectively. This points out to the strong nonlinearity of the neutron yield with respect to laser energy. Scaling laws based on data obtained from high-energy picosecond lasers suggest that neutron production increases by a power from 2.5 to 3.5 with the laser energy [12, 184]. The results obtained during this thesis show that for femtosecond lasers with lower energies, the neutron yield scales approximately with the power of 2.5 relative to laser energy (see Figure 4.1).

However, as demonstrated in the F2 experiment, this yield is also highly dependent on other laser parameters, particularly the laser temporal contrast. This can be enhanced using a plasma mirror, which improves laser/target interaction and ion acceleration, thereby boosting neutron production. During the final commissioning phase of the F1 beam, scheduled for 2025, the peak power is expected to increase to 10 PW, with an on-target energy of around 220 J. This could yield neutron fluences close to 10^{10} neutrons/sr/shot, with a repetition rate of 1 shot per minute, leading to record mean neutron fluxes exceeding 1×10^6 neutrons/cm²/s at 10 cm from the converter.

In the near future, mean neutron flux could be further improved with ongoing advancements in laser technology, such as enhancing laser amplification and repetition rates, which would result in higher neutron production. Multilayer converters, designed to optimize ion-to-neutron production yield, could also be implemented to increase neutron flux [184]. These developments indicate that laser-driven neutron sources could soon achieve mean neutron fluxes comparable to those of conventional neutron sources.

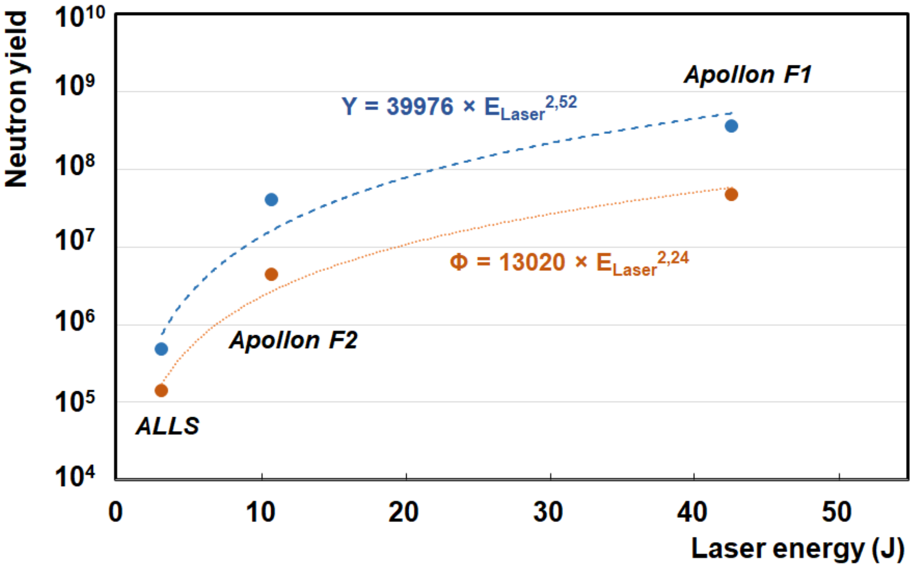

Figure 4.1 - Total neutron productions (blue) in neutrons/shot and neutron fluences (orange) in neutrons/sr/shot obtained during this thesis work as a function of laser energy, along with their corresponding scaling law.

Appendix A

Comparison between measured and simulated activities of SPAC samples irradiated at the AMANDE facility

Neutron energy	**Sample**	**Reaction**	**A$_{meas}$ (Bq)**	***Uncertainty***	**A$_{Geant4}$ (Bq) *JEFF-3.3***	***Relative difference***	**A$_{MCNP6}$ (Bq) *JEFF-3.3***	***Relative difference***	**A$_{MCNP6}$ (Bq) *IRDFF-II***	***Relative difference***
0.565 MeV	Mn	^{55}Mn(n,g)^{56}Mn	42,93	8,17%	46,15	7,51%	37,32	-13,06%	46,59	8,53%
	In	^{115}In(n,n')^{115m}In	30,26	22,09%	0,00	-100,00%	69,38	129,28%	58,23	92,45%
		^{115}In(n,g)^{116m}In	1964,07	6,04%	0,00	-100,00%	3992,96	103,30%	2627,59	33,78%
	SPAC Mn Av	^{55}Mn(n,g)^{56}Mn	62,17	7,99%	57,39	-7,70%	46,21	-25,67%	57,33	-7,79%
	SPAC Mn Ar	^{55}Mn(n,g)^{56}Mn	24,21	7,52%	29,35	21,26%	22,48	-7,13%	27,91	15,31%
	SPAC In	^{115}In(n,n')^{115m}In	0,00	N/A	0,00	N/A	47,29	N/A	39,40	N/A
		^{115}In(n,g)^{116m}In	1619,60	7,30%	0,00	-100,00%	2347,79	44,96%	1546,76	-4,50%
1.2 MeV	In	^{115}In(n,n')^{115m}In	153,25	7,08%	0,00	-100,00%	31,95	-79,15%	211,14	37,77%
		^{115}In(n,g)^{116m}In	752,83	6,53%	0,00	-100,00%	1363,44	81,11%	985,91	30,96%
1.86 MeV	In	^{115}In(n,n')^{115m}In	118,17	5,94%	0,00	-100,00%	5,51	-95,34%	113,03	-4,35%
		^{115}In(n,g)^{116m}In	101,50	8,23%	0,00	-100,00%	155,17	52,88%	140,90	38,82%
2.5 MeV	In	^{115}In(n,n')^{115m}In	267,82	6,04%	0,00	-100,00%	5,13	-98,08%	230,25	-14,03%
		^{115}In(n,g)^{116m}In	251,88	8,01%	0,00	-100,00%	228,18	-9,41%	181,06	-28,12%
	SPAC Mn Av	^{55}Mn(n,g)^{56}Mn	14,00	8,00%	19,76	41,15%	15,91	13,63%	13,19	-5,76%
	SPAC Mn Ar	^{55}Mn(n,g)^{56}Mn	8,28	31,45%	11,03	33,28%	8,61	4,06%	7,19	-13,15%
	SPAC In	^{115}In(n,n')^{115m}In	938,20	6,20%	0,00	-100,00%	20,57	-97,81%	872,94	-6,96%
		^{115}In(n,g)^{116m}In	603,36	8,24%	0,00	-100,00%	858,10	42,22%	680,90	12,85%
4 MeV	In	^{115}In(n,n')^{115m}In	41,09	6,40%	0,00	-100,00%	0,32	-99,21%	46,69	13,62%
		^{115}In(n,g)^{116m}In	13,66	19,91%	0,00	-100,00%	27,19	99,03%	14,36	5,13%
5 MeV	In	^{115}In(n,n')^{115m}In	221,54	5,65%	0,00	-100,00%	0,77	-99,65%	234,43	5,81%
		^{115}In(n,g)^{116m}In	19,59	23,10%	0,00	-100,00%	70,96	262,16%	34,86	77,90%
7.222 MeV	In	^{115}In(n,n')^{115m}In	249,29	5,59%	0,00	-100,00%	0,23	-99,91%	145,71	-41,55%
		^{115}In(n,g)^{116m}In	141,00	8,30%	0,00	-100,00%	15,16	-89,25%	9,61	-93,19%
	Fe	^{56}Fe(n,p)^{56}Mn	567,61	6,02%	363,90	-35,89%	354,03	-37,63%	373,86	-34,13%
	SPAC Mn Av	^{55}Mn(n,g)^{56}Mn	17,36	13,85%	4,10	-76,38%	3,22	-81,43%	2,65	-84,75%
	SPAC Mn Ar	^{55}Mn(n,g)^{56}Mn	0,00	N/A	5,42	N/A	1,94	N/A	1,62	N/A
	SPAC In	^{115}In(n,n')^{115m}In	1004,31	6,36%	0,00	-100,00%	1,77	-99,82%	533,31	-46,90%
		^{115}In(n,g)^{116m}In	755,40	8,22%	0,00	-100,00%	104,52	-86,16%	72,48	-90,41%
	SPAC Fe	^{56}Fe(n,p)^{56}Mn	756,26	6,82%	484,41	-35,95%	469,38	-37,93%	495,53	-34,48%
15.084 MeV	Fe	^{54}Fe(n,2n)^{53}Fe	114,45	16,71%	0,00	-100,00%	142,41	24,43%	76,62	-33,05%
		^{56}Fe(n,p)^{56}Mn	1172,00	5,67%	839,40	-28,38%	817,89	-30,21%	818,91	-30,13%
	Zr	^{90}Zr(n,2n)^{89}Zr	866,59	6,22%	0,00	-100,00%	630,68	-27,22%	631,63	-27,11%
	SPAC Mn Av	^{55}Mn(n,2n)^{54}Mn	6,59	15,80%	0,00	-100,00%	5,97	-9,39%	5,74	-12,88%
		^{55}Mn(n,g)^{56}Mn	17,21	13,02%	21,01	22,11%	16,10	-6,43%	15,73	-8,62%
	SPAC Mn Ar	^{55}Mn(n,2n)^{54}Mn	3,84	21,01%	0,00	-100,00%	3,41	-11,09%	3,28	-14,52%
		^{55}Mn(n,g)^{56}Mn	10,39	16,33%	14,06	35,40%	10,16	-2,19%	9,94	-4,31%
	SPAC In	^{115}In(n,n')^{115m}In	423,14	6,47%	0,00	-100,00%	7,06	-98,33%	420,11	-0,72%
		^{115}In(n,g)^{116m}In	326,76	10,92%	0,00	-100,00%	377,68	15,58%	279,90	-14,34%
	SPAC Fe	^{56}Fe(n,p)^{56}Mn	5254,99	5,90%	5106,61	-2,82%	4963,48	-5,55%	4969,56	-5,43%
	SPAC Zr	^{90}Zr(n,2n)^{89}Zr	930,39	6,34%	0,01	-100,00%	665,06	-28,52%	666,04	-28,41%
20.688 MeV	Fe	^{54}Fe(n,2n)^{53}Fe	90,15	15,64%	67,44	-25,19%	0,50	-99,45%	96,43	6,96%
		^{56}Fe(n,p)^{56}Mn	175,44	6,65%	196,90	12,23%	3,07	-98,25%	138,73	-20,92%
	Zr	^{90}Zr(n,2n)^{89}Zr	223,22	6,73%	135,69	-39,21%	0,85	-99,62%	171,68	-23,09%
	SPAC Mn Av	^{55}Mn(n,2n)^{54}Mn	0,60	12,43%	0,87	44,95%	0,63	5,99%	0,63	5,44%
		^{55}Mn(n,g)^{56}Mn	14,56	8,67%	0,61	-95,78%	1,13	-92,21%	1,00	-93,13%
	SPAC Mn Ar	^{55}Mn(n,2n)^{54}Mn	0,36	10,16%	0,50	38,92%	0,36	1,75%	0,36	1,20%
		^{55}Mn(n,g)^{56}Mn	0,00	N/A	0,43	N/A	0,76	N/A	0,68	N/A
	SPAC In	^{115}In(n,n')^{115m}In	503,00	6,97%	2,74	-99,46%	0,75	-99,85%	43,31	-91,39%
		^{115}In(n,g)^{116m}In	1081,02	7,89%	0,00	-100,00%	42,26	-96,09%	31,06	-97,13%
	SPAC Fe	^{54}Fe(n,2n)^{53}Fe	86,09	13,64%	64,29	-25,31%	0,80	-99,07%	92,18	7,08%
		^{56}Fe(n,p)^{56}Mn	320,42	6,96%	336,39	4,98%	8,40	-97,38%	237,71	-25,81%
	SPAC Zr	^{90}Zr(n,2n)^{89}Zr	117,92	12,36%	77,07	-34,64%	0,78	-99,33%	96,24	-18,38%

Appendix B

MCNP6 input file for the response matrix calculation of the SPAC

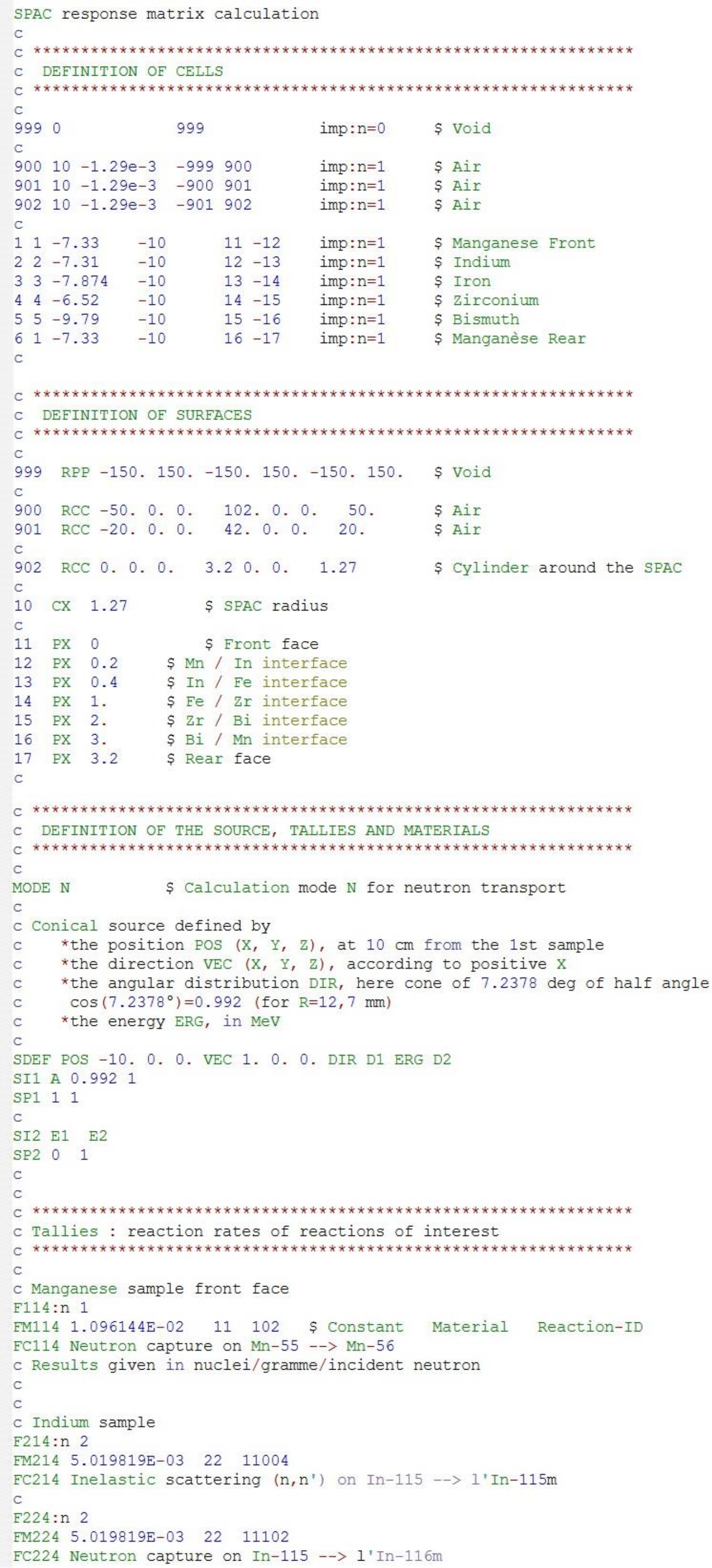

```
SPAC response matrix calculation
c
c ***************************************************************
c  DEFINITION OF CELLS
c ***************************************************************
c
999 0            999            imp:n=0     $ Void
c
900 10 -1.29e-3  -999 900       imp:n=1     $ Air
901 10 -1.29e-3  -900 901       imp:n=1     $ Air
902 10 -1.29e-3  -901 902       imp:n=1     $ Air
c
1 1 -7.33    -10      11 -12    imp:n=1     $ Manganese Front
2 2 -7.31    -10      12 -13    imp:n=1     $ Indium
3 3 -7.874   -10      13 -14    imp:n=1     $ Iron
4 4 -6.52    -10      14 -15    imp:n=1     $ Zirconium
5 5 -9.79    -10      15 -16    imp:n=1     $ Bismuth
6 1 -7.33    -10      16 -17    imp:n=1     $ Manganèse Rear
c

c ***************************************************************
c  DEFINITION OF SURFACES
c ***************************************************************
c
999  RPP -150. 150. -150. 150. -150. 150.   $ Void
c
900  RCC -50. 0. 0.   102. 0. 0.   50.      $ Air
901  RCC -20. 0. 0.   42. 0. 0.   20.       $ Air
c
902  RCC 0. 0. 0.   3.2 0. 0.   1.27        $ Cylinder around the SPAC
c
10  CX  1.27        $ SPAC radius
c
11  PX  0           $ Front face
12  PX  0.2     $ Mn / In interface
13  PX  0.4     $ In / Fe interface
14  PX  1.      $ Fe / Zr interface
15  PX  2.      $ Zr / Bi interface
16  PX  3.      $ Bi / Mn interface
17  PX  3.2     $ Rear face
c

c ***************************************************************
c  DEFINITION OF THE SOURCE, TALLIES AND MATERIALS
c ***************************************************************
c
MODE N          $ Calculation mode N for neutron transport
c
c Conical source defined by
c    *the position POS (X, Y, Z), at 10 cm from the 1st sample
c    *the direction VEC (X, Y, Z), according to positive X
c    *the angular distribution DIR, here cone of 7.2378 deg of half angle
c     cos(7.2378°)=0.992 (for R=12,7 mm)
c    *the energy ERG, in MeV
c
SDEF POS -10. 0. 0. VEC 1. 0. 0. DIR D1 ERG D2
SI1 A 0.992 1
SP1 1 1
c
SI2 E1  E2
SP2 0  1
c
c
c ***************************************************************
c Tallies : reaction rates of reactions of interest
c ***************************************************************
c
c Manganese sample front face
F114:n 1
FM114 1.096144E-02   11  102   $ Constant   Material   Reaction-ID
FC114 Neutron capture on Mn-55 --> Mn-56
c Results given in nuclei/gramme/incident neutron
c
c
c Indium sample
F214:n 2
FM214 5.019819E-03  22  11004
FC214 Inelastic scattering (n,n') on In-115 --> l'In-115m
c
F224:n 2
FM224 5.019819E-03  22  11102
FC224 Neutron capture on In-115 --> l'In-116m
```

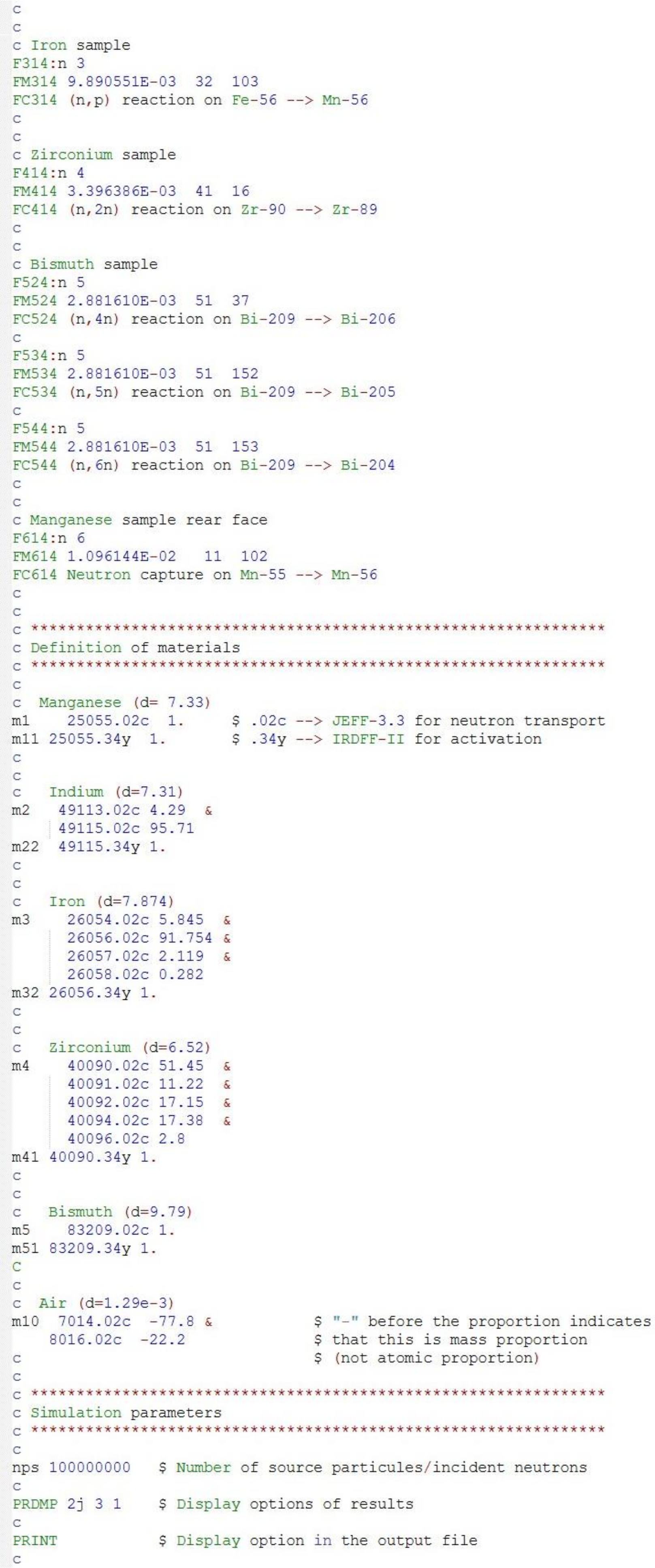

```
c
c
c Iron sample
F314:n 3
FM314 9.890551E-03  32  103
FC314 (n,p) reaction on Fe-56 --> Mn-56
c
c
c Zirconium sample
F414:n 4
FM414 3.396386E-03  41  16
FC414 (n,2n) reaction on Zr-90 --> Zr-89
c
c
c Bismuth sample
F524:n 5
FM524 2.881610E-03  51  37
FC524 (n,4n) reaction on Bi-209 --> Bi-206
c
F534:n 5
FM534 2.881610E-03  51  152
FC534 (n,5n) reaction on Bi-209 --> Bi-205
c
F544:n 5
FM544 2.881610E-03  51  153
FC544 (n,6n) reaction on Bi-209 --> Bi-204
c
c
c Manganese sample rear face
F614:n 6
FM614 1.096144E-02   11  102
FC614 Neutron capture on Mn-55 --> Mn-56
c
c
c ***************************************************************
c Definition of materials
c ***************************************************************
c
c  Manganese (d= 7.33)
m1    25055.02c  1.     $ .02c --> JEFF-3.3 for neutron transport
m11 25055.34y  1.       $ .34y --> IRDFF-II for activation
c
c
c   Indium (d=7.31)
m2   49113.02c 4.29  &
     49115.02c 95.71
m22  49115.34y 1.
c
c
c   Iron (d=7.874)
m3    26054.02c 5.845  &
      26056.02c 91.754 &
      26057.02c 2.119  &
      26058.02c 0.282
m32 26056.34y 1.
c
c
c   Zirconium (d=6.52)
m4    40090.02c 51.45  &
      40091.02c 11.22  &
      40092.02c 17.15  &
      40094.02c 17.38  &
      40096.02c 2.8
m41 40090.34y 1.
c
c
c   Bismuth (d=9.79)
m5    83209.02c 1.
m51 83209.34y 1.
C
c
c  Air (d=1.29e-3)
m10  7014.02c  -77.8 &           $ "-" before the proportion indicates
    8016.02c  -22.2              $ that this is mass proportion
c                                $ (not atomic proportion)
c
c ***************************************************************
c Simulation parameters
c ***************************************************************
c
nps 100000000   $ Number of source particules/incident neutrons
c
PRDMP 2j 3 1    $ Display options of results
c
PRINT           $ Display option in the output file
c
```

Appendix C

Results of calibration of bubble detectors performed with a ^{252}Cf neutron source

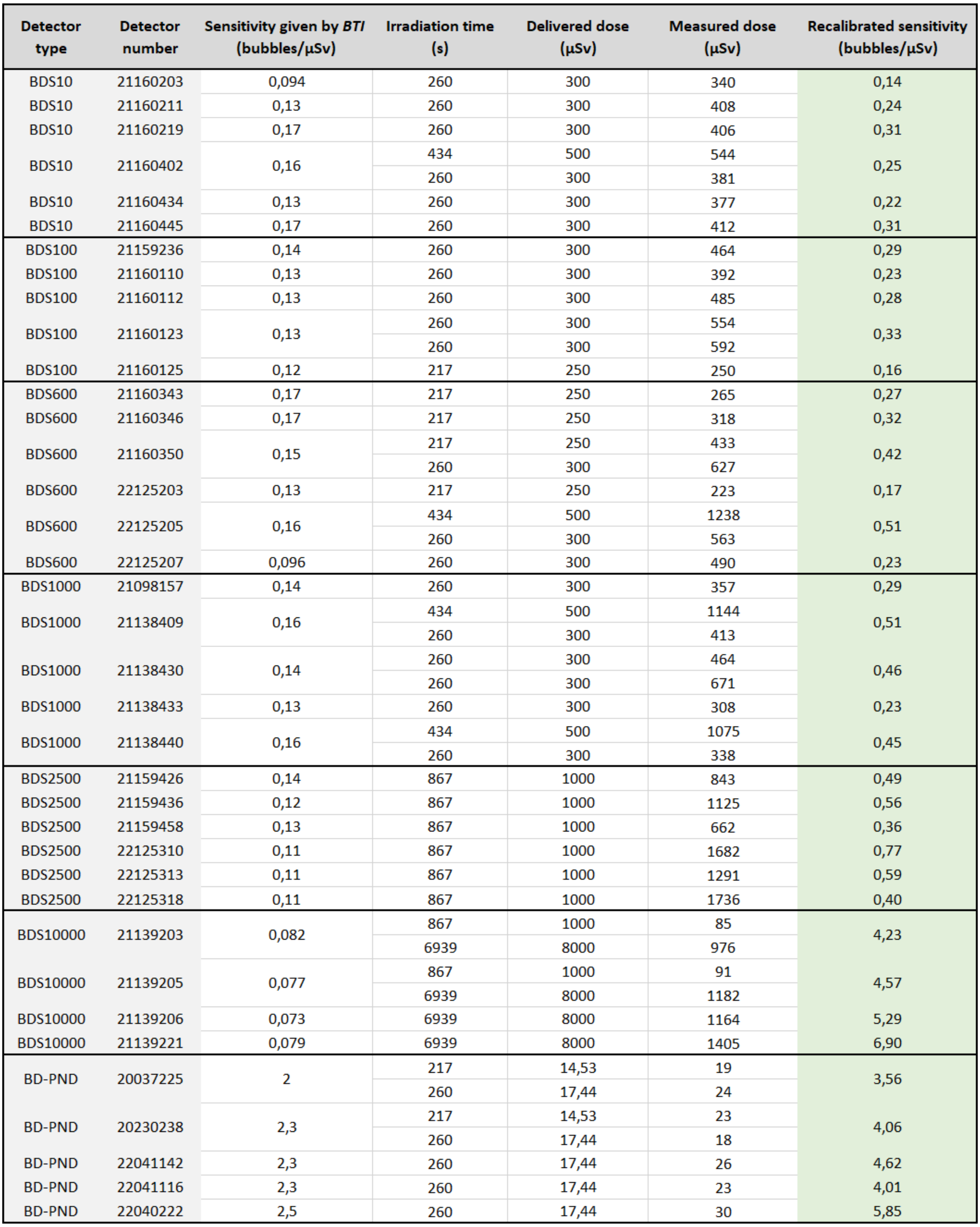

Detector type	Detector number	Sensitivity given by *BTI* (bubbles/µSv)	Irradiation time (s)	Delivered dose (µSv)	Measured dose (µSv)	Recalibrated sensitivity (bubbles/µSv)
BDS10	21160203	0,094	260	300	340	0,14
BDS10	21160211	0,13	260	300	408	0,24
BDS10	21160219	0,17	260	300	406	0,31
BDS10	21160402	0,16	434	500	544	0,25
			260	300	381	
BDS10	21160434	0,13	260	300	377	0,22
BDS10	21160445	0,17	260	300	412	0,31
BDS100	21159236	0,14	260	300	464	0,29
BDS100	21160110	0,13	260	300	392	0,23
BDS100	21160112	0,13	260	300	485	0,28
BDS100	21160123	0,13	260	300	554	0,33
			260	300	592	
BDS100	21160125	0,12	217	250	250	0,16
BDS600	21160343	0,17	217	250	265	0,27
BDS600	21160346	0,17	217	250	318	0,32
BDS600	21160350	0,15	217	250	433	0,42
			260	300	627	
BDS600	22125203	0,13	217	250	223	0,17
BDS600	22125205	0,16	434	500	1238	0,51
			260	300	563	
BDS600	22125207	0,096	260	300	490	0,23
BDS1000	21098157	0,14	260	300	357	0,29
BDS1000	21138409	0,16	434	500	1144	0,51
			260	300	413	
BDS1000	21138430	0,14	260	300	464	0,46
			260	300	671	
BDS1000	21138433	0,13	260	300	308	0,23
BDS1000	21138440	0,16	434	500	1075	0,45
			260	300	338	
BDS2500	21159426	0,14	867	1000	843	0,49
BDS2500	21159436	0,12	867	1000	1125	0,56
BDS2500	21159458	0,13	867	1000	662	0,36
BDS2500	22125310	0,11	867	1000	1682	0,77
BDS2500	22125313	0,11	867	1000	1291	0,59
BDS2500	22125318	0,11	867	1000	1736	0,40
BDS10000	21139203	0,082	867	1000	85	4,23
			6939	8000	976	
BDS10000	21139205	0,077	867	1000	91	4,57
			6939	8000	1182	
BDS10000	21139206	0,073	6939	8000	1164	5,29
BDS10000	21139221	0,079	6939	8000	1405	6,90
BD-PND	20037225	2	217	14,53	19	3,56
			260	17,44	24	
BD-PND	20230238	2,3	217	14,53	23	4,06
			260	17,44	18	
BD-PND	22041142	2,3	260	17,44	26	4,62
BD-PND	22041116	2,3	260	17,44	23	4,01
BD-PND	22040222	2,5	260	17,44	30	5,85

Bibliography

[1] J. M. Warren, H. Bilheux, M. Kang, S. Voisin, C.-L. Cheng, J. Horita and E. Perfect, "Neutron imaging reveals internal plant water dynamics," *Plant Soil,* vol. 366, pp. 683-693, 2013.

[2] T. M. Nakanishi and M. Matsubayashi, "Nondestructive water imaging by neutron beam analysis in living plants," *Journal of Plant Physiology,* vol. 151, no. 4, pp. 442-445, 1997.

[3] M. I. Prudêncio, C. Roldán, M. I. Dias, R. Marques, A. Eixea and V. Villaverde, "A micro-invasive approach using INAA for new insights into Palaeolithic flint archaeological artefacts," *Journal of Radioanalytical and Nuclear Chemistry,* vol. 308, no. 1, pp. 195-203, 2016.

[4] R. Hazenfratz, C. S. Munita, M. D. Glascock and E. G. Neves, "Study of exchange networks between two Amazon archaeological sites by INAA," *Journal of Radioanalytical and Nuclear Chemistry,* vol. 309, no. 1, pp. 195-205, 2016.

[5] A. Buffler and J. Tickner, "Detecting contraband using neutrons: challenges and future directions," *Radiation Measurements,* vol. 45, no. 10, pp. 1186-1192, 2010.

[6] J. Eberhardt, S. Rainey, R. Stevens, B. Sowerby and J. Tickner, "Fast neutron radiography scanner for the detection of contraband in air cargo containers," *Applied Radiation and Isotopes,* vol. 63, no. 2, pp. 179-188, 2005.

[7] A. Alejo, H. Ahmed, A. Green, S. R. Mirfayzi, M. Borghesi and S. Kar, "Recent advances in laser-driven neutron sources," *Il Nuovo Cimento C,* vol. 38, no. 6, pp. 1-7, 2016.

[8] J. Alvarez, J. Fernández-Tobias, K. Mima, S. Nakai, S. Kar, Y. Kato and J. Perlado, "Laser Driven Neutron Sources: Characteristics, Applications and Prospects," *Physics Procedia,* vol. 60, pp. 29-38, 2014.

[9] A. Macchi and C. Benedetti, "Ion acceleration by radiation pressure in thin and thick targets," *Nuc. Instrum. Meth. A,* vol. 620, no. 1, pp. 41-45, 2010.

[10] L. Disdier, J.-P. Garçonnet, G. Malka and J.-L. Miquel, "Fast Neutron Emission from a High-Energy Ion Beam Produced by a High-Intensity Subpicosecond Laser Pulse," *Physical Review Letters,* vol. 82, no. 7, pp. 1454-1457, 1999.

[11] K. L. Lancaster, S. Karsch, H. Habara, F. N. Beg, E. L. Clark, R. Freeman, M. H. Key, J. A. King, R. Kodama, K. Krushelnick, K. W. D. Ledingham, P. McKenna, C. D. Murphy, P. A. Norreys, R. Stephens, C. Stöeckl, Y. Toyama and M. S. Wei, "Characterization of Li7(p,n)7Be neutron yields from laser produced ion beams for fast neutron radiography," *Physics of Plasmas,* vol. 11, no. 7, pp. 3404-3408, 2004.

[12] A. Yogo, Z. Lan, Y. Arikawa, Y. Abe, S. R. Mirfayzi, T. Wei, T. Mori, D. Golovin, T. Hayakawa, N. Iwata, S. Fujioka, M. Nakai, Y. Sentoku, K. Mima, M. Murakami, M. Koizumi, F. Ito, J. Lee, T. Takahashi, K. Hironaka and S. Kar, "Laser-Driven Neutron Generation Realizing Single-Shot Resonance Spectroscopy," *Physical Review X,* vol. 13, no. 1, p. 011011, 2023.

[13] I. Pomerantz, E. McCary, A. R. Meadows, A. Arefiev, A. C. Bernstein, C. Chester, J. Cortez, M. E. Donovan, G. Dyer, E. W. Gaul, D. Hamilton, D. Kuk, A. C. Lestrade, C. Wang, T. Ditmire and B. M. Hegelich, "Ultrashort Pulsed Neutron Source," *Physical Review Letters,* vol. 113, no. 18, p. 184801, 2014.

[14] A. Kleinschmidt, V. Bagnoud, O. Deppert, A. Favalli, S. Frydrych, J. Hornung, D. Jahn, G. Schaumann, A. Tebartz, F. Wagner, G. Wurden, B. Zielbauer and M. Roth, "Intense, directed neutron beams from a laser-driven neutron source at PHELIX," *Physics of Plasmas,* vol. 25, no. 5, p. 053101, 2018.

[15] H. Geiger and E. Rutherford, "On the scattering of the α-particles by matter," *Proceedings of the Royal Society of London Series A,* vol. 81, no. 546, pp. 174-177, 1908.

[16] H. Geiger and E. Rutherford, "The scattering of the α-particles by matter," *Proceedings of the Royal Society of London Series A,* vol. 83, no. 565, pp. 492-504, 1910.

[17] E. Rutherford, "The scattering of the α and β particles by matter and the structure of the atom," *Phil. Mag. Ser. 6,* vol. 21, no. 125, pp. 669-688, 1910.

[18] E. Rutherford, "Scattering of the α particles by gases," *Phil. Mag. Ser. 6,* vol. 26, no. 154, pp. 702-712, 1913.

[19] J. Thomson, "Cathode Rays," *Phil. Mag.,* vol. 7, no. 44, pp. 237-265, 1904.

[20] E. Rutherford, "Collision of α particles with light atoms. IV. An anomalous effect in nitrogen," *The London, Edinburgh and Dublin Philosophical Magazine and Journal of Science,* vol. 37, no. 222, pp. 581-587, 1919.

[21] W. Bothe and H. Becker, "Künstliche Erregung von Kern-γ-Strahlen," *Z. Physik,* vol. 66, pp. 289-306, 1930.

[22] I. Joliot-Curie and F. Joliot-Curie, "Émission de protons de grande vitesse par les substances hydrogénées sous l'influence des rayons très pénétrants," *Comptes rends hebdomadaires des séances de l'Académie des Sciences,* vol. 198, no. 25, pp. 254-256, 1934.

[23] J. Chadwick, "The Existence of a Neutron," *Proceedings of the Royal Society of London Series A,* vol. 136, no. 830, pp. 692-708, 1932.

[24] M. Dewey, D. Gilliam, J. Nico, F. Wietfeldt, X. Fei, W. Snow, G. Greene, J. Pauwels, R. Eykens, A. Lamberty and J. Van Gestel, "Measurement of the Neutron Lifetime Using a Proton Trap," *Phys. Rev. Lett.,* vol. 91, no. 15, p. 152302, 2003.

[25] F. de Beer, "Neutron and X-ray tomography as research tools for applied research in South Africa," pp. 148-149, 2018.

[26] R. Taniguchi and N. Ito, "A Trial to Natural Neutron Radiography," *Physics Procedia,* vol. 69, pp. 374-381, 2015.

[27] E. Lehmann, "Basics of Neutron Imaging" Nuclear Fission - From Fundamentals to Applications, IntechOpen, 2024.

[28] N. Kardjilov, F. Fiori, G. Giunta, A. Hilger, F. Rustichelli, M. Strobl, J. Banhart and R. Triolo, "Neutron tomography for archaeology investigations," *Journal of Neutron Research,* vol. 14, no. 1, pp. 29-36, 206.

[29] G. Festa, G. Romanelli, R. Senesi, L. Arcidiacono, C. Scatigno, S. F. Parker, M. P. M. Marques and C. Andreani, "Neutrons for Cultural Heritage - Techniques, Sensors and Detection," *Sensors,* vol. 20, no. 2, p. 502, 2020.

[30] D. Berger, K. Hunger, S. Bolliger-Schreyer, D. Grolimund, S. Hartmann, J. Hovind, F. Müller, E. H. Lehmann, P. Vontobel and M. Wörle, "New insights into early bronze age damascene technique north of the alps," *The Antiquaries Journal,* vol. 93, pp. 25-53, 2013.

[31] I. S. Anderson, R. L. McGreevy and H. Z. Bilheux, Neutron Imaging and Applications - A Reference for the Imaging Community, Springer, 2009.

[32] F. Fiori, A. Hilger, N. Kardjilov and G. Albertini, "Crack detection in Al alloy using phase-contrast neutron radiography and tomography," *Meas. Sci. Technol.,* vol. 17, no. 9, p. 2479, 2006.

[33] N. Kardjilov, A. Hilger, I. Manke, M. Strobl, M. Dawson and J. Banhart, "New trends in neutron imaging," *Nuc. Instrum. Meth. A,* vol. 605, no. 1, pp. 13-15, 2009.

[34] A. E. Craft, D. M. Wachs, M. A. Okuniewski, D. L. Chichester, W. J. Williams, G. C. Papaioannou and A. T. Smolinski, "Neutron Radiography of Irradiated Nuclear Fuel at Idaho National Laboratory," *Physics Procedia,* vol. 69, pp. 483-490, 2015.

[35] H. Nozaki, H. Kondo, T. Shinohara, D. Setoyama, Y. Matsumoto, T. Sasaki, K. Isegawa and H. Hayashida, "In situ neutron imaging of lithium-ion batteries during heating to thermal runaway," *Sci. Rep.,* vol. 13, no. 1, p. 22082, 2023.

[36] R. F. Ziesche, N. Kardjilov, W. Kockelmann, D. J. L. Brett and P. R. Shearing, "Neutron imaging of lithium batteries," *Joule,* vol. 6, no. 1, pp. 35-52, 2022.

[37] M. Lanz, E. Lehmann, R. Imhof, I. Exnar and P. Novak, "In situ neutron radiography of lithium-ion batteries during charge/discharge cycling," *Journal of Power Sources,* vol. 101, no. 2, pp. 177-181, 2001.

[38] E. H. Lehmann, D. Mannes, A. P. Kaestner, J. Hovind, P. Trtik and M. Strobl, "The XTRA Option at the NEUTRA Facility - More Than 10 Years of Bi-Modal Neutron and X-ray Imaging at PSI," *Appl. Sci.,* vol. 11, no. 9, p. 3825, 2021.

[39] N. G. Cutmore, Y. Liu and J. R. Tickner, "Development and commercialization of a fast-neutron/x-ray Cargo Scanner," in *2010 IEEE International Conference on Technologies for Homeland Security (HST),* 2010.

[40] A. Kalicki, E. Panczyk, L. Rowinska, B. Sartowska, L. Walis, K. Pytel, B. Pytel, A. Koziel, L. Dabkowski, M. Wierzchnicka, L. Strzalkowski and T. Ostrowski, "Neutron autoradiography: working-out method and application in investigations of test paintings," *Radiation Measurements,* vol. 34, no. 1, pp. 567-569, 2001.

[41] A. Denke, C. Laurenze-Landsberg, K. Kleinert and B. Schröder-Smeibidl, Paintings Reveal Their Secrets: Neutron Autoradiography Allows the Visualization of Hidden Layers, 2017.

[42] G. B. González, "Investigating the Defect Structures in Transparent Conducting Oxides Using X-ray and Neutron Scattering Techniques," *Materials,* vol. 5, no. 5, pp. 818-850, 2012.

[43] M. P. Blakeley, "Neutron macromolecular crystallography," *Crystallography Reviews,* vol. 15, no. 3, pp. 157-218, 2009.

[44] M. P. Blakeley, P. Langan, N. Niimura and A. Podjarny, "Neutron crystallography: opportunities, challenges, and limitations," *Current Opinion in Structural Biology,* vol. 18, no. 5, pp. 593-600, 2008.

[45] S. C. Vogel, "A Review of Neutron Scattering Applications to Nuclear Materials," *ISRN Materials Science,* vol. 2013, no. 2356-7872, p. 302408, 2013.

[46] S. Schorr, "The crystal structure of kesterite type compounds: A neutron and X-ray diffraction study," *Solar Energy Materials and Solar Cells,* vol. 95, no. 6, pp. 1482-1488, 2011.

[47] H. Liu, Y. Chen, S. Hy, K. An, S. Venkatachalam, D. Qian, M. Zhang and Y. S. Meng, "Operando Lithium Dynamics in the Li-Rich Layered Oxide Cathode Material via Neutron Diffraction," *Advanced Energy Materials,* vol. 6, no. 7, p. 1502143, 2016.

[48] Y. Wei and M. J. A. Hore, "Characterizing polymer structure with small-angle neutron scattering; A Tutorial," *J. Appl. Phys.,* vol. 129, no. 17, p. 171101, 2021.

[49] K. Nishi, H. Asai, K. Fujii, Y.-S. Han, T.-H. Kim, T. Sakai and M. Shibayama, "Small-Angle Neutron Scattering Study on Defect-Controlled Polymer Networks," *Macromolecules,* vol. 47, no. 5, pp. 1801-1809, 2014.

[50] P. B. Yang, M. G. Davidson, K. J. Edler, N. Leaman, E. K. Bathke, S. N. McCormick, O. Matsarskaia and S. Brown, "Comparison of Cyclic and Linear Poly(lactide)s Using Small-Angle Neutron Scattering," *Macromolecules,* vol. 55, no. 24, pp. 11051-11058, 2022.

[51] M. Mathon, Y. d. Carlan, G. Geoffroy, X. Averty, A. Alamo and C. d. Novion, "A SANS investigation of the irradiation-enhanced α–α′ phases separation in 7–12 Cr martensitic steels," *Journal of Nuclear Materials,* vol. 312, no. 2, pp. 236-248, 2003.

[52] Z. Száraz, G. Török, V. Kršjak and P. Hähner, "SANS investigation of microstructure evolution in high chromium ODS steels after thermal ageing," *Journal of Nuclear Materials,* vol. 435, no. 1, pp. 56-62, 2013.

[53] M. Alinger, G. Odette and D. Hoelzer, "The development and stability of Y–Ti–O nanoclusters in mechanically alloyed Fe–Cr based ferritic alloys," *Journal of Nuclear Materials,* Vols. 329-333, pp. 382-386, 2004.

[54] L. Braun, M. Uhlig, R. v. Klitzing and R. A. Campbell, "Polymers and surfactants at fluid interfaces studied with specular neutron reflectometry," *Advances in Colloid and Interface Science,* vol. 247, pp. 130-148, 2017.

[55] A. Hafner, P. Gutfreund, B. P. Toperverg, M. Geoghegan and M. Sferrazza, "2D reflectometry for the investigation of polymer interfaces: off-specular neutron scattering," *Journal of Physics: Condensed Matter,* vol. 33, no. 36, p. 364002, 2021.

[56] J. Penfold and R. K. Thomas, "The application of the specular reflection of neutrons to the study of surfaces and interfaces," *Journal of Physics: Condensed Matter,* vol. 2, no. 6, p. 1369, 1990.

[57] G. Fragneto, "Neutrons and model membranes," *The European Physical Journal Special Topics,* vol. 213, no. 1, pp. 327-342, 2012.

[58] H. P. Wacklin, "Neutron reflection from supported lipid membranes," *Current Opinion in Colloid & Interface Science,* vol. 15, no. 6, pp. 445-454, 2010.

[59] A. Junghans, E. B. Watkins, R. D. Barker, S. Singh, M. J. Waltman, H. L. Smith, L. Pocivavsek and J. Majewski, "Analysis of biosurfaces by neutron reflectometry: From simple to complex interfaces," *Biointerphases,* vol. 10, no. 1, p. 019014, 2015.

[60] B. Pérot, C. Carasco, C. Eléon, S. Bernard, A. Sardet, W. E. Kanawati, C. Deyglun, G. Perret, G. Sannié, V. Valkovic, D. Sudac, J. Obhodas, S. Moretto, G. Nebbia, C. Fontana, F. Pino, A. Donzella, A. Zenoni, A. Iovene, C. Tintori, M. Moszynski and M. Gierlik, "Sea container inspection with tagged neutrons," *EPJ Nuclear Sci. Technol.,* vol. 7, no. 6, 2021.

[61] R. Zeisler, N. Vajda, G. Kennedy, G. Lamaze and G. L. Molnár, "Activation Analysis," in *Handbook of Nuclear Chemistry - Second Edition,* Springer, 2011, p. 1566.

[62] A. Buffler, "Contraband detection with fast neutrons," *Radiation Physics and Chemistry,* vol. 71, no. 3, pp. 853-861, 2004.

[63] H. E. Martz and S. Glenn, "Chapter 10 - Nuclear techniques to detect explosives," in *Counterterrorist Detection Techniques of Explosives (Second Edition),* 2022, pp. 339-381.

[64] J. B. Tandoh, B. J. B. Nyarko, S. B. Dampare, Y. Bredwa-Mensah, O. Gyampo and H. Ahiamadjie, "The use of INAA technique in provenance studies of ancient pottery from the Greater Accra region of Ghana," *Journal of Radioanalytical and Nuclear Chemistry,* vol. 284, no. 3, pp. 567-573, 2010.

[65] F. S. Olise, O. F. Oladejo, S. M. Almeida, O. K. Owoade, H. B. Olaniyi and M. C. Freitas, "Instrumental neutron activation analyses of uranium and thorium in samples from tin mining and processing sites," *Journal of Geochemical Exploration,* vol. 142, pp. 36-42, 2014.

[66] A. El-Taher and A. E. Khater, "Elemental characterization of Hazm El-Jalamid phosphorite by instrumental neutron activation analysis," *Applied Radiation and Isotopes,* vol. 114, pp. 121-127, 2016.

[67] I. A. Alnour, H. Wagiran, N. Ibrahim, S. Hamzah, B. S. Wee and M. S. Elias, "Rare earth elements determination and distribution patterns in granite rock samples by using INAA absolute method," *Journal of Radioanalytical and Nuclear Chemistry,* vol. 303, no. 3, pp. 1999-2009, 2015.

[68] A. El-Taher, "Rare-earth elements in Egyptian granite by instrumental neutron activation analysis," *Applied Radiation and Isotopes,* vol. 65, no. 4, pp. 458-464, 2007.

[69] V. N. Ermolaeva, A. V. Mikhailova, L. N. Kogarko and G. M. Kolesov, "Leaching rare-earth and radioactive elements from alkaline rocks of the Lovozero Massif, Kola Peninsula," *Geochemistry International,* vol. 54, no. 7, pp. 633-639, 2016.

[70] D. Brown, M. Chadwick, R. Capote, A. Kahler, A. Trkov, M. Herman, A. Sonzogni, Y. Danon, A. Carlson, M. Dunn and e. al., "ENDF/B-VIII.0: The 8th Major Release of the Nuclear Reaction Data Library with CIELO-project Cross Sections, New Standards and Thermal Scattering Data," *Nuclear Data Sheets,* vol. 148, pp. 1-142, 2018.

[71] H. Postma and P. Schillebeeckx, "Neutron Resonance Capture and Transmission Analysis," in *Encyclopedia of Analytical Chemistry,* John Wiley & Sons, Ltd, 2009.

[72] S. P, B. B, H. H and K. S, "Neutron resonance spectroscopy for the characterisation of materials and objects," Publications Office of the European Union, 2014.

[73] V. W. Yuan, J. D. Bowman, D. J. Funk, G. L. Morgan, R. L. Rabie, C. E. Ragan, J. P. Quintana and H. L. Stacy, "Shock Temperature Measurement Using Neutron Resonance Spectroscopy," *Phys. Rev. Lett.,* vol. 94, no. 4, p. 125504, 2005.

[74] H. J. Stone, M. G. Tucker, F. M. Meducin, M. T. Dove, S. A. T. Redfern, Y. Le Godec and W. G. Marshall, "Temperature measurement in a Paris-Edinburgh cell by neutron resonance spectroscopy," *Journal of Applied Physics,* vol. 98, no. 6, p. 064905, 2005.

[75] H. Stone, M. Tucker, Y. L. Godec, F. Méducin, E. Cope, S. Hayward, G. Ferlat, W. Marshall, S. Manolopoulos, S. Redfern and M. Dove, "Remote determination of sample temperature by neutron resonance spectroscopy," *Nucl. Instr. and Meth. A,* vol. 547, no. 2, pp. 601-615, 2005.

[76] A. Coc and E. Vangioni, "Primordial nucleosynthesis," *Internation Journal of Modern Physics E,* vol. 26, no. 7, p. 1741002, 2017.

[77] C. Iliadis, Nuclear Physics of Stars, Wiley-VCH, 2007.

[78] F. Käppeler, R. Gallino, S. Bisterzo and W. Aoki, "The s process: Nuclear physics, stellar models, and observations," *Reviews of Modern Physics,* vol. 83, no. 1, pp. 157-193, 2011.

[79] C. Fröhlich, G. Martínez-Pinedo, M. Liebendörfer, F.-K. Thielemann, E. Bravo, W. R. Hix, K. Langanke and N. T. Zinner, "Neutrino-Induced Nucleosynthesis of A>64 Nuclei: The νp Process," *Physical Review Letters,* vol. 96, no. 4, p. 142502, 2006.

[80] S. N. Chen, F. Negoita, K. Spohr, E. d’Humières, I. Pomerantz and J. Fuchs, "Extreme brightness laser-based neutron pulses as a pathway for investigating nucleosynthesis in the laboratory," *Matter and Radiation at Extremes,* vol. 4, no. 5, p. 054402, 2019.

[81] J. J. Cowan, C. Sneden, J. E. Lawler, A. Aprahamian, M. Wiescher, K. Langanke, G. MartÍnez-Pinedo and F.-K. Thielemann, "Origin of the heaviest elements: The rapid neutron-capture process," *Reviews of Modern Physics,* vol. 93, no. 85, p. 015002, 2021.

[82] M. Arnould, S. Goriely and K. Takahashi, "The r-process of stellar nucleosynthesis: Astrophysics and nuclear physics achievements and mysteries," *Physics Reports,* vol. 450, no. 4, pp. 97-213, 2007.

[83] E. Pian, P. D'Avanzo, S. Benetti, M. Branchesi, E. Brocato, S. Campana, E. Cappellaro, S. Covino, V. D'Elia and J. P. U. Fynbo, "Spectroscopic identification of r-process nucleosynthesis in a double neutron-star merger," *Nature,* vol. 551, pp. 67-70, 2017.

[84] D. Kasen, B. Metzger, J. Barnes, E. Quataert and E. Ramirez-Ruiz, "Origin of the heavy elements in binary neutron-star mergers from a gravitational-wave event," *Nature,* vol. 551, pp. 80-84, 2017.

[85] V. Horný, S. N. Chen, X. Davoine, L. Gremillet and J. Fuchs, "Quantitative feasibility study of sequential neutron captures using intense lasers," *Physical Review C,* vol. 109, no. 2, p. 025802, 2024.

[86] Nuclear Regulatory Commission, "Neutron Sources," 13 10 2010. [Online]. Available: https://www.nrc.gov/docs/ML1122/ML11229A704.pdf. [Accessed 12 07 2024].

[87] H. R. Vega-Carrillo and S. A. Martinez-Ovalle, "Few groups neutron spectra, and dosimetric features, of isotopic neutron sources," *Applied Radiation and Isotopes,* vol. 117, pp. 42-50, 2016.

[88] G. F. Knoll, Radiation Detection and Measurement, Third Edition ed., John Wiley & Sons Inc, 2000.

[89] International Atomic Energy Agency, Isotopic Neutron Sources for Neutron Activation Analysis, Vienna: TECDOC Series, 1988.

[90] Physikalisch-Technische Bundesanstalt, "Neutron reference fields from radionuclide sources," 2024. [Online]. Available: https://www.ptb.de/cms/en/ptb/fachabteilungen/abt6/fb-64/644-neutron-dosimetry/neutron-reference-fields-from-radionuclide-sources.html. [Accessed 15 07 2024].

[91] Y. Liu, B. Sowerby and J. Tickner, "Comparison of neutron and high-energy X-ray dual-beam radiography for air cargo inspection," *Applied Radiation and Isotopes*, vol. 66, no. 4, pp. 463-473, 2008.

[92] International Atomic Energy Agency, Compact Accelerator Based Neutron Sources, Vienna: TECDOC Series, 2021.

[93] Starfire Industries, "nGen Neutron Generators," 2023. [Online]. Available: https://www.starfireindustries.com/ngen.html#nGen400. [Accessed 15 07 2024].

[94] ThermoFisher, "P 385 Neutron Generator," 2024. [Online]. Available: https://www.thermofisher.com/order/catalog/product/10135952?SID=srch-srp-10135952. [Accessed 15 07 2024].

[95] ThermoFischer, "D 711 Neutron Generator," 2024. [Online]. Available: https://www.thermofisher.com/order/catalog/product/10135694?SID=srch-srp-10135694. [Accessed 15 07 2024].

[96] V. Gressier, J. F. Guerre-Chaley, V. Lacoste, L. Lebreton, G. Pelcot, J. L. Pochat, T. Bolognese-Milstajn and D. Champion, "AMANDE: a new facility for monoenergetic neutron fields production between 2 keV and 20 MeV," *Radiation Protection Dosimetry,* vol. 110, no. 1-4, pp. 49-52, 2004.

[97] M. Bunce, D. Thomas, N. Roberts, G. Taylor and A. Boso, "Plans for neutron metrology at NPL," *Journal of Physics: Conference Series,* vol. 1643, no. 1, p. 012201, 2020.

[98] R. Nolte and D. J. Thomas, "Monoenergetic fast neutron reference fields: I. Neutron production," *Metrologia,* vol. 48, no. 6, p. S263, 2011.

[99] B. Pavel, B. Radomír, G. Miloslav, P. Petr, P. Dušan, Š. Milan, Š. Jan and Z. Václav, "High-power TR-24 cyclotron-based p-n convertor cooled by submerged orifice jet," *EPJ Web of Conferences,* vol. 231, p. 03005, 2020.

[100] M. Mosconi, E. Musonza, A. Buffler, R. Nolte, S. Röttger and F. D. Smit, "Characterisation of the high-energy neutron beam at iThemba LABS," *Radiation Measurements,* vol. 45, no. 10, pp. 1342-1345, 2010.

[101] G. S. Bauer, "Physics and technology of spallation neutron sources," *Nuc. Instrum. Meth. A,* vol. 463, no. 3, pp. 505-543, 2001.

[102] T. Brückel, G. Heger, D. Richter, G. Roth and R. Zorn, Neutron Scattering, Jülich: Forschungszentrum Jülich GmbH, 2012.

[103] S. Teixeira, G. Zaccai, J. Ankner, M. Bellissent-Funel, R. Bewley, M. Blakeley, P. Callow, L. Coates, R. Dahint, R. Dalgliesh, N. Dencher, V. Forsyth, G. Fragneto, B. Frick, R. Gilles, T. Gutberlet, M. Haertlein, T. Hauß and W. Häußler, "New sources and instrumentation for neutrons in biology," *Chemical Physics,* vol. 345, no. 2, pp. 133-151, 2008.

[104] International Atomic Energy Agency, "Development opportunities for small and medium scale accelerator driven neutron sources," TECDOC Series, Vienna, 2004.

[105] European Investment Bank, "European Spallation Neutron Source - ESS," 4 07 2016. [Online]. Available: https://www.eib.org/en/projects/pipelines/all/20160569. [Accessed 17 07 2024].

[106] I. S. Anderson, C. Andreani, J. M. Carpenter, G. Festa, G. Gorini, C.-K. Loong and R. Senesi, "Research opportunities with compact accelerator-driven neutron sources," *Physics Reports,* vol. 654, pp. 1-58, 2016.

[107] ESFRI Physical Sciences and Engineering Strategy Working Group, Neutron Landscape Group, "Neutron scattering facilities in Europe - Present statuts and future perspectives," Milan, 2016.

[108] A. Einstein, "Zur Quantentheorie der Strahlung (On the Quantum Theory of Radiation)," *Physika Zeitschrift,* vol. 18, pp. 121-128, 1917.

[109] T. H. Maiman, "Stimulated Optical Radiation in Ruby," *Nature,* vol. 187, pp. 493-494, 1960.

[110] F. J. McClung and R. W. Hellwarth, "Giant Optical Pulsations from Ruby," *Journal of Applied Physics,* vol. 33, no. 3, pp. 828-829, 1962.

[111] L. E. Hargrove, R. L. Fork and M. A. Pollack, "Locking of He–Ne Laser Modes Induced by Synchronous Intracavity Modulation," *Applied Physics Letters,* vol. 5, no. 1, pp. 4-5, 1964.

[112] D. Strickland and G. Mourou, "Compression of amplified chirped optical pulses," *Optics Communications,* vol. 55, no. 6, pp. 447-449, 1985.

[113] R. Baumgartner and R. Byer, "Optical parametric amplification," *IEEE Journal of Quantum Electronics,* vol. 15, no. 6, pp. 432-444, 1979.

[114] R. Danielius, A. Piskarskas, A. Stabinis, G. P. Banfi, P. D. Trapani and R. Righini, "Traveling-wave parametric generation of widely tunable, highly coherent femtosecond light pulses," *Journal of the Optical Society of America B,* vol. 10, no. 11, pp. 2222-2232, 1993.

[115] C. N. Danson, C. Haefner, J. Bromage, T. Butcher, J.-C. F. Chanteloup, E. A. Chowdhury, A. Galvanauskas, L. A. Gizzi, J. Hein and D. I. Hillier, "Petawatt and exawatt class lasers worldwide," *High Power Laser Science and Engineering,* vol. 7, p. e54, 2019.

[116] K. Burdonov, A. Fazzini, V. Lelasseux, J. Albrecht, P. Antici, Y. Ayoul, A. Beluze, D. Cavanna, T. Ceccotti, M. Chabanis, A. Chaleil, S. N. Chen, Z. Chen, F. Consoli, M. Cuciuc, X. Davoine, J. P. Delaneau, E. d’Humières and J. Dubois, "Characterization and performance of the Apollon short-focal-area facility following its commissioning at 1 PW level," *Matter and Radiation at Extremes,* vol. 6, no. 6, p. 064402, 2021.

[117] W. Yao, R. Lelièvre, T. Waltenspiel, I. Cohen, A. Allaoua, P. Antici, A. Beck, E. Cohen, X. Davoine, E. d’Humières, Q. Ducasse, E. Filippov, C. Gautier, L. Gremillet and P. Koseoglou, "Enhanced Energy, Conversion Efficiency and Collimation of Protons Driven by High-Contrast and Ultrashort Laser Pulses," *Applied Sciences,* vol. 14, no. 14, p. 6101, 2024.

[118] J. W. Yoon, Y. G. Kim, I. W. Choi, J. H. Sung, H. W. Lee, S. K. Lee and C. H. Nam, "Realization of laser intensity over 1023 W/cm2," *Optica,* vol. 8, no. 5, pp. 630-635, 2021.

[119] K. Nakamura, H.-S. Mao, A. J. Gonsalves, H. Vincenti, D. E. Mittelberger, J. Daniels, A. Magana, C. Toth and W. P. Leemans, "Diagnostics, Control and Performance Parameters for the BELLA High Repetition Rate Petawatt Class Laser," *IEEE Journal of Quantum Electronics,* vol. 53, no. 4, pp. 1-21, 2017.

[120] A. Gold and H. B. Bebb, "Theory of Multiphoton Ionization," *Physical Review Letters,* vol. 14, pp. 60-63, 1965.

[121] G. Mainfray and G. Manus, "Multiphoton ionization of atoms," *Reports on Progress in Physics,* vol. 54, no. 10, pp. 1333-1372, 1991.

[122] S. Augst, D. Strickland, D. D. Meyerhofer, S. L. Chin and J. H. Eberly, "Tunneling ionization of noble gases in a high-intensity laser field," *Physical Review Letters,* vol. 63, pp. 2212-2215, 1989.

[123] N. B. Delone and V. P. Krainov, "Tunneling and barrier-suppression ionization of atoms and ions in a laser radiation field," *Physics-Uspekhi,* vol. 41, no. 5, p. 469, 1998.

[124] V. P. KRAINOV, "Theory of Barrier-suppression Ionization of Atoms," *Journal of Nonlinear Optical Physics & Materials,* vol. 04, no. 04, pp. 775-798, 1995.

[125] P. Mora, Plasmas créés par laser, EDP Sciences, 2021.

[126] M. Borghesi, J. Fuchs, S. V. Bulanov, A. J. MacKinnon, P. K. Patel and M. Roth, "Fast Ion Generation by High-Intensity Laser Irradiation of Solid Targets and Applications," *Fusion Science and Technology,* vol. 49, no. 3, pp. 412-439, 2006.

[127] P. Mulser and D. Bauer, High Power Laser-Matter Interaction, Berlin: Springer, 2010.

[128] M. Roth and M. Schollmeier, "Ion Acceleration - Target Normal Sheath Acceleration," *Proceedings of the 2014 CAS-CERN Accelerator School: Plasma Wake Acceleration,* vol. 1, pp. 231-270, 2016.

[129] E. L. Clark, K. Krushelnick, J. R. Davies, M. Zepf, M. Tatarakis, F. N. Beg, A. Machacek, P. A. Norreys, M. I. K. Santala, I. Watts and A. E. Dangor, "Measurements of Energetic Proton Transport through Magnetized Plasma from Intense Laser Interactions with Solids," *Physical Review Letters,* vol. 84, no. 4, pp. 670-673, 2000.

[130] R. A. Snavely, M. H. Key, S. P. Hatchett, T. E. Cowan, M. Roth, T. W. Phillips, M. A. Stoyer, E. A. Henry, T. C. Sangster, M. S. Singh, S. C. Wilks, A. MacKinnon, A. Offenberger, D. M. Pennington, K. Yasuike, A. B. Langdon and B. F. Lasinski, "Intense High-Energy Proton Beams from Petawatt-Laser Irradiation of Solids," *Physical Review Letters,* vol. 85, no. 14, pp. 2945-2948, 2000.

[131] A. Macchi, M. Borghesi and M. Passoni, "Ion acceleration by superintense laser-plasma interaction," *Reviews of Modern Physics,* vol. 85, no. 2, pp. 751-793, 2013.

[132] S. C. Wilks, A. B. Langdon, T. E. Cowan, M. Roth, M. Singh, S. Hatchett, M. H. Key, D. Pennington, A. MacKinnon and R. A. Snavely, "Energetic proton generation in ultra-intense laser–solid interactions," *Physics of Plasmas,* vol. 8, no. 2, pp. 542-549, 2001.

[133] L. Romagnani, J. Fuchs, M. Borghesi, P. Antici, P. Audebert, F. Ceccherini, T. a. G. T. Cowan, S. Kar, A. Macchi, P. Mora, G. Pretzler, A. Schiavi, T. Toncian and O. Willi, "Dynamics of Electric Fields Driving the Laser Acceleration of Multi-MeV Protons," *Physical Review Letters,* vol. 95, no. 19, p. 195001, 2005.

[134] M. Allen, P. K. Patel, A. Mackinnon, D. Price, S. Wilks and E. Morse, "Direct Experimental Evidence of Back-Surface Ion Acceleration from Laser-Irradiated Gold Foils," *Physical Review Letters,* vol. 93, no. 26, p. 265004, 2004.

[135] J. Fuchs, P. Antici, E. d'Humières, E. Lefebvre, M. Borghesi, E. Brambink, C. A. Cecchetti, M. Kaluza, V. Malka, M. Manclossi, S. Meyroneinc, P. Mora, J. Schreiber, T. Toncian, H. Pépin and P. Audebert, "Laser-driven proton scaling laws and new paths towards energy increase," *Nature Physics,* vol. 2, no. 1, pp. 48-54, 2006.

[136] M. Zimmer, S. Scheuren, T. Ebert, G. Schaumann, B. Schmitz, J. Hornung, V. Bagnoud, C. Rödel and M. Roth, "Analysis of laser-proton acceleration experiments for development of empirical scaling laws," *Physical Review E,* vol. 104, no. 4, p. 045210, 2021.

[137] E. Catrix, F. Boivin, K. Langlois, S. Vallières, C. Y. Boynukara, S. Fourmaux and P. Antici, "Stable high repetition-rate laser-driven proton beam production for multidisciplinary applications on the advanced laser light source ion beamline," *Review of Scientific Instruments,* vol. 94, no. 10, p. 103003, 2023.

[138] D. Raffestin, L. Lecherbourg, I. Lantuéjoul, B. Vauzour, P. E. Masson-Laborde, X. Davoine, N. Blanchot, J. L. Dubois, X. Vaisseau, E. d'Humières, L. Gremillet, A. Duval, C. Reverdin, B. Rosse, G. Boutoux, J. E. Ducret and C. Rousseaux, "Enhanced ion acceleration using the high-energy petawatt PETAL laser," *Matter and Radiation at Extremes,* vol. 6, no. 5, p. 056901, 2021.

[139] T. Ziegler, I. Göthel, S. Assenbaum, C. Bernert, F.-E. Brack, T. E. Cowan, N. P. Dover, L. Gaus, T. Kluge, S. Kraft, F. Kroll, J. Metzkes-Ng, M. Nishiuchi and I. Prencipe, "Laser-driven high-energy proton beams from cascaded acceleration regimes," *Nature Physics,* vol. 20, no. 7, pp. 1211-1216, 2024.

[140] L. Yin, B. J. Albright, B. M. Hegelich and J. C. Fernández, "GeV laser ion acceleration from ultrathin targets: The laser break-out afterburner," *Laser and Particle Beams,* vol. 24, pp. 291-298, 2006.

[141] D. Jung, L. Yin, D. C. Gautier, H.-C. Wu, S. Letzring, B. Dromey, R. Shah, S. Palaniyappan, T. Shimada, R. P. Johnson, J. Schreiber, D. Habs, J. C. Fernández, B. M. Hegelich and B. J.

Albright, "Laser-driven 1 GeV carbon ions from preheated diamond targets in the break-out afterburner regime," *Physics of Plasmas*, vol. 20, no. 8, p. 083103, 2013.

[142] B. M. Hegelich, I. Pomerantz, L. Yin, H. C. Wu, D. Jung, B. J. Albright, D. C. Gautier, S. Letzring, S. Palaniyappan, R. Shah, K. Allinger, R. Hörlein, J. Schreiber, D. Habs, J. Blakeney, G. Dyer, L. Fuller, E. Gaul, E. Mccary, A. R. Meadows and C. Wang, "Laser-driven ion acceleration from relativistically transparent nanotargets," *New Journal of Physics,* vol. 15, no. 8, p. 085015, 2013.

[143] P. L. Poole, L. Obst, G. E. Cochran, J. Metzkes, H.-P. Schlenvoigt, I. Prencipe, T. Kluge, T. Cowan, U. Schramm, D. W. Schumacher and K. Zeil, "Laser-driven ion acceleration via target normal sheath acceleration in the relativistic transparency regime," *New Journal of Physics,* vol. 20, no. 1, p. 013019, 2018.

[144] A. Macchi, S. Veghini and F. Pegoraro, ""Light Sail" Acceleration Reexamined," *Physical Review Letters,* vol. 103, no. 8, p. 085003, 2009.

[145] P. Liu, J. Qu, X. Liu, X. Li, L. Cai, J. Tang and Q. Kong, "Beam quality improvement in the later stage of radiation pressure acceleration," *Physical Review Accelerators and Beams,* vol. 23, no. 1, p. 011303, 2020.

[146] A. McIlvenny, D. Doria, L. Romagnani, H. Ahmed, N. Booth, E. J. Ditter, O. C. Ettlinger, G. S. Hicks, P. Martin, G. G. Scott, S. D. R. Williamson, A. Macchi, P. McKenna, Z. Najmudin, D. Neely, S. Kar and M. Borghesi, "Selective Ion Acceleration by Intense Radiation Pressure," *Physical Review Letters,* vol. 127, no. 19, p. 194801, 2021.

[147] I. J. Kim, K. H. Pae, I. W. Choi, C.-L. Lee, H. T. Kim, H. Singhal, J. H. Sung, S. K. Lee, H. W. Lee, P. V. Nickles, T. M. Jeong, C. M. Kim and C. H. Nam, "Radiation pressure acceleration of protons to 93 MeV with circularly polarized petawatt laser pulses," *Physics of Plasmas,* vol. 23, no. 7, p. 070701, 2016.

[148] S. Kar, K. F. Kakolee, B. Qiao, A. Macchi, M. Cerchez, D. Doria, M. Geissler, P. McKenna, D. Neely, J. Osterholz, R. Prasad, K. Quinn, B. Ramakrishna, G. Sarri, O. Willi, X. Y. Yuan, M. Zepf and M. Borghesi, "Ion Acceleration in Multispecies Targets Driven by Intense Laser Radiation Pressure," *Physical Review Letters,* vol. 109, no. 18, p. 185006, 2012.

[149] J.-R. Marquès, L. Lancia, P. Loiseau, P. Forestier-Colleoni, M. Tarisien, E. Atukpor, V. Bagnoud, C. Brabetz, F. Consoli, J. Domange, F. Hannachi, P. Nicolaï, M. Salvadori and B. Zielbauer, "Collisionless shock acceleration of protons in a plasma slab produced in a gas jet by the collision of two laser-driven hydrodynamic shockwaves," *Matter and Radiation at Extremes,* vol. 9, no. 2, p. 024001, 2023.

[150] S. Tochitsky, A. Pak, F. Fiuza, D. Haberberger, N. Lemos, A. Link, D. H. Froula and C. Joshi, "Laser-driven collisionless shock acceleration of ions from near-critical plasmas," *Physics of Plasmas,* vol. 27, no. 8, p. 083102, 2020.

[151] A. Pak, S. Kerr, N. Lemos, A. Link, P. Patel, F. Albert, L. Divol, B. B. Pollock, D. Haberberger, D. Froula, M. Gauthier, S. H. Glenzer, A. Longman, L. Manzoor, R. Fedosejevs, S. Tochitsky, C. Joshi and F. Fiuza, "Collisionless shock acceleration of narrow energy spread ion beams from mixed species plasmas using $1\text{ }\text{ }\ensuremath{\mu}\mathrm{m}$ lasers," *Physical Review Accelerators and Beams,* vol. 21, no. 10, p. 103401, 2018.

[152] D. Haberberger, S. Tochitsky, F. Fiuza, C. Gong, R. A. Fonseca, L. O. Silva, W. B. Mori and C. Joshi, "Collisionless shocks in laser-produced plasma generate monoenergetic high-energy proton beams," *Nature Physics,* vol. 8, no. 1, pp. 95-99, 2012.

[153] K. W. D. Ledingham, I. Spencer, T. McCanny, R. P. Singhal, M. I. K. Santala, E. Clark, I. Watts, F. N. Beg, M. Zepf, K. Krushelnick, M. Tatarakis, A. E. Dangor, P. A. Norreys, R. Allott, D. Neely, R. J. Clark, A. C. Machacek and J. S. Wark, "Photonuclear Physics when a Multiterawatt Laser Pulse Interacts with Solid Targets," *Physical Review Letter,* vol. 84, no. 5, pp. 899-902, 2000.

[154] C. Danson, P. Brummitt, R. Clarke, J. Collier, B. Fell, A. Frackiewicz, S. Hancock, S. Hawkes, C. Hernandez-Gomez, P. Holligan, M. Hutchinson, A. Kidd, W. Lester, I. Musgrave, D. Neely, D. Neville, P. Norreys and D. Pepler, "Vulcan Petawatt — An ultra-high-intensity interaction facility," *Nuclear Fusion,* vol. 44, no. 12, p. S239, 2004.

[155] M. Martinez, E. Gaul, T. Ditmire, S. Douglas, D. Gorski, W. Henderson, J. Blakeney, D. Hammond, M. Gerity, J. Caird, A. Erlandson, I. Iovanovic, C. Ebbers and B. Molander, "The Texas Petawatt Laser," in *Laser-Induced Damage in Optical Materials,* 2006.

[156] M. M. Günther, O. N. Rosmej, P. Tavana, M. Gyrdymov, A. Skobliakov, A. Kantsyrev, S. Zähter, N. G. Borisenko, A. Pukhov and N. E. Andreev, "Forward-looking insights in laser-generated ultra-intense γ-ray and neutron sources for nuclear application and science," *Nature Communications,* vol. 13, no. 1, p. 170, 2022.

[157] V. Bagnoud, B. Aurand, A. Blazevic, S. Borneis, C. Bruske, B. Ecker, U. Eisenbarth, J. Fils, A. Frank, E. Gaul, S. Goette, C. Haefner, T. Hahn, K. Harres, H.-M. Heuck, D. Hochhaus, D. H. H. Hoffmann, D. Javorková, H.-J. Kluge and T. Kuehl, "Commissioning and early experiments of the PHELIX facility," *Applied Physics B,* vol. 100, no. 1, pp. 137-150, 2010.

[158] J. Lilley, Nuclear Physics: Principles and Applications, Wiley, 2013.

[159] I. Cohen, T. Cohen, A. Levinson, M. Elkind, Y. Rakovsky, A. Levanon, D. Michaeli, E. Cohen, A. Beck and I. Pomerantz, "Accumulated laser-photoneutron generation," *The European Physical Journal Plus,* vol. 139, no. 7, p. 585, 2024.

[160] C. Ur, D. Balabanski, G. Cata-Danil, S. Gales, I. Morjan, O. Tesileanu, D. Ursescu, I. Ursu and N. Zamfir, "The ELI–NP facility for nuclear physics," *Nuc. Instrum. Meth. B,* vol. 355, pp. 198-202, 2015.

[161] T. Ditmire, J. Zweiback, V. P. Yanovsky, T. E. Cowan, G. Hays and K. B. Wharton, "Nuclear fusion in gases of deuterium clusters heated with a femtosecond laser," *Physics of Plasmas,* vol. 7, no. 5, pp. 1993-1998, 2000.

[162] H. Y. Lu, J. S. Liu, C. Wang, W. T. Wang, Z. L. Zhou, A. H. Deng, C. Q. Xia, Y. Xu, X. M. Lu, Y. H. Jiang, Y. X. Leng, X. Y. Liang, G. Q. Ni, R. X. Li and Z. Z. Xu, "Efficient fusion neutron generation from heteronuclear clusters in intense femtosecond laser fields," *Physical Review A,* vol. 80, no. 5, p. 051201, 2009.

[163] A. Curtis, R. Hollinger, C. Calvi, S. Wang, S. Huanyu, Y. Wang, A. Pukhov, V. Kaymak, C. Baumann, J. Tinsley, V. N. Shlyaptsev and J. J. Rocca, "Ion acceleration and D-D fusion neutron generation in relativistically transparent deuterated nanowire arrays," *Physical Review Research,* vol. 3, no. 4, p. 043181, 2021.

[164] K. W. Madison, P. K. Patel, M. Allen, D. Price and T. Ditmire, "Investigation of fusion yield from exploding deuterium-cluster plasmas produced by 100-TW laser pulses," *J. Opt. Soc. Am. B,* vol. 20, no. 1, pp. 113-117, 2003.

[165] L. Willingale, G. M. Petrov, A. Maksimchuk, J. Davis, R. R. Freeman, A. S. Joglekar, T. Matsuoka, C. D. Murphy, V. M. Ovchinnikov, A. G. R. Thomas, L. Van Woerkom and K. Krushelnick, "Comparison of bulk and pitcher-catcher targets for laser-driven neutron production," *Physics of Plasmas,* vol. 18, no. 8, p. 083106, 2011.

[166] A. Alejo, A. G. Krygier, H. Ahmed, J. T. Morrison, R. J. Clarke, J. Fuchs, A. Green, J. S. Green, D. Jung, A. Kleinschmidt, Z. Najmudin, H. Nakamura, P. Norreys, M. Notley, M. Oliver, M. Roth, L. Vassura, M. Zepf, M. Borghesi, R. R. Freeman and S. Kar, "High flux, beamed neutron sources employing deuteron-rich ion beams from D2O-ice layered targets," *Plasma Physics and Controlled Fusion,* vol. 59, no. 6, p. 064004, 2017.

[167] J. Nuckolls, L. Wood, A. Thiessen and G. Zimmerman, "Laser Compression of Matter to Super-High Densities: Thermonuclear (CTR) Applications," *Nature,* vol. 239, no. 5368, pp. 139-142, 1972.

[168] S. Eliezer and K. Mima, Applications of Laser-Plasma Interactions, CRC Press, 2009.

[169] T. Boehly, D. Brown, R. Craxton, R. Keck, J. Knauer, J. Kelly, T. Kessler, S. Kumpan, S. Loucks, S. Letzring, F. Marshall, R. McCrory, S. Morse, W. Seka, J. Soures and C. Verdon, "Initial performance results of the OMEGA laser system," *Optics Communications,* vol. 133, no. 1, pp. 495-506, 1997.

[170] V. Gopalaswamy, R. Betti, J. P. Knauer, N. Luciani, D. Patel, K. M. Woo, A. Bose, I. V. Igumenshchev, E. M. Campbell, K. S. Anderson, K. A. Bauer, M. J. Bonino, D. Cao, A. R. Christopherson, G. W. Collins, T. J. B. Collins and J. R. Davies, "Tripled yield in direct-drive laser fusion through statistical modelling," *Nature,* vol. 565, no. 7741, pp. 581-586, 2019.

[171] S. P. Regan, V. N. Goncharov, I. V. Igumenshchev, T. C. Sangster, R. Betti, A. Bose, T. R. Boehly, M. J. Bonino, E. M. Campbell, D. Cao, T. J. B. Collins, R. S. Craxton, A. K. Davis, J. A. Delettrez, D. H. Edgell, R. Epstein and C. Forrest, "Demonstration of Fuel Hot-Spot Pressure in Excess of 50 Gbar for Direct-Drive, Layered Deuterium-Tritium Implosions on OMEGA," *Physical Review Letters,* vol. 117, no. 2, p. 025001, 2016.

[172] T. R. Boehly, R. S. Craxton, T. H. Hinterman, J. H. Kelly, T. J. Kessler, S. A. Kumpan, S. A. Letzring, R. L. McCrory, S. F. B. Morse, W. Seka, S. Skupsky, J. M. Soures and C. P. Verdon, "The upgrade to the OMEGA laser system," *Review of Scientific Instruments,* vol. 66, no. 1, pp. 508-510, 1995.

[173] J.-L. Miquel and E. Prene, "LMJ & PETAL status and program overview," *Nuclear Fusion,* vol. 59, no. 3, p. 032005, 2019.

[174] W. Cayzac, G. Boutoux, S. Brygoo, A. Denoeud, S. Depierreux, V. Tassin, F. Albert, E. Alozy, C. Baccou, D. Batani, N. Blanchot, M. Bonneau, M. Bonnefille, R. Botrel, C. Bowen, P. Bradford, M. Brochier, T. Caillaud, A. Chaleil, S. Chardavoine and C. Chollet, "Experimental capabilities of the LMJ-PETAL facility," *High Energy Density Physics,* vol. 52, p. 101125, 2024.

[175] S. Liberatore, P. Gauthier, J. L. Willien, P. E. Masson-Laborde, F. Philippe, O. Poujade, E. Alozy, R. Botrel, G. Boutoux, J. Bray, T. Caillaud, C. Chicanne, C. Chollet, A. Debayle, S. Depierreux, W. Duchastenier, M. Ferri and O. Henry, "First indirect drive inertial confinement fusion campaign at Laser Megajoule," *Physics of Plasmas,* vol. 30, no. 12, p. 122707, 2023.

[176] E. I. Moses, "The National Ignition Facility and the National Ignition Campaign," *IEEE Transactions on Plasma Science,* vol. 38, no. 4, pp. 684-689, 2010.

[177] H. Abu-Shawareb, "Achievement of Target Gain Larger than Unity in an Inertial Fusion Experiment," *Physical Review Letters,* vol. 132, no. 6, p. 065102, 2024.

[178] S. H. Batha, R. Aragonez, F. L. Archuleta, T. N. Archuleta, J. F. Benage, J. A. Cobble, J. S. Cowan, V. E. Fatherley, K. A. Flippo, D. C. Gautier, R. P. Gonzales, S. R. Greenfield, B. M. Hegelich, T. R. Hurry, R. P. Johnson and J. L. Kline, "TRIDENT high-energy-density facility experimental capabilities and diagnostics," *Review of Scientific Instruments,* vol. 79, no. 10, p. 10F305, 2008.

[179] D. Jung, K. Falk, N. Guler, O. Deppert, M. Devlin, A. Favalli, J. C. Fernandez, D. C. Gautier, M. Geissel, R. Haight, C. E. Hamilton, B. M. Hegelich, R. P. Johnson, F. Merrill, G. Schaumann, K. Schoenberg, M. Schollmeier and T. Shimada, "Characterization of a novel, short pulse laser-driven neutron source," *Physics of Plasmas,* vol. 20, no. 5, p. 056706, 2013.

[180] M. Roth, D. Jung, K. Falk, N. Guler, O. Deppert, M. Devlin, A. Favalli, J. Fernandez, D. Gautier, M. Geissel, R. Haight, C. E. Hamilton, B. M. Hegelich, R. P. Johnson, F. Merrill, G. Schaumann, K. Schoenberg, M. Schollmeier and T. Shimada, "Bright Laser-Driven Neutron Source Based on the Relativistic Transparency of Solids," *Physical Review Letters,* vol. 110, no. 4, p. 044802, 2013.

[181] N. Guler, P. Volegov, A. Favalli, F. E. Merrill, K. Falk, D. Jung, J. L. Tybo, C. H. Wilde, S. Croft, C. Danly, O. Deppert, M. Devlin, J. Fernandez, D. C. Gautier, M. Geissel, R. Haight, C. E. Hamilton, B. M. Hegelich and D. Henzlova, "Neutron imaging with the short-pulse laser

driven neutron source at the Trident laser facility," *Journal of Applied Physics,* vol. 120, no. 15, p. 154901, 2016.

[182] M. Zimmer, S. Scheuren, A. Kleinschmidt, N. Mitura, A. Tebartz, G. Schaumann, T. Abel, T. Ebert, M. Hesse, Ş. Zähter, S. C. Vogel, O. Merle, R.-J. Ahlers, S. Duarte Pinto, M. Peschke, T. Kröll, V. Bagnoud, C. Rödel and M. Roth, "Demonstration of non-destructive and isotope-sensitive material analysis using a short-pulsed laser-driven epi-thermal neutron source," *Nature Communications,* vol. 13, no. 1, p. 1173, 2022.

[183] J. Kawanaka, N. Miyanaga, H. Azechi, T. Kanabe, T. Jitsuno, K. Kondo, Y. Fujimoto, N. Morio, S. Matsuo, Y. Kawakami, R. Mizoguchi, K. Tauchi, M. Yano, S. Kudo and Y. Ogura, "3.1-kJ chirped-pulse power amplification in the LFEX laser," *Journal of Physics: Conference Series,* vol. 112, no. 3, p. 032006, 2008.

[184] M. Zimmer, "Laser-Driven Neutron Sources - A Compact Approach to Non-Destructive Material Analysis," p. 57, 2020.

[185] B. Martinez, S. N. Chen, S. Bolaños, N. Blanchot, G. Boutoux, W. Cayzac, C. Courtois, X. Davoine, A. Duval, V. Horny, I. Lantuejoul, L. Le Deroff, P. E. Masson-Laborde, G. Sary, B. Vauzour, R. Smets, L. Gremillet and J. Fuchs, "Numerical investigation of spallation neutrons generated from petawatt-scale laser-driven proton beams," *Matter and Radiation at Extremes,* vol. 7, no. 2, p. 024401, 2021.

[186] V. Horný, S. N. Chen, X. Davoine, V. Lelasseux, L. Gremillet and J. Fuchs, "High-flux neutron generation by laser-accelerated ions from single- and double-layer targets," *Scientific Reports,* vol. 12, no. 1, p. 19767, 2022.

[187] A. Yogo, S. R. Mirfayzi, Y. Arikawa, Y. Abe, T. Wei, T. Mori, Z. Lan, Y. Hoonoki, D. O. Golovin, K. Koga, Y. Suzuki, M. Kanasaki, S. Fujioka, M. Nakai, T. Hayakawa, K. Mima, H. Nishimura, S. Kar and R. Kodama, "Single shot radiography by a bright source of laser-driven thermal neutrons and X-rays," *Applied Physics Express,* vol. 14, no. 10, p. 106001, 2021.

[188] International Atomic Energy Agency, Development opportunities for small and medium scale accelerator driven neutron sources, Vienna: TECDOC Series, 2005.

[189] G. Mank, G. Bauer and F. Mulhauser, "Accelerators for Neutron Generation and Their Applications," *Reviews of Accelerator Science and Technology,* vol. 04, no. 01, pp. 219-233, 2011.

[190] D. J. Thomas, R. Nolte and V. Gressier, "What is neutron metrology and why is it needed?," *Metrologia,* vol. 48, no. 6, p. S225, 2011.

[191] J. A. Frenje, C. K. Li, F. H. Séguin, D. G. Hicks, S. Kurebayashi, R. D. Petrasso, S. Roberts, V. Y. Glebov, D. D. Meyerhofer, T. C. Sangster, J. M. Soures, C. Stoeckl, C. Chiritescu, G. J. Schmid and R. A. Lerche, "Absolute measurements of neutron yields from DD and DT implosions at the OMEGA laser facility using CR-39 track detectors," *Review of Scientific Instruments,* vol. 73, no. 7, pp. 2597-2605, 2002.

[192] D. P. Higginson, R. Lelièvre, L. Vassura, M. M. Gugiu, M. Borghesi, L. A. Bernstein, D. L. Bleuel, B. L. Goldblum, A. Green, F. Hannachi, S. Kar, S. Kisyov, L. Quentin, M. Schroer, M. Tarisien, O. Willi, P. Antici, F. Negoita, A. Allaoua and J. Fuchs, "Global characterization of a laser-generated neutron source," *Journal of Plasma Physics,* vol. 90, no. 3, p. 905900308, 2024.

[193] S. Gaillard, J. Fuchs, N. Renard-Le Galloudec and T. E. Cowan, "Study of saturation of CR39 nuclear track detectors at high ion fluence and of associated artifact patterns," *Review of Scientific Instruments,* vol. 78, no. 1, p. 013304, 2007.

[194] H. Ing, R. A. Noulty and T. D. McLean, "Bubble detectors — A maturing technology," *Radiation Measurements,* vol. 27, no. 1, pp. 1-11, 1997.

[195] Bubble Technology Industries, "Bubble Detectors Neutron Dosimeters," 2009. [Online]. Available: https://www.bubbletech.ca/wp-

content/uploads/2022/04/BTI_BUBBLE_General_2007-May-07_A.pdf. [Accessed 30 08 2024].

[196] International Organization for Standardization, "Neutron reference radiation fields - Part 3: Calibration of area and personal dosemeters and determination of their response as a function of neutron energy and angle of incidence (ISO 8529-3:2023)," 2023.

[197] F. d'Errico, "Radiation dosimetry and spectrometry with superheated emulsions," *Nuc. Instrum. Meth. B,* vol. 184, no. 1, pp. 229-254, 2001.

[198] C. Di and Augusto, "Characterization of a stilbene organic scintillator for use as a broadband neutron spectrometer in mixed radiations fields," 2022.

[199] N. Zaitseva, A. Glenn, L. Carman, R. Hatarik, S. Hamel, M. Faust, B. Schabes, N. Cherepy and S. Payne, "Pulse Shape Discrimination in Impure and Mixed Single-Crystal Organic Scintillators," *IEEE Transactions on Nuclear Science,* vol. 58, no. 6, pp. 3411-3420, 2011.

[200] J. B. Birks, The Theory and Practice of Scintillation Counting, Pergamon, 1964.

[201] C. N. Chou, "The Nature of the Saturation Effect of Fluorescent Scintillators," *Physical Review Journals Archive,* vol. 87, no. 5, pp. 904-905, 1952.

[202] O. Landoas, V. Yu Glebov, B. Rossé, M. Briat, L. Disdier, T. C. Sangster, T. Duffy, J. G. Marmouget, C. Varignon, X. Ledoux, T. Caillaud, I. Thfoin and J.-L. Bourgade, "Absolute calibration method for laser megajoule neutron yield measurement by activation diagnostics," *Review of Scientific Instruments,* vol. 82, no. 7, p. 073501, 2011.

[203] D. L. Bleuel, C. B. Yeamans, L. A. Bernstein, R. M. Bionta, J. A. Caggiano, D. T. Casey, G. W. Cooper, O. B. Drury, J. A. Frenje, C. A. Hagmann, R. Hatarik, J. P. Knauer, M. G. Johnson, K. M. Knittel, R. J. Leeper, J. M. McNaney and M. Moran, "Neutron activation diagnostics at the National Ignition Facility," *Review of Scientific Instruments,* vol. 83, no. 10, p. 10D313, 2012.

[204] International Atomic Energy Agency, Dosimetry for Criticality Accidents, Vienna: Technical Reports Series, 1982.

[205] M. Buxerolle, J. Kurdjian and J.-C. Colonges, "La dosimétrie de zone SNAC2 - Principe, description, utilisation," Institut de Protection et de Sûreté Nucléaire, Centre d'Études Nucléaires de Cadarache, 1991.

[206] N. Soppera, M. Bossant and E. Dupont, "JANIS 4: An Improved Version of the NEA Java-based Nuclear Data Information System," *Nuclear Data Sheets,* vol. 120, pp. 294-296, 2014.

[207] N. Otuka, E. Dupont, V. Semkova, B. Pritychenko, A. Blokhin, M. Aikawa, S. Babykina, M. Bossant, G. Chen, S. Dunaeva, R. Forrest, T. Fukahori, N. Furutachi, S. Ganesan, Z. Ge, O. Gritzay, M. Herman, S. Hlavač, K. Katō, B. Lalremruata and Y. Lee, "Towards a More Complete and Accurate Experimental Nuclear Reaction Data Library (EXFOR): International Collaboration Between Nuclear Reaction Data Centres (NRDC)," *Nuclear Data Sheets,* vol. 120, pp. 272-276, 2014.

[208] National Nuclear Data Center, Brookhaven National Laboratory, "NuDat (Nuclear Structure and Decay Data," 18 03 2008. [Online]. Available: https://www.nndc.bnl.gov/nudat3/. [Accessed 04 09 2024].

[209] S. Agostinelli, J. Allison, K. Amako, J. Apostolakis, H. Araujo, P. Arce, M. Asai, D. Axen, S. Banerjee, G. Barrand, F. Behner, L. Bellagamba, J. Boudreau, L. Broglia, A. Brunengo, H. Burkhardt, S. Chauvie, J. Chuma, R. Chytracek, G. Cooperman and G. Cosmo, "Geant4 - A simulation toolkit," *Nuc. Instrum. Meth. A,* vol. 506, no. 3, pp. 250-303, 2003.

[210] M. E. Rising, J. C. Armstrong, S. R. Bolding, F. B. Brown, J. S. Bull, T. P. Burke, A. R. Clark, D. A. Dixon, R. A. a. G. J. F. Forster, T. S. Grieve, H. G. Hughes, C. J. Josey, J. A. Kulesza, R. L. Martz and A. P. McCartney, "MCNP, a general Monte Carlo code for neutron and photon transport: a summary," Los Alamos National Laboratory, 2023.

[211] V. Lacoste and V. Gressier, "Experimental characterization of the IRSN long counter for the determination of the neutron fluence reference values at the AMANDE facility," *Radiation Measurements,* vol. 45, no. 10, pp. 1254-1257, 2010.

[212] T. Vidmar, "EFFTRAN - A Monte Carlo efficiency transfer code for gamma-ray spectrometry," *Nuc. Instrum. Meth. A,* vol. 550, no. 3, pp. 603-608, 2005.

[213] S. Chagren, M. Ben Tekaya, N. Reguigui and F. Gharbi, "Efficiency transfer using the GEANT4 code of CERN for HPGe gamma spectrometry," *Applied Radiation and Isotopes,* vol. 107, pp. 359-365, 2016.

[214] L. Moens, J. De Donder, L. Xi-lei, F. De Corte, A. De Wispelaere, A. Simonits and J. Hoste, "Calculation of the absolute peak efficiency of gamma-ray detectors for different counting geometries," *Nuclear Instruments and Methods in Physics Research,* vol. 187, no. 2, pp. 451-472, 1981.

[215] A. J. M. Plompen, O. Cabellos, C. De Saint Jean, M. Fleming, A. Algora, M. Angelone, P. Archier, E. Bauge, O. Bersillon, A. Blokhin, F. Cantargi, A. Chebboubi, C. Diez, H. Duarte, E. Dupont, J. Dyrda, B. Erasmus, L. Fiorito and U. Fischer, "The joint evaluated fission and fusion nuclear data library, JEFF-3.3," *The European Physical Journal A,* vol. 56, no. 7, p. 181, 2020.

[216] D. Brown, M. Chadwick, R. Capote, A. Kahler, A. Trkov, M. Herman, A. Sonzogni, Y. Danon, A. Carlson, M. Dunn, D. Smith, G. Hale, G. Arbanas, R. Arcilla, C. Bates, B. Beck, B. Becker, F. Brown, R. Casperson, J. Conlin and D. Cullen, "ENDF/B-VIII.0: The 8th Major Release of the Nuclear Reaction Data Library with CIELO-project Cross Sections, New Standards and Thermal Scattering Data," *Nuclear Data Sheets,* vol. 148, pp. 1-142, 2018.

[217] A. Koning, D. Rochman, J.-C. Sublet, N. Dzysiuk, M. Fleming and S. van der Marck, "TENDL: Complete Nuclear Data Library for Innovative Nuclear Science and Technology," *Nuclear Data Sheets,* vol. 155, pp. 1-55, 2019.

[218] A. Trkov, P. Griffin, S. Simakov, L. Greenwood, K. Zolotarev, R. Capote, D. Aldama, V. Chechev, C. Destouches, A. Kahler, C. Konno, M. Koštál, M. Majerle, E. Malambu, M. Ohta, V. Pronyaev, V. Radulović, S. Sato, M. Schulc and E. Šimečková, "IRDFF-II: A New Neutron Metrology Library," *Nuclear Data Sheets,* vol. 163, pp. 1-108, 2020.

[219] C. Varignon, X. Ledoux, I. Lantuéjoul, G. Alloy, N. Arnal, I. Bailly, J. Baldys, D. Boutet, J. Brisset, F. Goffart, V. Jacob, J. Laborie, J. Lochard, J. Marmouget and P. Pras, "A new neutron beam line for (n,xn) reaction studies," *Nuc. Instrum. Meth. B,* vol. 248, no. 2, pp. 329-335, 2006.

[220] M. Reginatto, B. Wiegel, A. Zimbal and F. Langner, UMG 33, Analysis of data measured with spectrometers using unfolding techniques, Manual of the UMG package, Braunschweig: PTB, 2004.

[221] M. Reginatto, P. Goldhagen and S. Neumann, "Spectrum unfolding, sensitivity analysis and propagation of uncertainties with the maximum entropy deconvolution code MAXED," *Nuc. Instrum. Meth. A,* vol. 476, no. 1, pp. 242-246, 2002.

[222] M. Bouhadida, A. Mazzi, M. Brovchenko, T. Vinchon, M. Z. Alaya, W. Monange and F. Trompier, "Neutron spectrum unfolding using two architectures of convolutional neural networks," *Nuclear Engineering and Technology,* vol. 55, no. 6, pp. 2276-2282, 2023.

[223] J. Wang, Y. Zhou, Z. Guo and H. Liu, "Neutron spectrum unfolding using three artificial intelligence optimization methods," *Applied Radiation and Isotopes,* vol. 147, pp. 136-143, 2019.

[224] S. A. Hosseini, "Neutron spectrum unfolding using artificial neural network and modified least square method," *Radiation Physics and Chemistry,* vol. 126, pp. 75-84, 2016.

[225] S. Vallières, M. Salvadori, P. Puyuelo-Valdes, S. Payeur, S. Fourmaux, F. Consoli, C. Verona, E. d'Humières, M. Chicoine, S. Roorda, F. Schiettekatte and P. Antici, "Thomson parabola

and time-of-flight detector cross-calibration methodology on the ALLS 100 TW laser-driven ion acceleration beamline," *Review of Scientific Instruments,* vol. 91, no. 10, p. 103303, 2020.

[226] J. F. Ziegler, M. Ziegler and J. Biersack, "SRIM – The stopping and range of ions in matter (2010)," *Nuc. Instrum. Meth. B,* vol. 268, no. 11, pp. 1818-1823, 2010.

[227] Eljen Technology, "Boron Loaded EJ-254," [Online]. Available: https://eljentechnology.com/products/plastic-scintillators/ej-254. [Accessed 13 09 2024].

[228] ET Enterprises, "9112B Series," [Online]. Available: https://et-enterprises.com/products/photomultipliers/product/p9112b-series. [Accessed 13 09 2024].

[229] Pico Technology, "PicoScope 6000E Series ultra-deep-memory oscilloscopes," [Online]. Available: https://www.picotech.com/oscilloscope/6000/picoscope-6000-overview. [Accessed 13 09 2024].

[230] A. Mancic, J. Robiche, P. Antici, P. Audebert, C. Blancard, P. Combis, F. Dorchies, G. Faussurier, S. Fourmaux, M. Harmand, R. Kodama, L. Lancia, S. Mazevet, M. Nakatsutsumi, O. Peyrusse, V. Recoules, P. Renaudin, R. Shepherd and J. Fuchs, "Isochoric heating of solids by laser-accelerated protons: Experimental characterization and self-consistent hydrodynamic modeling," *High Energy Density Physics,* vol. 6, no. 1, pp. 21-28, 2010.

[231] A. Lévy, T. Ceccotti, P. D'Oliveira, F. Réau, M. Perdrix, F. Quéré, P. Monot, M. Bougeard, H. Lagadec, P. Martin, J.-P. Geindre and P. Audebert, "Double plasma mirror for ultrahigh temporal contrast ultraintense laser pulses," *Optics Letters,* vol. 32, no. 3, pp. 310-312, 2007.

[232] F. Nürnberg, M. Schollmeier, E. Brambrink, A. Blažević, D. C. Carroll, K. Flippo, D. C. Gautier, M. Geißel, K. Harres, B. M. Hegelich, O. Lundh, K. Markey, P. McKenna, D. Neely, J. Schreiber and M. Roth, "Radiochromic film imaging spectroscopy of laser-accelerated proton beams," *Review of Scientific Instruments,* vol. 80, no. 3, p. 033301, 2009.

[233] S. Vallières, C. Bienvenue, P. Puyuelo-Valdes, M. Salvadori, E. d'Humières, F. Schiettekatte and P. Antici, "Low-energy proton calibration and energy-dependence linearization of EBT-XD radiochromic films," *Review of Scientific Instruments,* vol. 90, no. 8, p. 083301, 2019.

[234] CAEN, "VX1730 / VX1730S," [Online]. Available: https://www.caen.it/products/vx1730/. [Accessed 16 09 2024].

[235] W. ZHUO, W. LIU, G. HUANG, G. ZHU and G. MA, "Comparisons of dosimetric properties between GD-300 series of radiophotoluminescent glass detectors and GR-200 series of thermoluminescent detectors," *Nuclear Science and Techniques,* vol. 18, no. 6, pp. 362-365, 2007.

[236] V. Lelasseux, P.-A. Söderström, S. Aogaki, K. Burdonov, M. Cerchez, S. N. Chen, S. Dorard, A. Fazzini, M. Gugiu, S. Pikuz, F. Rotaru, O. Willi, F. Negoita and J. Fuchs, "Design and commissioning of a neutron counter adapted to high-intensity laser matter interactions," *Review of Scientific Instruments,* vol. 82, no. 11, p. 113303, 2021.

[237] J. Vyskočil, O. Klimo and S. Weber, "Simulations of bremsstrahlung emission in ultra-intense laser interactions with foil targets," *Plasma Physics and Controlled Fusion,* vol. 60, no. 5, p. 054013, 2018.

[238] S. N. Ryazantsev, A. S. Martynenko, M. V. Sedov, I. Y. Skobelev, M. D. Mishchenko, Y. S. Lavrinenko, C. D. Baird, N. Booth, P. Durey, L. N. K. Döhl, D. Farley, K. L. Lancaster, P. McKenna, C. D. Murphy, T. A. Pikuz, C. Spindloe, N. Woolsey and S. A. Pikuz, "Absolute keV x-ray yield and conversion efficiency in over dense Si sub-petawatt laser plasma," *Plasma Physics and Controlled Fusion,* vol. 64, no. 10, p. 105016, 2022.

[239] M. Chen, Z.-M. Shenga, J. Zheng, Y.-Y. Ma, M. A. Bari, Y.-T. Li and J. Zhang, "Surface electron acceleration in relativistic laser-solid interactions," *Optics Express,* vol. 14, no. 7, pp. 3093-3098, 2006.

[240] D. A. Serebryakov, E. N. Nerush and I. Y. Kostyukov, "Near-surface electron acceleration during intense laser–solid interaction in the grazing incidence regime," *Physics of Plasmas,* vol. 24, no. 12, p. 123115, 2017.

[241] M. Thévenet, A. Leblanc, S. Kahaly, H. Vincenti, A. Vernier, F. Quéré and J. Faure, "Vacuum laser acceleration of relativistic electrons using plasma mirror injectors," *Nature Physics,* vol. 12, no. 4, pp. 355-360, 2016.

[242] P. Puyuelo-Valdes, S. Vallières, M. Salvadori, S. Fourmaux, S. Payeur, J.-C. Kieffer, F. Hannachi and P. Antici, "Combined laser-based X-ray fluorescence and particle-induced X-ray emission for versatile multi-element analysis," *Scientific Reports,* vol. 11, no. 1, p. 9998, 2021.

[243] D. L. Williams, C. M. Brown, D. Tong, A. Sulyman and C. K. Gary, "A Fast Neutron Radiography System Using a High Yield Portable DT Neutron Source," *Journal of Imaging,* vol. 6, no. 12, 2020.

[244] R. Zboray, R. Adams and Z. Kis, "Scintillator screen development for fast neutron radiography and tomography and its application at the beamline of the 10 MW BNC research reactor," *Applied Radiation and Isotopes,* vol. 140, pp. 215-223, 2018.

[245] K. Bergaoui, N. Reguigui, C. K. Gary, J. T. Cremer, J. H. Vainionpaa and M. A. Piestrup, "Design, testing and optimization of a neutron radiography system based on a Deuterium–Deuterium (D–D) neutron generator," *Journal of Radioanalytical and Nuclear Chemistry,* vol. 299, no. 1, pp. 41-51, 2014.

[246] T. S. Alvarenga, I. O. Polo, W. W. Pereira and L. V. Caldas, "Use of Monte Carlo simulation and the Shadow-Cone Method to evaluate the neutron scattering correction at a calibration laboratory," *Radiation Physics and Chemistry,* vol. 170, p. 108624, 2020.

[247] S. I. Kim, B. H. Kim, J. L. Kim and J. I. Lee, "A review of neutron scattering correction for the calibration of neutron survey meters using the shadow cone method," *Nuclear Engineering and Technology,* vol. 47, no. 7, pp. 939-944, 2015.

[248] L. Vassura, "Generation and characterization of short-duration and high-brightness laser-driven neutron sources," p. p.66, 2018.

List of contributions

Publications

- **A Comprehensive Characterization of the Neutron Fields Produced by the Apollon Petawatt Laser**
  R. Lelièvre, W. Yao, T. Waltenspiel, I. Cohen, V. Anthonippillai, A. Beck, E. Cohen, D. Michaeli, I. Pomerantz, D. C. Gautier, F. Trompier, Q. Ducasse, P. Koseoglou, P.-A. Soderstrom, F. Mathieu, A. Allaoua and Julien Fuchs
  European Physical Journal Plus, vol.139, no.11, p.1035, 2024
  https://doi.org/10.1140/epjp/s13360-024-05679-x

- **High repetition-rate 0.5 Hz broadband neutron source driven by the Advanced Laser Light Source**
  R. Lelièvre, E. Catrix, S. Vallières, S. Fourmaux, A. Allaoua, V. Anthonippillai, P. Antici, Q. Ducasse and J. Fuchs
  Physics of Plasmas, vol.31, no.9, p.093106, 2024
  https://doi.org/10.1063/5.0218582

- **Global characterization of a laser-generated neutron source**
  D. P. Higginson, R. Lelièvre, L. Vassura, M. M. Gugiu, M. Borghesi, L. A. Bernstein, D. L. Bleuel, B. L. Goldblum, A. Green, F. Hannachi, S. Kar, S. Kisyov, L. Quentin, M. Schroer, M. Tarisien, O. Willi, P. Antici, F. Negoita, A. Allaoua and J. Fuchs
  Journal of Plasma Physics, vol.90, no.8, p.905900308, 2024
  https://doi.org/10.1017/S0022377824000618

- **Enhanced Energy, Conversion Efficiency and Collimation of Protons Driven by High-Contrast and Ultrashort Laser Pulses**
  W. Yao, R. Lelièvre, T. Waltenspiel, I. Cohen, A. Allaoua, P. Antici, A. Beck, E. Cohen, X. Davoine, E. d’Humières, Q. Ducasse, E. Filippov, D. C. Gautier, L. Gremillet, P. Koseoglou, D. Michaeli, D. Papadopoulos, S. Pikuz, I. Pomerantz, F. Trompier, Y. Yuan, F. Mathieu and J. Fuchs
  Applied Sciences, vol.14, no.14, 2024
  https://doi.org/10.3390/app14146101

- **Absolute calibration up to 20 MeV of an online readout CMOS system suitable to detect high-power lasers accelerated protons**
  K. Burdonov, R. Lelièvre, P. Forestier-Colleoni, T. Ceccotti, M. Cuciuc, L. Lancia, W. Yao and J. Fuchs
  Review of Scientific Instruments, vol.94, no.8, p.083303, 2023
  https://doi.org/10.1063/5.0150373

- **Experimental capabilities of the LMJ-PETAL facility**
  W. Cayzac, G. Boutoux, S. Brygoo, A. Denoeud, S. Depierreux, V. Tassin, F. Albert, E. Alozy, C. Baccou, D. Batani, N. Blanchot, M. Bonneau, M. Bonnefille, R. Botrel, C. Bowen, P. Bradford, M. Brochier, T. Caillaud, A. Chaleil, S. Chardavoine, C. Chollet, C. Courtois, S. Darbon, X. Davoine, S. Debesset, V. Denis, R. Diaz, A. Dizière, R. Du Jeu, W. Duchastenier, P. Dupré, A. Duval, C. Esnault, B. Etchessahar, M. Ferri, J. Fuchs, I. Geoffray, L. Gremillet, A. Grolleau, E. D'Humières, T. Jalinaud, S. Laffite, M. Lafon, M. A. Lagache, O. Landoas, I. Lantuejoul, L. Le-Deroff, S. Le Tacon, J.P. Leidinger, R. Lelièvre, S. Liberatore, B. Mahieu, P.E. Masson-Laborde, C. Meyer, J. L. Miquel, R. Parreault, F. Philippe, V. Prévot, P. Prunet, O. Raphaël, C. Reverdin, L. Ribotte, R. Riquier, C. Rousseaux, G. Sary, G. Soullié, M. Sozet, K. Ta-Phuoc, J. Trela, V. Trauchessec, X. Vaisseau, B. Vauzour, B. Villette and E. Lefebvre
  High Energy Density Physics, vol.52, p.101125, 2024
  https://doi.org/10.1016/j.hedp.2024.101125

- **Saturation of the compression of two interacting magnetic flux tubes evidenced in the laboratory**
  A. Sladkov, C. Fegan, W. Yao, A.F.A. Bott, S. N. Chen, H. Ahmed, E.D. Filippov, R. Lelièvre, P. Martin, A. McIlvenny, T. Waltenspiel, P. Antici, M. Borghesi, S. Pikuz, A. Ciardi, E. d'Humières, A. Soloviev, M. Starodubtsev and J. Fuchs
  Nature Communications, vol. 15, p.10065, 2024
  https://doi.org/10.1038/s41467-024-53938-3

- **Characterization and performance of the Apollon main short-pulse laser beam following its commissioning at 2 PW level**
  W. Yao, R. Lelièvre, I. Cohen, T. Waltenspiel, A. Allaoua, P. Antici, Y. Ayoul, A. Beck, A. Beluze, C. Blancard, D. Cavanna, M. Chabanis, S. N. Chen, E. Cohen, Q. Ducasse, M. Dumergue, F. El Hai, C. Evrard, E. Filippov, A. Freneaux, D. C. Gautier, F. Gobert, F. Goupille, M. Grech, L. Gremillet, Y. Heller, E. d'Humières, H. Lahmar, L. Lancia, N. Lebas, L. Lecherbourg, S. Marchand, D. Mataja, G. Meyniel, D. Michaeli, D. Papadopoulos, F. Perez, S. Pikuz, I. Pomerantz, P. Renaudin, L. Romagnani, F. Trompier, E. Veuillot, T. Vinchon, F. Mathieu and J. Fuchs
  Submitted to Physics of Plasmas
  https://doi.org/10.48550/arXiv.2412.09267

Presentations

- **League of advanced European Neutron Sources (LENS) Workshop on Laser-Driven Neutron Sources**
  Characterization of neutron generation at Apollon
  1-3 March 2023
  Lund, Sweden

- **Journées des Thèses de l'IRSN 2023**
  Mesure des émissions de neutrons produits par lasers extrêmes
  28-31 March 2023
  La Grande-Motte, France

- **LMJ-PETAL User Meeting**
  Assessment of neutron production using the high-energy PETAL laser
  8-9 June 2023
  Bordeaux, France

- **Groupement de Recherche Accélérateurs Plasma PompÉs par Lasers (GdR APPEL)**
  Characterization of neutron emissions produced by ultra-intense lasers
  13-15 November 2023
  Saclay, France

- **Journées des Thèses de l'IRSN 2024**
  Caractérisation des émissions de neutrons produits par lasers extrêmes
  2-5 April 2024
  Arles, France

- **Journées Scientifiques du Neutron**
  Characterization of neutron emissions produced at the Apollon laser facility
  2-4 October 2024
  Saint-Paul-Lez-Durance, France

ECOLE
DOCTORALE

Titre : Caractérisation des émissions de neutrons produites par laser

Mots clés : lasers de puissance, sources de neutrons, détecteurs de neutrons, interactions laser-plasma

Résumé : Les lasers ultra-intenses représentent un nouveau moyen de produire des champs neutroniques, plus compact que les réacteurs nucléaires ou les accélérateurs et avec moins de contraintes radiologiques que ces sources conventionnelles. Le champ électrique créé par une impulsion laser ultra-intense au sein d'une cible de taille micrométrique peut atteindre plusieurs TV/m, permettant l'accélération de protons de plusieurs dizaines de MeV. Ces protons peuvent ensuite être interceptés par une seconde cible, appelée convertisseur, dans laquelle ils induisent des réactions nucléaires et donc la production de neutrons. Cette technique, dite du « pitcher-catcher », est ainsi capable de générer des flux très intenses (> 10^{17} n/cm^2/s) à des énergies allant jusqu'à quelques dizaines de MeV, permettant alors d'envisager des applications diverses telles que l'imagerie neutronique ou la reproduction en laboratoire du processus rapide de nucléosynthèse responsable de la création des éléments les plus lourds.

Pour prouver la faisabilité de ces applications et afin d'assurer la radioprotection de ces installations laser, il est nécessaire de caractériser ces champs neutroniques. Les détecteurs passifs, ou munis d'une électronique ultra-rapide, semblent être des candidats de choix pour s'adapter aux caractéristiques des sources de neutrons produits par laser (émissions très brèves et intenses, environnement bruité, …).

Ce travail de thèse s'articule donc autour de la poursuite du développement d'un spectromètre neutron par activation (SPAC), particulièrement adapté pour mesurer des champs neutroniques intenses avec une forte composante gamma. En complément d'un travail de simulation des termes sources attendues et de la réponse des détecteurs via l'utilisation des codes Monte-Carlo Geant4 et MCNP, des dosimètres à bulles, un dispositif de Temps de Vol ainsi que des échantillons d'activation ont été utilisés sur diverses installations laser telles que ALLS (Canada) et Apollon (France), afin d'optimiser et de caractériser les émissions neutroniques générées.

Title: Characterization of laser-driven neutron emissions

Keywords: ultra-intense lasers, neutrons, laser-driven neutron sources, detection, nuclear physics

Abstract: Ultra-intense lasers represent a new way to produce neutron fields, more compact than nuclear reactors or accelerators and with fewer radiological constraints than these conventional sources. The electric field induced by an ultra-intense laser pulse within a micrometer-sized target can reach several TV/m, allowing for the acceleration of protons to several tens of MeV. These protons can then be intercepted by a second target, called a converter, in which they induce nuclear reactions and thus produce neutrons. This technique, known as the pitcher-catcher technique, is capable of generating very intense fluxes (> 10^{17} n/cm^2/s) at energies up to several tens of MeV, making it possible to envision applications such as neutron imaging or the laboratory reproduction of the rapid nucleosynthesis process responsible for the creation of the heaviest elements.

To demonstrate the feasibility of these applications and ensure the radiological protection of these laser facilities, these neutron fields must be optimally characterized. Detectors with ultra-fast electronics or passive detectors appear to be most compatible to the characteristics of laser-driven neutron sources (very brief and intense emissions, noisy environment, etc.).

This thesis work focuses on optimizing the development of a neutron activation spectrometer (SPAC), particularly suitable for measuring intense neutron fields with a strong gamma component. In addition to simulations of the expected source terms and detector responses using Geant4 and MCNP Monte Carlo codes, bubble dosimeters, Time-of-Flight detectors and activation samples were used on various laser facilities such as ALLS (Canada) and Apollon (France), to optimize and characterize the produced neutron emissions.

Institut Polytechnique de Paris
91120 Palaiseau, France